DEVELOPMENT OF MULTIFUNCTIONAL CALCIUM PHOSPHATE PARTICLES FOR DRUG DELIVERY AND FORMATION OF CROSS-LINKED MATERIALS

by

RICHARD LEE WILLIAMS

A thesis submitted to
University of Birmingham
for the degree of
DOCTOR OF PHILOSOPHY

School of Chemical Engineering
College of Engineering and Physical Sciences
University of Birmingham
March 2014

UNIVERSITY OF
BIRMINGHAM

University of Birmingham Research Archive

e-theses repository

This unpublished thesis/dissertation is copyright of the author and/or third parties. The intellectual property rights of the author or third parties in respect of this work are as defined by The Copyright Designs and Patents Act 1988 or as modified by any successor legislation.

Any use made of information contained in this thesis/dissertation must be in accordance with that legislation and must be properly acknowledged. Further distribution or reproduction in any format is prohibited without the permission of the copyright holder.

Abstract

Calcium phosphates (CaPs) have been used extensively as bone replacement materials, substrates for drug release and transfection agents because of their non-cytotoxic nature and chemical similarity to the mineral component of human bone. However, biomolecule attachment to CaPs usually rely upon adsorption, which can lead to inconsistent coverage and variable release, and the fate of CaPs upon cellular internalisation is not fully understood. The difficulty in tracking the particles can be related to the visual similarity to granulation within the cells.

This thesis sought to modify the surface of CaP particles with (3-mercaptopropyl)trimethoxysilane (MPTS) to enable the engraftment of biomolecules onto the particle surface and the formation of a cross-linked matrix. The engraftment of a thiol-reactive fluorescent dye gave visual confirmation that molecules can be bound to the surface and enabled silicon-substituted hydroxyapatite (SiHA) particle tracking within MC3T3 cells. Volume and size distribution analysis suggested that internalised particles $>1\mu$m, but not encapsulated within lysosomes, correlated with observations of cell death. The method was expanded for other CaPs and demonstrated through engraftment of a novel antimicrobial peptide, which was shown to be more effective at preventing biofilm formation than surface adsorbed peptide, and the fabrication of a new organic/inorganic composite.

Acknowledgements

Many thanks to my supervisor Prof. Liam Grover who has provided invaluable guidance and support during the challenge to complete my PhD in two years. No doubt that he has helped shape the researcher I am today. I would like to thank other members of staff who co-supervised my research including Dr. Joshua Rappoport, Dr. Hamid Dehghani and Prof. Paula Mendes. Thanks to my fellow office colleagues who have been part of a close knit group full of support and laughs during my PhD - especially the office banter with Erik Hughes, Parastoo Jamshidi, Amir Anvarian and Alistair Bannerman. Parastoo ('Paras'), has been like a big sister to me in my time in the group - thanks for the constant exchange of jokes, support and, of course, for teaching me Farsi. I am particularly grateful to Dr. Jennifer Paxton for sharing her immense knowledge and guidance for the step up to being a Post-doc. Also thanks to Erik Hughes for our numerous lab sessions testing our 'back of the envelope ideas' - They always remind me why I love science so much.

It has been a pleasure to be part of PSIBS and I'd like to put forward my gratitude to fellow PSIBS members for many intellectual discussions and social shenanigans. Special thanks to Jonathan Robinson (my PSIBS 'buddy') for his support over the last few years and Eric Pitkeathley as the co-founder of the hugely successful 'thesis-club' (consisting of two members). Special thanks also for access to equipment: Dr. Alan Smith (University of Huddersfield - zeta sizer); Jackie Deans and Adrian Wright (access to XRD), Stuart Arkless (access to AM1 lab) and Dr. Javier Salado (Zientzia eta Teknologia Fakultatea - free lab equipment)

I have had the privilege to meet some great people at conferences including: Uwe Gbureck (and his group), Frank Müller, Jake Barralet, Dave Basset, Grace Stephenson (JRI), Luuk, Yon and Jetsma (Medics based in Maastricht) not to mention my own supervisor. Many fantastic scientific discussions and legendary nights out.

Laura Rowley has been my best friend during my PhD - her emotional support, patience and constant supply of food has been fantastic. My sincerest thanks go to my parents for their continued financial and understanding, not only during my PhD, but throughout my life so far. I wouldn't be where I am now without their years of hard work.

Publications

1. Thiol modification of silicon-substituted hydroxyapatite nanocrystals facilitates fluorescent labelling and their intracellular tracking. Richard L. Williams, Martin J. Hadley, Peggy Jiang, Neil A. Rowson, Paula Mendes, Josh Z. Rappoport and Liam M. Grover., *Journal of Materials Chemistry B*, 2013, 1, 4370-4378., DOI: 10.1039/C3TB20775G.

2. Quantification of Volume and Size Distribution of Internalised Calcium Phosphate Particles and Their Influence on Cell Fate. Richard L. Williams, Isaac Vizcaíno-Castón and Liam M. Grover., *Biomaterials Science*, [in press, DOI: 10.1039/C4BM00238E].

3. Exploration of the effects of cobalt chromium wear particles in vitro on T cell populations a possible gateway for prognostic testing. Mark J. Pearson, Richard L. Williams, Ashleigh Plunkett, David Bodansky, Hannah L. Smith, Hema Chahal, Liam M. Grover, Edward T. Davis, Janet M. Lord., *Biomaterials*, [submitted].

4. Covalent attachment of a novel antimicrobial agent to functionalised hydroxyapatite surfaces. Felicity De Cogan, Richard L. Williams, Liam M. Grover, Robert Scott, Ann Logan., [submitted].

Oral Presentations

1. "The Aggregation of Internalised Calcium Phosphate Nanoparticles Influences Biological Response", *European Orthopaedic Research Society (EORS) 22nd Annual Meeting*, 3rd July 2014, Nantes, France.

2. "Intracellular tracking of fluorescently labelled calcium phosphate particles.", *8th Combined Meeting of Orthopaedic Research Societies (CORS 2013)*. 16th October 2013, Venice, Italy.

3. "Thiol Modification of Silicon-Substituted Hydroxyapatite Nanocrystals Facilitates Fluorescent Labelling and their Intracellular Tracking.", *UK Society for Biomaterials Annual Conference*, 24th June 2013, University of Birmingham, UK.
   Won best Oral Presentation Prize.

Invited talks

1. ”Calcium Phosphates as building blocks for Implants, Drug delivery and Imaging.”, *University of Bedfordshire, UK.*, 30th October 2013.

Poster Presentations

1. ”The Aggregation of Internalised Calcium Phosphate Nanoparticles Influences Biological Response”, *The Royal Society Bionano Interactions Meeting*, 30th April - 1st May 2014, The Royal Society at Chicheley Hall, Buckinghamshire, UK.

2. ”Thiol functionalised Silicon-Substituted Hydroxyapatite (SiHA) Nanoparticles - Synthesis, Characterisation and Fluorescent Labelling for Live Cell Imaging.”, *European Society for Biomaterials 2013 - 25th European Conference on Biomaterials*, 8th-12th September 2013, Madrid, Spain.

3. ”Development of surface functionalised silicon-substituted hydroxyapatite nanoparticles for localised drug delivery.”, UK Society for Biomaterials Annual Conference, 27th-28th June 2012, University of Nottingham, UK.

4. ”Development and tracking of multifunctional calcium phosphate particles for localised drug delivery.”, *The 9th World Biomaterials Congress*, 1st-5th June 2012, Chengdu, China.

CONTENTS

LIST OF FIGURES

LIST OF TABLES

CHAPTER 1

INTRODUCTION

Calcium phosphate (CaP) ceramics such as hydroxyapatite (HA) have been used widely for the restoration of function in diseased and damaged hard tissue. In addition, they have found application in a diverse selection of sectors as food additives, adsorbents in chromatography columns and even as substrates to enable absorption of pollutants from wastewater [1, 2]. Within the biomedical sector, CaP salts have been used principally because of their similarity to the mineral component of bone and also since their dissolution products are non-toxic. Relatively recent work has seen calcium phosphate salts used for the delivery of biological materials into cells in the form of peptides, polymers and DNA sequences [3, 4, 5, 6, 7, 8]. CaP materials have a critical safety advantage over other vectors such as viruses in that they pose no risk of pathogenicity due to mutation. Although it is known that CaP-DNA complexes cause no apparent cytotoxicity, the fate of the particles on internalisation is not yet known [9]. The difficulty in tracking the particles can be related to their visual similarity to granulation within the cells [9].

The large crystal lattice of the apatites means that their structure may incorporate numerous substitutions, which can be used to tailor material chemistry to induce a particular biological reaction [10, 11, 12, 13]. One main focus of research into the development of new calcium phosphate based materials has been the substitution of silicon into the hydroxyapatite lattice ('silicon-substituted hydroxyapatite', SiHA) to enable additional biomolecule attachment and their controlled release *in vivo* [9]. Silicon-substitution is of particular interest since silicon is well established to be an important factor in the production of new bone matrix and functions to assist in the production of collagen by osteoblasts [13, 14, 15, 16]. CaP composites have been used widely as implant materials due to the low toxicity of their ionic components and

the intimate bond that they are able to form with a wide range of hard and soft tissues. Two sites in crystalline HA have been proposed with potential to introduce functionalisation; at the hydroxyl site and the phosphate site [17, 18, 19]. Previous studies have shown that the surface hydroxyl (OH) groups of HA may react with organic isocyanate groups and this has been exploited for the attachment of polymers such as poly(ethylene glycol) (PEG), poly(methyl methacrylate) (PMMA), poly(n-butyl methacrylate) (PBMA), poly(2-hydroxyethyl methacrylate) (poly(HEMA)) to the crystal surfaces [20, 21]. In addition, it has been found that substitution by alkylphosphonates causes calcium phosphate monolith structures to become mesoporous with high specific surface area [22], which is of course crucial for biological applications where cell attachment, proliferation, bioresorbability, and tissue/interface regeneration rely on materials with specific surface areas approaching that of native biomineral. Of these reagents containing hydroxyl groups, phosphoric acid based reactants are favoured because the P−OH groups facilitate the adsorption of proteins, as demonstrated for the model protein, bovine serum albumin [23]. However, the limited availability and reactivity of OH groups can result in low numbers of biomolecules being grafted on to the HA surface [7, 24]. An alternative strategy widely reported in the literature involves exploiting Ca^{2+} ions exposed at the surface of calcium phosphate (particularly HA) substrates as an attachment site for molecules of interest. For example, Lee *et al.* [7] have reported the thiol modification of HA using 3-mercaptopropionic acid and Ganesan *et al.* [8] attached porphyrins to the HA surface as a potential drug carrier. Silicon substitution has drawn much attention as a route to surface modification [25] with organosilanes, particularly those containing amino or thiol terminal groups. For example, previous work has demonstrated that osteoblast adhesion to HA is increased when functionalised with 3-aminopropyltriethoxysilane [26]. Although much attention has been given to the use of (3-mercaptopropyl)trimethoxysilane (MPTS) for the surface modification of silicon oxide [27, 28, 29], there is scarcely any research on the surface modification of calcium phosphates with MPTS [9].

Surface modification of ceramics can extend far beyond use as an imaging tool - they also enable selective attachment of peptides, polymers and drugs along with cross linking capabil-

ities for the formation of macroscale structures. Most antimicrobial agents are adsorbed on to ceramic surfaces through dip coating processes, which can lead to inconsistent coverage between batches and variation in coating stability over time while under physiological conditions. These drawbacks may hinder achieving a release period of days to weeks which may be required in some cases. There is a drive in the biomaterials field to develop implant materials that can also act as platforms for the selective attachment (or patterning) and controlled release of therapeutic drugs and ensure clinically relevant doses are administered during the healing process.

This thesis describes a method of surface modification of CaP particles to enable: 1) the engraftment of a fluorescent dye as a tool for the intracellular tracking of the particles, and 2) co-delivery of drugs in a localised manner. As such, the thesis is split into two parts as shown in the diagram in figure 1.1. The first results chapter describes the modification of SiHA with (3-mercaptopropyl)trimethoxysilane (MPTS) to present thiol groups from the particle surface and subsequent engraftment of the commercially available thiol-reactive dye, fluorescein-5-maleimide. The aim is to demonstrate how this surface modification can be used as a tool for developing a deeper understanding of particle internalisation and fate. The ability to visually discriminate between internalised material from the natural environment will be shown through live cell confocal fluorescence microscopy of MC3T3 cells in Chapter 6. Co-labelling of lysosomes and estimation of the volume and size of the internalised material through computational image analysis will provide the first insight into the fate of such materials in live cells. The second results chapter uses the surface modification method from Chapter 6 to functionlise hydroxyapatite (HA) and will demonstrate the surface modification as a foundation technology for the localised delivery of drugs. This will involve the immobilisation of a novel antimicrobial agent (developed by the University of Birmingham and the Royal Centre for Defence Medicine, Queen Elizabeth Hospital Birmingham) and a comparison of the ability of the system to resist biofilm formation against adsorbed peptide. Finally, the same modification chemistry was used for the fabrication of organic-inorganic composites and explore their potential as degradable matrices for localised drug delivery. The wider implication of this approach is the ability to

engraft drugs throughout the volume of the material rather than reliance on surface attachment alone.

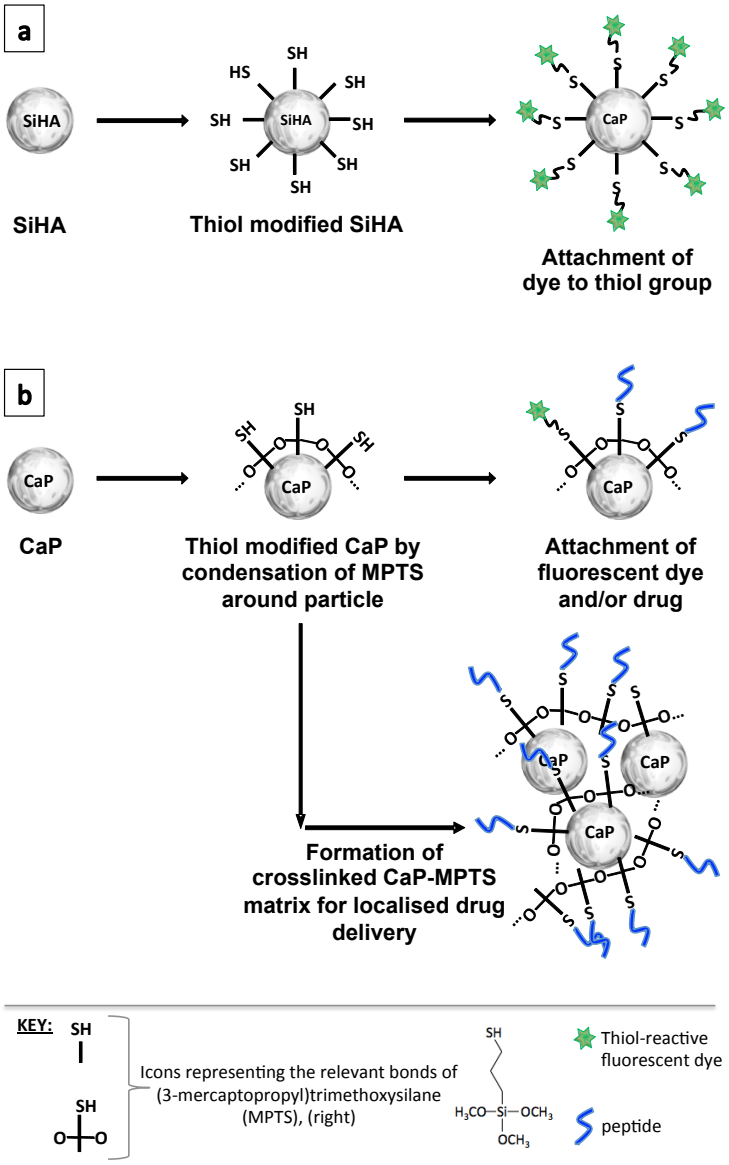

Figure 1.1: Diagram summarising the aims of the work described within this thesis. A method will be described for the surface modification of SiHA and HA to enable: a) fluorescent tagging to be used as a tool for tracking internalised particles and, b) co-delivery of drugs in a localised manner.

CHAPTER 2

CALCIUM ORTHOPHOSPHATES

Calcium phosphates (CaPs) have found use as binding agents in the food industry; adsorbents for chromatography columns and for the adsorption for pollutants in wastewater. Additionally, they are used within the biomedical industry where they act as the solid component of injectable cements; scaffolds; and coatings for metal bone implants for the repair or replacements of diseased or damaged hard tissue. Calcium phosphates can exist in many crystalline forms (as shown in Table 2.1) with each form exhibiting distinct solubility, thermal stability and density. The major mineral component of bone is *calcium-deficient* hydroxyapatite, with additional ion substitutions which influences the chemical properties of the material. Considerable efforts have been made to produce bone replacement implants and cements that mimic the structural proprieties of bone, with tuneable dissolution properties to permit natural tissue regeneration and integration.

This chapter will focus on the fundamental crystal structure of hydroxyapatite and explain why this structure enables chemical stability to be maintained while permitting ionic substitutions. The synthesis process of hydroxyapatite by chemical precipitation methods will be described. Reaction temperature, ionic strength, choice of precursor salts, initial pH and ageing time all influence the chemical pathway though various intermediate phases before hydroxyapatite forms the final product and the effects of these variables on crystallite size and shape will be explored.

Table 2.1: Table of calcium orthophosphates commonly used in tissue engineering including their chemical formula and basic chemical properties. [a] cannot be synthesised via aqueous precipitation. [b] estimation only, CDHA not found in pure form - often contains ionic substitutions which may influence solubility and density. [c] cannot be measured precisely and is dependent on exact composition and pH. Reported solubility values at given pH: 10.9-25.7 (pH 7.40), 12.2-29.9 (pH 6.00) and 13.1-32.7 (pH 5.28) [30]. [d] stable above $100\,^{\circ}\mathrm{C}$. Table amended from [31] with additional information from [30, 32, 33, 34, 35].

Calcium phosphate	Chemical formula	Space group	Density g/cm^3	Ca:P ratio	Solubility $-Log(K_sp)$ at $25\,^{\circ}\mathrm{C}$	pH stability range at $25\,^{\circ}\mathrm{C}$
Tetracalcium Phosphate (TTCP, Hilgenstockite)	$Ca_4(PO_4)_2O$	Monoclinic $P2_1$	3.05	2.00	38-44	[a]
Hydroxyapatite (HA)	$Ca_{10}(PO_4)_6OH_2$	Pseudohexagonal $P6_3/m$	3.16	1.67	116.8	9.5-12.0
Calcium-deficient Hydroxyapatite (CDHA)	$Ca_{(10-x)}(HPO_4)_x(PO_4)_{(6-x)}(OH)_{(2-x)}$, $0<x<1$.	Pseudohexagonal $P6_3/m$ [b]	[b]	1.50-1.67	85	6.5-9.5
β-Tricalcium Phosphate (β-TCP, Whitlockite)	β-$Ca_3(PO_4)_2$	Rhombohedral R3cH	3.07	1.50	28.9	[a]
α-Tricalcium Phosphate (α-TCP)	α-$Ca_3(PO_4)_2$	Monoclinic $P2_1/a$	2.86	1.50	25.5	[a]
Octacalcium Phosphate (OCP)	$Ca_8H_2(PO_4)_6 \cdot 5\,H_2O$	Triclinic P^1	2.61	1.33	96.6	5.5-7.0
Amorphous Calcium Phosphate (ACP)	$Ca_xH_y(PO_4)_z \cdot nH_2O$, n=3-4.5; 15-20% H_2O	-	-	1.00-2.20	[c]	always metastable
Dicalcium Phosphate Dihydrate (DCPD, Brushite)	$CaHPO_4 \cdot 2\,H_2O$	Monoclinic I_a	2.32	1.00	6.59	2.0-6.0
Dicalcium Phosphate (DCPA, Monetite)	$CaHPO_4$	Triclinic P^1	2.89	1.00	6.9	[d]
Monocalcium phosphate monohydrate (MCPM)	$Ca(H_2PO_4)_2 \cdot H_2O$	Triclinic P^1	2.23	0.50	1.14	0.0-2.0
Monocalcium phosphate anhydrous (MCPA)	$Ca(H_2PO_4)_2$	Triclinic P^1	2.58	0.50	1.14	[d]

2.1 Hydroxyapatite

Hydroxyapatite (HA) is a mineral belonging to the apatite family with the general chemical formula $M_5(ZO_4)_3X$, where M represents an alkaline-earth metal such as $Ca^{2+}, Sr^{2+}, Mg^{2+}$ or other metals including $Zn^{2+}Cd^{2+}$ or Pb^{2+}, ZO_4 could take the form of PO_4^{3-}, CO_3^{2-} or SO_4^{2-}, and X is OH^-, F^-, CO_3^{2-} or Cl^- [31]. Although the chemical formula for HA is $Ca_5(PO_4)_3OH$, the unit cell formula $Ca_{10}(PO_4)_6OH_2$ is more commonly used as HA is typically found as two crystal units bound together [31]. HA can exist in two crystal forms - monoclinic and hexagonal - however the monoclinic is easily destabilized by the presence of very low concentrations of foreign ions (i.e ions other than Ca^{2+}, PO_4^{3-} and OH^- native to the HA structure) and hence it is the hexagonal form which is of the most practical significance in bioengineering [36, 37]. In the hexagonal form, the ten calcium (Ca) atoms contained in the unit cell are distributed between two different crystallographic Ca^{2+} sites, which are referred to as Ca(I) and Ca(II) herein (Figure 2.1). The four Ca atoms at the Ca(I) positions are strongly bound by six oxygen atoms with an additional weaker bonding influence from a further three oxygen atoms. As a result, the Ca(I) ions are tightly confined in columns along the c-axis and exhibit the hexagonal arrangement in a plane across the c-axis. Disruption of the metal-oxygen interactions at the Ca(I) sites compromises the entire HA crystal structure and therefore only the substitutions of Ca for ions smaller than Ca (or possibly slightly larger than Ca at low concentrations) are permitted at the Ca(I) site. The six Ca(II) atoms are staggered over consecutive planes cutting the c-axis and are surrounded by seven oxygen atoms - six of them belonging to PO_4^{3-} tetrahedra and the remaining oxygen coming from an OH group. This arrangement allows for localised displacements of the Ca(II) atoms without compromising the overall crystal structure and thus permits cations larger than Ca to be substituted into the Ca(II) site [36].

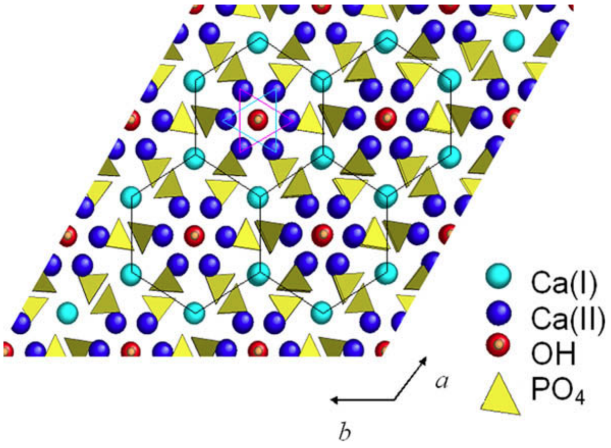

Figure 2.1: Diagram of the HA structure along the c-axis. The hexagonal form is highlighted by the black lines connecting the Ca(I) positions (cyan spheres), which are tightly confined into columns by the surrounding oxygen atoms from the PO_4^{3-} tetrahedra. The Ca(II) positions (blue spheres) are staggered down the c-axis in interlocking triangles, allowing greater structural flexibility for the substitution for larger ions. Reproduced with permission from [36]. © 2009 Elsevier Ltd. All rights reserved.

2.2 Formation of hydroxyapatite through precipitation

There is a vast array of methods available for the synthesis of HA, the most widely used methods include; wet chemical precipitation, hydrothermal processing, sol-gel and mechanical, but extend to; spray pyrolysis, magnetron sputtering, high temperature decomposition of other calcium phosphate phases, hydrolysis, reverse micro emulsion, ultrasonication, solid-state, supercritical fluid methods, electrospraying, microwave assessed, sol-gel and surfactant templated precipitation. The most widely used methods can be roughly divided into high and low temperature methods - high temperature methods involving the annealing of mixed calcium and phosphate precursor salts at around $1000°C$, while low temperature methods involve the ageing of precipitates from dissolved calcium and phosphate salts at supersaturation. Both routes have complimentary advantages and disadvantages with respect to control over final composition and physical size and shape of the particles. With high temperature methods, the required amounts of reactants to maintain stoichiometry can be accurately set, however producing nanoscopic crystals can be difficult and the high temperatures required can be considered a downside[31]. Meanwhile, precipitation methods offer greater control over crystal size and

shape in the nanoscale range through controlled changes in synthesis conditions (eg. temperature, pH; to be discussed later), but the HA product can include other intermediate calcium phosphate phases from the reaction unless the synthesis conditions are carefully controlled and the precipitate sufficiently aged in the mother solution.

Figure 2.2 shows the pathways towards crystallisation of a product and the free energy barriers involved along the way. The thermodynamic route can involve high temperature heating of the reactants which can directly result in HA as a the final product. However, precipitation follows a 'kinetic' route and involves overcoming the free energy barriers for the formation of intermediate CaP phases en route to HA which is the most stable and sparingly soluble phase over a wide range of pH values. The precipitation of HA from supersaturated solutions can be roughly divided into the following stages [31]: (i) homogeneous nucleation of CaP clusters [38, 39, 40]; (ii) aggregation of clusters to amorphous CaP [38, 39, 40, 41]; (iii) aggregation of amorphous particles into chain-like structures [39, 41, 42, 43]; (iv) growth of these structures [39, 40]; (v) secondary precipitation and phase transformation [39, 40, 43].

Several physicochemical mechanisms have been proposed as models to explain the stages of HA formation including; repeated dissolution/recrystallisation between intermediate phases, diffusion/surface mediated processes and, a transformation from intermediate phases purely through rearrangement of ions within the precipitate ending at HA (solid-solid transformation). An in-depth discussion of the history and reasoning behind each of these mechanisms and their claims to being exclusively involved in the HA formation process is beyond the scope of this section. In fact our latest understanding of HA formation reactions suggests that all three of these mechanisms play a part in the formation process, with arguably one mechanism dominant at certain stages of the formation process.

Under the Ostwald-Lussac rule, the least stable (most soluble) phase will have the highest nucleation rate when the supersaturation limit is exceeded at a particular pH and ionic concentration. Consequently, amorphous calcium phosphate is usually the first phase to form in the process and consists of randomly packed CaP clusters. This phase has a low structural order and therefore has the lowest interfacial energy (defined as the work required to increase the surface

area of a material by one unit area) compared to any of the crystalline CaPs. The amorphous phase then undergoes transformation through a series of different CaP phases before reaching a stable HA phase - this series of transformations is called the kinetic pathway. From this point a synthesis reaction can follow a number of kinetic pathways (each differing in the order of precipitation of the phases) and is dependent on the user defined pH, ionic strength, temperature and Ca:P ratio. Furthermore, the reaction can switch kinetic pathway in response to slight changes in the experimental conditions during the synthesis process.

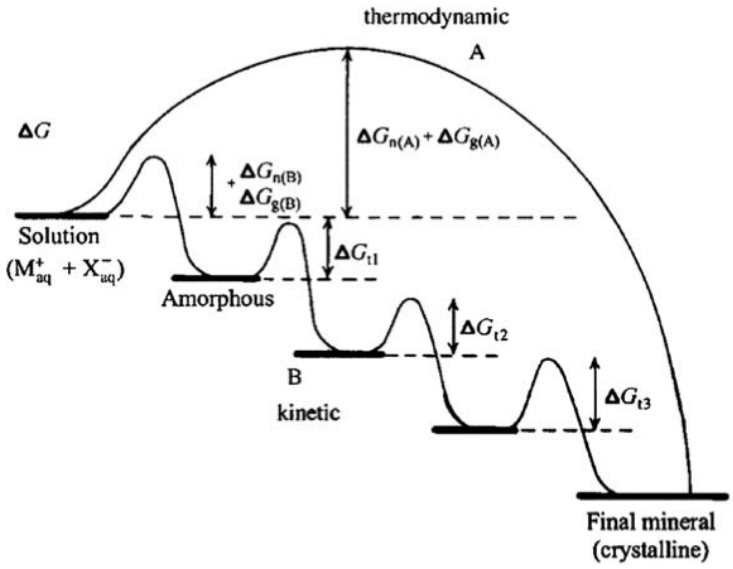

Figure 2.2: The thermodynamic (pathway A) and kinetic (pathway B) crystallisation pathways from an initial calcium and phosphate ion solution to a final crystalline mineral phase. The pathway a reaction may follow depends on the free energy of activation ΔG associated with the nucleation (n), growth (g), and phase transformation (t) processes. Reproduced with permission from [44]. © 2003 Wiley-VCH Verlag GmbH.

Typically, the transformation order of the amorphous phase to HA should follow Octacalcium phosphate (OCP) to Dicalcium Phosphate Dihydrate (DCPD) to HAP at pH $<$ 6.70 and switches to DCPD to OCP to HA at pH $>$ 6.70. The pH can actually influence the Ca:P ratio of the amorphous phase (so before any crystalline phases appear at all) and can be anywhere between 1.00 (low pH) and 1.50 (at high pH)[45], but will eventually tend towards 1.67 to form HA. This shifting of the Ca:P ratio occurs through release of phosphate species back into the bulk solution and hence the process is accelerated by increasing the pH of the reaction. Indeed

the evolution of the precipitation process induces pH changes of its own. The nucleation of CaP clusters and random packing to form of amorphous CaP particles is accompanied by a small decrease in the pH of the reaction solution as the higher alkalinity Ca ions, which dominate over the acidity of the HPO_4^{3-} ions, are incorporated into the phase (figure 2.3).

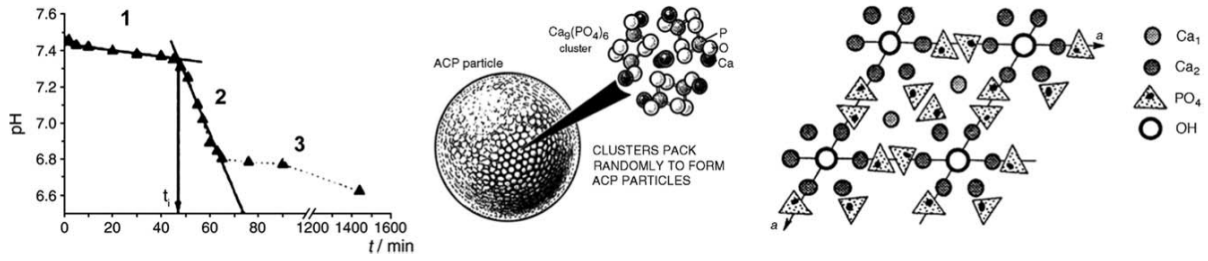

Figure 2.3: Plot of measured pH over time during CaP precipitation and formation of HA showing the three characteristic pH trends (left). Random packing of amorphous CaP clusters to form an amorphous CaP particle (middle) and eventual rearrangement to form the HA crystal structure. Reproduced with permission from [46] © 2006 Elsevier Ltd. and [38] © 1980 Elsevier Ltd.

The onset of HA formation incurs a more significant pH drop in the solution as the free OH^- ions are incorporated into the crystal structure. The time between mixing of the reactants and the onset of HA formation is called the induction time (or the nucleation lag time [31]). Gradual stabilisation of the phase occurs as the exchange of ions between the solid and the bulk solution decreases and hence the rate of pH change also decreases. Levelling of the pH over time can in principle signify complete stabilisation of precipitated phase, but in reality the phase is still undergoing transformation by restructuring of the ions within the solid phase to form a stable crystal structure. Most precipitation methods maintain a high pH of 9.00-10.00 by drop wise addition of an alkaline solution in order to provide enough free OH^- ions for HA formation. Meanwhile, keeping the pH under strongly alkaline conditions ensures the balance of phosphate species are heavily tipped towards PO_4^{3-} and minimising the protonated HPO_4^{2-}, $H_2PO_4^-$ and H_3PO_4 species which would make precipitation less favourable [31].

Ionic strength of the initial reaction solution also plays a role as ions can screen the charge of other ions within the solution or that of CaP particle surface itself. Increasing the concentration of the electrolyte compresses the diffuse layer of counter ions around that are attracted the HA

particle surface increase the propensity for the particles to agglomerate (see Chapter 4.2.4 for a more in-depth discussion of the 'electric double layer' of ions around a charged particle surface and the relation to particle-particle interactions.).

The effect of Ca:P molar ratio on HA formation is partly related to the different activation energies of Ca^{2+} and PO_4^{3-} and intimately linked with the effects of altering the reaction pH. As described in section 2.1 the HA is formed around the hexagonal arrangement of Ca^{2+} ions strongly held in place by the phosphates which give the crystal its stability. The structure is therefore sensitive to pH changes through protonation of the phosphate groups as mentioned earlier. This could be due to the weaker hydration attraction of $H_xPO_4^{x-3}$ to the protons compared to the attraction of Ca^{2+} to OH^- and therefore a higher activation energy is associated to the Ca^{2+} ions in the reaction solution. This an important factor when the growth rate of a particular CaP phase is limited by the availability of one of the ions. The extensive adsorption of HPO_4^{3-} ions on the particle surface relative to Ca^{2+} can shift the Ca:P ratio of the bulk solution heavily in favour of calcium, while the ionic composition of the precipitate remains roughly stoichiometric [45]. Other phases in addition to HA can form from the bulk solution and exist in stable forms in the final product depending on the stoichiometric ratio of Ca^{2+} and $H_xPO_4^{x-3}$ [31].

2.3 Ionic substitutions into CaP structures.

The major mineral component of hard tissues is calcium-deficient HA (CDHA), which incorporates an array of ionic substitutions into the structure including; CO_3^{2-} (3-5%wt), Na^+ (0.5-1%wt), K^+ (0.03-0.07%wt), Mg^{2+} (0.2-1.2%wt), K^+ (0.03-0.07%wt), Sr^{2+} (0.03-0.05%wt), Cl^- (0.1-0.4%wt) and F^- (0.01-0.07) with further contributions from Zn, Fe, Cr, Co, Mn and Si ions in the ppm scale [31, 36]. In fact, pathological calcifications such as urinary calculi [33], mitral valve [47] and breast cancer calcifications [48] have also been found to made of ion-substituted calcium phosphates. The complex composition of these structures reflects the composition of the surrounding serum environment where the mineralisation process takes place. Furthermore, in the case of hard tissues, these ions serve biological roles that include acting as a buffer in the

bloodstream [49] to modulation of osteoblast and osteoclast activity of proliferation [50, 51]. The flexibility in the chemical structure of hydroxyapatite to allow incorporation of foreign ions combined with the stability of the overall crystal structure at physiological pH may explain why bones function as highly effective ion storage areas. There is a drive towards exploiting these biologically relevant ions through their incorporation into ceramic implants/implant coatings and cements in order to enhance the regeneration of tissue around the implant and promote osseointegration [36, 50, 52]. This section will consider the ion substitutes most prominent in the biomaterials literature, summarise their mechanism of incorporation into CaPs and the resulting changes to the physicochemical properties of the bulk material, and link these changes to reported observations from *in vitro* and *in vivo* models.

2.3.1 Silicon/anionic silicon compounds

Silicon (Si) (or compounds of) plays a well established role in the biomineralisation process with the earliest reports coming from electron microscopy images of young rat tibiae, showing localisation of silicon at active calcification sites [53]. It has been established to be an important factor in the production of new bone matrix and functions to assist in the production of collagen by osteoblasts [13, 14, 15, 16]. Further animal studies showing that Si deficiency can result in reduced bone mass, reduction in collagen in cartilage and physical bone deformities [54, 55]. Aqueous Si at concentrations 0-1.4ppm has been shown to increase collagen type-1 synthesis in human osteoblasts while 0.1-100ppm Si over 48 hours has been shown to increase osteoblast proliferation and differentiation [56]. The measured abundance of silicon in the extracellular matrix (200-500ppm) compared to bone (approximately 100ppm) led to the suggestion that Si acts a biological cross linker in connective tissues thus contributing to their ordered structure and mechanical resilience [57]. The essential metabolic role of Si in bone formation at the fundamental scale has attracted much attention as a route to enhancing the bioactivity of CaP-based implant materials.

Most studies have synthesised HA, mixed apatite/amorphous CaP and Si-TCP materials

using aqueous precipitation with tetraethyl orthosilicate (TEOS), silicon tetraacetate or nano-particulate silica as the Si source. SiO_4^{4-} substitutes PO_3^{4-}, but this is a non-isoelectronic process and therefore a second charge compensation process must take place in order to avoid the potentially large energy cost of the substitution. The charge compensation could take the form of an oxygen or anion vacancy or an excess of Ca (for two Si ion substitutions) and/or an excess of H - the dominating mechanism determined by the thermodynamic conditions during the synthesis process [14, 36]. Cosubstitution with CO_3^{2-} can also compensate for the charge deficit. Si incorporation has been reported to be up to 5%wt, but a few studies have suggested that the upper limit of substitution is may be closer to 1.5-1.6%wt as any excess above this has been reported to polymerise on the surface of the apatite [58, 59]. Regardless, silicon content between 0.1%wt and 1%wt has been shown to be sufficient to enhance the bioactive response to such materials [36]. Increasing levels of Si-substitution into the apatite lattice has been reported to inhibit crystal growth, decrease crystallite size and increase solubility[14, 36, 60]. Qui *et al.* (2012) performed an extensive study of this and their X-Ray Diffraction (XRD) and Transmission Electron Microscopy (TEM) data is presented in figure 2.4. The effect on the solubility and bioactivity of the apatite has been suggested to be due to increased numbers of defects around grain boundaries where dissolution has been reported to begin [36]. The phase composition of the final Si substituted product is highly dependent of the initial Ca:(P+Si) ratio, %wt of Si addition and, most notably, the sintering temperature [14], but a single phase SiHA can be obtained by ensuring the Ca:(P+Si) ratio is maintained at 1.67 (as in the case of stoichiometric HA) with up to 1.6%wt Si with maximum sintering temperature of $950\,^{\circ}\mathrm{C}$ [61].

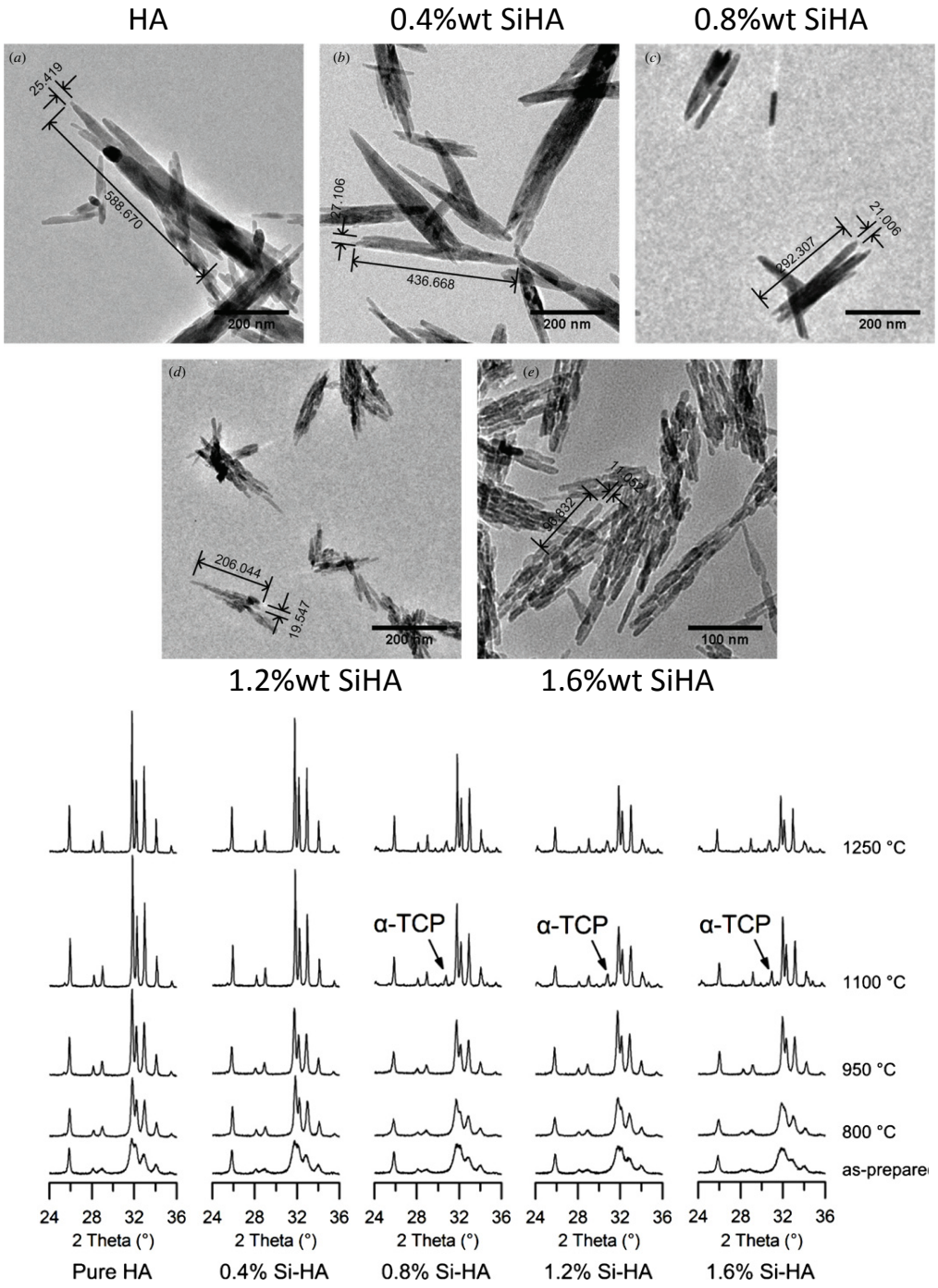

Figure 2.4: TEM images (top) of Si doped HA samples from the work of Qui *et al.* (2012) showing how increasing %wt Si content decreases crystal size and crystallinity - (a): pure HA; (b): 0.4%wt SiHA; (c): 0.8%wt SiHA; (d): 1.2%wt SiHA; (e): 1.6%wt SiHA. The XRD patterns (below) show the effect of %wt Si content and sintering temperature, highlighting the reduction in crystallinity and onset of thermal decomposition. TEM images and XRD patterns reproduced with permission from [61]. © 2012 IOP Publishing Ltd.

The known effects of aqueous Si on bone remodelling processes have been reported to extend to SiHA and Si-substituted TCP (SiTCP) materials with reports of increased osteoblast-like cell activity and dissolution compared to HA controls both *in vitro* [60] and *in vivo* [62, 63, 64]. In particular, Thian *et al.* (2006) developed SiHA coatings of up to 4.9%wt Si using magnetron sputtering and reported increased growth of human osteoblast-like cells exhibiting well formed actin stress fibers with evidence of extracellular matrix formation *in vitro* (figure 2.5). The effects Si ions on bone healing appears to be highly dose dependent with some reports claiming rapid bone mineralisation with 4.9%wt Si, but 2.2%wt being optimal to avoid rapid dissolution of the implant [13]. As little as 0.8%wt Si incorporation has been shown to have a positive effect on healing [62, 65]. However an 'optimum' dose cannot be defined as, to date, there is a lack of dose-dependent studies involving a range of common ceramic materials. Lai *et al.* (2002) investigated the fate of the Si once released from the implant material over 7 months from time of implantation and concluded that the Si localises only in the bone region surrounding the implant with no increase in Si levels found in the major organs and that it is mainly excreted through urine at a rate of 1.8mg/day [66]. The work of Porter *et al.* (2004) found that dissolution and reprecipitation of SiHA differs between *in vivo* and *in vitro* condition [67]. While their findings did agree in principle that Si ions are not released over a large distance from the implant, it also highlights the need for careful comparison of results between *in vitro* models attempting assess the role of Si ions in effects observed in *in vivo* experiments.

Although *in vivo* studies have shown evidence of resorption, one has to consider the possible effects on the implant in load bearing areas [68] together with the compounds in synovial fluid promoting osteoclastogenesis [69]. The extent and manner of the influence of Si doped materials on the remodelling process may need to be reassessed in such cases. It is still not clear whether the widely reported effects of silicon doped ceramics are due to: i) release of Si incorporated into the apatite or ii) changes in the apatite micro-architecture and surface chemistry as a result of silicon incorporation. The influence of the material surface roughness, which itself may well vary as a function of %wt Si addition, on the reported osteoclast effects is also not fully understood. The work Gomi *et al.* highlighted the need for further work in this area as they

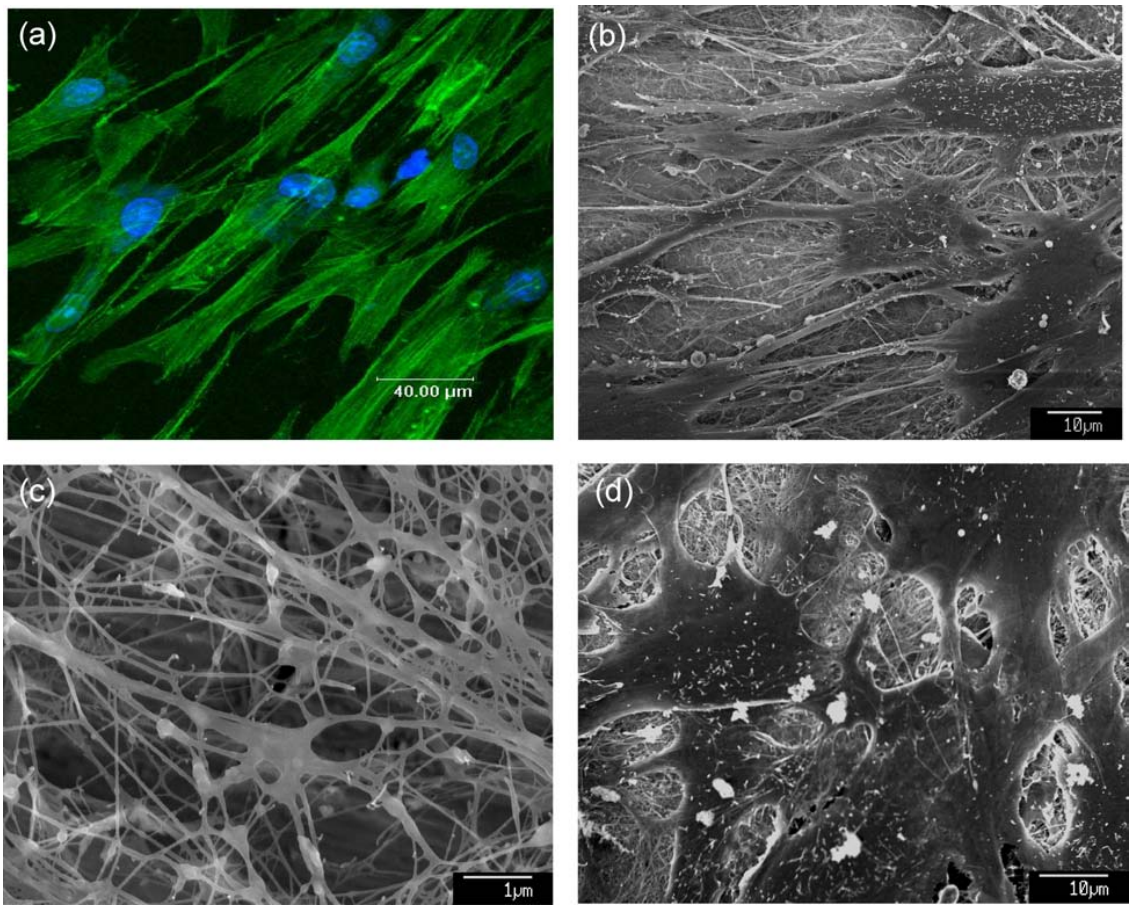

Figure 2.5: Light and confocal fluorescence microscopy images from the work of Thian *et al.* (2006) of human primary osteoblast-like cells on SiHA coatings produced by magnetron co-sputtering [60]. The cells exhibited well defined actin stress fibers (a, green) and evidence of cell stacking (d) which correlated with the increased cell growth. Evidence of extracellular matrix deposition was also seen during the study (c). Figure reproduced with permission from [60]. © 2006 Springer Science.

showed the nature of the osteoclast response was modulated by surface roughness of undoped HA. Higher numbers of TRAP+ (Tartrate-resistant acid phosphatase-positive) cells were found on rough HA surfaces, but more resorption lacunae were found on smooth HA surfaces [70]. There is some evidence to suggest that effects may be due to direct chemical interaction with the Si rather than through changes to the apatite structure as studies on Si doped (0.5%mol) alumina implants have also showed osseous remodelling [71]. Although this interpretation agrees with the previously mentioned studies using aqueous Si compounds which showed enhanced bone formation, Bohner argued that the solubility of Si substituted HA is still similar to HA,

which is very low at physiological conditions, and therefore the biological response could not be purely down to release of the Si ions from the lattice [72]. This raised the alternative view that the Si may actually exist to some extent as a soluble compound within the HA [58, 73, 74].

Si has been exploited in Bioglass (Na-Ca-P-Si), Pseudowollastonite ($CaSiO_3$), Si-TCP for higher dissolution rates and SiHA. Si-substituted CaPs currently manufactured commercially include a single phase SiHA called ACTIFUSE^{TM} by Apatech Ltd. and a multiphase Si-stabilised product primarily consisting of Si-α-TCP called Skelite^{TM} by Millennium Biologix Corporation. These products come in the form of either a microporous scaffold or granules designed for filling defects in non-load bearing bones.

2.3.2 Strontium

Strontium (Sr) has been administered in the form of the strontium ranelate in the treatment of osteoporosis. Sr acts by stimulating Ca^{2+} receptors resulting in differentiation of pre-osteoblasts to osteoblasts (thus promoting bone deposition) while reducing the bone resorption rate through inhibition of osteoclast resorption activity and osteoclast differentiation [36, 75, 76]. Sr has an ionic radius of approximately 0.12nm (slightly larger than the 0.099nm ionic radius of Ca) and thus in principle Sr preferentially replaces calcium at the C(II) site with substitution at C(I) possible at very low strontium concentrations [36]. The most notable effects of Sr substitution on HA occur at low concentrations and include reduced crystallinity and disruption of crystal structure. This has been attributed to the modest preference for substitution at the C(I) rather than C(II) site at low concentrations where metal-oxygen interactions responsible for the integrity of the crystal structure are most sensitive. The disruption of the crystal structure corresponds with the known higher solubility of SrHA leading to increased Ca^{2+} release from SrHA into Hank's synthetic fluids compared to stoichiometric HA [77] and reduced precipitation of CaP in synthetic body fluids with increasing concentrations of Sr^{2+}. At higher concentrations, the HA crystal morphology changes from needle-like to rectangular plate shapes, increase in crystal size and crystallinity at high ion concentrations [12].

2.3.3 Magnesium

Magnesium (Mg) plays a key role in bone growth by modulating osteoblast and osteoclast activity with magnesium levels in biological apatites decreasing as the calcification process progresses [36]. Although the smaller ionic radius of magnesium (0.065nm) compared to calcium (0.099nm) could permit substitution in either Ca positions, there is a preference for the Ca(II) position which is possibly due to the greater flexibility of the anion geometry at the this position [36]. Nuclear Magnetic Resonance (NMR) studies agree with Ca(II) site substitution up to 10% Mg [78]. Magnesium addition has a marked inhibitory effect on the nucleation and growth of HA crystals causing a reduction in crystallinity [79], while stabilising the more acidic CaP intermediate phases during synthesis [80].

The stabilising effect has been exploited in the formation of Mg-substituted biphasic HA/β-TCP, where the TCP component has been reported to remain stable at sintering temperatures of up to $1400\,^{\circ}\mathrm{C}$ [80, 49]. The work of Kalita *et al.* (2007) showed a moderate increase in sintered density of Mg-substituted HA (MgHA) at $1300\,^{\circ}\mathrm{C}$ [81]. Incorporation levels have been limited to 5.7%wt with excess Mg reported to be in the form of an additional amorphous phase [36] or adsorbed on to the HA surface [79]. The effects of free magnesium ions on early bone formation have been exploited through the production of MgHA (5.7%wt Mg) granules as bone defect fillers. Rabbit femoral defect models filled with MgHA granules showed osteoconductivity and resorption consistent with increased solubility of the material [82]. Interpretation of the dissolution properties of such implant studies must consider the potential influence of any co-substituted carbonates from the synthesis process on the solubility of the implant material. While there are no specific studies which isolate the role of Mg ions in adjusting material dissolution properties, there is evidence that Mg ion association with CaPs may influence surface structure in way that implies increased solubility. High resolution TEM studies of MgHA synthesised under controlled nitrogen atmosphere by Ren *et al.* (2010) revealed the creation of multiple grain boundaries with increasing Mg content (figure 2.6) [83].

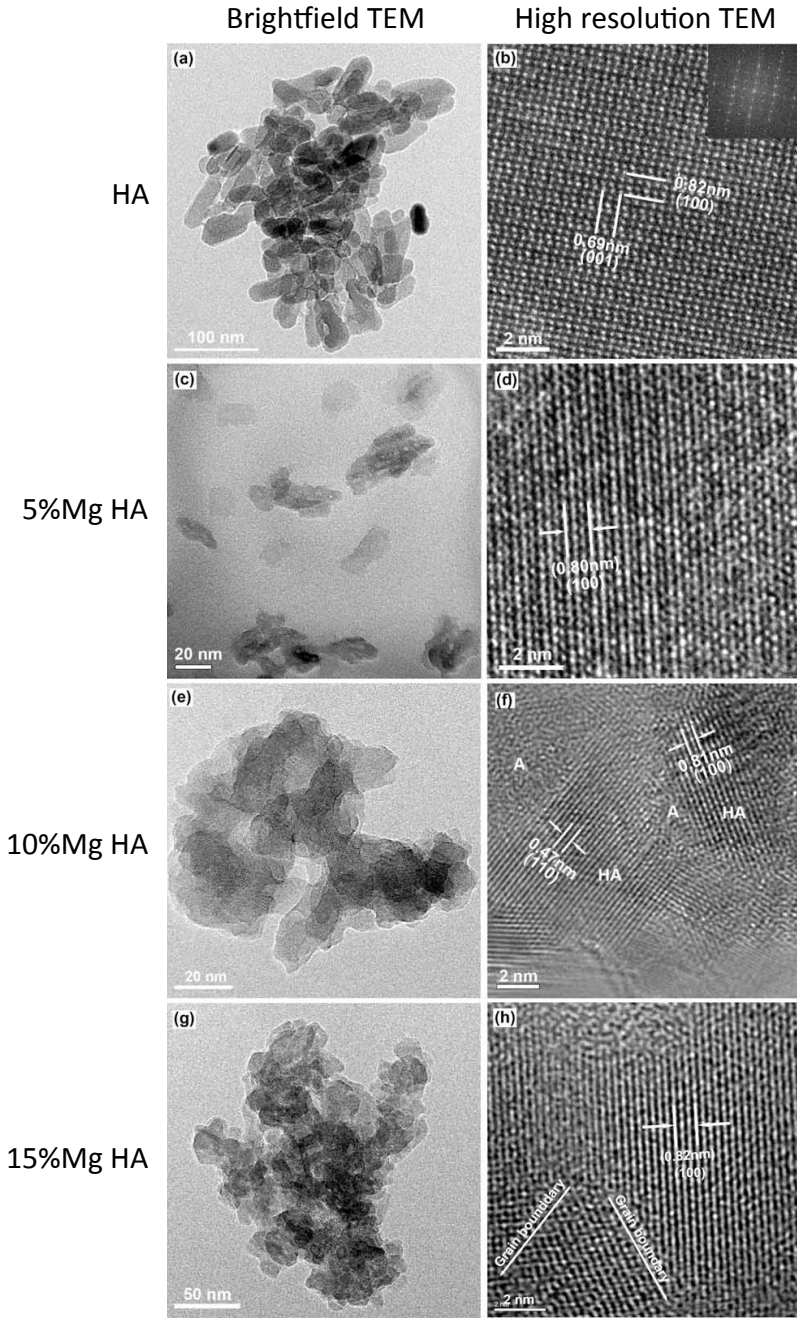

Figure 2.6: High resolution TEM images of HA with varying mole% amounts of magnesium incorporation by Ren *et al.* (2010). The MgHA materials were synthesised under a nitrogen atmosphere to minimise the co-substitution of carbonate ions resulting from exposure to air. Increased number of grain boundaries were observed from 10%molMg incorporation upwards which suggests the structure would be more vulnerable to dissolution compared to HA. Figure amended and reproduced with permission from [83]. © 2010 Elsevier Ltd.

2.3.4 Zinc

Zinc (Zn) has an important role in many biological functions within the body including: nucleic acid metabolism, aiding the maintenance of membrane structure and, acting as a cofactor in enzyme mediated processes such as protein synthesis [36, 84]. Zn also promotes bone formation by inhibiting osteoclast differentiation and enhancing osteoblast activity [36].

Zn-substituted HA (ZnHA) has been obtained largely by ion exchange synthesis in aqueous solutions [85, 86, 83, 87] and hydrolysis of Zn-salts with α-TCP [88] resulting in Zn contents of 1.20-2.7%wt. The smaller ionic radius of Zn (0.075nm compared to 0.099nm Ca) can result in a reduction in the lattice parameters of the apatite[86]. Zn inhibits the crystal growth of the apatite, reportedly though adsorption onto active growth sites which may explain why (Ca+Zn)/P ratio and hence stoichiometry is not preserved [87, 79, 36]. Whether substitution actually takes place is not fully clear. There is much debate over the mechanism of Zn incorporation into HA. Some theoretical studies remark that ion substitution is not energetically favoured and that Zn occupation at Ca vacancies (particularly at the C(II) site) is probable with significant local structural distortion. Contrarily, Tang *et al* reported that Zn ions may favour the C(II), but also reasoned that Zn ions could be entrapped and act as a defect site given the fast crystallisation kinetics of precipitation [89]. Ion adsorption experiments have shown significantly higher amounts of Zn ions were found to associate with HA - beyond what would be physically possible by substitution alone. One such study by Fuierer *et al.* (2004) showed that Zn ions were more potent at arresting crystal growth than Mg ions [79]. Two possible explanations include the formation of zinc-phosphate complexes at the surface and the ability of the surface bound Zn species to undergo hydrolysis and potentially block multiple active growth sites [79]. As with other ion substitutions which result in significant reduction in crystallinity, determination of Zn substitution by XRD and Rietveld refinement is complicated by the broadening of the diffraction peaks.

Attempts have been made to translate the biological properties of Zn ions to mainly HA-based biomaterials with reports of enhancement of human osteoblast adhesion and differentiation [90]

2.3.5 Manganese

Manganese (Mn) influences the regulation of bone remodelling by driving organic matrix synthesis and endochondral osteogenesis. Mn is also implicated in the activation of integrin receptors which mediate cellular interactions with the exctracellular matrix and ligands involved in cell adhesion [91]. Mn deficiency has been shown to result in a reduction in bone thickness and length [36].

Mn^{2+} ions in solution inhibits HA crystallisation with high concentrations adsorbing on to the HA surface, causing a dramatic decrease in the the crystal growth rate [36]. At low concentrations ($<$2%wt), Mn incorporation does not affect the lattice parameters appreciably, but does reduce the thermal stability of the material as evidenced by the partial transformation of MnHA (with carbonate content less than 2%wt) to β-TCP at $600\,^{\circ}\mathrm{C}$ [92]. Morphology of MnHA strongly depends on the Mn ion concentration. Electron microscopy studies on Mn^{2+} and CO_3^{2-} substituted HA showed that crystals have a plate or large needle-like morphology at low Mn (0.73%wt) and high carbonate (3.6%wt) concentrations and small needle-like morphologies with high Mn (1.23%wt) and low carbonate (2.1%wt) concentrations [36]. Other works have reported Mn plate and fiber morphologies in addition to the needle-like phase although its unclear as the precise role of Mn in dictating particle morphology use chemical precipitation routes [91]. Specifically, Mayer *et al.* (2008) correlated the plate shaped and needle-like particles to low Mn-doping (0.71%wt) and smaller needle-like particles at higher (1.23%wt) Mn-doping [92].

Mn-doped carbonated apatite coatings have deposited on Ti implants and shown to enhance osteoblast proliferation and differentiation [93].

2.3.6 Carbonate

Carbonate forms approximately 7-8%wt of the chemical composition of human bone [33] - the highest contribution to ion substitution in adult human calcified tissues. Carbonate ion (CO_3^{2-}) substitution can occur at two different sites within the apatite the lattice. The first involves

the substitution of two OH^- for every one carbonate ion, termed 'A-Type substitution', and can be achieved through heating stoichiometric HA in a CO_2 atmosphere at $1000°C$ for 15-145 hours or through soaking the material in an aqueous CO_2 saturated solution for a period of months. The second route involves the substitution of PO_4^{3-} (B-type substitution) and is typically achieved through precipitation from aqueous solutions of calcium and phosphate precursor salts along with sodium or ammonium carbonate at elevated pH and while under a controlled inert atmosphere (e.g. Argon or Nitrogen). Carbonate substitution can occur purely by performing the precipitation reaction in an open vessel exposed to air whereby carbon dioxide can readily dissolve into the aqueous solution at room temperature to form carbonic acid. This highlights the importance of a controlled inert atmosphere when attempting to control the %wt CO_2 incorporated into the apatite. It must be noted that A-type substitute does not exclusively occur through annealing. Perhaps the best evidence of this is the presence of A-type carbonate substitution in bone at 3-8%wt. Additionally, precipitation reactions have produced apatites with both A and B-type substitutions (AB-type). Co-substitution with another ion is required to compensate for the charge imbalance created by the substitution of the trivalent PO_4^{3-} or monovalent OH^- for the divalent (CO_3^{2-}). In the example stated above of a pure B-type substitution using sodium carbonate, it is the Na^{2+} ions which act as the co-substituted ion.

Increasing %wt of carbonate in the material results in increased material solubility, reduced crystal growth rate and reduction in the sintering temperature where HA decomposes into β-TCP [36, 94]. Carbonated apatite shown to have enhanced bioactivity *in vitro* owing to increased solubility [31, 95]. Although, *in vivo* studies of carbonated CaP implants appear to show increased rates of implant dissolution, they indicate that this may not be due purely to changes in material solubility. Spencer *et al.* (2008) reported increased collagen synthesis by human osteoblasts on both fresh carbonated HA and on carbonated HA subjected to osteoclast activity, although the effect was observed at an earlier time point in the latter case [96]. The suggestion from these results was that osteoclasts condition the surface and influence subsequent osteoblast response [96]. Further speculation included the surface chemistry of carbonated HA enhancing protein adsorption [96]. Increased solubility has been reported at substitutions as low as

1.2-2%wt [95] with 9%wt reported to result in rapid implant dissolution [97]. This may not be ideal in restoring some level of load bearing capability on the implant post-surgery as quickly as possible as rapid dissolution may not allow for adequate supporting tissue formation.

CHAPTER 3

CHEMICAL MODIFICATION OF CALCIUM PHOSPHATES

3.1 The motivation for modifying CaP surface chemistry properties

The body's response to any implant involves two conflicting and complex biological processes, which have been reviewed extensively [98]. The body acts to seal off the implant from the rest of body by rapidly forming blood clots on the material surface, which ultimately leads to the formation of a wall of fibrous tissue around the implant surface [25, 99]. Meanwhile, the body attempts to regenerate bone through the migration of progenitor cells into the region which differentiate into osteoblast cells before secreting and mineralising collagen to form new bone. The rejection and regeneration processes compete with one another as the rapid formation of fibrous tissue can hinder the migration of progenitor cells into the bone site, which in turn inhibits the integration of the implant with the surrounding natural tissue [100]. This is particularly an issue with metal implants in which the material is considered wholly foreign to the body. The structural nature of bone-implant interface is critical to the mechanical stability of the implant. Intimate bone-implant contact ensures good implant stability with respect to the surrounding bone which aids restoration of limb function. On the other hand, a fibrous tissue layer between the bone and implant acts as a mechanical weak point leading to micromotion and premature aseptic loosening of the implant [25]. The modification of material chemistry aims to minimise the effect of the body's response to foreign materials while simultaneously promoting tissue regeneration in the damaged or diseased bone site.

The chemical similarity of hydroxyapatite-coated or -based implants to the surrounding hard tissue (and therefore not recognised as 'foreign' in principle) has made them the subject of intensive research as a bone replacement materials [101, 100]. Synthetic hydroxapatite has been shown to accelerate osteoblast precursor differentiation [102] and promote osteoblast adhesion and migration. CaPs such as TCP and HA-TCP biphasic systems offer tuneable resorption characteristics [103] with the degradation products, Ca^{2+} and PO_4^{3-}, already found at concentrations of 90-110mgL^{-1} and 73-125mgL^{-1} respectively in the bloodstream [50, 101]. These findings are perhaps form the main rationale that such materials would permit fast fixation of the implant with minimal fibrous tissue ingression [25, 99]. This clinical outcome has multiple benefits to the patient including reduced recovery time before regaining load bearing mobility, prevention of bone atrophy and collectively leading to improved quality of life [25]. These benefits are coupled with reduced hospitalisation time and costs to the state/patient. In fact, benefits extend to non-load bearing applications such as bone fixation screws and plates where their degradation over time removes the need for their painful and costly retrieval. Biomineralisation of, along with cellular attachment to, the implant occurs through a passivation later of adsorbed ions and other biomolecules rather than though direct contact with the material surface itself [17, 104, 105]. Therefore, much research has been directed toward controlling the chemical composition of the calcium phosphate surface in order to: promote the osteogenic cell recruitment and adhesion; modulate cell signalling pathways implicated in bone remodelling and; minimising the risk of infection through attachment of antimicrobial agents. Chemical modification is also being employed to strengthen ceramic implants and coatings, which to date have been too brittle to be used as the major material component of load bearing implants. Their common aim is to enhance the bone regeneration properties of calcium phosphates and accelerate bone healing with numerous strategies proposed to achieving this goal.

3.2 Methods for the surface modification of calcium phosphates

Chemical modification methods in the literature can be roughly divided into two approaches as shown in figure 3.1. The first approach is through adsorption of biomolecules onto the CaP surface, which relies upon non-specific electrostatic interaction with the surface ions of the CaP. The second approach involves grafting an organic molecule through covalent bonding with a particular surface ion or chemical group of the CaP surface. e.g. OH^-. Co-precipitation method (in which the biomolecule is integrated with the CaP during CaP synthesis) has been extensively used, but the precise nature of the attachment with the CaP is not clear and therefore will be discussed separately. What is common throughout the literature is that the vast majority of these approaches are low temperature wet chemical methods. They receive intense interest because of the their ability to precisely control surface morphology at the nanometer scale along with the composition; the reaction conditions are suitable for the incorporation of organic and biological material; and require relatively simple experimental setups incurring low costs [25].

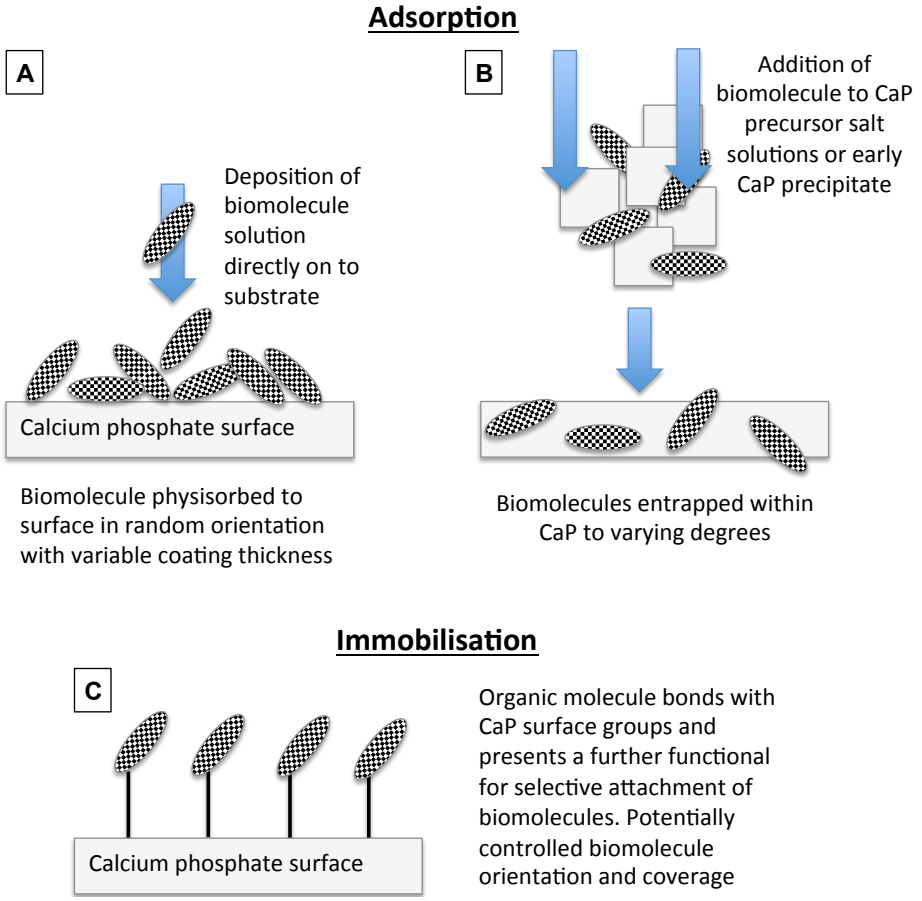

Figure 3.1: Schematic diagram showing the two main strategies used to attach biomolecules (e.g. functionalisation agents, antibiotics, growth factors) to calcium phosphate (CaP) nano-/micro-particles and large surfaces. Adsorption an be subdivided into two subcategories - deposition on to preformed CaP materials (A) or co-precipitation of the CaP material with the biomolecule (B). These methods are favoured for their simplicity, but precise coating is not always repeatable and CaP morphology and size can be influenced by co-precipitation. Immobilisation involves the grafting of an organic molecule to the CaP surface, which then facilitates selective binding of the desired biomolecule. The key advantages include: control over biomolecule coverage, robust biomolecule attachment and the potential to control biomolecule orientation.

3.2.1 Direct biomolecule attachment to CaP surface by adsorption

Direct attachment methods involve those which the deposited biomolecules rely upon non-specific electrostatic interaction with the surface ions of CaPs. Dip coating and electrospray techniques are perhaps the most widely used methods of adsorbing molecules on surfaces particularly for providing antibiotic coatings [106], but their main drawback is burst release of the

drug. Burst release occurs when a variable amount of the biomolecule is uncontrollably liberated (usually over the period of minutes to a few hours) from the surface due to the weak binding nature between the substrate and the biomolecules themselves. The electrostatic binding between a biomolecule in direct contact with the surface may well appear robust, but the strength of this attractive force decays rapidly from the surface ($1/r^2$) and hence multilayers of biomolecules may not remain bound to the surface. Mechanical agitation of the substrate and even changes in the ionic strength and pH of the surrounding liquid environment can liberate adsorbed biomolecules. The uncontrolled loss over a such a short period of time does not lend the method well to applications involving antibiotic release where high doses are initially required post-surgery before a lower prolonged dose needs to be maintained.

In an attempt to reduce the rate of loss during burst release, secondary layers of material have been deposited over the adsorbed antibiotic in order to act as a 'kinetic barrier'. Here, the diffusion rate of the adsorbed drug is reduced by the relative low solubility of the secondary material in the surrounding liquid which increase its degradation time. Alternatively, the porosity and pore interconnectivity of the kinetic barrier material can be controlled in order to increase the path length and therefore the elution time of the biomolecules between the substrate and the surrounding medium. Lipid layers have been successfully used to increase the release period from 24 hours to 72 hours *in vitro* [106]. It is important to note that the use of secondary layers as kinetic barriers can only reduce the peak burst release amount and offer a degree of control over the burst release period - often not independently. Therefore, assessment as to whether this really offers 'controlled release' would depend on the drug delivery application. The effect of the degradation products of the kinetic barrier material on the structure and function of the biomolecules must also be considered. For example, the acid degradation products of poly(lactic-co-glycolic)acid (PLGA) may denature encapsulated proteins [107] with rate of change of pH in the local area around the implant dependent on the choice of inorganic filler [108].

An alternative approach to reducing the loss or degradation of adsorbed biomolecules is to integrate them within a gel form of CaP. In these case, the the carrier material itself acts

as kinetic barrier while offering increase surface area for attachment. Barralet *et al.* showed reduced rate of short term release of ovine albumin from carbonated HA gels compared to microcystalline HA in both phosphate buffered saline and double-distiled water. They also showed that the albumin could remain within the gel under physiological conditions undegraded for up to a year [109]

Perhaps the best exploitation of adsorption has been for the attachment of polyphosphonates such as clondronate [110] and alendronate - two examples of a class of drugs known to be the gold standard in controlling bone remodelling rates through inhibition of osteoclastic activity. Polyphosphonates have a very high affinity for CaP substrates, which offer the potential for highly localised delivery to bone defect sites. This is of great interest clinically as current oral and systemic administration routes of bisphosphonates ultimately yield a poor bioavailability of the drug at the bone site and often are accompanied by unpleasant side affects to the patient.

3.2.2 Co-precipitation with (and delayed addition) of biomolecules

Co-precipitation methods involve the addition of the biomolecule of interest into the CaP synthesis reaction such that CaP precipitation and attachment of the biomolecule occurs simultaneously. The commonly reported advantage is that combining the two processes into one reaction negates the need for further chemical processing or intermediate washing steps and therefore creates a simple, very low cost and fast attachment method. These features together with the already discussed desirable non-cytotoxic nature of CaPs has resulted in co-precipitation methods being used extensively for the attachment of DNA for cell transfection [6, 101, 111, 112, 113, 114, 115, 116] and siRNA for gene silencing [3].

Sokolova *et al.* (2006) constructed a core-triple shell CaP-siRNA complex (CaP(core)-siRNA/CaP/siRNA(shells)) and showed higher gene silencing efficiency (46%) over one the main commercially available transfection reagents, PolyFect® (10%) [3]. Triple shell configuration reportedly offered increased maximum loading mass of genetic material to the CaP vector and a degree of protection from the cellular environment. The authors correctly highlight the importance of future investigation of the protective effect of the CaP shells on the oligonucelotides

before the technology can be used for DNA transfection. This is because, unlike siRNA, DNA requires delivery into the nucleus and the vector would potentially need to withstand enzymatic degradation along the way. Further work by the same group revealed the triple shell system was robust against lysosomal degradation with transfection efficiencies roughly on par with PolyFect® [115] in T-HUVEC cells. Further attempts have been made to increase the stability of CaP-DNA complexes by introducing porphyrin[8] coatings and poly(ethyleneimine) (PEI) shells with the later reported to raise transfection efficiency in T24, HeLa and NIH-3T3 cells [6, 116].

Despite the reported successes with co-precipitation techniques, there does not seem to be a clear understanding of the physicochemical characteristics of co-precipitated CaP-DNA systems or the key parameters underlying their action. Few works demonstrate the effect of the DNA addition during CaP synthesis on the ultimate CaP particle size, morphology and composition. Neither is there a complete understanding of how the CaP-DNA complex interacts with the cell at the molecular level in order to explain why CaP-DNA transfection efficiency is better or worse than commercial transfection reagents across different cell lines. Pedraza *et al.* (2008) highlighted this issue when they showed that $CaCl_2$ was considerably more effective than $Ca(NO_3)_2$ and other divalent metal salts at binding free DNA to the CaP particle surface [117] (separate particle synthesis and DNA complexing processes). This finding showed that the role of excess calcium involved not only condensing the DNA, but to condense the DNA in a manner which maintains biological function (also reported by [118]). This precise role was elegantly demonstrated by the significant increase in GFP expression when using $CaCl_2$ over other divalent metal salts. With this effect being calcium salt concentration dependent, it is clear that optimal CaP-DNA complexing is a precise process itself. It has been suggested that cationic particles bind to components of cell membrane responsible for Ca^{2+}-mediates anchoring the the extracellular matrix[119] and therefore the final particle composition and dissolution properties may also be key[120]. It is still not clear whether CaP composition and CaP-DNA binding can be controlled independently enough using a co-precipitation technique.

The method has also been used to increase CaP colloidal stability and for drug delivery.

Andres *et al.* (2006) functionalised brushite particles with carboxyl groups by the delayed addition of 2-carboxyethylphosphonic acid (CEPA) to the synthesis reaction [121]. Addition of CEPA (and phosphates in general) to the CaP synthesis reaction resulted in chelation of the surface Ca^{2+} ions and arrested further crystal growth on the particles. The organic carboxylic acid presented on the particle surface increased the electrostatic repulsion between the particles and therefore improved colloidal stability. The carboxyl groups presented on the surface could potentially be used an attachment site for proteins or drugs [121]. Co-precipitation has been used for the integration of anticancer supramolecular drugs with calcium and phosphate salts shown to facilitate higher drug loading in HeLa cells compared to exposure to the drug alone [122]. However, still no explanation of the chemical interaction and what degree of control over the particle size, morphology and dissolution properties when adding the drug during synthesis.

The most promising uses of co-precipitation methods for bioengineering applications focus on the modification/optimisation of CaP surface chemistry in preparation for subsequent biomolecule attachment rather than direct attachment in one step. Examples typically include the addition of organic molecules to create additional attachment sites on the particle surface and to influence particle shape, size and reactivity. Lee *et al.* used 3-mercaptopropionic acid during the hydrothermal synthesis of HA to provide carboxylate groups at the particle surface. The authors suggested that the nature of the binding was ionic and demonstrated its potential in the biomedical/tissue engineering fields by immobilising ethylene glycol methacrylate phosphate (EGMP) (figure 3.2) on the particle surface. The potential behind such a modification included enhancing protein adsorption and templating mineral growth [7].

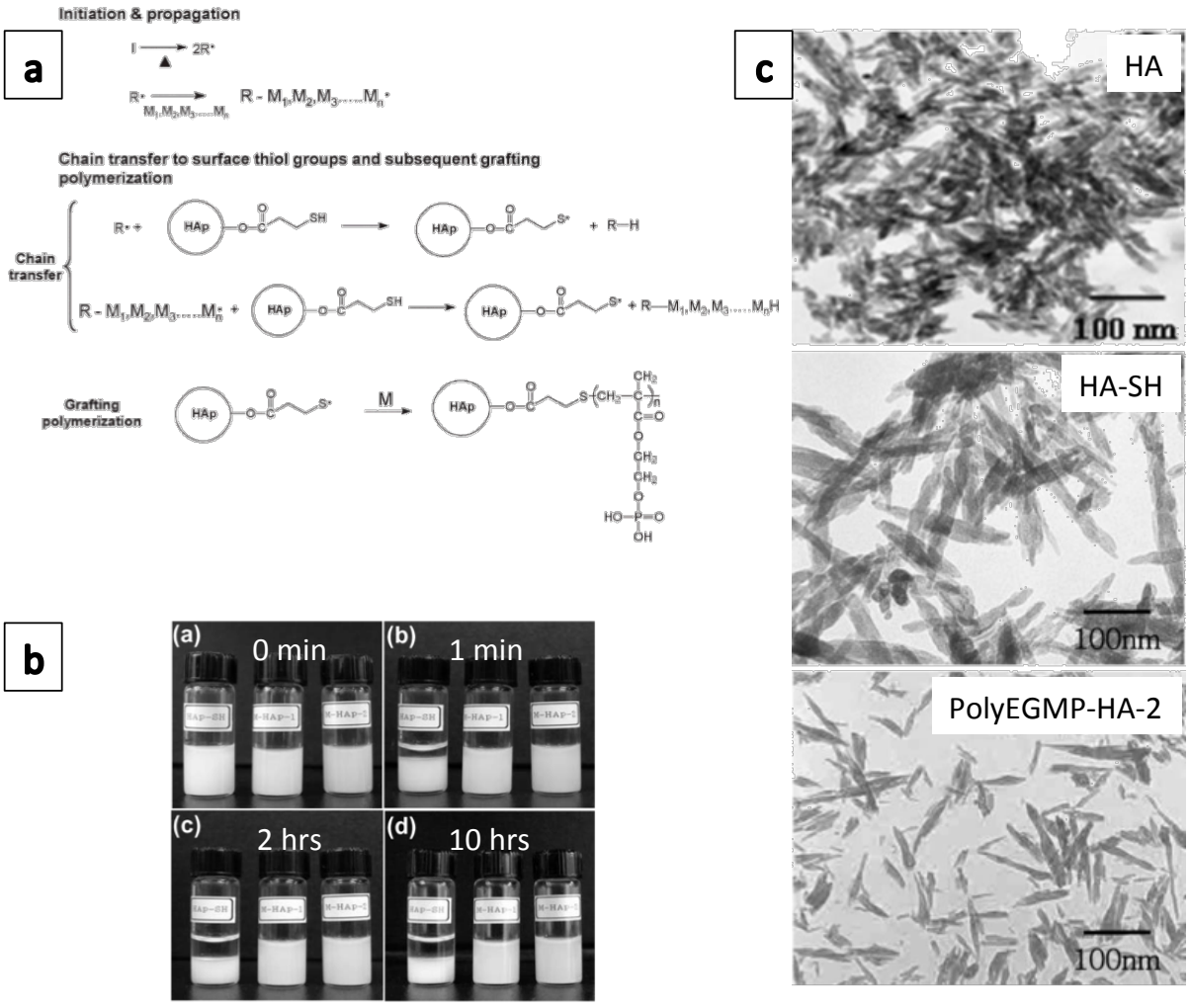

Figure 3.2: Schematic diagram of the carboxyl functionalisation and subsequent ethylene glycol methacrylate phosphate (EGMP) engraftment process (a), developed by Lee *et al.* (2007). (b) shows the colloidal stability of HA-SH, PolyEGMP-HA-1 and PolyEGMP-HA-2 (left to right) after each functionalisation step. TEM images of the HA particles at various stages of the process (c). Reproduced with permission from[7]. © 2007 The Royal Society of Chemistry.

Amino acids including glycine, alanine, serine, lysine and arginine have used to form positively charged CaP nano rods [123]. The effect of amino acid addition on particle size and morphology was investigated and found that increased side-chain residue size and hydrophobicity resulted in a decrease in the aspect ratio of the HA nano crystals along the c-axis. Interestingly, asparagine affects both the crystal c- and a-axis while aspartic acid did not destabilise the nanoscrystals at all. It was suggested that these interactions preferentially occurred on crystal planes parallel to the c-axis and that hierarchal structures could be formed through cross link-

ing. The high Ca^{2+} binding affinity of poly(aspartic acid) and poly(glutamic acid) have been further exploited to enhance both the adsorption rate and total loading capacity of of peptides on HA surfaces [124]. CaPs expressing C=C groups on the surface have been formed by HA co-precipitation with methacrylic acid, 4-pentenoic acid, and vinyl phosphonic acid [125]. The choice of acid was reported to have a marked effect on HA surface topography ranging from angular block-like shapes to fine needle structures (figure 3.3). It has been proposed that cortical bone substitutes could be formed through polymerisation of methacrylate polymer with these C=C functionalised CaPs [125].

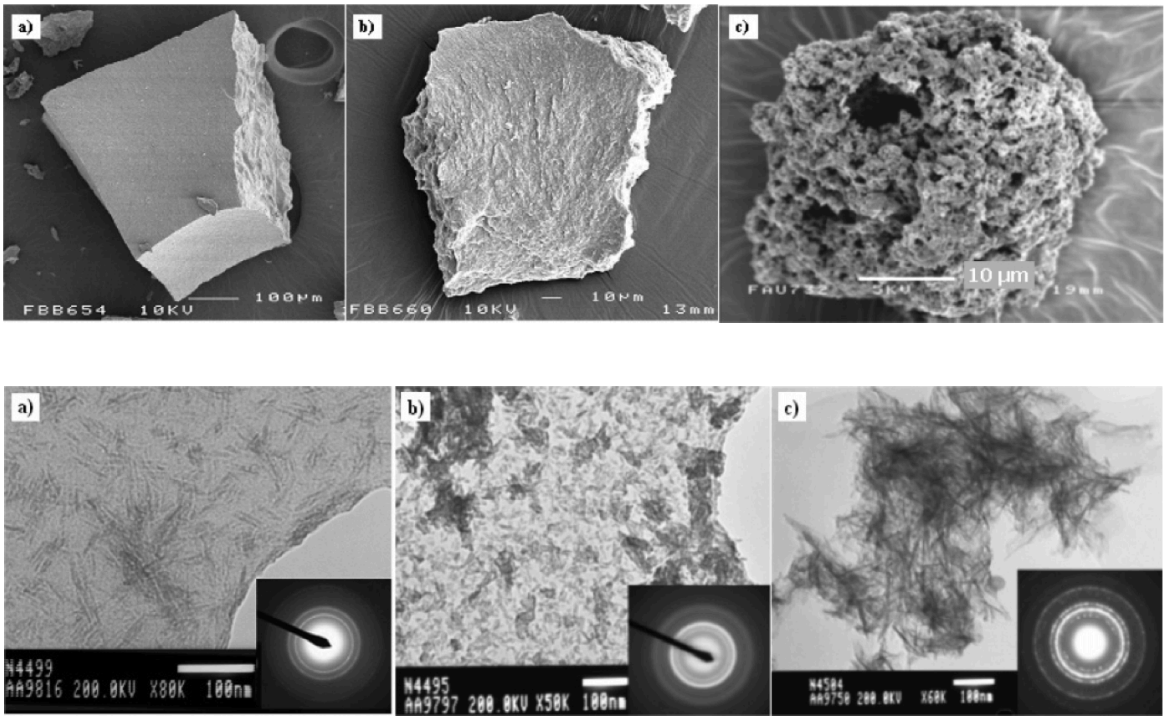

Figure 3.3: Scanning electron microscopy (SEM) images (top row) of HA synthesised in the presence of methacrylic acid (a), 4-pentenoic acid (b), and vinyl phosphonic acid (c). Corresponding TEM images of the HA crystals are shown in the bottom row. From the work of Haque *et al.* (2007). Reproduced with permission from [125]. © 2007 American Chemical Society.

3.2.3 Immobilisation of biomolecules on functionalised CaP surfaces

In this class functionalisation methods, organic molecules or polymers are attached the particle surface and present a functional group. This functional group can then be used for the selective

attachment of the desired biomolecule or designed purely to alter the physicochemical characteristics of the surface enhance, for example, cellular attachment or colloidal stability. Usually, the CaP materials are prepared in separate process prior to functionalisation. The key advantage to this approach is the opportunity to control the morphology, size and, in principle, the bulk composition of the CaP material with minimal interference from the functionalisation process. Or at the very least, the separated processes allows for any changes in CaP physico-chemical properties to be traced back to either the synthesis or functionlisation process and thus aid in their optimisation. This benefit in turn permits functionalisation of not only CaP nano- or micro particles, but also CaP sheets, blocks and CaP coated structures.

Most of the applications of this functionalisation approach appear to focus on developing CaP-based bone implant materials. Organophosphonic acids ($RP(O)(OH)_2$) have been used to improve surface adsorption and wettabiltity properties of HA with a view to producing tailored HA-based fillers and biomaterials. For example, D'Andrea *et al.* modified HA with n-Alkyl- and n-Fluoroalkylphosphonic acids through covalent P-O-P bonding, which proved to be robust against extensive washing, exposure to solvents and ultrasonic agitation [126]. Qui *et al.* attached L-lactic acid (LLA) to the surface of HA particles via ionic Ca^{2+}-$RCOO^{-}$ bonding, which acted as an attachment site for L-lactide in the presence of a catalyst [24]. Polymerisation of the lactides (PLLA) resulted in the formation of HA/PLLA composite materials with a tensile strength of 67 MPa and Young's Modulus of 2.1 GPa [24]. The improved mechanical properties compared to their previous work on HA/PLLA composites was attributed to the high LLA grafting ratios, which increased the dispersion of HA through the PLLA matrix yielding a more homogenous bulk structure as shown in figure 3.4.

A similar observation was made by Lee *et al.* using poly(e-caprolactone) (PCL) as the functional agent in PCL/HA composites as shown in figure 3.5 [127, 17]. Here, the improved mechanical strength over unmodified HA was due to enhanced adhesion between organicinorganic phases [127]. It's most likely that the improved strength relates to the colloidal stability allowing good dispersion of the HA throughout the material and increased the overall material specific surface area. The composite material also showed improved NIH-3T3 cell adhesion

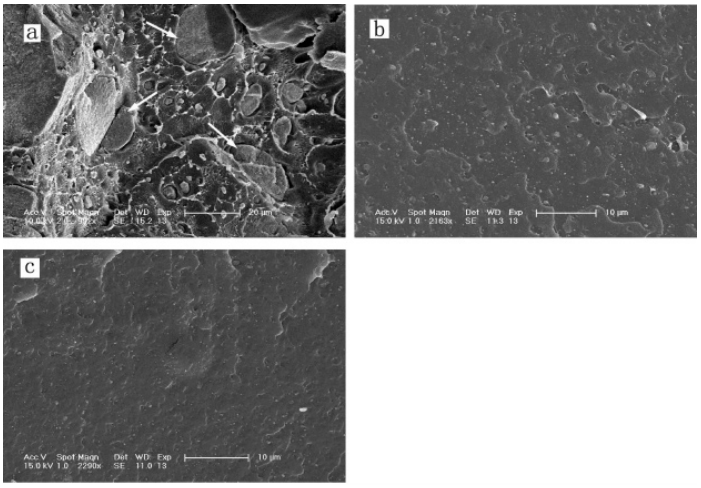

ESEM micrographs of HA(30%wt)/PLLA (a), L-HA(30%wt)/ PLLA (b) and p-HA(30%wt)/PLLA (c) composites.

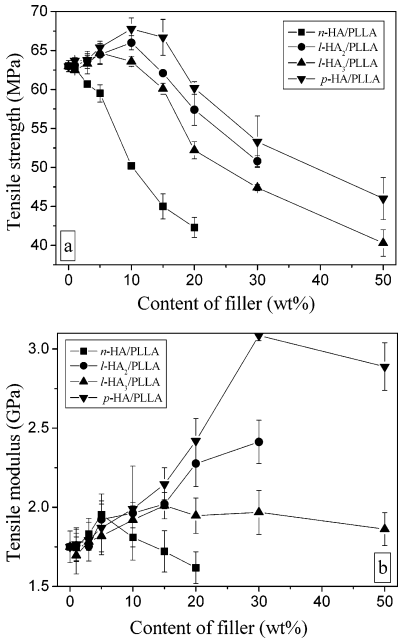

Dependence of tensile properties on filler content.: (a) tensile strength and, (b) tensile modulus.

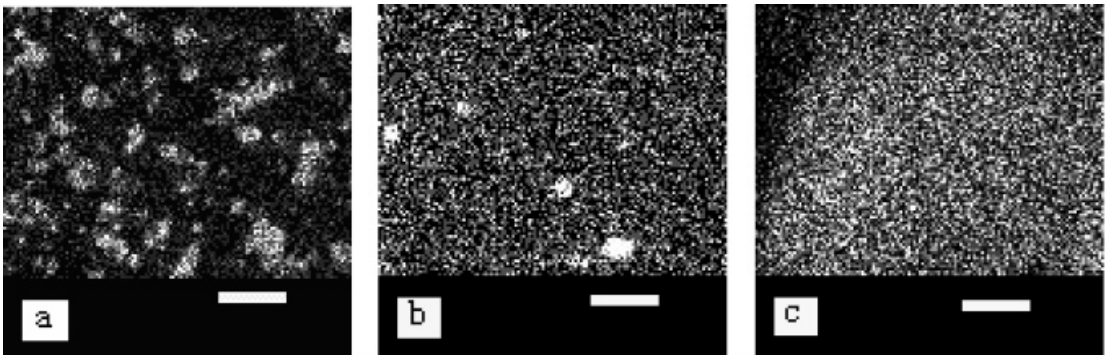

Elemental Ca distribution in the fracture surface determined by EDS for HA(30%wt)/PLLA, PLLA (a), L-HA(30%wt)/PLLA (b) and p-HA(30%wt)/PLLA (c).

Figure 3.4: Functionalisation on nanocrystaline (n-HA) HA with L-lactic acid (L-HA) and polymerisation of lactides to poly-l-lactides to form HA/PLLA composite materials by Qui *et al* (2005). The functionalisation enhanced HA dispersion throughout the PLLA as seen in the EDS images (bottom), resulting in a more homogenous bulk structure (ESEM images, top) and increased tensile strength and modules (right). Scale bar of the EDS images (bottom row) = 10μm. Reproduced with permission from [24]. © 2005 American Chemical Society.

and proliferation compared to HA controls, which was attributed to the swelling of the PCL phase in culture media partially exposing the HA substrate.

CaPs stability in non-aqueous solvents has been enhanced through esterification of the HA surface using dodecyl alcohol, which is important for further attachment to many bioactive polymers [128]. Similar studies have been carried out with hexyl, octyl, and decyl phosphate in acetone and water [129, 130] where surface structure and morphology was maintained after the reactions. Surface charge of HA has been modulated by modification with 12-aminododecanoic acid (positive) and dodecanedioic acid (negative), without changing the crystal structure, in order to control cellular internalisation [131]. Interestingly, the esterification of HA has been used a precursor for the formation of a silica layer around the particle surface [132]. Borum *et al.* (2003) formed silica layers using tetraethylorthosilicate ranging 5-75%wt. Silica coating resulted in increased specific area from $50 m^2 g$ (bare HA) to $138 m^2 g$, increased colloidal stability and resistance against 1M HCl. Closer inspection of the particle surface using SEM revealed the silica layer existed as packed silica clusters rather than a homogenous layer, which may explain the increased specific surface area. To date, the use of a secondary silica layer on CaP has not been used a platform for further biomolecule attachment in a bioengineering context, but the concept of assembling clusters on a CaP surface may provide a route to altering the material topography.

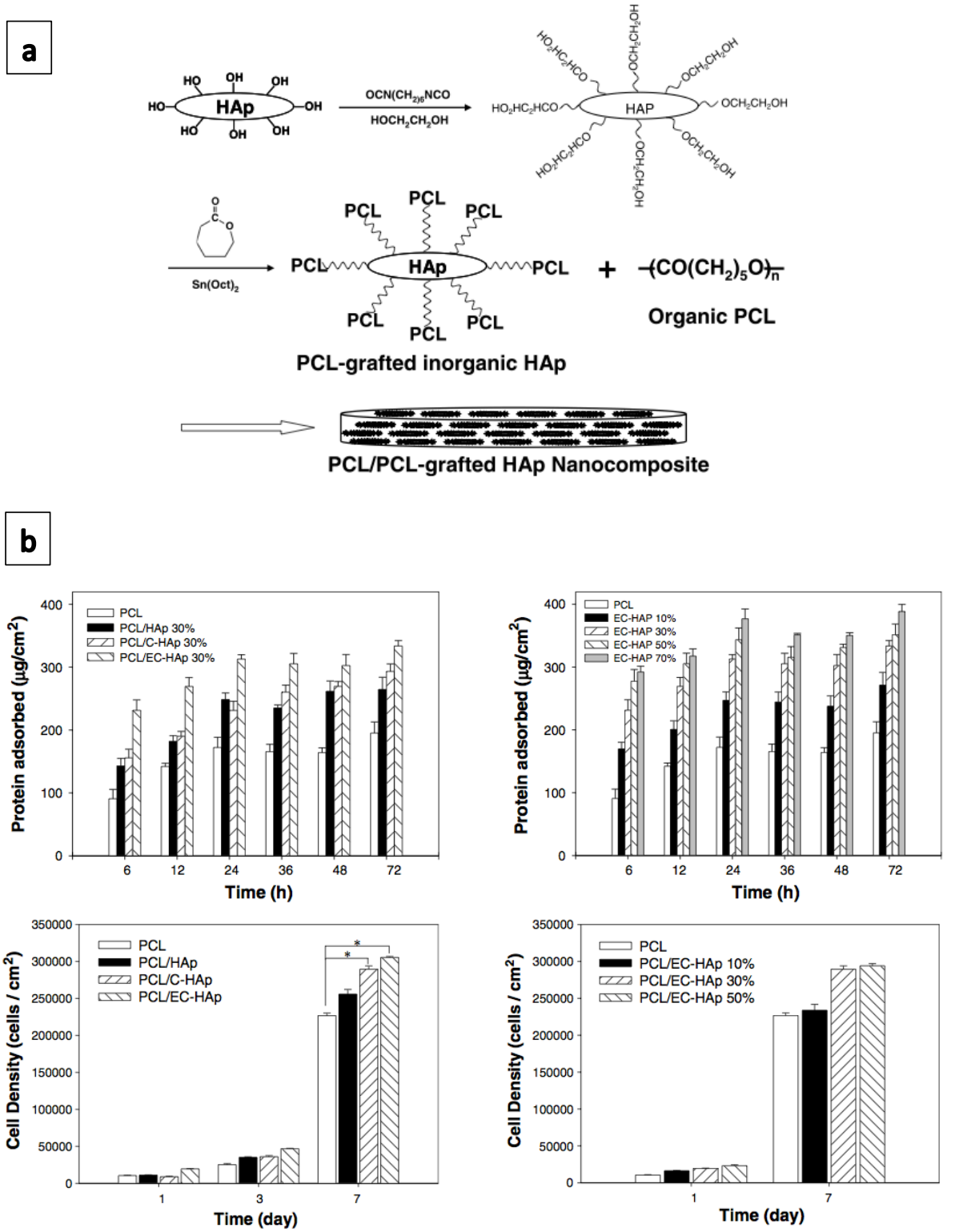

Figure 3.5: Formation of poly(e-caprolactone) (PCL)-hydroxyapattite (HA) composite materials (a) by Lee *et al.* (2007). Protein adsorption and NIH-3T3 cell attachment, (b), increased with PCL modified HA content and attributed to increasing specific surface area swelling of the material in culture media. Amended and reproduced with permission from [17]. © 2007 Elsevier Ltd.

Silane chemistry

The most widely used silane coupling agents are classed as organosilanes consisting of an organic component and three hydrolysable subcomponents bound to a central silicon atom ($R(Si)R_3^{'}$) as can be seen in the bond diagram at the top of figure 3.6. The hydrolysable groups can take the form of methoxy, ethoxy or acetoxy groups; while R represents a non-hydrolysable alkyl, aryl, aromatic, organofunctional or a combination of any of these. Possession of both organic and inorganic properties permit these molecules to react and bind with polymers, minerals and metals [133]s. As result, silane coupling agents have been used for: the dispersion of coating and paint pigments [134]; adjustment of the wettability of gold [135], silica [135], aluminium [136] and silver [137] surfaces; and modification of glass fibers, paints and elastomers [138]. Some interest has grown in applying silane coupling to biomaterials engineering as, for example, amino and carboxyl terminated silanes offer the potential to bind ceramics to biopolymers and biological matter.

Silane modification of surfaces generally involves a four stage process consisting of: i) hydrolysis of the silane coupling agent, ii) condensation of hydrolysed silane to form oligomers, iii) hydrogen bonding with the substrate, and iv) conversion of hydrogen bonds to covalent bonds through dehydration of the sample. The reaction is outlined in the diagram at the bottom of figure 3.6. Hydrolysis degrades the methoxy or ethoxy groups to release methanol or ethanol respectively and leave OH groups behind on the silane agent. In this state, the molecules can form oligomers by condensation of two of the OH groups of multiple molecules to form Si-O-Si bonds. Meanwhile, the third hydrolysed alkoxy group orients itself with OH groups presented on the substrate surface and interface through hydrogen bonding [133]. This interaction can be then be converted to covalent bonding through a heating or curing process at temperatures ranging $50\,^{\circ}\mathrm{C}$-$120\,^{\circ}\mathrm{C}$ for a few hours. In reality, the hydrolysis and condensation processes can progress simultaneously, but at rates depending on the reaction pH. Very generally speaking, hydrolysis is typically carried out under acid conditions (pH 3-6) while condensation is favoured under basic conditions (pH 7-9). Optimal pH, along with the required reaction times, is dependent on the choice of coupling agent, surface chemistry of the substrate and the availability of

Figure 6. Silane coupling agent variations – basic structure.

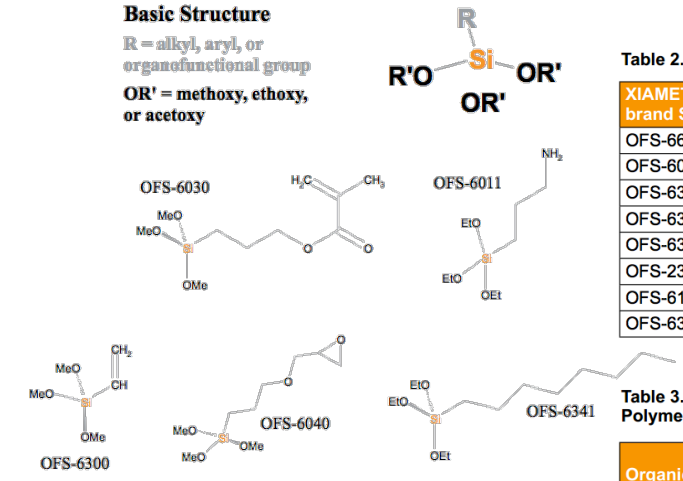

Table 2. Non-Organoreactive Alkoxysilanes

XIAMETER® brand Silane	Organic Group	Alkoxy Group	Chemical Name
OFS-6697	-	Ethoxy	TetraEthoxysilane
OFS-6070	Methyl	Methoxy	Methyltrimethoxysilane
OFS-6366	Methyl	Methoxy	Methyltrimethoxysilane (HP)
OFS-6370	Methyl	Ethoxy	Methyltriethoxysilane
OFS-6383	Methyl	Ethoxy	Methyltriethoxysilane (HP)
OFS-2306	i-Butyl	Methoxy	Isobutyltrimethoxysilane
OFS-6124	Phenyl	Methoxy	Phenyltrimethoxysilane
OFS-6341	n-Octyl	Ethoxy	n-Octyltriethoxysilane

More Hydrophobic

Table 1. Characteristics of Various Organic Substituents on Silanes

Organosilanes R-Si(OMe)$_3$	
R	**Characteristics of "R"**
Me	Hydrophobic, Organophilic
Ph	Hydrophobic, Organophilic, Thermal Stability
i-Bu	Hydrophobic, Organophilic
Octyl	Hydrophobic, Organophilic
-NH(CH$_2$)$_3$NH$_2$	Hydrophilic, Organoreactive
Epoxy	Hydrophilic, Organoreactive
Methacryl	Hydrophobic, Organoreactive

Table 3. Silane Coupling Agent Recommendations for Various Polymers – Matching Organoreactivity to Polymer Type

Organic Reactivity	Application (suitable polymers)
Amino	Acrylic, Nylon, Epoxy, Phenolics, PVC, Urethanes, Melamines, Nitrile Rubber
Benzylamino	Epoxies for PCBs, Polyolefins, All Polymer Types
Chloropropyl	Urethanes, Epoxy, Nylon, Phenolics, Polyolefins
Disulfido	Organic Rubber
Epoxy	Epoxy, PBT, Urethanes, Acrylics, Polysulfides
Epoxy/Melamine	Epoxy, Urethane, Phenolic, PEEK, Polyester
Mercapto	Organic Rubber
Methacrylate	Unsaturated Polyesters, Acrylics, EVA, Polyolefin
Tetrasulfido	Organic Rubber
Ureido	Asphaltic Binders, Nylon, Phenolics; Urethane
Vinyl	Graft to Polyethylene for Moisture Crosslinking, EPDM Rubber, SBR, Polyolefin
Vinyl-benzyl-amino	Epoxies for PCBs, Polyolefins, All Polymer Types

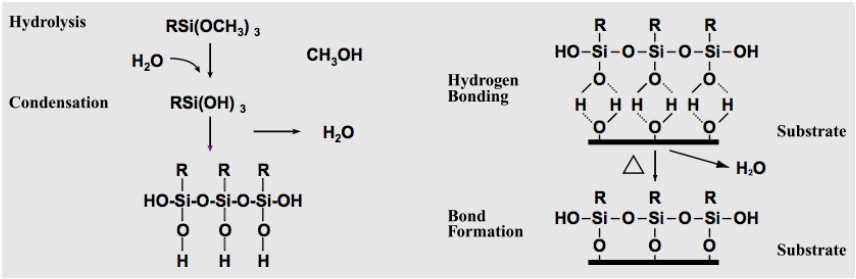

Figure 3.6: Information on a range of commercially available silanes (in this case, Xiameter® silanes sold by Dow Corning Corporation). The basic structure consists of three alkoxy groups bound to a central Si atom, which in turn is bound to alkyl or aryl chain. 'R' is functional group (e.g. amino, mercapto, epoxy) capable of binding to a range of materials (such as urethanes , organic rubbers or acrylics). Tables and figures reproduced from [139]. © 2013 Dow Corning Corp.

water for hydrolysis (in some cases, moisture from air on surfaces is enough while other silanes require addition of water). Silanes can therefore be viewed a 'Lego building brick' approach to constructing a diverse range of functionalised surfaces requiring only standard laboratory apparatus operating at room temperature.

Amine, acetyl, and carboxyl modification of CaPs has been performed causing a shift in the overall surface charge to neutral or negative, which has proven important to modulating cellular attachment to surfaces and internalisation in nano particle form [140]. Carboxyl and hydroxy terminated silanes have been reported to promote the nucleation and growth of calcium phosphate on silane monolayers [141]. The grafting of organic polymers has also been achieved using hexamethylene diisocyanate as a coupling agent to enable attachment of Polyethylene glycol (molecular weight = 1500) [142]. Silane modification has also been employed to improve the dispersion of inorganic fillers and reinforce the filler-polymer interface for a range of CaP filler-polymer combinations including $Ca(CO_3)$ and polypropylene [143, 144, 145].

One of the major examples of the use of silane modification in a biomaterials/bioengineering context is for the engraftment of Arginylglycylaspartic acid (RGD) peptide onto HA (RGD peptides are implicated in cellular attachment to surfaces) and enhance osseointegration of the material [146, 147]. Durrieu *et al.* (2004) achieved RGD grafting via a three step process (figure 3.7) i) 3-aminopropyltriethoxysilane (APTES) functionalisation of the apatite surface, ii) further attachment of a hetero-crosslinker N-sucinimidyl-3-maleimidopropionate (SMP) and finally, iii) attachment of cell-adhesive peptides (cyclo and linear) through maleimide-thiol covalent binding. Although the approach is somewhat extensive, the concept behind the modification permitted controlled highly repeatable monolayer functionalisation, resulting in increased osteoprogenitor cell attachment and proliferation after just 3 hours in culture. The method was later extended for use with nanocrystalline HA and amorphous CaP [147].

There are some reports that the CaP particle morphology has an effect on the attachment of silanes to the particle surface. Vasiliev *et al.* showed that hexagonal HA particles of increasing aspect ratio resulted in lower silane attachment and spherical HA particles displayed the lowest silane attachment of all [148]. This is an important finding as it highlighted that not all crystal

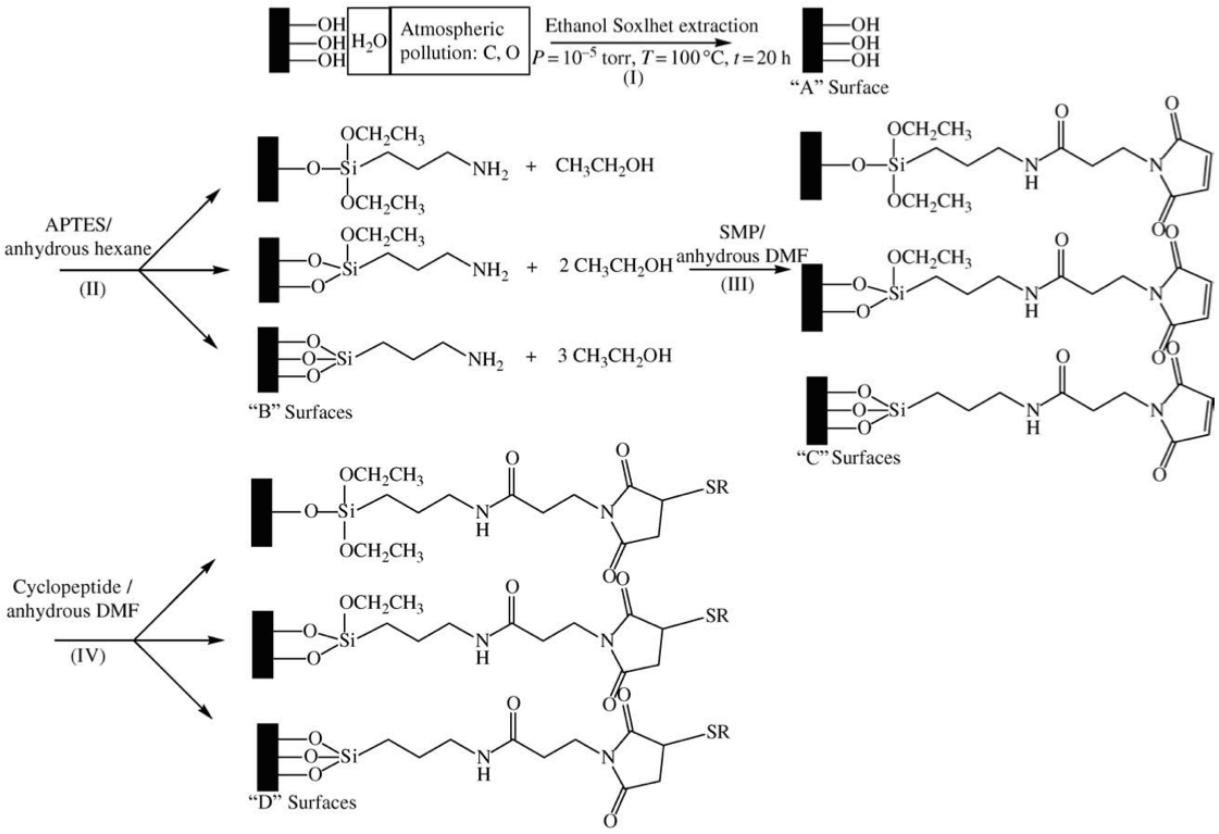

Figure 3.7: Schematic diagram of the three step process for the immobilisation of Arginyl-glycylaspartic acid (RGD) peptide on to HA surfaces by Durrieu *et al.* (2004). The method consisted of: i) 3-aminopropyltriethoxysilane (APTES) functionalisation of the apatite surface, ii) further attachment of a hetero-crosslinker N-sucinimidyl-3-maleimidopropionate (SMP) and finally, iii) attachment of cell-adhesive peptides (cyclo and linear) through maleimide-thiol covalent binding. Diagram reproduced with permission from [146]. © 2004 Kluwer Academic Publishers.

planes of HA are equally reactive which needs to be factored into estimation of loaded drug concentration. Therefore, particle morphology and size would need to be optimised to enable drug loading to the desired concentration while maintaining their ability to be internalised by cells. Another report on polymer-clay nanocomposites facilitated by two methacryloxy-based silanes indicated that some silanes may have had a preference to bind to edge-defects in the clay structure over the clay particle surface, although it could not be determined for sure if this was exclusively due to varying reactivity of the mineral structure or partially due to steric effects from the cross linking silane [149].

CHAPTER 4

CHARACTERISATION OF CHEMICALLY FUNCTIONALISED CALCIUM PHOSPHATE-BASED MATERIALS

The development of any calcium phosphate based material for a given tissue engineering application requires characterisation of its chemical composition and structural properties. This is to aid in the understanding how the material may response while under similar conditions to those in which it is required to function. This is particularly important for materials based around calcium phosphates which can assume a variety of crystal forms (exhibiting different chemical properties) in response to changes in pH or ionic composition of the surrounding environment as explored in Chapter 2. Biological response to these materials can be highly dependent on shape, size and chemical composition and therefore methods of visualising changes in cell morphology and established tests for specific cell responses (e.g. apoptosis) are required to verify the suitability as a biomaterial. This chapter will explain the theory behind, typical experimental setup, and capability of the methods used in this work to characterise the chemically modified calcium phosphates. The techniques are divided between three sections - i) those enabling determination of physical size, shape and composition of the material; ii) those capable of identifying chemical functional groups (arguably at levels below the limit of detection of chemical methods outlined in section in (i); and methods for visualising or testing the cellular response to the materials developed within this work.

4.1 Physical and chemical characterisation of calcium phosphate powders

4.1.1 Compositional characterisation

X-Ray diffraction (XRD)

One of the key demands of materials science is to determine the chemical composition and structure of materials in order to confirm it's purity and understand material properties and performance. While chemical elements bond together to form compounds, the compounds can crystallise into a variety of crystal structures (or phases). Perhaps the most pertinent example is the bonding of calcium, phosphorus and oxygen units to form the compound calcium phosphate, which can assume one of several crystal structures to form distinct materials such as hydroxyapatite and brushite. Conversion between two phases of the same compound can occur as a product of a chemical reaction or through thermal treatment and as a result, differentiating these phases through elemental analysis alone can prove difficult. Powder X-ray diffraction provides a powerful tool for characterising materials through their constituent crystal structures.

X-rays are electromagnetic waves in the wavelength range of 0.01-10nm. A crystal is a three-dimensional array of atoms located at fixed positions, formed by the periodic repetition of a basic motif in space along three non-coplanar vectors [150]. The atoms which make up the crystal are often visualised as lying in a set of planes with interplanar spacing, *d*. The long-range order of these planes and the fact that X-ray wavelengths are comparable to chemical bond lengths led to the discovery that crystals can act as diffraction gratings when irradiated by monochromatic X-rays (Von Laue, 1912). William Henry Bragg and William Laurence Bragg later simplified the Von Laue's theory by considering the diffracted X-rays as being reflected from parallel planes of atoms. Figure 4.1 shows a schematic diagram of Bragg's interpretation where the X-rays from the source at points A and D are in phase.

X-ray $A \rightarrow B \rightarrow C$ is reflected at point B, but X-ray $D \rightarrow E \rightarrow F$ travels an extra distance $JE + EK$ through the crystal in the act of reflecting off the second plane. For diffraction to

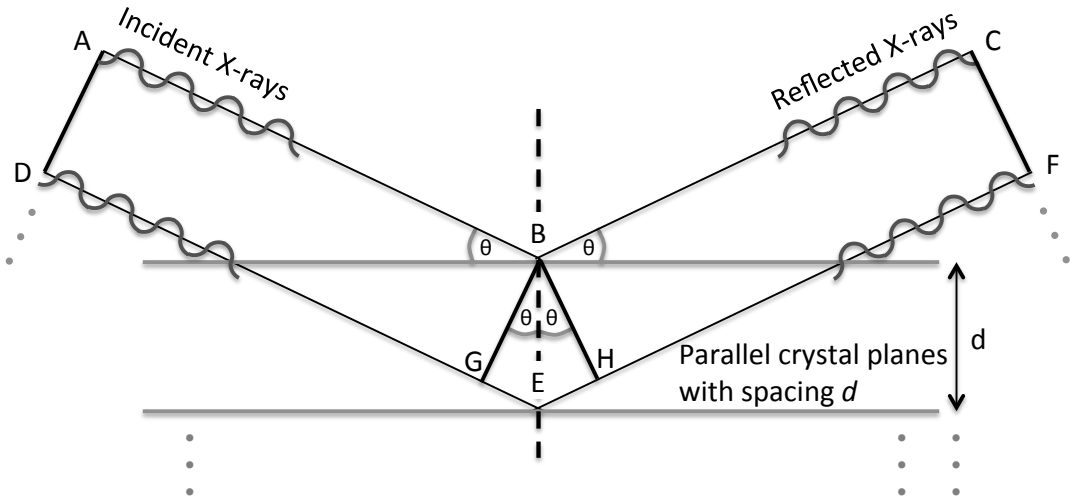

Figure 4.1: Schematic diagram illustrating the Bragg condition for the diffraction of two monochromatic in phase X-rays, $A \rightarrow B \rightarrow C$ and $D \rightarrow E \rightarrow F$, from two successive parallel crystal planes with interplanar spacing *d*. The path length difference, GE+EH, between the waves is related to the plane spacing d and reflected X-rays constructively interfere when the path length difference equals an integer number of wavelengths, resulting in the detection of the reflected beam with intensity I at the precise angle θ. When the Bragg condition is broken, the reflected waves destructively interfere and little or no signal is detected over those range of angles.

occur, the X-rays must be in phase at points B and H and therefore the following condition is enforced:

$$n\lambda = GE + EH \tag{4.1}$$

meaning that the path difference must be equal an integral number of wavelengths of the incident X-ray. Meanwhile, the path length difference either side of the line normal to the crystal planes can be related to the interplanar spacing *d* ($= BE$) by:

$$\sin(\theta) = \frac{GE}{BE} = \frac{GE}{d} \tag{4.2}$$

$$\sin(\theta) = \frac{EH}{BE} = \frac{EH}{d} \tag{4.3}$$

Adding 4.2 and 4.3 together:

$$2\sin(\theta) = \frac{GE + EH}{d} \tag{4.4}$$

and finally, by substituting equation 4.1 into equation 4.4, we obtain the Bragg condition X-ray reflection from successive parallel planes in a crystal:

$$n\lambda = 2d\sin(\theta) \tag{4.5}$$

When this condition is met, X-rays diffract off planes through the crystal in phase and constructively interfere before reaching the detector where the intensity is recorded. When the condition is not met, the wavelets are slightly out of phase (and become more and more out of phase across the many crystal planes) and destructively interfere. The resulting diffraction pattern serves as a unique 'finger-print' of the crystalline composition of the sample. Given that both λ and d are fixed, it is θ - the angle of X-ray incidence/reflection - that is varied when analysing the intensity of reflected beam. Experimentally, this is achieved by rotating the X-ray source and detector symmetrically about a line normal to the sample with a typical setup shown in figure 4.2. In this example, the X-ray source is fixed while the sample and detector are mounted on two independent circular goniometers which rotate at a 1:2 angular ratio respectively. During the measurement, the sample powder spins about an axis normal to the plane of the sample to ensure that crystallites in all possible orientations are exposed to the incident X-ray beam.

Usually, a graph of intensity against 2θ is plotted where each peak on the diffraction pattern allowing calculation of d-spacings within the crystal lattice, mean crystallite size and identification of deformities in the structure. Identification of the different phases of a given compound is achieved by comparison of the acquired pattern with patterns from a database such as the JCPDS database.

Mean crystallite size across particular crystal planes can be estimated using the Scherrer equation:

$$\tau = \frac{K\lambda}{Lcos(\theta)} \tag{4.6}$$

where τ is the mean size of the crystalline domains (less than or equal to the grain size), K is a dimensionless shape factor of the particles, λ is the X-Ray wavelength, θ is the Bragg angle

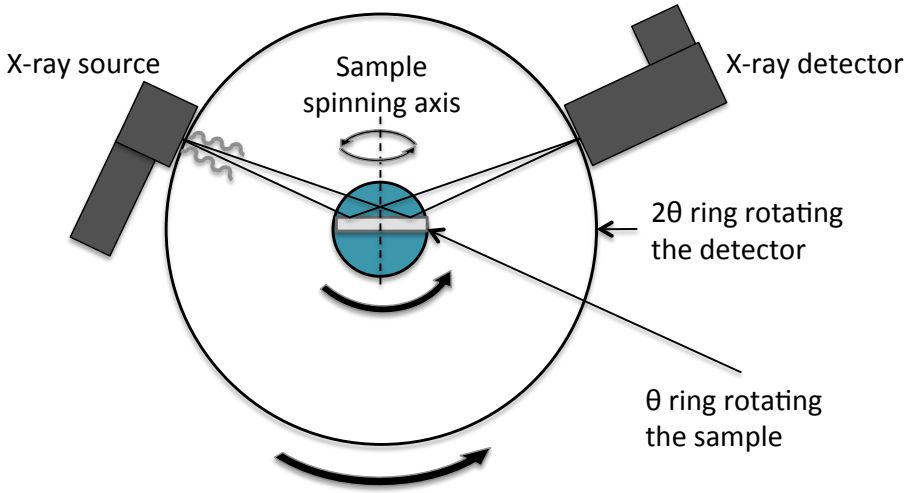

Figure 4.2: Schematic diagram of a X-ray powder diffractometer in reflection mode, whereby the sample and X-ray detector rotate independently on two circular goniometers relative the X-ray source. The sample and detector rotate in unison at an angular ratio of 1:2 respectively in order to simulate the symmetric movement of the source and detector as shown in figure 4.1. The scintillator detector records the intensity of the reflected X-rays over a range of angles to form a diffraction pattern of the sample. Rotation of the sample ensures that the diffraction pattern represents reflections from all possible crystallite orientations.

and *L* is the full width at half maximum of the diffraction peaks after correction for instrumental line broadening.

X-Ray fluorescence (XRF)

XRF is an analytical technique used to determine the chemical composition of solids, liquids and powders with the possibility of quantifying the amount of particle elements or compounds in the sample through careful calibration with known standards.

X-rays can interact with matter in three different ways: i) Absorption and subsequent fluorescence, ii) Compton (or inelastic) scattering and iii) Rayleigh (or elastic) scattering. The contribution of fluorescence and scattering effects within the X-ray interaction with the material depends on the thickness, density and composition of the sample along with the energy of the incident X-rays. The top part of the figure 4.3 shows the interaction of an X-ray with a Bromine atom. The electrons of the Bromine are arranged in the shells *K, L, M, N* with the energy *E* of the electrons in each shell ordered such that $E_N > E_M > E_L > E_K$. An incident X-

ray can expel an electron with one of these to produce a 'hole' with the example in figure 4.3 showing the loss of an electron from the K-shell. However, the atom is energetically unstable in this state and the hole in must be filled through the transfer of an electron from a higher energy L- or M-shell. The surplus energy from the transition, defined by the difference between E_L and E_K is emitted in the form of an X-ray photon which can be detected as an 'emission line' on a plot of intensity against photon energy. Each atom has specific energy levels and multiple electron transitions can occur upon interaction with X-rays and hence the set of emission lines act as a fingerprint for each element in a sample. Measuring the energy of the emitted fluorescence allows the user to determine which elements are present and is hence termed qualitative analysis. Measurement of the intensity of the emission at given energies, along with suitable calibration samples with known amounts of elements of interest, allows quantification of the amount of each element identified in the sample.

Typical lab-based XRF instruments employ an X-ray tube as the X-ray source with a rhodium, indium, gallium or tungsten cathode. The energy/wavelength of the beam incident on the sample can be tuned either via a series of interchangeable X-ray filters or by reflecting the beam off a diffraction grating which rotates precisely with respect to the sample such that only the fraction of the beam of the desired energy/wavelength is incident on the sample (as shown in figure 4.3). The detection mechanism can either be based on an energy-dispersive or a wavelength-dispersive principle, with the latter being able to detect a slightly wider range of elements in terms of atomic number along with offering higher resolution and better detection limits. The work undertaken in this thesis employed a wavelength-dispersive system that consisted of: a set of collimators to collect the emitted X-ray photons, a set of diffraction crystals (or 'analyser' crystals) and two interchangeable detectors including a scintillation detector (general elemental range Na to U) and a proportional detector (for light elements such as Si). The analyser crystals work in the same way as described in the section 4.1.1, but in this case Bragg's diffraction condition is exploited by using perfect crystals of known lattice spacing d to reflect X-rays with wavelengths of interest towards the detectors which rotate through the diffracted emission along an arc. A range of crystals of varying d-spacing are mounted on a rotating stage

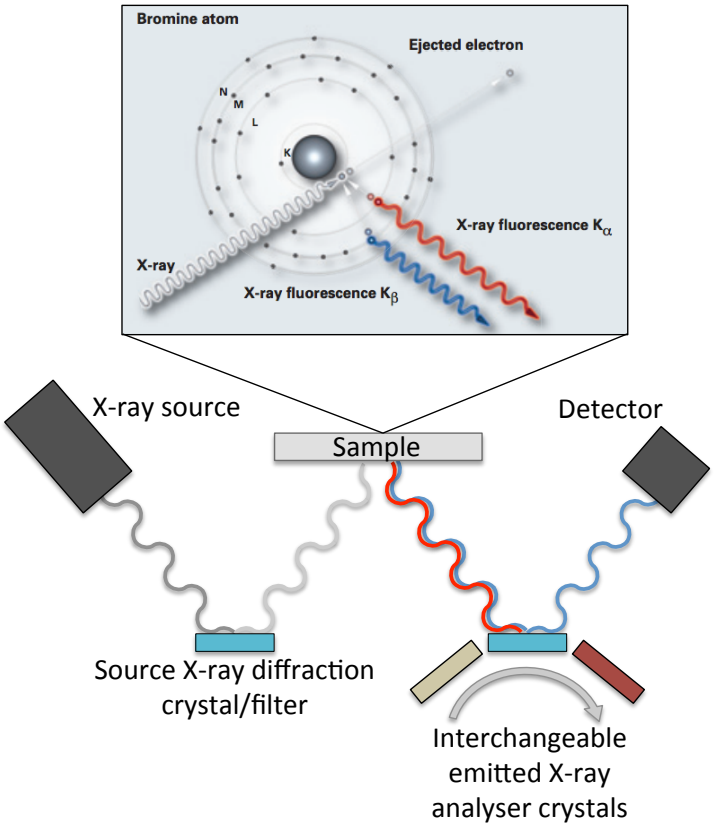

Figure 4.3: Illustration of X-ray interaction with a Bromine atom (top, amended from[151]) along with a schematic of the basic components of a Wavelength-Dispersive X-Ray Fluorescence (WDXRF) instrument (bottom). X-rays can knock an electron out of a shell causing an electron from a higher energy shell to fill the hole. The surplus energy from the transition is released as X-ray photon and is element specific. The energy of the incident beam from an X-ray tube is controlled by the use of a diffraction grating or filter before exposing the sample. The emitted photons are dispersed by reflecting the emission off a series of analyser diffraction crystals, which directs the wavelength of interest towards the scintillation detector.

to allow the instrument to disperse a wide range of emission wavelengths and thus enable detection of range of elements - typically Na to U, but some instruments claim to able to detect elements as light as Be.

4.1.2 Determination of particle size and shape

Laser-diffraction

Laser diffraction based particle sizing instruments enable the size distribution of a powder to be determined within the size range of 0.1μm-2000μm. The technique involves measuring the angular variation of light scattered from a particle to build a diffraction pattern and exploiting the well established *Mie solution* to the diffraction of electromagnetic waves, which predicts the diffraction pattern of a semi-opaque spherical or cylindrical particle of a given volume, to estimate the size of the original particle.

A typical experimental setup is shown in figure 4.4 where a powdered sample is dispersed in a solvent and injected into the glass flow cell of the sizing instrument. A collimated laser beam strikes and is scattered by each particle through an angle measured relative to the direction of the incident light. Generally, the smaller the particle, the larger the range of the scattering angles although the Mie solution also accounts for the partial absorption or transmission of the incident laser light. A set of multi-channel detecters (similar to a single row of pixels in a CCD chip) are positioned around the flow cell to measure the intensity of the scattered light over a range of angles. A computer then reconstructs the diffraction pattern of the particle and builds an optical model using this pattern and the user defined refractive indices of the particle material and solvent along with the absorption coefficient of the material if necessary. The optical model is inverted to obtain the volume of the particle from which the particle radius is then estimated.

The volume/size of around 10^6 particles can be estimated in 1 second and the use of a flow cell enables the size distribution of a typical sample to be acquired in 1 minute without the need for calibration. Hence, laser diffraction particle sizing has established itself as a high-throughput technique capable of measuring a wide dynamic range of particle sizes.

Transmission Electron Microscopy (TEM)

Transmission electron microscopy is an imaging technique allowing the shape and surface structure of a sample to be determined with single nanometer to several hundred micrometers scale

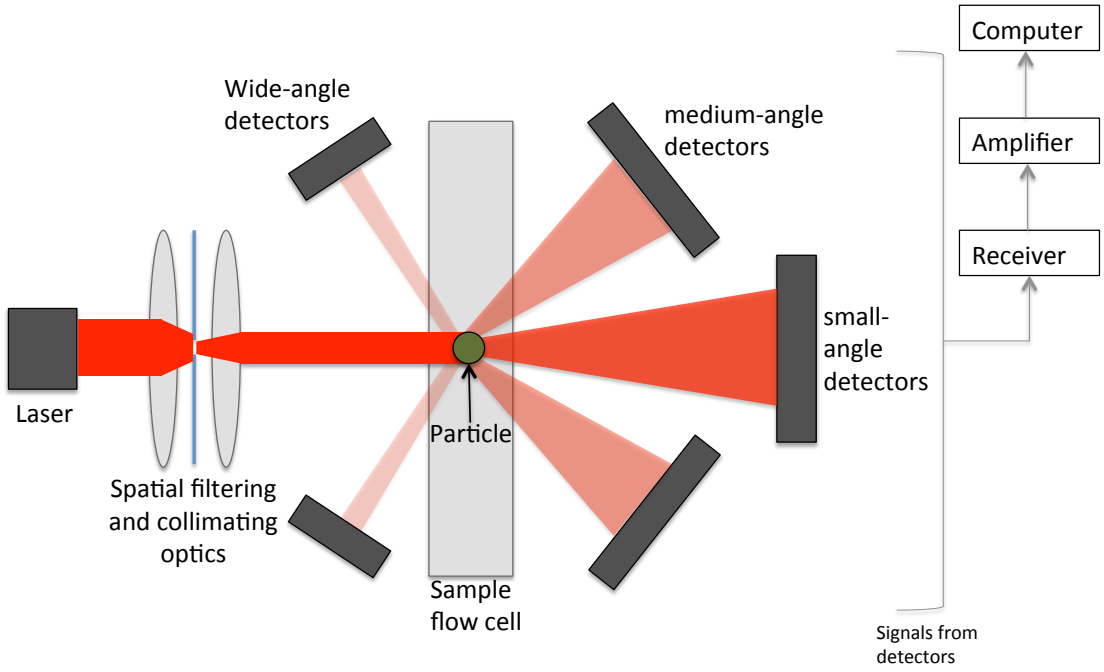

Figure 4.4: Schematic diagram showing the basic components of a laser-diffraction particle sizing instrument. Particles dispersed in a solvent are pumped through a flow cell and pass through the path of a collimated laser beam which is orthogonal to the direction of flow. Large particles scatter the incident light through small angles while small particles will scatter the incident light through large angles. The scattered light is detected by a set of multi-channel detectors positioned around the flow cell and hence a scatter pattern is acquired. Using the acquired diffraction pattern and the user defined refractive indices of the particle material and solvent, a computer optical model based around the *Mie solution* is produced and used to estimate the volume of the particle. The final result is then presented as the radius of a sphere or radius/length of a cylinder of equivalent volume. This is a high throughput technique capable to analysing thousands of particles between 0.1-2000μm.

resolution. The essential components of such an instrument is shown in the Figure 4.5. A tungsten filament gun is employed an electron source, which is heated to a sufficient temperature to cause the release of electrons from the filament. A set of ion optics shapes and collimates the electrons to form a beam, which is then accelerated towards the sample by a potential difference of 5-200kV to form a spot approximately 5nm-2μm in size on the sample surface. Samples are mounted on a copper TEM grid typically by pipetting a small amount of the material dispersed in a solvent on to the surface of the grid. The transmitted part of the electron beam is then collected and focused on to the CCD detector via another set of ion optics. The physical principle behind image contrast in TEM depends on the mode of operation, but the most common mode

(and the mode used to observe the shape of HA crystals) is called 'bright-field' mode. In this mode, the electrons can be treated under classical physics principles as being occluded or absorbed by the sample. Image contrast is then obtained because fewer electrons are transmitted through thicker regions (or regions containing elements of higher atomic number) compared to thinner regions (or regions containing elements of low atomic number) which appear as dark and bright regions on the image respectively. The image formed at the detector can then be regarded as a 2D projection of the volume of the sample irradiated by the electron beam.

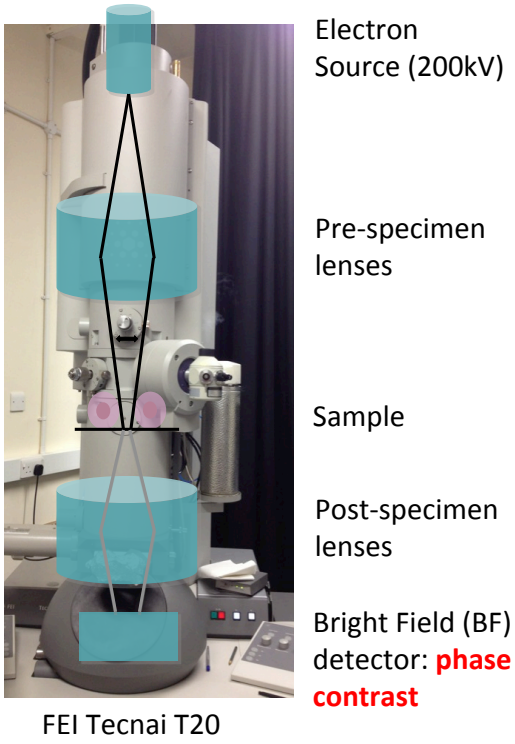

Figure 4.5: Schematic diagram of the basic internal components of a transmission electron microscope overlaid on a photograph of a real TEM instrument, a Tecnai T20. The electrons emitted from an electron gun are focused on to the sample by a set of electrostatic ion lenses. The transmitted component of the incident electron beam is collated by another set of electrostatic lenses and focused on to a CCD detector. The attenuation of the electron beam by the sample (and hence the intensity of the transmitted beam) is dependent on both the atomic number of the constituent elements of the sample and the sample thickness. Amended and reproduced with permission from Miriam Dowle, University of Birmingham, UK. © 2013 Miriam Dowle.

The power of TEM resides in its ability to overcome the diffraction limits imposed on light microscopy systems. A generalised approximation of the Abbe diffraction limit states that the size of the smallest sample feature resolvable using an optical system is approximately equal

to half the wavelength of the light. The De Broglie wavelength of electrons is 1.23nm (assuming kinetic energy of 1eV and rest mass 0.511MeV) which is between two and three orders of magnitude smaller than the wavelengths typically used in light microscopy (eg. 532nm green laser line). It then becomes clear that TEM can resolve features in the pm-nm range and hence achieve atomic scale resolution, which cannot currently be achieved with light microscopy techniques.

4.2 Identification of chemical functional groups and their effect on surface chemistry

4.2.1 Fourier Transform Infrared Spectroscopy (FTIR)

Fourier transform Infrared spectroscopy is a non-destructive high-throughput method used for the identification chemical functional groups present in a sample. Infrared (IR) generally refers to wavelengths of the electromagnetic spectrum between 700nm-1000μm, however the most relevant wavelengths are between 2.5μm-25μm which can be absorbed by molecules and cause stretching, twisting and rocking modes of their chemical bonds. The frequency of light required to resonate with such modes are highly dependent on the constituent elements of a molecule, the nature of the bonding between those elements along with their geometry within the overall structure. A broadband IR beam incident on a sample may resonate with multiple modes of several different chemical bonds creating a spectrum of well-defined absorption peaks unique to the molecule.

Modern FTIR instruments are based around a broadband infrared source, a Michelson-Morley interferometer and an infrared detector as shown in figure 4.6. Powdered samples are usually combined at 1-3%wt with an IR invisible binding agent such as potassium bromide to form a thin and optically clear pellet. It is also possible to perform measurements on liquid samples with a suitable attachment to instrument which then operates in reflection mode.

The IR beam, consisting of a range of frequencies, hits a beamsplitter where 50% of the

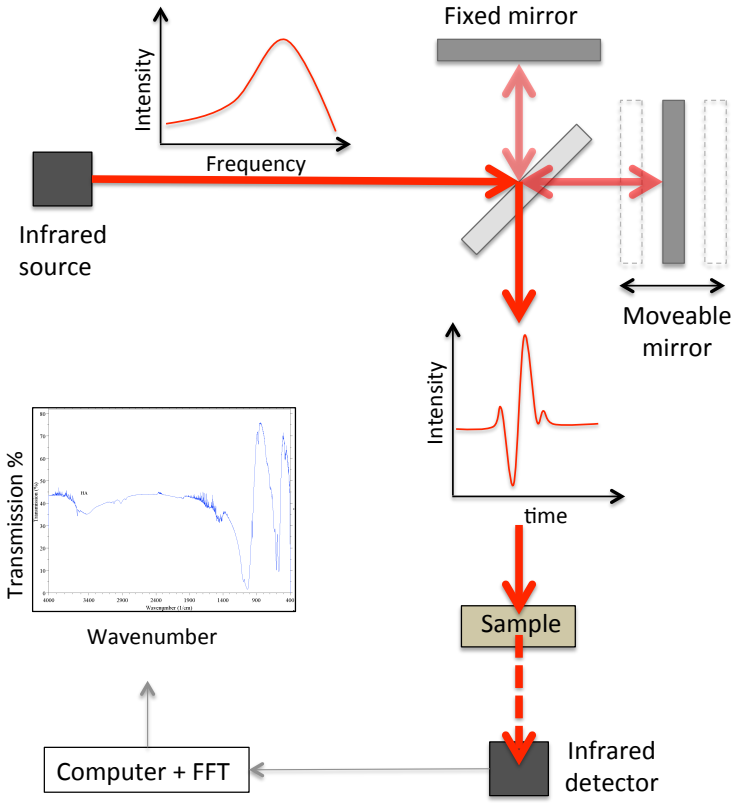

Figure 4.6: Schematic diagram of the basic components of FTIR instrument. A broadband beam of infrared (IR) light is directed into an interferometer - a beam splitter with half of the beam reflecting off a fixed mirror and the other half reflecting from a movable mirror. The beams recombine and undergo constructive and destructive interference at various frequencies in the spectrum, which varies according to mirror position. When the beam passes through the sample, certain frequencies of the IR spectrum are absorbed due for resonance with stretch, twisting and rocking modes of the chemical bonds that make up the sample. These appear as sharp and well defined absorption peaks on a plot of % transmitted intensity against wavenumber.

beam is reflected off a fixed mirror and while the other 50% reflects back off mirror mounted on a movable stage. The mirror moves over the range of a few mm and causes constructive and destructive interference of the waves when the two beams recombine at the beamsplitter. At this stage only certain frequencies of the original IR beam remain in the spectrum and this selection of frequencies is modulated by the position of the mirror. Note, that this is in stark contrast to other absorption spectrum techniques such as UV-Vis, where a measurement is taken at one specific frequency of light before sequentially scanning through a range of wavelengths to obtain the final spectrum. The beam is then represented as an interferogram, showing how the intensity of the light changes with time, and passes through the sample. The emerging beam is then detected at the IR detector and the interferogram is converted to and intensity against frequency plot through a mathematical operation called a Fourier Transform. Fast oscillation of the mirror enables the acquisition of interferograms over the entire IR spectrum in a short period of time (typically 1 minute as for fairly high spectral resolution measurements). The data is usually presented as a plot of % absorbance or % transmission of the incident beam energy at a given wavenumber (=1 divided by the wavelength in cm.). Although moisture absorbs significantly in the IR region of the spectrum, careful drying and preparation of sample powders and reagents can allow for detection of functional groups to very high sensitivity.

4.2.2 Raman Spectroscopy

Raman spectroscopy is another form of bond vibration spectroscopy involving the polarization of a molecule upon irradiation with visible, near infrared or near ultraviolet light and subsequent inelastic scattering of that light causing a measured frequency shift which represents the vibrational modes of the molecule. This is in contrast to the mechanism of FTIR, which is relies on the absorption of the light and depends on the dipole moment of the molecule. This allows Raman to analyse transitions in molecules that are inaccessible to FTIR (such as those exhibited by centrosymmetric molecules) and therefore Raman and FTIR can be considered complementary techniques for characterising the chemical structure of samples [152]. Raman spectroscopy has found use in chemistry, molecular identification of disease in tissues and even for revealing

the chemical structure of soils from Mars [153]. The most recent hardware developments to Raman system have enabled imaging of samples with chemical contrast at high spatial resolutions [152].

Commercial Raman spectroscopy instruments are based around an optical microscope, as shown in figure 4.7, with a set of lasers and spectrometer attached.

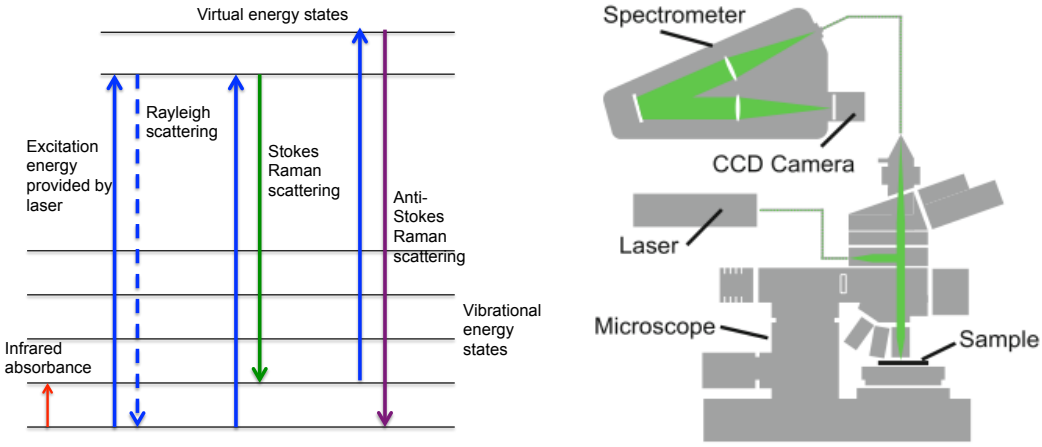

Figure 4.7: Schematic diagram of the three Raman scattering processes compared to IR (left) and a schematic diagram of a typical Raman spectroscopy system built around an optical microscope (right, adapted from [152]. © 2010 Springer-Verlag).

The incident light excites the molecules in the sample to a 'virtual energy state' - a notional state usually considered when a system is not supplied with enough energy to be excited to a discrete energy level as would happen during an absorption/fluorescence process. The molecule relaxes from the virtual state to a different rotational or vibrational state, emitting a photon in the process. The difference in energy between the initial and final state leads to a frequency shift of the emitted light relative to the incident light. If the final state of the molecule is more energetic than the initial state, then the emitted light is shifted to the lower frequency and known as Stokes scattering. If the final state of the molecule is less energetic than the initial state, then the emitted light has a higher frequency and considered as Anti-Stokes scattering. The light scattered from the illuminated sample area is collected by the objective lens and sent to the spectrometer. The degree of polarisation about an axis along the vibrational mode of interest determines the intensity of the Raman scattering of that mode. A plot of Raman intensity against

frequency- or wavenumber- shift is produced where the pattern of Raman peaks represents the rotational and vibrational modes of the molecules in the sample. Optical filters are employed to remove the Rayleigh scattered (elastically scattered) light which would otherwise dominate over the weak Raman signal. Most systems also use a pinhole in front of the detector to suppress fluorescence generated in the sample, which can be in worst cases up 10^6 times more intense than the Raman signal [152].

4.2.3 UV-visible (UV-Vis) absorption spectroscopy and colourimetric assays

Colorimetric assays are now common place for the quantification of a particular chemical compound or ion in solution through a known chemical reaction with a reagent to form a product which 'reports' the presence of the compound of interest. The chemical product often has a known absorption/fluorescence profile which varies predictably with its concentration in solution and hence the concentration of the compound of interest can be inferred. The absorption measurements themselves are performed on a spectrophotometer capable of measuring the absorption and emission over the ultraviolet (250-400nm) and visible (400nm-700nm) wavelengths which is why the instrument/technique is often called 'UV-vis spectroscopy'. The measurement process exploits the Beer-Lambert Law, which states that the absorbance of light by an absorbing medium is directly proportional to the concentration of the absorbing medium and the path length of the light passing through that medium. In a spectrophotometer, the path length is fixed by using a cuvette of known dimensions to contain the liquid and the intensity of the incident and transmitted light is measured. Through comparison with absorbance measurements of standards of known concentrations of the compound of interest, the concentration of the unknown sample can be determined. There are various assays available for quantifying chemical functional groups such as thiols, amines and carboxyl groups. In addition, the calcium/phosphate ion content of solutions can be determined and can be applied to estimating the composition of CaP-based powders and studying the release of ions from such materials during degradation studies.

The presence of Ca^{2+} ions in solution can be determined by reacting with Arsenazo III (2,2-[1,8-Dihydroxy-3,6-disulphonaphthylene-2,7-bisazo]-bisbenzenear-sonic acid) under slightly alkaline conditions to form a purple coloured complex. The absorbance of the complex is measured at 650nm (or measured bichromatically at 660nm and 700nm to calculate an 'absorbance increase'[154]) and is proportional to the calcium concentration [155]. This relationship is linear in the Ca^{2+} concentration range of 4.0 to 18.0mg/dL and therefore sample dilution may be required to ensure accurate measurements[154]. The Arsenazo III assay can be extended to estimate the Ca^{2+} ion content of a powder by fully dissolving the sample in nitric acid and re-suspending a small volume of the sample solution in water before adjusting to a slightly alkaline pH.

Phosphate mass in solution can be quantified in by mixing with ammonium vanadomolybdate at slightly acidic pH and following a similar protocol to that described above for calcium ions. In this case, the absorbance is measured at 720nm and compared to appropriate phosphate controls.

Thiol concentration can be estimated by using Ellman's reagent 5,5-dithio-bis-(2-nitrobenzoic acid) (DTNB). This compound binds to the free sulphydryl group of the thiol to form the yellow-coloured product 2-nitro-5-thiobenzoic acid (TNB). The absorbance of the assay solution at 412nm is measured and is proportional to the concentration of free sulphydryl groups in the sample as will be explained further in section 6.1.2. Tryptophan salts dissolved in solution are typically used as the mass calibration standard. The number of the thiols present in the sample can be under estimated if a proportion of the thiols were oxidised to the addition of the Ellman's reagent, but can be easily reduced by addition of dithiolthreitol (DTT) before repeating the measurement process.

4.2.4 Zeta potential measurements

Colloidal systems comprising of one phase (e.g. solid CaP nano crystals) dispersed in another phase (e.g. liquid water) have high interfacial energy and thus ultimately unstable. As result, the dispersed phase will have a tendency to flocculate, coalesce or sediment from the solvent

over a period of time in order to minimise the interface area and the total potential energy of the system [156]. How fast this process happens depends on the electrical characteristics of the particle surface and that of the immediate surrounding media the particles are dispersed in [156]. A net surface charge develops on the particle surface through a variety mechanisms including the simple presence of the constituent ions of the material to dissociation of functional groups at the surface and adsorption of ions from the solution. The net surface charge influences the distribution of ions in the immediate suspension medium close to the particle surface such that counter ions preferentially localise at the surface of the particle to create an *electrical double layer* as shown in figure 4.8. The electrical double layer consists of two parts: i) the *Stern layer*, containing the counter ions which are strongly bound or specifically adsorbed to the particle surface and; ii) the *Diffuse layer*, where the ions are less strongly bound to the particle surface and their distribution determined by electrostatic forces and thermal motion within the entire system [156, 157]. The potential of this double layer decays with distance from the particle surface where a zero value is considered to exist within the bulk dispersion medium. As the particle moves under the influence of gravity or through an applied electric field, the most closely bound ions from the Stern and Diffuse layers move with the particle and shear against the ions left behind in the bulk medium. The notional plane that exists where shear occurs is called the *slipping plane*, the potential at which is called the *zeta potential*.

The magnitude of the zeta potential can indicate the stability of the colloidal system. Large positive or negative zeta potential values suggest that the particles will tend to strongly repel each other with minimal risk of flocculation, while low zeta potential values suggest that the interparticle forces are not strong enough to prevent flocculation.

The zeta potential of a sample can be calculated from the electrophoretic mobility of the sample placed in an electric field. Figure 4.9 shows the basic components of a zeta-sizing instrument. The sample powder is dispersed in an electrolyte such as 10mM aqueous KOH at low concentrations and injected in a glass flow cell. When a voltage is applied across the electrodes, an electric field is created between them, which imparts a force on the suspended charged particles and accelerates them towards the electrode of opposite charge. A viscous

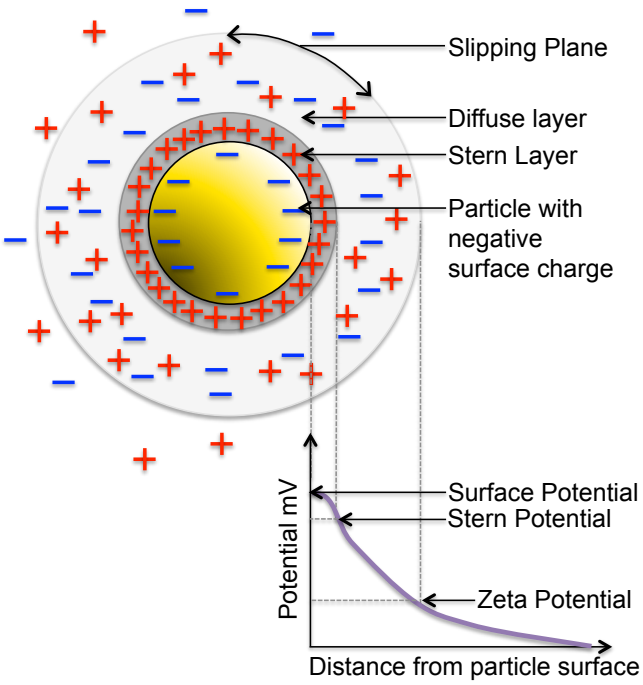

Figure 4.8: Illustration of the formation of the Electrical Doublelayer caused by influence of the particle net surface charge on the local distribution of charges in the electrolyte. Counter ions are strongly attracted to the particle surface to form the Stern layer which in turn influences the formation of a second Diffuse layer. The electrical double layer follows the movement of the particle while shearing against the stationary bulk electrolyte. The potential at this 'Slipping plane' represents the zeta potential.

force acts against the direction of motion due to friction at the shear plane between the diffuse layer and the bulk solution. The particles move with constant velocity when these forces are in equilibrium and the velocity is then dependent on the voltage gradient, the dielectric constant of the medium, the viscosity of the medium and the particle zeta potential [158]. The particle velocity is determined by measuring the frequency shift of a laser beam scattered by oncoming or retreating particles relative to a reference beam (the physical principle is called Doppler shift with its application in this case called Laser Doppler Velocimetry). The velocity is dependent on the strength of electric field or voltage gradient, the dielectric constant of the medium, the viscosity of the medium and the zeta potential. Electrophoretic mobility refers to the velocity of a particle per unit of electric field strength and hence the zeta potential is calculated from the Henry equation [156, 158]:

$$U_E = \frac{2\epsilon z f(\kappa a)}{3\eta} \tag{4.7}$$

where U_E is the electrophoretic mobility, ϵ is the dielectric constant of the medium, η is the viscosity of the medium and $f(\kappa a)$ is the Henry function. κ, the Debye length, is taken to represent the 'thickness' of the electric double layer, while a is refers to the particle radius. Hence κa can be taken to represent the ratio of particle radius to electrical double layer thickness [158]. $f(\kappa a)$ can be taken to be = 1.5 for zeta potential measurements in aqueous media at moderate (more than 10^{-3} molar) salt concentrations and = 1.0 for non-aqueous low dielectric constant media [158].

There are a number of electrokinetic effects that can influence the velocity of the moving charged particles and have to be accounted for. The most prominent effect - one which affects any flow of charged particles in an enclosed cell - is *electroosmotic flow*. The glass walls of the flow cell carry a surface charge, causing a build up mobile ions at the glass interface in order to maintain chemical equilibrium with the electrolyte. When the electric field is applied to a closed cell, this net charge moves along the walls in the direction opposite to the electrophoretic flow, returns along the centre line of the cell and superimposes on the electrophoretic movement of the particles. As can be seen in figure 4.9, the measured velocity profile of particles has a

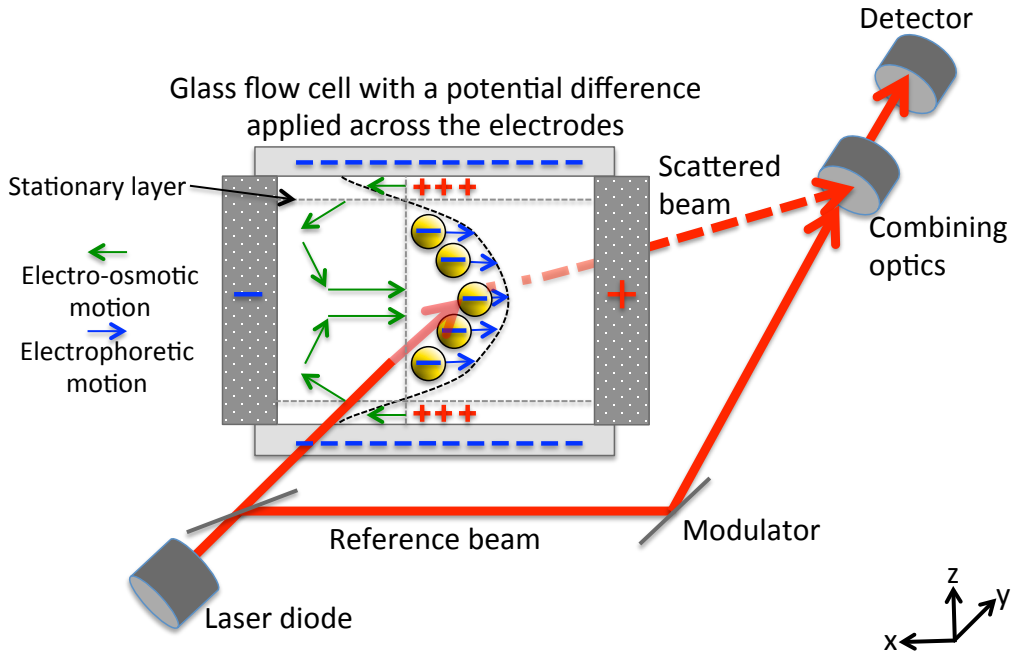

Figure 4.9: Schematic diagram of a typical zeta-sizer instrument where zeta potential is determined by measuring the electrophoretic mobility of the charged particles. The particles are dispersed in an electrolyte and injected into the a glass electrocell. When electric field is applied across the cell, the charged particles move towards the electrode of opposite charge. The velocity of the particles is measured by analysing the Doppler shift of a laser scattered by the moving particles relative to a reference beam and the zeta potential calculated by using the Henry equation (equation 4.7). However, electroosmotic effects superimpose with the electrophoretic flow resulting in a parabolic velocity profile. True electrophoretic velocity can be measured at the 'stationary layer', where the electroosmotic flows cancel (horizontal dotted line), and the precise location of these layers are determined by taking multiple velocity measurements along the z-direction of the cell. The vertical dotted line in the z-direction is a line of zero net particle velocity.

parabolic shape as a result. However, the dotted lines running parallel to the cell wall represent levels where the two components of the electroosmotic flow (the flow along the wall and flow returning back along the centre) cancel out and therefore the velocity measured at these levels represents the true electrophoretic velocity of the particles. The precise location of these levels is determined by taking a series of velocity measurements at different points along a line perpendicular to the flow (labelled as the z-axis in figure 4.9 and referred to as 'z-positions' in materials and methods chapter 5.1.5.

The zeta potential of a particulate system can thus be considered as an index of particle

stability based on the surface charge properties of the particle. The measurement process typically takes 5 minutes and does not require calibration since the measurement is based on first principles.

4.3 Characterising biological response to calcium phosphate-based materials

4.3.1 Live/Dead assay

The Live/Dead® assay (and variations thereof from other life science suppliers) is a fast and easy to prepare method for visually identifying individual live and dead cells. The assay involves exposing a population of the cells to two compounds: Calcein AM, which is cleaved by esterases in the cytoplasm of living cells to produce green fluorescence and; ethidium homodimer-1, which labels the nucleic acids of membrane compromised cells to produce red fluorescence. The cell population is then observed under an epi-fluorecence microscope where the live (green coloured) and dead (red coloured) cells can be identified.

4.3.2 Confocal fluorescence microscopy

Confocal fluorescence microscopy is a powerful extension to conventional epi-fluorescence microscopy. It's ability to 'optically' section cells treated with organelle specific fluorescent dyes, enables internal structure to be revealed at high spatial resolution and high signal-to-noise ratio. The basic set up of a confocal microscope is shown in figure 4.10, but the key features are (i) the use of a point light excitation and (ii) a pinhole placed in front of the detector.

A point light source (solid blue line) is created by focusing a laser beam onto a pinhole. After collimation, the excitation light is reflected off a dichroic mirror and focused by the objective lens to illuminate a diffraction limited area of the focal plane of the sample (rather than entire field of view as with widefield or epi-fluorescence microscopy). However, the excitation light that converges to and diverges from this area can also excite fluorophores above and below the

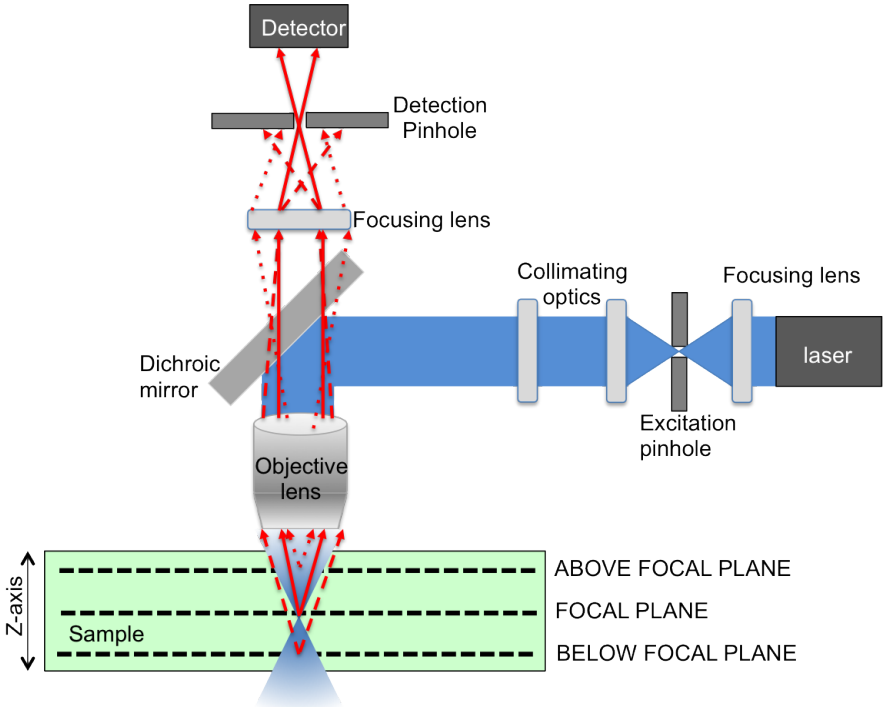

Figure 4.10: Schematic diagram showing the basic components of a confocal microscope. Imaging a point light source on to the sample excites a diffraction limited region of the focal plane, but this region is extended in the z-axis both above and below the focal plane. The objective lens collects fluorescence from these planes, but out of focus light is suppressed by pinhole, which is placed in the conjugate plane of the objective in front of the detector. Only the collimated fluorescence from the focal plane passes through the pinhole and on to the detector (red solid line). fluorescence from below (dashed red line) and above (dotted red line) the focal plane are not focused on to the pinhole and are mostly blocked.

focal plane and thus extends the excitation region in the z-axis to create an excitation volume. The fluorescence generated within the excitation volume is collected by the same objective lens and transmitted through the dichroic mirror. To suppress the out of focus fluorescence before it reaches the detector, a spatial pinhole is positioned in front of the detector in the conjugate plane to the objective lens. In figure 4.10 it can seen that fluorescence from the focal plane is collimated at the back aperture of the objective lens and brought to focus on the pinhole. Light from below the focal plane (dashed red line) converges from the back aperture of the objective and is rapidly brought to focus in front of the pinhole before it diverges and is mostly blocked. Light from above the focal plane (dotted red line) diverges from the back aperture of the objectives and is brought to focus behind the pinhole and therefore is also mostly blocked. In practice, the

focal plane is a section of finite thickness which is approximately proportional to the diameter of the detection pin hole which is adjustable on confocal microscopes. In essence, the wider the pinhole, the thicker the image slice through the object. Confocal fluorescence images are generated by rastering the excitation light over the sample and recording the fluorescence signal at each spatial point. The position of the focal plane within the sample can be varied by changing the distance (along z-axis) between the objective lens and the sample surface. 2D images acquired at different points along the z-axis can reconstructed to form a 3D fluorescence image of the sample.

The spatial resolution of commercial systems can theoretically reach approximately 139nm laterally and 528nm axially (assuming objective NA=1.4 and a 488nm laser line as the excitation source). Images can be acquired at 1 frame per second as standard, but specialist systems can achieve 30 frames per second, potentially enabling the imaging of cellular dynamics such as vesicle tracking.

CHAPTER 5

ROUTINE MATERIALS AND METHODS

5.1 Routine characterisation methods

This section describes the materials and methods used for the structural and chemical characterisation of the starting CaP material prior to chemical functionalisation and processing experiments detailed in this thesis and hence were considered 'routine' procedures.

5.1.1 X-ray Diffractometry (XRD)

Prior to XRD analysis, samples were dried overnight $65°$C. After drying, the samples were ground using a marble mortar and pestle before distributing 200mg of the ground sample powder over a 10mm diameter circular area of 25mm Magic® tape (Scotch Magic Tape, 3M, France) which was in turn folded over the sample and attached to the sample holder. XRD patterns were acquired using a Bruker D8 Advance Diffractometer (Bruker ASX Gmbh, Karlsruhe, Germany) using the copper K_α line λ=1.5406nm at 40kV and 30mA. Each data set was collected from 2θ = $5°$ to $60°$ at a step rate of $0.05°$/s. The sample was rotated about its axis during the entire measurement to minimise the influence of preferential crystal orientation. Baseline correct of the diffraction patterns was implemented using the Bruker DIFFRAC.SUITE software (Bruker ASX Gmbh, Karlsruhe, Germany).

5.1.2 X-ray Fluorescence (XRF)

Samples were dried and powdered as described for XRD analysis. For loose powder samples, 1g of powder sample was evenly distributed over 2μm thick Mylar film held taut over a loose powder sample holder. For pelleted samples, sample powder and wax were mixed to a 1:5 mass ratio (typically 0.5g of ground sample powder to 2.5g of wax) and compacting into a pellet using a 13mm evacuuable pellet press kit (Specac Ltd., Kent, UK) with an applied load of 2 tons held for 15 seconds. The samples were analysed using a Bruker S8 Tiger (Bruker ASX Gmbh, Karlsruhe, Germany) with a measurement time of 18 minutes per sample.

5.1.3 Fourier Transform InfraRed (FTIR) spectroscopy

1g of sample and 1g of potassium bromide (KBr) (FT-IR grade, 221864, Sigma-Aldrich Ltd., Dorset, UK) were ground separately using a mortar and pestle and heated overnight in oven at $80°\mathrm{C}$ to remove moisture. To make one FTIR pellet, 2mg of dried powdered sample was mixed with 298mg of KBr, transferred to a 13mm evacuuable pellet press set (Specac Ltd., Dorset, UK) and pressed with an applied load of 10 tons held for 15 seconds. FTIR spectra of the sample pellets were acquired with a Nicolette 380 FTIR instrument (ThermoScientific Inc., Waltham, MA, USA), a spectral resolution of 0.4822cm^{-1} and represented the sum of 64 consecutive scans. A background spectrum was acquired of a pure KBr pellet made by pressing 300mg of dried KBr using the same pressing protocol and FTIR scan parameters as the sample-KBr pellets.

5.1.4 Raman spectroscopy

Raman spectra of ground powdered hydroxyapatite samples were acquired using a Renishaw InVia Raman microscope (Renishaw plc., Gloucestershire, UK) using a 532nm laser line at 10% power delivered to the sample via a x50 Plan-N objective lens with the detection range set to 400-3600cm^{-1}. The scan time was set to 10 seconds and 5 scans were acquired and summed to produce the final spectrum for analysis using the Wire 3.0 software (Renishaw plc,

Gloucestershire, UK.).

5.1.5 Zeta-potential analysis

Stock dispersions of hydroxyapatite particles in de-ionised water were prepared to a concentration of 0.1mg/mL and 10mM potassium chloride (Sigma-Aldrich Ltd., Dorset, UK) as the electrolyte. Adjustments to the pH were performed using 10mM hydrochloric acid (Sigma-Aldrich Ltd., Dorset, UK) and 100mM potassium hydroxide (Sigma-Aldrich Ltd., Dorset, UK) at an ambient temperature of $25°C$. The samples were left to equilibrate overnight before checking the pH with a Mettler S20 pH meter (Mettler-Toledo Ltd., Leicestershire, UK) and correcting the pH if necessary prior to analysis. Zeta potential analysis was performed using a Beckman & Coulter Delsa Nano C zeta-sizer (Beckman & Coulter, High Wycombe, UK) with a high concentration flow cell. The cell and electrodes were cleaned by repeatedly flushing 100mM potassium chloride through the chamber and measurements were taken while the sample temperature was maintained at $25°C$. Electrophoretic mobility was measured at 9 z-positions, with 10 accumulations at each point, repeated over 3 runs before repeating the whole process with a fresh sample 3 times. The pH of the remaining sample solution was measured and recorded again immediately after zeta-potential measurements so that the possible effect of pH changes on the zeta-potential results could be considered during the analysis of the data.

5.1.6 Transmission Electron Microscopy (TEM)

HA and SiHA in de-ionised water samples were diluted from 10mg/mL to 400μg/mL and a 5 μL drop placed on square mesh-100 copper TEM grids (AGG2100C, Agar Scientific Elektron Technology UK Ltd., Essex, UK). TEM images were acquired using a JEOL JEM 1200EX (JEOL Ltd., Tokyo, Japan) microscope with a beam energy of 80kV.

5.1.7 Atomic Absorption Spectroscopy

Dissolving of the samples was performed by Richard Williams - 1g of powder was dissolved in 50mL nitric acid (70%, >99.999% trace metal basis, 225711-475ML, Sigma-Aldrich Ltd., Dorset, UK). The sample were diluted using de-ionised Millipore® water (18MΩ) and analysed using an Atomic Absorption Spectrometer (Agilent 280FS AA, Agilent Technologies UK Ltd., Berkshire, UK). The analysis was performed by Jamie McLeod (Guardian Laboratories (Midlands) Ltd., Unit 1, Rocky Lane Trading Estate, William Henry Street, Aston, Birmingham, B7 5ER.).

5.2 Hydroxyapatite and Silicon-substituted hydroxyapatite synthesis

5.2.1 Hydroxyapatite (HA)

$$\begin{aligned} &10\,\mathrm{Ca(NO_3)_2\cdot 4\,H_2O} + 6\,\mathrm{(NH_4)_2HPO_4} + 8\,\mathrm{NH_4OH} \longrightarrow \\ &\mathrm{Ca_{10}(PO_4)_6(OH)_2} + 20\,\mathrm{NH_4NO_3} + 20\,\mathrm{H_2O} \end{aligned} \tag{5.1}$$

Aqueous solutions of calcium nitrate 1M (Fisher Scientific UK Ltd., Loughborough, UK) and Diammonium hydrogen phosphate dibasic 0.6M (Sigma-Aldrich Ltd., Dorset, UK) were prepared and pH adjusted to 10.00 through drop wise addition of 37-39% ammonium hydroxide (Sigma-Aldrich Ltd., Dorset, UK). The phosphate salt solution was added drop wise to the calcium salt solution using a burette while stirring and maintaining a pH of 10.00 through further addition of ammonium hydroxide. After ageing overnight while under stirring, the nano crystals were washed by five cycles of centrifugation at 4000rpm and resuspension with deionised water before filtering the suspension using a vacuum Buchner funnel and filter paper (Fisher Scientific UK Ltd., Loughborough, UK). Typical yield of solid product was approximately 30g, with 1g resuspended at 1mg per mL in deionised water adjusted to pH 7.00 and the remaining solid material dried overnight in an oven at $60\,^{\circ}\mathrm{C}$.

5.2.2 Silicon-substituted hydroxyapatite (SiHA)

To form stoichiometric SiHA, the molar ratio condition Ca:(P+Si) was maintained when preparing the salt solutions for the reaction.

$$\begin{aligned} &10\,\mathrm{Ca(NO_3)_2\cdot 4\,H_2O} + (6-x)\,\mathrm{(NH_4)_2HPO_4} + x\,\mathrm{Si(OCOCH_3)_4} + 8\,\mathrm{NH_4OH} \longrightarrow \\ &\mathrm{Ca_{10}(PO_4)_{(6-x)}(SiO_4)_x(OH)_{(2-x)}} + 20\,\mathrm{NH_4NO_3} + 20\,\mathrm{H_2O} \end{aligned} \tag{5.2}$$

As such, an aqueous solution of calcium nitrate 1M (Fisher Scientific UK Ltd., Loughborough, UK) and a separate solution of diammonium hydrogen phosphate dibasic 0.55M (Sigma-Aldrich Ltd., Dorset, UK) and 0.05M silicon tetraacetate (95%, 345156, Sigma-Aldrich Ltd., Dorset, UK) were prepared and pH adjusted to 10.00 through drop wise addition of 37-39% ammonium hydroxide (Sigma-Aldrich Ltd., Dorset, UK). The phosphate-silicon salt solution was added drop wise to the calcium solution using a burette while stirring and maintaining a pH of 10.00 through further addition of ammonium hydroxide. After ageing overnight while under stirring, the nano crystals were washed by five cycles of centrifugation at 4000rpm and resuspension with deionised water before filtering the suspension using a vacuum Buchner funnel and filter paper (Fisher Scientific UK Ltd., Loughborough, UK). Typical yield of solid product was approximately 30 grams, with 1 gram resuspended at 1mg per mL in deionised water adjusted to pH 7.00 and the remaining solid material dried overnight in an oven at $60\,^{\circ}\mathrm{C}$.

CHAPTER 6

RESULTS CHAPTER 1: THIOL MODIFICATION OF SILICON-SUBSTITUTED HYDROXYAPATITE NANOCRYSTALS

The work in this chapter represents a proof of principle that silicon-substituted hydroxyapatite (SiHA) could be modified with functional groups (in this case thiol, but could include amine, carboxylic etc) for the engraftment of biomolecules useful to imaging, drug delivery or to allow for the general alteration of the surface chemistry of SiHA. The method involves the functionalisation of SiHA nano particles with the silane MPTS via covalent bonding, which in turn presents a thiol functional group from the particle surface. The influence of the modification method on the physicochemical properties of the material were determined using X-ray diffraction (XRD), X-ray fluorescence (XRF), Zeta potential (ZP) measurement, and Fourier Transform Infra-red Spectroscopy (FTIR) with hydroxyapatite (HA) exposed to the modification process used as a control. The surface modification of the SiHA particles was evaluated by the attachment of the commercially available fluorescent dye Fluorescein-5-Maleimide, which is capable of selectively binding to thiol groups, and demonstrated by live cell confocal fluorescence imaging of the particles after internalisation by MC3T3 cells.

6.1 Materials and Methods:

6.1.1 Thiol modification of SiHA and dye-labelling with Fluorescein-5-Maleimide

This is a two stage process involving: i) the functionalisation of the SiHA surface with the (3-mercaptopropyl)trimethoxysilane (MPTS) via covalent bonding, which in turn presents a thiol functional group from the particle surface and, ii) the attachment of the commercially available thiol reactive probe fluorescein-5-maleimide as shown in figure 6.1.

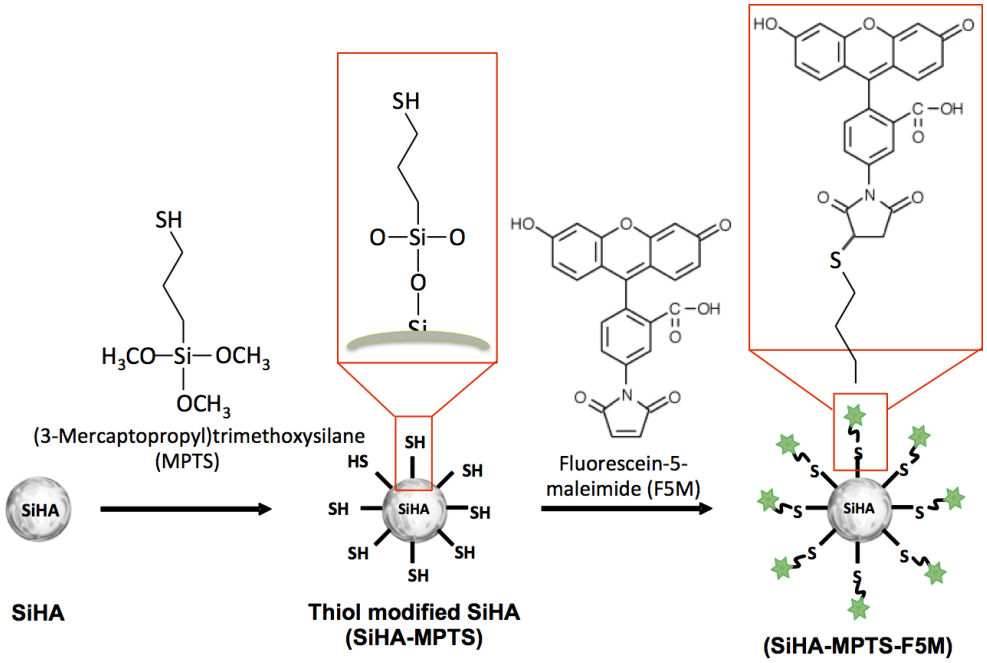

Figure 6.1: Schematic diagram of the thiol functionalisation process of SiHA using MTPS and the subsequent labelling with fluorescein-5-maleimide (F5M) Reproduced with permission from [9]. © 2013 The Royal Society of Chemistry.

Surface functionalisation with MPTS

230mg of HA/SiHA in double distilled water was centrifuged at 4000rpm for 10mins and the supernatant removed. The particles were then resuspended in 16.4mL of absolute ethanol filtered with a 0.22μm pore size syringe filter before adding 100μL of MPTS. The samples were mixed

using a ThermoMixer (ThermoMixer Comfort, Eppendorf AG., Hamburg, Germany) at $37\,^{\circ}\mathrm{C}$ for 3 hours at 1000rpm and then washed five times with double distilled water by centrifuging at 4000rpm for 10 minutes.

Labelling with Fluorescein-5-maleimide

A stock solution of 5.2mg Fluorescein-5-Maleimide (F-150, Life Technologies Ltd., Paisley, UK) in 1mL $MgCl_2$ and $CaCl_2$-free PBS (Sigma-Aldrich Ltd., Dorset, UK.). 1mL of MPTS functionalised SiHA/HA (SIHA/HA-MPTS) (containing approximately 6mg of solid material) was centrifuged at 4000rpm for 10 min (ThermoScientific Inc., Waltham, MA, USA). The supernatant was removed and the pellet resuspended in 500μL of $MgCl_2$ and $CaCl_2$-free PBS before adding 470μL of the fluorescein-5-maleimide stock solution and mixed on a ThermoMixer for 2 hours at $37\,^{\circ}\mathrm{C}$. Finally, the SiHA-MPTS-F5M particles were washed twice with absolute ethanol and five times with double distilled water (both filtered beforehand using a 0.22μm pore size filter). As a control, SiHA particles, without thiol modification, were mixed with fluorescein-5-maleimide using the above method.

6.1.2 Quantification of thiol groups

Thiol presentation on the particle surface was quantified based on an assay using 5,5-dithio-bis-(2-nitrobenzoic acid) (DTNB), also known as Ellmans Reagent (D8130 $\geq$98% BioReagent, Sigma-Aldrich Ltd., Dorset, UK.), which binds to the free -SH groups to form the yellow-coloured product 2-nitro-5-thiobenzoic acid (TNB). The absorbance of the assay solution is proportional to the concentration of free -SH groups in the sample.

A Reaction Buffer was prepared consisting of 100mM $Na_3(PO_4)$ and 1mM EDTA in deionised water and adjusted to pH 8.00 by drop wise addition of Na(OH). A stock Ellmans reagent solution was prepared by dissolving 4mg of the Ellman's reagent powder in 1mL of Reaction Buffer. 50μL of the Ellman's stock solution was added to 2.50mL of Reaction Buffer in a centrifuge tube with a separate tube for each sample plus an additional tube for a control sample. 250μL

of the functionalised HA/SiHA particle dispersion was then added to the tube, mixed using a vortex mixer and incubated at room temperature for 15 minutes to form an assay solution. For the control, an additional 250μL of reaction buffer was added to the tube instead of HA/SiHA particle solution. After incubation, 1mL of the assay solution was transferred to a UV cuvette (14-377-009, Brand Tech Scientific, Fisher Scientific UK Ltd., Loughborough, UK) and the absorbance measured at 412nm using a spectrophotometer (Cecil CE7500, Buck Scientific, East Norwalk, CT, USA) zeroed on the control sample. The relationship between molar absorptivity, E ($M^{-1}cm^{-1}$), and concentration of TNB, c (moles/litre), was defined as follows[159]:

$$E = \frac{A}{bc} \tag{6.1}$$

where A = measured absorbance and b = path length of the cuvette in centimetres. The concentration of TNB (and hence concentration of free -SH groups) in the solution in the cuvette was then calculated by solving equation 6.1 for c and substituting b=1cm and E = 14,150 $M^{-1}cm^{-1}$. The number of moles of -SH groups in the assay solution, m_{assay}, was then calculated using equation 6.2 [159]:

$$m_{assay}(mol) = \left[2.80mL \times \frac{1L}{1000mL}\right] \times c(mol/L) \tag{6.2}$$

where the factor '2.80mL' represents the total volume of the assay solution when 250μL of sample and 50μL of Ellman's reagent is added to the 2.5mL of reaction buffer and is converted into litres for consistency. Given that the -SH groups were contributed solely by the 250μL fraction of the assay solution from the addition of the particles, the final molar concentration of free -SH groups in the original particle solutions, C_{sample} was determined to be:

$$C_{sample}(moles/litre) = \frac{m_{assay}(moles)}{0.25mL} \times \frac{1000mL}{1L} \tag{6.3}$$

The dynamic range of the Ellman's assay using a particular spectrophotometer was determined by running the assay with samples of known concentration of a cysteine containing salt (the cysteine residue contains the sulfydryl which DTNB binds to). This also allowed the linear

relationship in equation 6.1, which theoretically relates the absorbance of a solution containing TNB-sulfhydrl complexes to the molar concentration of those complexes, to be experimentally verified.

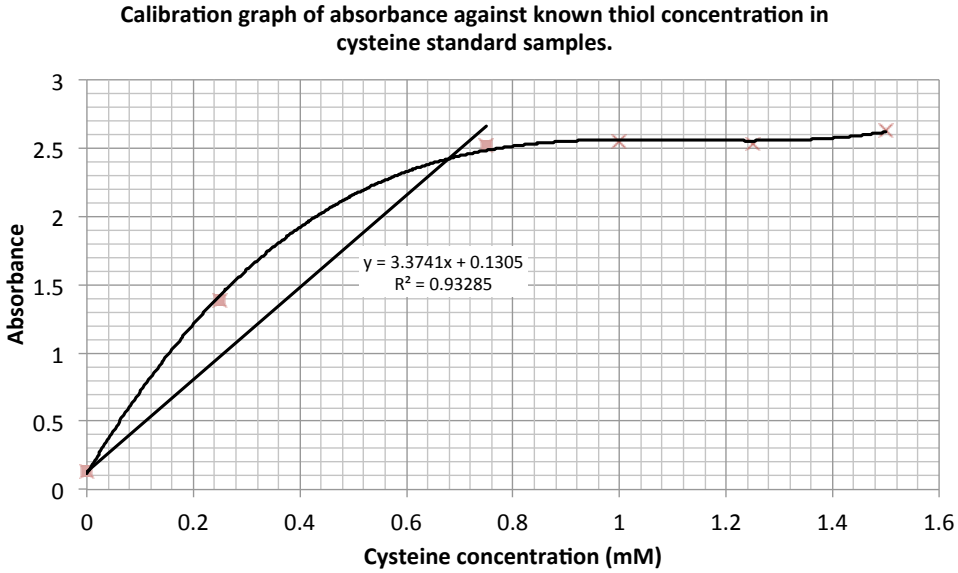

Figure 6.2: Calibration graph mapping measured absorbance of solutions with known cysteine residue concentrations in order to experimentally verify the linearity (or the extend thereof) of the relation between the absorbance of TNB in solution upon binding to free thiol groups with thiol concentration (equation 6.1). The relation was found to be linear up to a thiol concentration of approximately 0.76mM.

As can be seen in figure 6.2, the relationship can be considered linear up to approximately 0.76mM (R^2 = 0.93), but absorbance values appeared to saturate at higher cysteine concentrations. Therefore it was deemed that the experimental setup could reliably determine concentrations up 0.76mM without the need for sample dilution. Further calibration curves focused on the cysteine concentration range 0 - 0.6mM were produced to verify sample measurements.

6.1.3 Determining DNA binding capability of thiol-modified SiHA

A dispersion of 100μg of HA/SiHA particles in $MgCl_2$ and $CaCl_2$-free PBS (D8537, Sigma-Aldrich Ltd., Dorset, UK). 100μg of particles in solution was mixed with 10, 20, 50, 80 and 100 μg of DNA (31149, Sigma-Aldrich Ltd., Dorset, UK) and incubated for 15 minutes at 37 °C.

The particle-DNA solutions were then centrifuged in order to remove the particles and particle-bound DNA before measuring the absorption of the supernatant at 260nm using a Varian Cary 5000 Spectrophotometer (Agilent Technologies UK Limited, Stockport, UK). The absorbance of the sample was proportional to the amount of unbound DNA and was quantified in terms of mass through the absorbance-mass calibration curve shown in figure 6.3. The amount of DNA bound to the particle surface was then determined by subtracting the mass of the unbound DNA from the amount of DNA added to the particle solution at the start of the experiment.

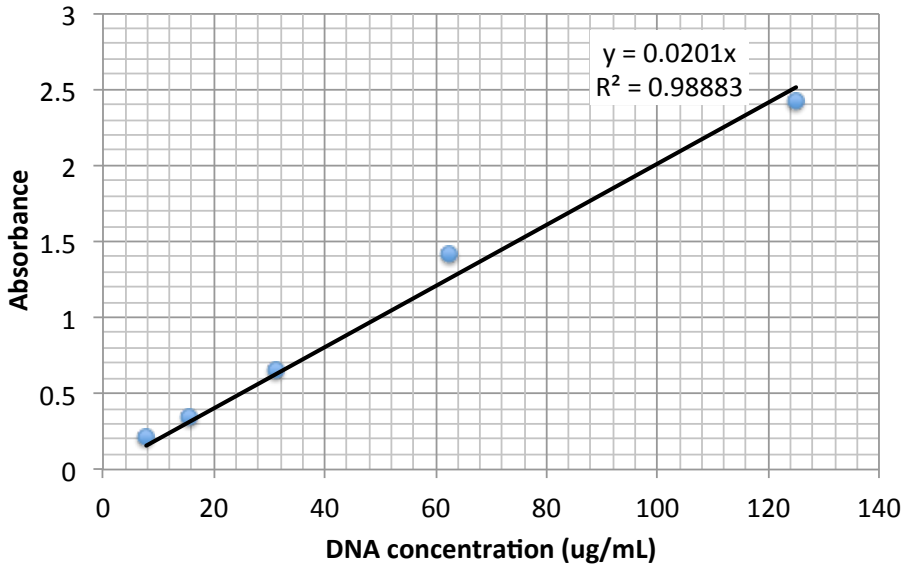

Figure 6.3: Calibration graph mapping measured absorbance of solutions with known DNA concentrations in order to quantify the mass of DNA bound to the calcium phosphate particles.

6.1.4 Preparation of MC3T3 cells for live cell imaging

MC3T3 (passage 10) osteoblast precursor cells were cultured in T-75 flasks using DMEM (D6545, Sigma-Aldrich Ltd., Dorset, UK) supplemented with (v/v) 10% Foetal Bovine Serum (A15-105 Mycoplex, PAA, Yeovil, UK), 2.4% Hepes Buffer (H0887, Sigma-Aldrich, Dorset, UK), 2.4% L-Glutamine (G7513, Sigma-Aldrich Ltd., Dorset, UK.) and 1% Penicillin and Streptomycin (P4333, Sigma-Aldrich Ltd., Dorset, UK) - this will be referred to as 'supplemented media' herein. For imaging, the cells were seeded at a density of $3x10^4$ cells per quad-

rant in a 4-segmented live cell imaging dish (code: 627870, Greiner-Bio One Ltd., Gloucester, UK) and incubated overnight at $37\,^{\circ}\mathrm{C}$ and 5% CO_2 in the supplemented media. HA and SiHA in supplemented media was prepared to concentration of 300μg/mL, mixed using a vortex mixer and sonicated for 5 mins before being kept in a water bath at $37\,^{\circ}\mathrm{C}$ until required. After 24 hours, the media was removed and replaced with 1mL of supplemented media containing HA or SiHA-media solutions at the desired final concentration while gently agitating the dish to ensure even distribution of the particles across the surface. The media was removed 24 hours after exposure to the particles, the cells in each quadrant washed three times with 1mL PBS and replaced with 1mL per quadrant of cell imaging media (A14291DJ, Life Technologies Ltd., Paisley, UK). Lysosome labelling of the cells was carried out during the last 30 minutes of the 24 hour exposure to the labelled particles. A 1mM stock of LysoTracker Red® (L-7528, Life Technologies Ltd., Paisley, UK) was diluted in supplemented culture media to a working concentration of 75nM. 500μL of the working concentration dye solution was added to each quadrant of the imaging dish containing cells and incubated for 30 minutes at $37\,^{\circ}\mathrm{C}$ and 5% CO_2. The cells were then washed prior to imaging as described above.

6.1.5 Live cell confocal fluorescence microscopy

The confocal microscope system consisted of a Zeiss Axio Observer.Z1 inverted microscope attached to a Zeiss LSM 710 ConfoCor 3 confocal unit containing a 34-channel spectral detector. A Zeiss EC Plan-Neofluar x63 NA = 1.40 oil objective lens, a 488nm laser diode, a 458nm/488nm beam splitter were employed with the spectral set to divert the fluorescein fluorescence between 500nm and 650nm to a photomultiplier tube detector. 1024x1024 12-bit images were acquired with a 3μs pixel dwell time and 0.1% laser power to minimise photo-induced damage to the cells. Detector gains were altered within the Zeiss ZEN software and care was taken to avoid saturation of the image in regions of interest such as the cells under investigation.

6.1.6 Live cell fluorescence spectroscopy

A QUASAR 34-channel detector attached to the Zeiss LSM 710 confocal microscope was set to detect fluorescence within 5nm bandwidth bins ranging from 494nm-654nm. Confocal images were acquired at each detection 5nm detection bin before shifting to the next detection bin sequentially to form a 'lambda-stack'. The emission profile was reconstructed post-image acquisition by segmenting the pixels belonging to the cell and internalised particles using grey-level thresholding in ImageJ (version 1.47m, Open Source, Wayne Rasband, National Institutes of Health, USA) and summing their intensity values. The process was repeated for each image to produce a bar chart of intensity against binned wavelengths, with each bar labelled with the central wavelength of the bin.

6.1.7 Live/Dead assay

Cells were seeded on to glass coverslips (VWR International Ltd., Leicestershire, UK) placed in 6-well plates with 2mL of supplemented cell culture media (as defined in section 6.1.4) containing 0.6μg/mL of SiHA-MPTS-F5M particles and left in a cell culture incubator at $37\,^{\circ}\mathrm{C}$ and 5% CO_2 for 24 hours. Live/Dead assay was performed by removing the media in each well and replacing with an assay solution comprising of 2mL supplemented media, 7μL of a Calcein AM (C3100MP, Life Technologies Ltd., Paisley, UK) (1mg/mL in anhydrous DMSO) and 25μL of Propidium Iodide (1mg/mL). The 6-well plate was then placed in a cell culture incubator at $37\,^{\circ}\mathrm{C}$, 5%wt CO_2 for 15 minutes. Images of the live/dead stained cells in the acquired while in the 6-well plate using an epi-fluorescence microscope.

6.1.8 Computational image analysis of cellular internalisation events

A computer program was developed to process the the confocal fluorescence images in order to extract the internalised structures and analyse their shape and size (on an image pixel basis) before summarising the results in the form of size-distributions calibrated to the micron scale. The image analysis was performed within the numerical computation and visualisation pro-

gramming language, MATLAB R2011a version 7.12.0.635 (The Mathworks Inc., Natick, MA, USA). All of the computation work was run on an Apple MacBook Pro with a 2.4GHz Intel Core i7 processor, 4GB RAM, 128GB Solid-state hard drive and an AMD Radeon HD 6770M graphics card with 1GB VRAM (Apple Inc., Cupertino, CA, USA) running OS X (10.9.1) operating system. With additional information from the image acquisition parameters, the total mass of the CaP material internalised by the cell was estimated. Specific details of these two computational methods are given in the following subsections.

Determination of internalised particle/aggregate size-distribution

The confocal image stack in its native .lsm Zeiss file format was imported into ImageJ (version 1.47m, Wayne Rasband, National Institutes of Health, USA., http://imagej.nih.gov/ij.) running the LSM Toolbox plugin (© 2003-2009 Patrick Pirrotte, Jérôme Mutterer). The fluorescence channel of the image stack, showing the fluorescently particles/aggregates in the field of view, was extracted to a separate image stack and the background removed using grey-level thresholding. The workflow of the program developed in MATLAB to identify and analyse objects inside the cell(s) is shown in figure 6.4 and consisted of the following steps:

1. The user selects an unlimited series of points around the perimeter of the cell(s) on an interactive bright field image, which leads to the creation of a polygon approximating the perimeter of the cell(s).

2. The thresholded fluorescence image corresponding to the brightfield image selected in (1) was selected. This image was in binary format such that all pixels with a value of one represented objects of interest to the user and pixel values of zero were classed as background and ignored. Objects in the image were identified by the program by grouping all pixels connected in at least one of eight possible geometries in two dimensions (x,y) - four geometries representing the four unique arrangements that two pixels can be in contact along their edges and a further four geometries representing contact of the corner of one pixel to the corner of another pixel. This approach is commonly termed as the

'8-connected neighbourhood'. The program numbered each detected object and recorded the co-ordinates of the pixels the forming those objects.

3. Objects located outside of the cell(s) perimeter (defined in step 1 by the polygon) were removed by employing a logical AND operation between the polygon image and the image containing all detected objects. The resulting binary image contained the objects deemed to be located fully and partially within the cell perimeter.

4. Objects located partially within the cell(s) were removed by a another logical AND operation with the inverse of the polygon image (which therefore highlights all points outside of the cell). The pixels remaining in the image were matched to the database of detected objects and removed.

5. The area of each object (in pixels squared) was calculated by summing the number of pixels assigned to each numbered object and then fitting an ellipse to the shape in order to determine major and minor axis lengths. In addition, the diameter of a circle with equivalent area to the object was computed. The estimated lengths were converted from pixel units to microns by extracting the pixel-micron scale factor from the original .lsm microscope data file.

6. A histogram of equivalent diameters of internalised objects was computed by binning the calculated diameters in 0.1μm wide bins with the total number of bins determined automatically by the program by calculating the upper range limit of sizes.

Estimation of the total volume of internalised CaP particles/aggregates

The volume of each slice through an image object was calculated by multiplying the area obtained using the algorithm outlined in section 6.1.8 by the slice thickness (which can be estimated from the user-defined confocal pinhole diameter recorded in the original .lsm data file). The total estimated volume of each object was then computed multiplying the volume of each slice through the object by the inter-slice spacing set during the image acquisition process as

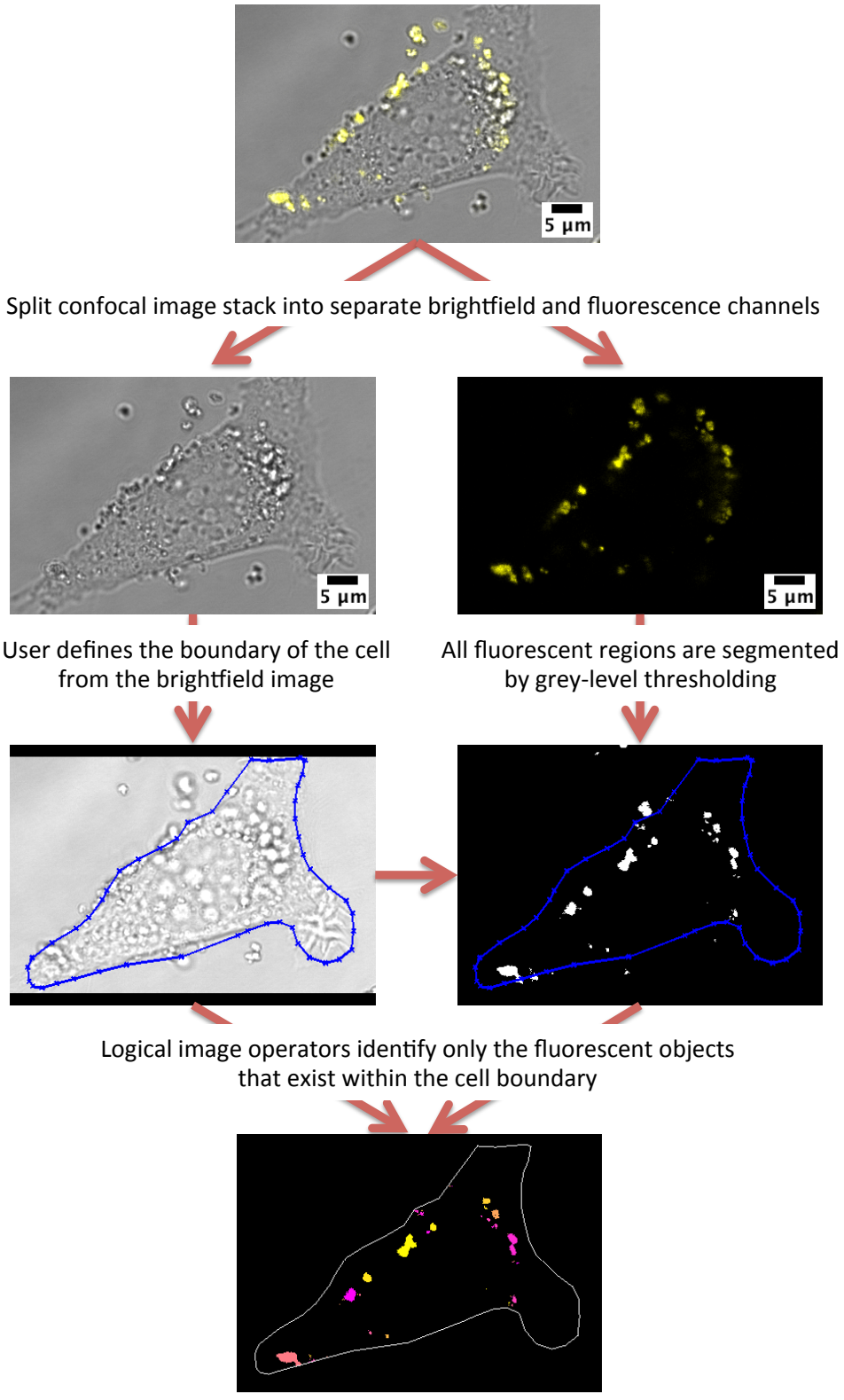

Figure 6.4: Workflow diagram of the image processing steps 1-4 in section 6.1.8 showing an image of the result after each step with sub captions where appropriate. Once program identified each of the coloured objects in the last image, their size and area (in pixel units) were estimated using shape fitting and converted to μm using the calibration factor in the original data file.

shown in figure 6.5. This method of mass estimation was based on the following assumptions: i) that all detected objects in every two-dimensional image slice extended perpendicularly to the image plane by the same length equal to the inter-slice spacing and, ii) that all objects were solid and consisted only of the CaP material, which was homogeneously distributed throughout the volume of the objects. The perhaps more realistic situation of the internalised material being loosely compacted into discrete masses with air/fluid acting as filler rather than solid masses was considered, however these 'filler' regions could not be resolved from preliminary imaging experiments at a suitable magnification for capturing multiple cells within a field of view at the best resolution possible. This suggested that filler regions existed, but the average volume they occupied was insignificant in comparison to the overall size of the internalised object and therefore the total mass could be roughly considered to be evenly distributed. Furthermore, the assumption of a solid object simplified the algorithm for estimating the mass of the internalised objects. An example 3D reconstruction of a confocal image stack is presented as supplementary movie with this thesis and shows close up views of a population of labelled particles (*Filename: SiHA-MPTS-F5M in MC3T3s 3D.mov*).

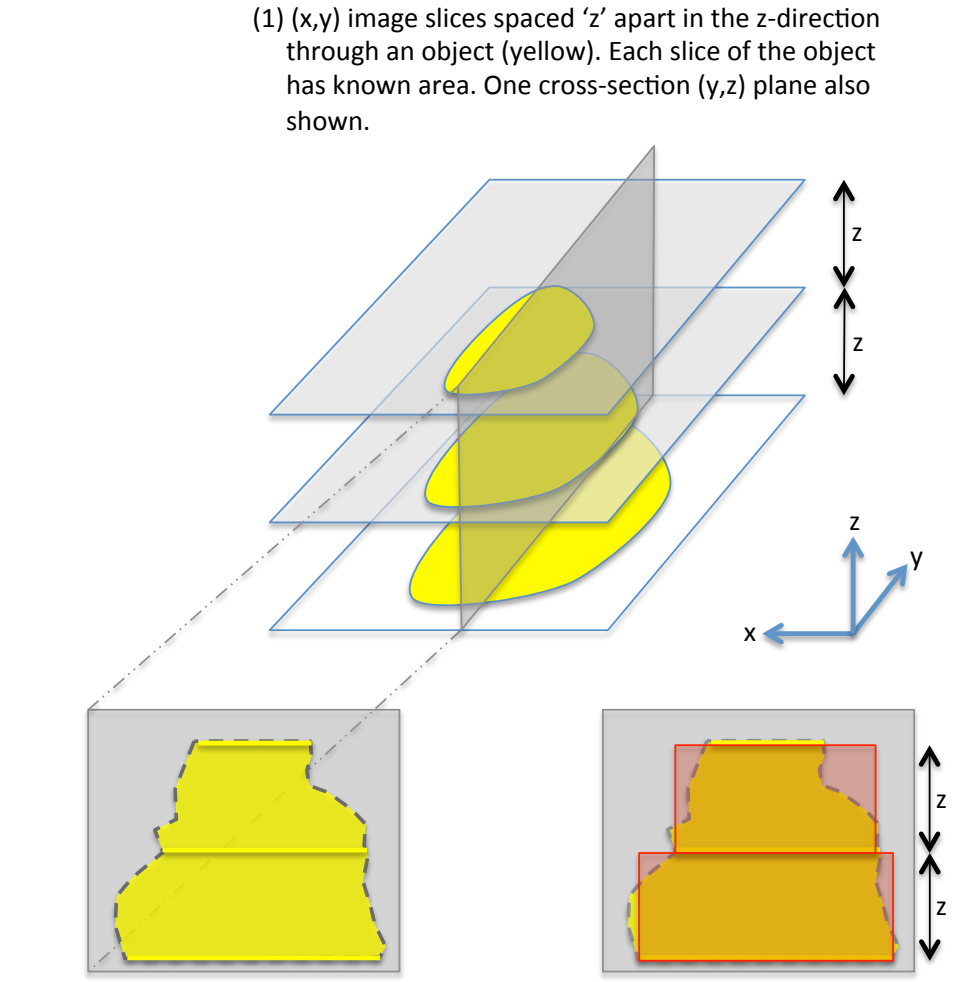

Figure 6.5: Schematic diagram illustrating how the volume of an object in a confocal microscopy image z-stack can be estimated. For clarity, this illustrated example uses a 2D cross-section (y,z) through the object. The total volume of the object can be reconstructed by multiplying the volume of each slice by the known slice spacing, z. As can be seen in (3), the true volume can be over- and under- estimated using this approach. However, decreasing the spacing between each slice and increasing the number of images taken along the z-direction (both parameters controlled during image acquisition) can reduce these errors.

6.2 Structure and composition analysis

Peaks were identified in the XRD patterns of as-precipitated HA shown in figure 6.6 at around $26\,^{\circ}$, $32\,^{\circ}$, $40\,^{\circ}$ and between $47 - 53\,^{\circ}$, which appeared to align well with the most intense peaks from reference data for HA (ICDD PDF card no. 00-009-0432). However, it was ev-

ident that the broad HA peak at $32\,^{\circ}$ in figure 6.6 was an envelope of the three most intense peaks in the reference pattern data and thus imposing a limit on quality of the match between the measured data and the HA reference. Two shoulder peaks were identified within the main peak of SiHA, but were still poorly resolved. Furthermore, it is known that the XRD patterns of various apatites could resemble those of as-precipitated HA and therefore an assessment of the chemical/structural changes in sintered samples is required in order to confirm the phase composition and structure of the original as-precipitated samples. Figure 6.6 shows the XRD pattern of HA sintered at $650\,^{\circ}\mathrm{C}$ for 2 hours. Dominant peaks were identified at $25.83\,^{\circ}$, $31.81\,^{\circ}$, $32.20\,^{\circ}$, $32.88\,^{\circ}$ and were attributed to the (002), (211), (112) and (300) planes of HA respectively. Sharper and more intense peaks were observed in sintered HA (HA 650), compared to as-prepared HA, indicating an increase in the crystallinity of the sample. Secondary phases consisting of α-TCP and β-TCP were not observed in the diffraction patterns of the HA or SiHA samples when compared to ICDD reference patterns 00-009-0348 and 00-009-0169, respectively. TCP phases were not detected in HA even after sintering at $900\,^{\circ}\mathrm{C}$, but SiHA decomposed into a mixture of HA and α-TCP (data not shown).

The TEM images of HA and SiHA shown in figure 6.7 displayed the needle like morphology commonly reported with wet chemical precipitation methods[7, 31, 160]. Additional phases such as α-TCP, β-TCP and $CaCO_3$, which normally have a plate-like morphology, were not observed in either the HA or SiHA samples. The SiHA crystals appeared smaller and their edges were not as clearly defined compared with HA which may indicate that the SiHA sample was of lower crystallinity compared to HA. This observation corresponds well with the broad peaks observed for SiHA in the XRD patterns.

XRF was used to determine the %wt of Ca and P oxides and corresponding mole ratios of the elements are presented in table 6.1. The Ca:P ratio of the HA sample was 1.64 and compares well with the theoretical Ca:P ratio of HA of 1.67 to within experimental error using this technique. Ca:P ratio of HA-MPTS (1.95) was higher than expected and may have been due to CO_3^{2-} ions substituting the PO_4^{3-} ions in the crystal structure, thus reducing the phosphorus content of the sample and hence increasing the Ca:P ratio.

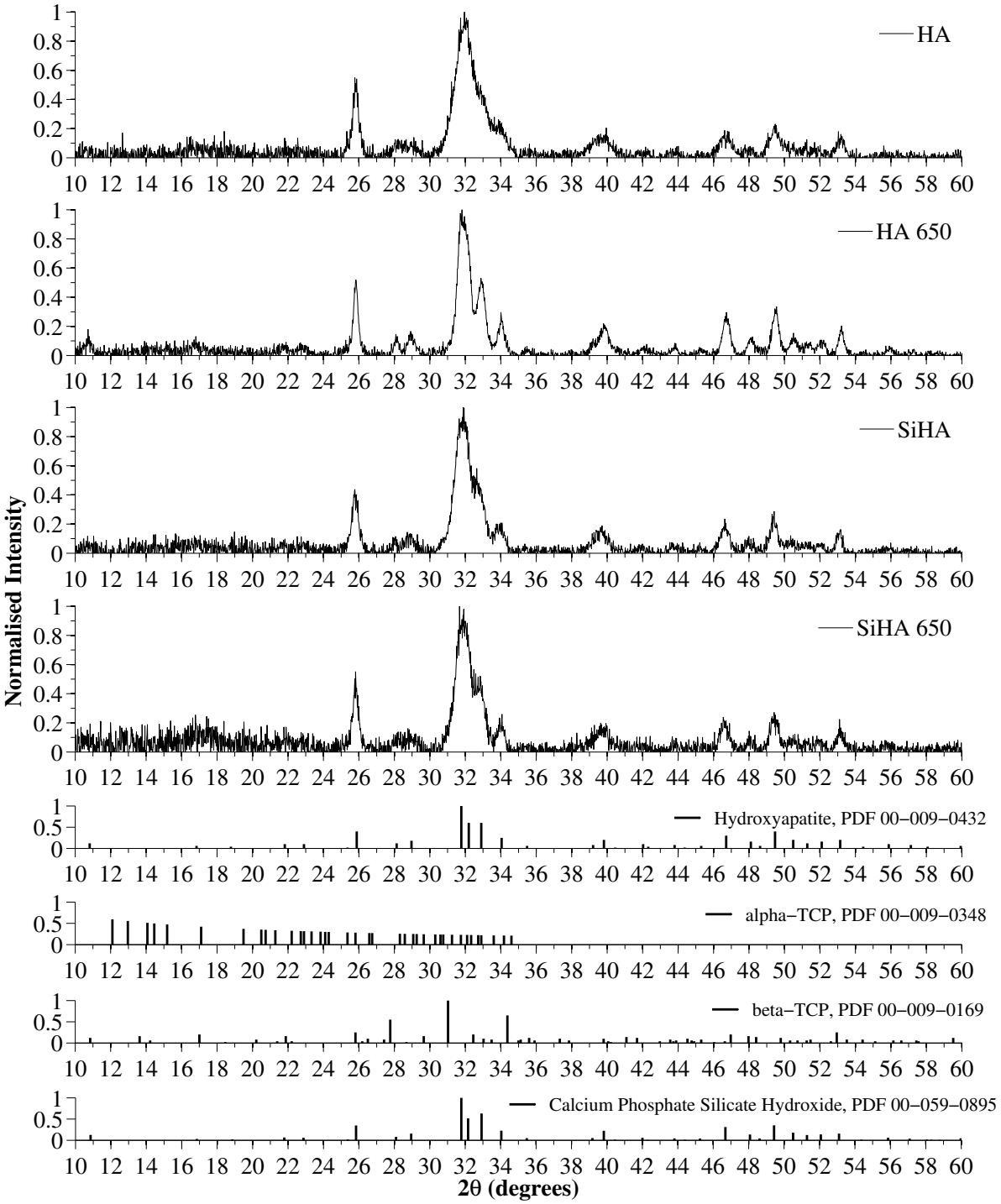

Figure 6.6: XRD patterns of as precipitated HA/SiHA along with HA/SiHA sintered at 650 degrees (HA 650/SiHA 650) along with JCPDS card number 00-009-0432 (Hydroxyapatite).Intensity values of all samples were normalised to the most intense diffraction peak of the HA sample. The broad diffraction peaks suggested the samples were made of nanosized crystals and no other phases of calcium phosphate were detected. Reproduced with permission from [9]. © 2013 The Royal Society of Chemistry.

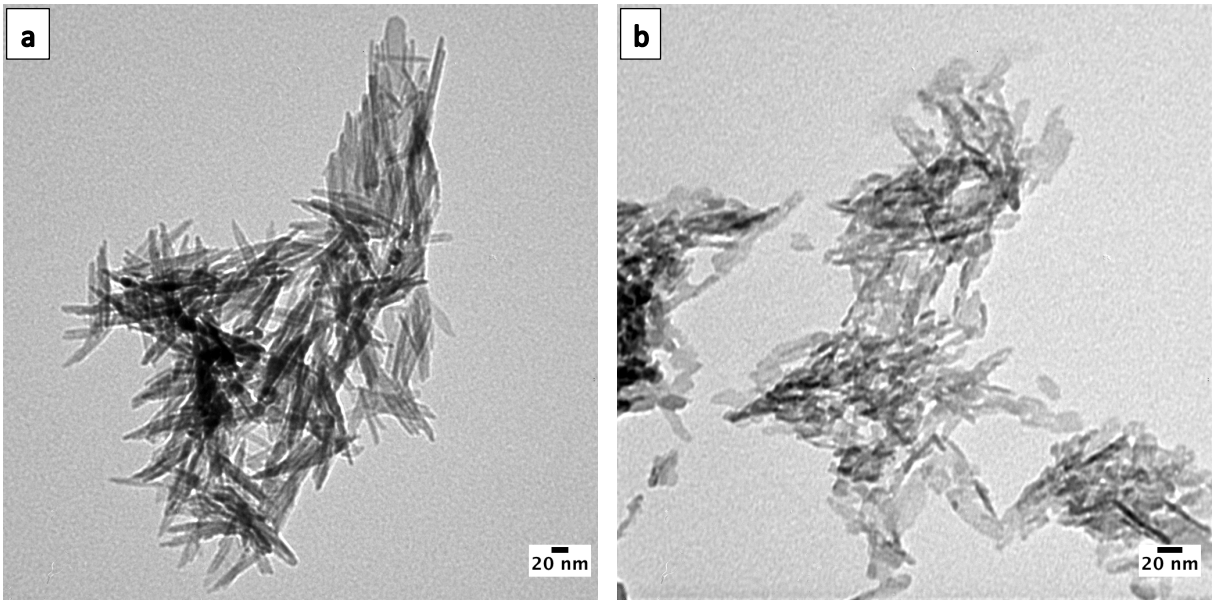

Figure 6.7: TEM images of as-precipitated (a) HA and (b) SiHA. Both samples showed the well reported needle-like morphology, but the crystal edges are not as well defined compared to those of HA, indicating reduced crystallinity.

Table 6.1: Ca:P ratios determined from XRF data and zeta potential data for HA, HA-MPTS, SiHA and SiHA-MPTS. Reproduced with permission from [9]. © 2013 The Royal Society of Chemistry.

Sample	Ca:P ratio	Zeta potential (mV) at pH 7.4
HA	1.64	-1.97
HA-MPTS	1.95	-1.99
SiHA	1.97	-1.66
SiHA-MPTS	1.94	-11.66

Atomic absorption spectroscopy measurements of the dissolved CaP samples showed that the silicon ion content of SiHA was 0.47mg/mL and HA was 0.06mg/mL with the solvent control containing $<$0.05mg/mL.

Figure 6.8 shows the FTIR spectra of HA, SiHA along with thiol-terminated silane functionalised HA and SiHA (HA-MPTS and SiHA-MPTS respectively). A summary of the peaks identified from the spectra, along with the chemical bond and mode the peak was assigned to, is presented in Table 6.2. The characteristic peaks of hydroxyapatite were identified in all

of the samples including the OH modes (3569cm^{-1} and 632cm^{-1}, the P-O stretching modes (1091,1044-1032 and 962cm^{-1}), the O-P-O bending modes (602, 575-561cm^{-1}) and the O-P-O stretching modes (473, 463-460cm^{-1}) from the PO_4^{3-} groups. The OH stretching mode at 3569cm^{-1} was partially obscured by the water band between 2500-3800cm^{-1} as the samples were not sintered prior to FTIR analysis. Evidence of some B-type carbonate substitution was found in both HA and SiHA by the presence of peaks located at 1454cm^{-1}, 1423cm^{-1} and 873cm^{-1}.

A peak assigned to the Si-O vibrational mode of the SiO_4^{4-} ions was detected in the SiHA-MPTS sample at around 875cm^{-1}. Although the corresponding peak in the SiHA sample was not as well resolved, another SiO_4^{4-} vibrational mode at 470cm^{-1} SiO_4^{4-} was identified. The translational mode of water associated to HA generally exists between 300cm^{-1} and 600cm^{-1}, which would also obscure the peaks within this range related to the presence of SiO_4^{4-}.

Evidence of surface modification was obtained from zeta potential measurements of HA, SiHA, HA-MPTS and SiHA-MPTS at pH 7.4, shown in table 6.1. The zeta potential of HA and SiHA was measured to be -1.97mV and -1.66mV, respectively. Most notably, the zeta potential of SiHA SiHA-MPTS was measured to be -11.66mV.

The presence of thiol groups was confirmed and quantified using an Ellman's reagent assay. For SiHA-MPTS, the thiol content was estimated to be 1.60×10^{-5} moles/mg of solid material. DNA binding efficiency experiments showed that 100μg of SiHA-MPTS particles could completely bind up to 10μg DNA whereas only 85% and 65% of this DNA mass was bound to 100μg of unfunctionalised SiHA and HA respectively. At higher DNA masses of 50-100μg, 20% of the DNA was bound to SiHA-MPTS while only 1-10% of the DNA was bound to SiHA and HA.

Table 6.2: FTIR absorption peaks identified in HA, HA-MPTS, SiHA and SiHA-MPTS along with references to other works which support the peak assignments. Reproduced with permission from [9]. © 2013 The Royal Society of Chemistry.

Peak (cm^{-1})	Assignment	References
Absorption peaks for hydroxyapatite		
3569	stretching mode of OH group	[18, 61, 161, 162]
1454	ν_4 or ν_3 bending mode of CO_3^{2-} groups in A- and B-type carbonated HA	[18, 161, 163]
1423	B-type CO_3^{2-} stretching mode	[161]
1091,1044-1032	triply degenerated asymmetric stretching mode of P-O bond of the PO_4 groups	[18, 61, 161, 164, 165]
962	symmetric stretching mode of the P-O bonds	[18, 61, 161, 164, 165]
873	ν_4 or ν_3 bending mode of CO_3^{2-} groups in carbonated HA	[161]
632	vibrational mode of OH group	[61, 161]
602, 575-561	triply degenerated O-P-O bending modes	[161]
473, 463-460	double degenerated O-P-O bending modes of the PO_4 groups	[61, 161]
Absorption peaks for silicates in SiHA		
880	Si-O vibrational mode of SiO_4^{4-}	[164]
875	Si-O vibrational mode of SiO_4^{4-}	[61, 163]
470	Si-O-Si vibrational mode of SiO_4^{4-}	[163]
Absorption peaks for MPTS		
1100	Si-O-C stretching from MPTS	[166]

6.3 Demonstration of application: Live cell imaging of SiHA internalisation by MC3T3 cells using a thiol reactive fluorescent probe

Using confocal fluorescence microscopy, unmodified SiHA treated with fluorescein-5-maleimide showed very weak fluorescence (figure 6.9b) in the regions of the image where particles could be seen in bright field (figure 6.9a and c). The fluorescence from SiHA modified with MPTS (SiHA-MPTS) shown in figure 6.9e was brighter than the fluorescence from unmodified SiHA. Furthermore, the intensity of the fluorescence was even across the vast majority of the structures shown in figure 6.9d and f and was retained after extensive washing.

The images in Figure 6.11 are combined confocal fluorescence and brightfield images of MC3T3 cells after a 24 hour exposure to thiol-terminated silane functionalised SiHA parti-

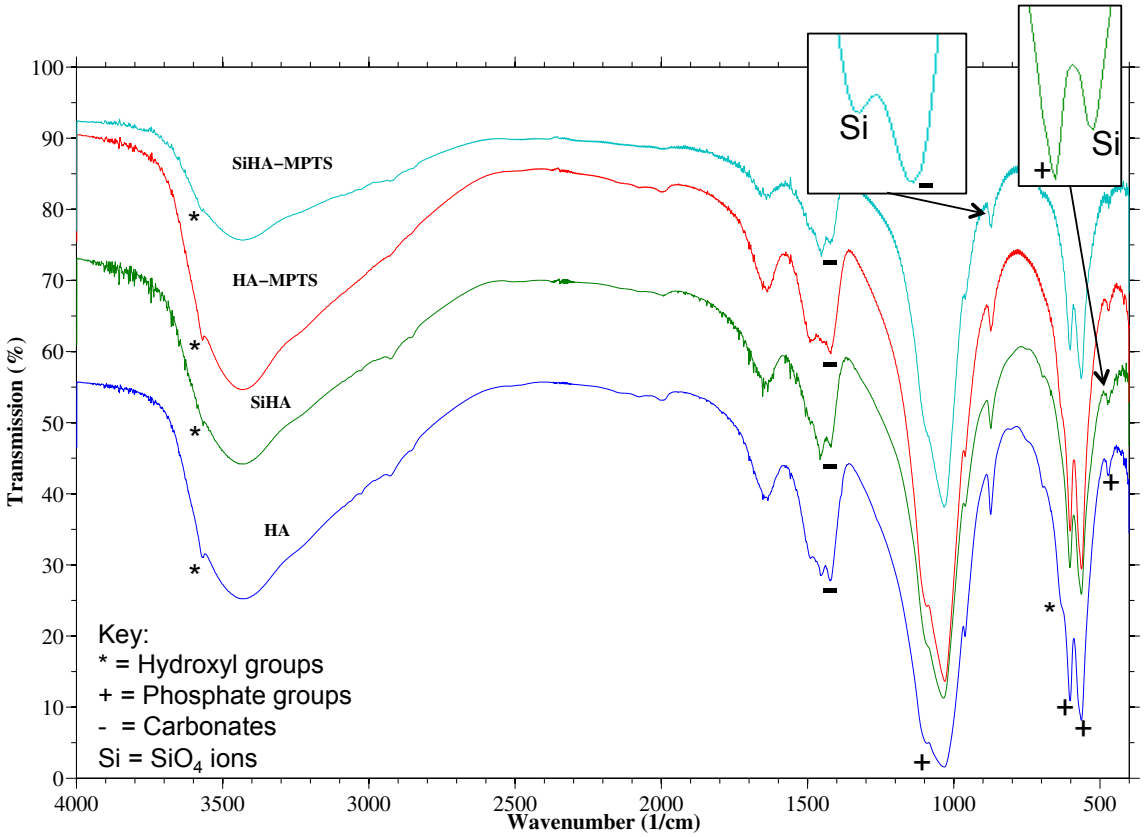

Figure 6.8: FTIR spectra of as-precipitated HA and SiHA along with thiol functionalised HA and SiHA (HA-MPTS and SiHA-MPTS respectively). Reproduced with permission from [9]. © 2013 The Royal Society of Chemistry.

cles conjugated to fluorescein-5-maleimide dye (SiHA-MPTS-F5M). In Figure 6.11(c-e), the SiHA-MPTS-F5M particles appeared to form small aggregates, approximately 500-1000nm in diameter, which aligned along the cell membrane. These structures could not be removed from the cell membrane despite repeated washing in PBS, indicating a strong affinity for the cell membrane. When focusing on an image plane through the middle of the cell (figure 6.11f-j), bright fluorescence was detected in new locations within the boundary of the cell as shown in the composite image. Furthermore, fluorescence from the few particles on the coverslip could no longer be detected at this new focal plane, demonstrating that any detected fluorescence was not an integration of fluorescence from particles at the bottom of or underneath the cell. The internalised structures measured approximately 400-500nm in diameter. Live/dead assay results of the SiHA-MPTS-F5M samples at the same concentration used for the imaging experiment (figure 6.10) did not show evidence of extensive cell death amongst a population of MC3T3s

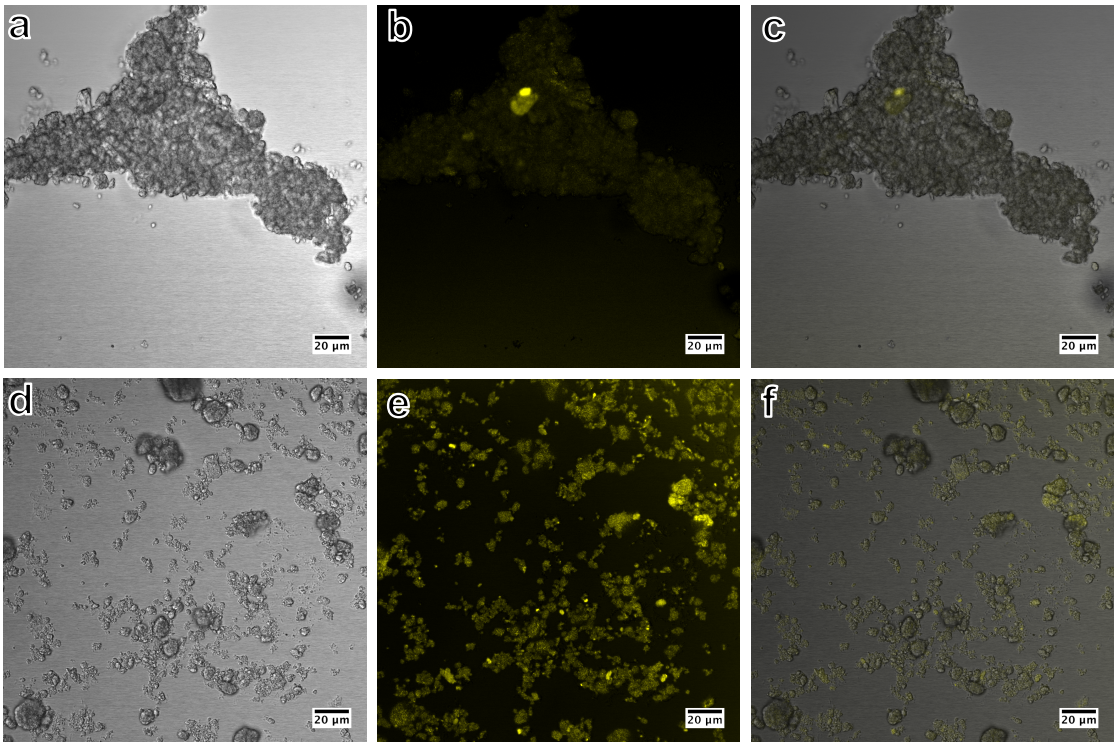

Figure 6.9: Bright field, confocal fluorescence and composite images of SiHA exposed to fluorescein-5-maleimide (SiHA-F5M) (a,b,c) and MPTS functionalised SiHA particles conjugated to fluorescein-5-maleimide dye (SiHA-MPTS-F5M) (d,e,f); Specific binding of fluorescein-5-maleimide to the thiol group of SiHA-MPTS was demonstrated by the even fluorescence across the particulates (d,e,f) and very weak non-specific fluorescence in the samples not treated with MPTS (a,b,c). Scale bar length represents 20μm. Reproduced with permission from [9]. © 2013 The Royal Society of Chemistry.

24 hours after exposure. Internalised particles were observed again while focusing up towards the top of the cell.

The fluorescence profile of SiHA-MPTS-F5M was obtained during confocal fluorescence imaging of the particles in order to confirm that the fluorescence signal shown in in figure 6.11 was indeed from the fluorescein dye. The reconstructed emission profile, shown in blue in figure 6.12 showed a single well-defined peak between 522nm-527nm while the reference spectrum for the free dye in solution showed a wide peak centred around 515nm. The shape of both emission profiles matched well over the whole wavelength range suggesting that the F5M dye was the dominant source of the fluorescence detected in the confocal images.

Post acquisition image analysis of the particle fluorescence channel enabled the size distribution of the internalised material to be computed (figure 6.13) and showed that structures

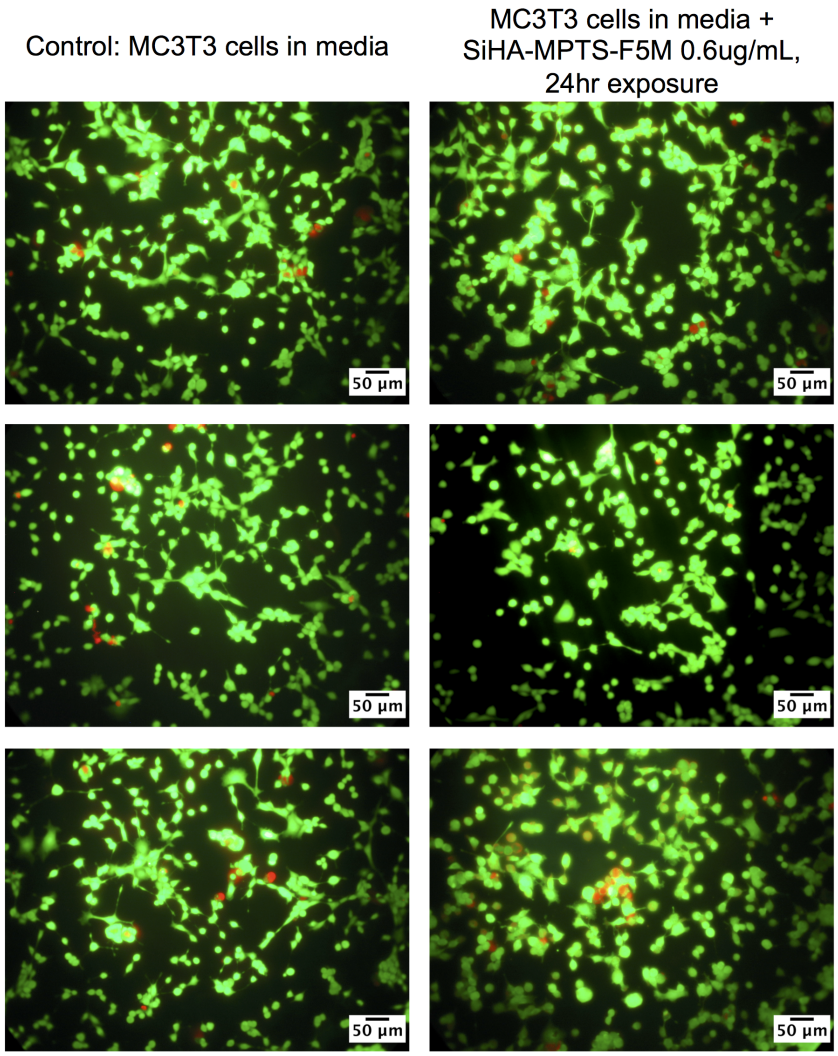

Figure 6.10: Epi-fluroescence images of live/dead assay performed on MC3T3 cells in media as a control (left column) and MC3T3 cells exposed to 0.6μg/mL SiHA-MPTS-F5M for 24 hours (right column). Three images were taken at different locations across the slide for both samples. Reproduced with permission from [9]. © 2013 The Royal Society of Chemistry.

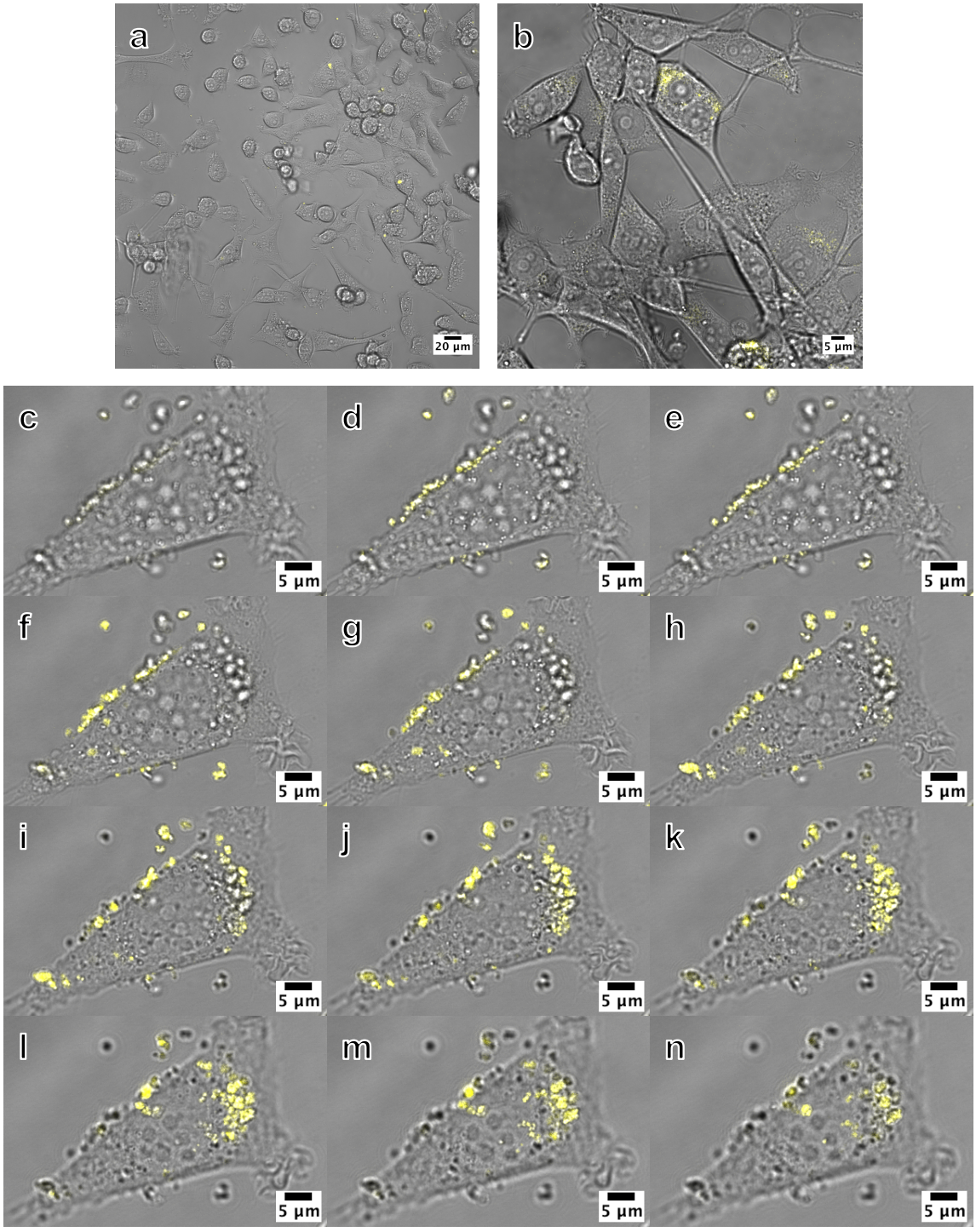

Figure 6.11: Combined bright field and fluorescence images of MC3T3 cells exposed to 0.6μg/mL SiHA-MPTS-F5M particles. (a) is a low magnification image showing a population of cells and (b) is a higher magnification image where fluorescence was just visible. Images (c)-(n) are slices from a confocal z-stack taken at: the coverslip/bottom of the cell plane (c,d,e), through the middle of the cell (f,g,h,i,j) and at the top of the cell (k,l,m,n). Bright localised fluorescence was observed within the cell and enabled internalised SiHA to be visually discriminated from the other cellular material of similar morphology and optical contrast as shown in the bright field images. Scale bars: (a)=20μm, (b)=5μm. Reproduced with permission from [9]. © 2013 The Royal Society of Chemistry.

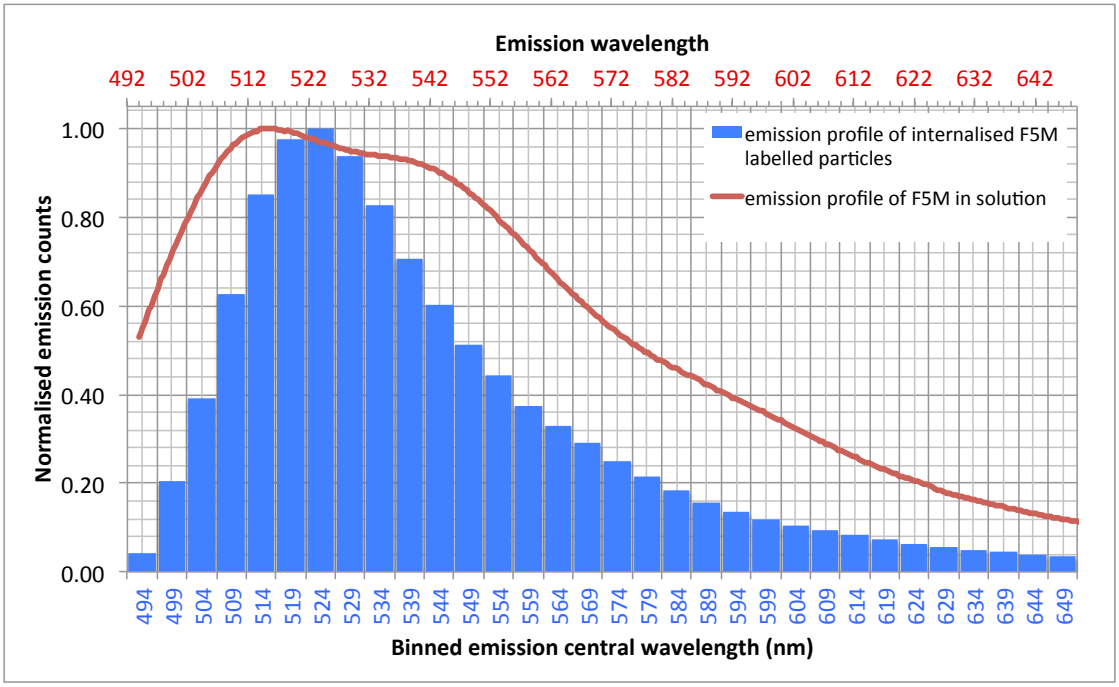

Figure 6.12: Fluorescence histogram of the light from particles detected inside MC3T3 cells during live cell imaging compared to the fluorescence profile of free fluorescein in solution as measured by UV-vis spectrophotometry. Intensity of both samples was normalised to their respective maximum intensity values. Both profiles appeared to have the same shape over the entire wavelength range and the emission maxima differed by only around 10nm, which may be due to differences in the pH of the environment in both samples.

between 0.3μm and 0.5μm were the most prevalent by number, but the population of cells analysed also contained structures of the order of a few microns with the largest being around 5μm.

6.4 Cellular processing and fate of internalised material: An initial semi-quantitative investigation

Further evidence of cellular internalisation of the functionalised material was obtained from live cell imaging experiments showing colocalisation of the particles with lysosomes labelled with LysoTracker® Red. An image from one dataset showing several cells within the field of view is presented in figure 6.14 where the yellow coloured regions of the image represent spatial overlap of the green fluorescence detected from the fluorescein-5-maleimide and the red fluorescence detected from the lysosomes.

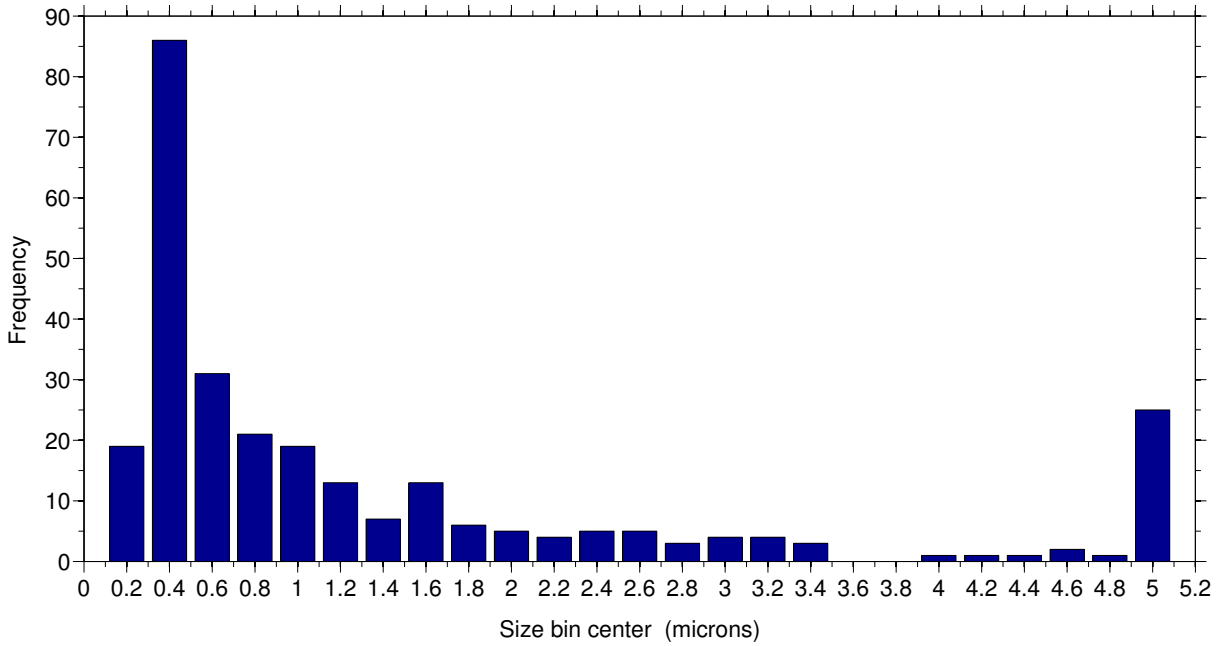

Figure 6.13: Size distribution of internalised SiHA-MPTS-F5M inside MC3T3 cells.

Labelling of the lysosomes enabled the discrimination between material located in the cytoplasm of the cell and material which had been encapsulated by lysosomes, which dissolve foreign material under highly acidic conditions. Figure 6.15 shows two size histograms of i) all internalised material detected within the cell (blue coloured bars) and, ii) the proportion of that material that also colocalised with the fluroescently labelled lysosomes (red coloured bars). A similar trend in the size distribution of internalised material was found to figure 6.13, i.e particles/aggregates of up to 0.4μm being the most prevalent, but structures of the order of microns (up to 3μm) also featured across the majority of cells. While the vast majority of the material up to 1μm was found within the lysosomes, structures above 1.8μm were found to remain exposed in the cytoplasm of the cells 24 hours post-exposure.

The presence of these larger structures exposed within the cell even after 24 hours despite evidence in each repeat experiment that lysosomes were capable of processing smaller structures of the same material, led to the suggestion that there could be a limit to the mass of CaP that MC3T3 cells could internalise and process. Computational analysis of the volume of material within lysosomes and total material within a population of 19 cells (figure 6.16a) generally showed that no more than 20 cubic μm of material was located within the lysosomes irrespec-

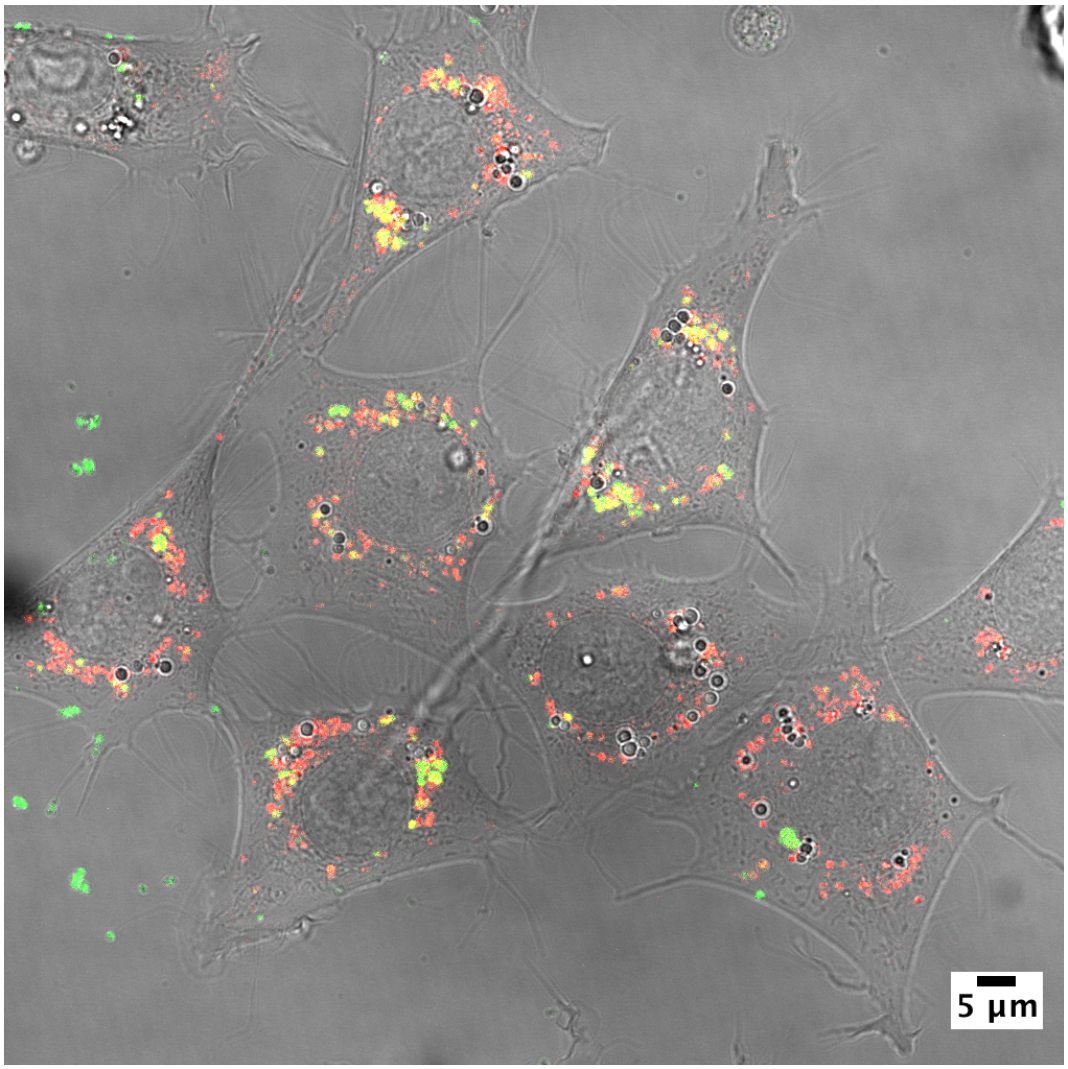

Figure 6.14: Combined bright field and confocal fluorescence image of a population of MC3T3 cells 24 hours after exposure to SiHA-MPTS-F5M particles (green) with the lysosomes labelled with LysoTracker® Red (red). Regions of colocalisation of the particles (or aggregates of) with the lysosomes is shown in yellow. The particle concentration was 0.6 μg/mL in supplemented media. The image further demonstrated that the labelling mechanism remains intact after 24 hours within the cellular environment after endocytosis and, up to the time point of this image, remained active within the acidic environment of the lysosome.

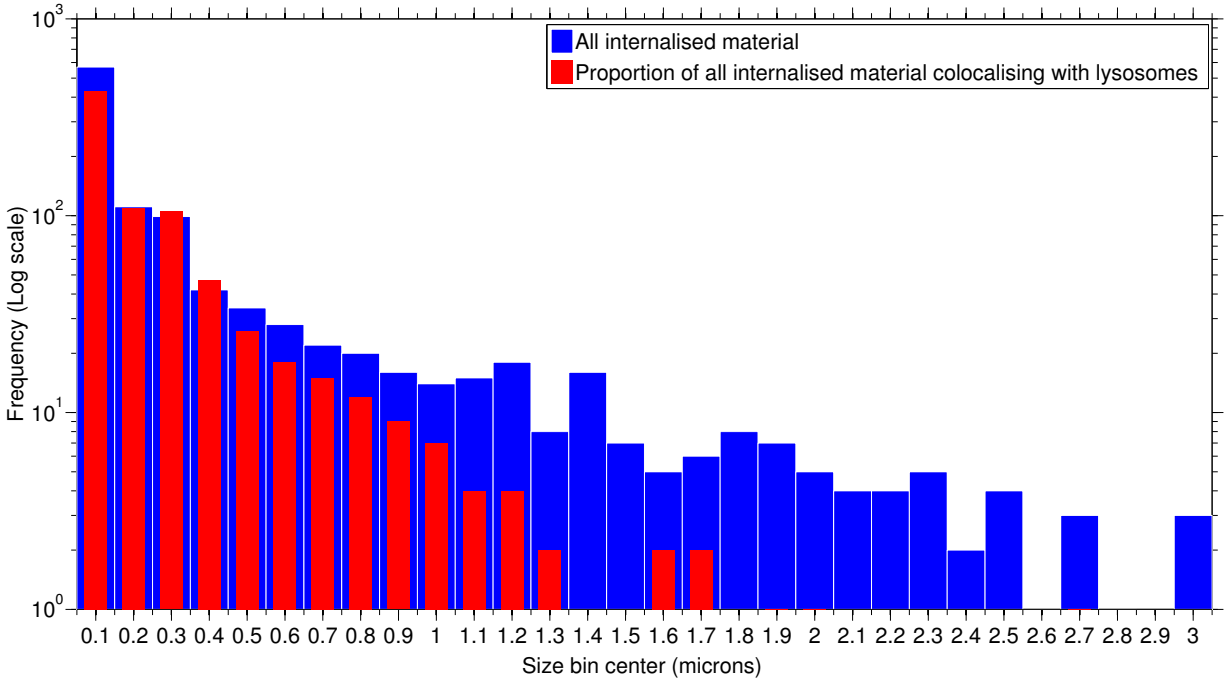

Figure 6.15: Size distribution of: i) all material detected within the cell membrane (blue bars) and, ii) the proportion of all material detected within the cell membrane which also colocalised within the lysosomes. Frequency values represent the sum of all frequency values for each given size class over all repeat experiments. Each size bin is 0.1μm wide and is represented on the x-axis by the mid-value ('bin center'). Both size distributions were computed using the same size bin widths, but the red bars are narrowed compared to the blue bars purely to allow for a more clear comparison between the two data sets.

tive of the total volume of material in the cells as a whole (which ranged from 20-220 cubic μm) with the exception of one data point. This may not be surprising given that each cell has a finite volume. Even at a given volume or small volume range, there was inconsistancy in the proportion of that material located within the lysosomes. For example, the cells estimated to contain 20-40 cubic μm of material showed that anywhere between 5-80% (v/v) of that material was located within the lysosomes.

Four particular cases of interest were highlighted in the scatter diagram (figure 6.16a) and related to observations of changes in cell behaviour during live imaging, namely; 1: cell morphology appearing rounded rather than elongated, 2: much higher number and convergence of lysosomes relative to any other experiments and, 3,4: sudden detachment and retraction of part of the cell from the culture dish. Size histograms of the internalised material for each of these cases are presented in figure 6.16b. Figures 6.17 and 6.18 show confocal fluorescence images

for all four cases of interest described above, with orthogonal projections to enable visualisation of the lysosome-particles interaction in all three dimensions. In the case of changes in cell morphology (labelled as 1 in figure 6.16b), the majority of all of the material, consisting of structures between 0.2-3μm, were taken up by the lysosomes. Total encapsulation of the micron scale material is clearly shown in the highlighted region on the right-hand side of figure 6.17a.

In the second case involving a dramatic increase in lysosome recruitment, no material with size above 2μm was found within the lysosomes, resulting in 90% of the material remaining within the cytoplasm. In the cases where partial cell detachment was observed, no structures larger than 1μm were detected within the lysosomes, which can be clearly seen in figures 6.18c where little colocalisation (yellow coloured pixels) could be seen across the vast majority of the labelled material.

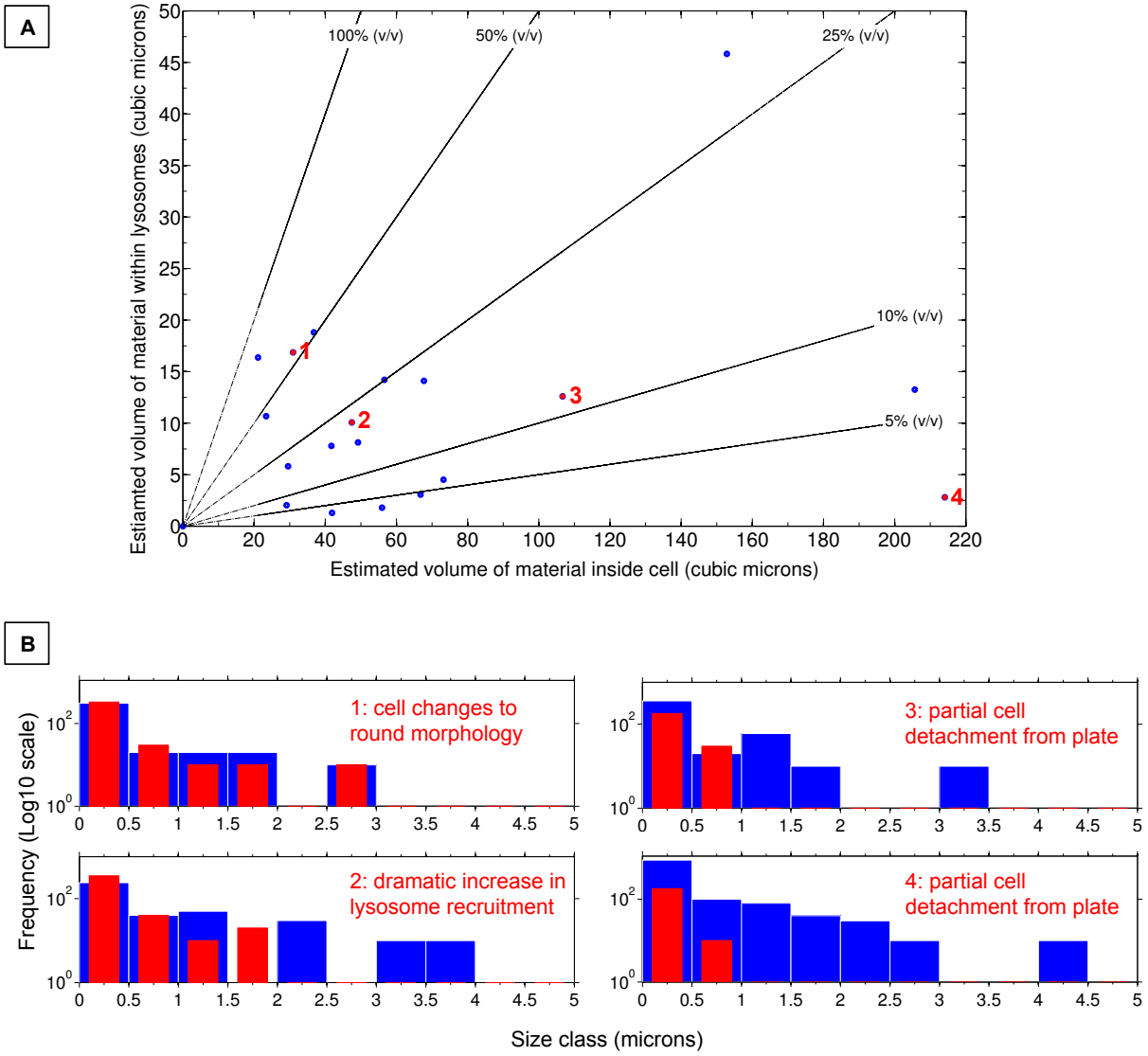

Figure 6.16: A: scatter plot of total volume of internalised material colocalised within lysosomes against total volume of material within the cell as a whole. There was no clear relationship between how much material was transferred to the lysosomes and the total amount of material within the cell as a whole. Four data points of interest are labelled and numbered in red and relate to observations of changes in cell morphology/behaviour. B: Size distributions of material inside the cell (blue bars) and within the lysosomes (red bars) for each of the four data points of interest labelled in (A). Structures larger than 1-1.5μm not encapsulated within lysosomes appear to correlate with the observations cell death suggesting an interplay between total amount and size distribution of CaP internalised on cell fate.

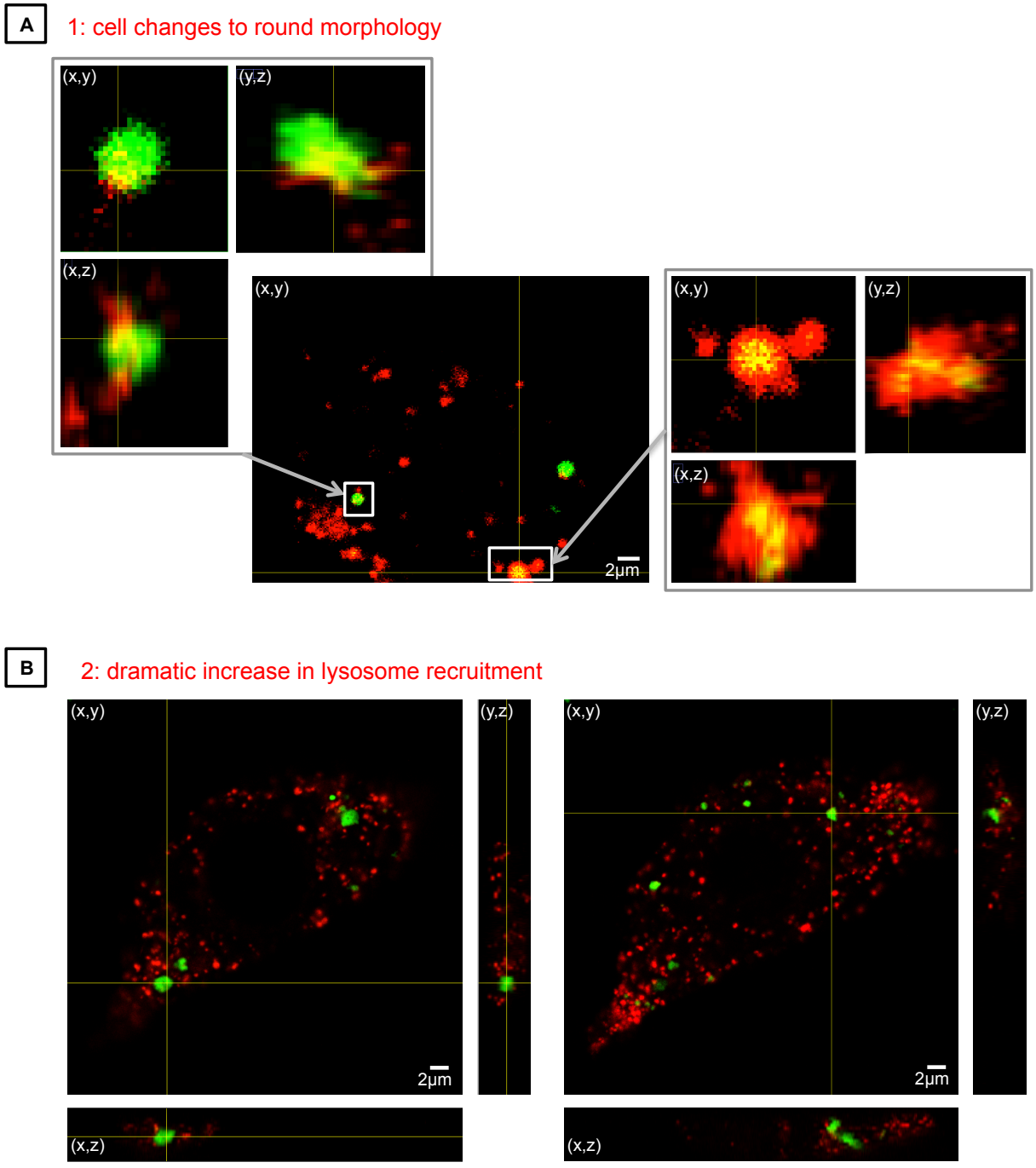

Figure 6.17: Confocal fluorescence images, with orthogonal (x,z) and (y,z) views, showing fluroescently labelled SiHA (green) and lysosomes (red) with high resolution insets of colocalisation to varying degrees in relation to the cases of: changes in cell morphology (a), and increase in lysosome recruitment (b).

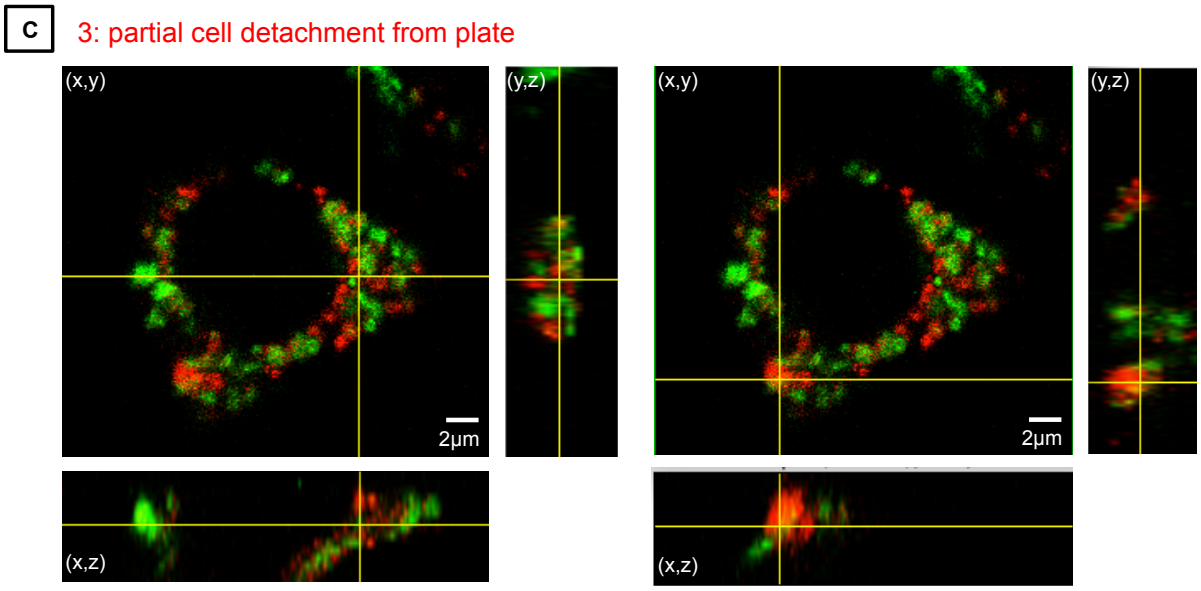

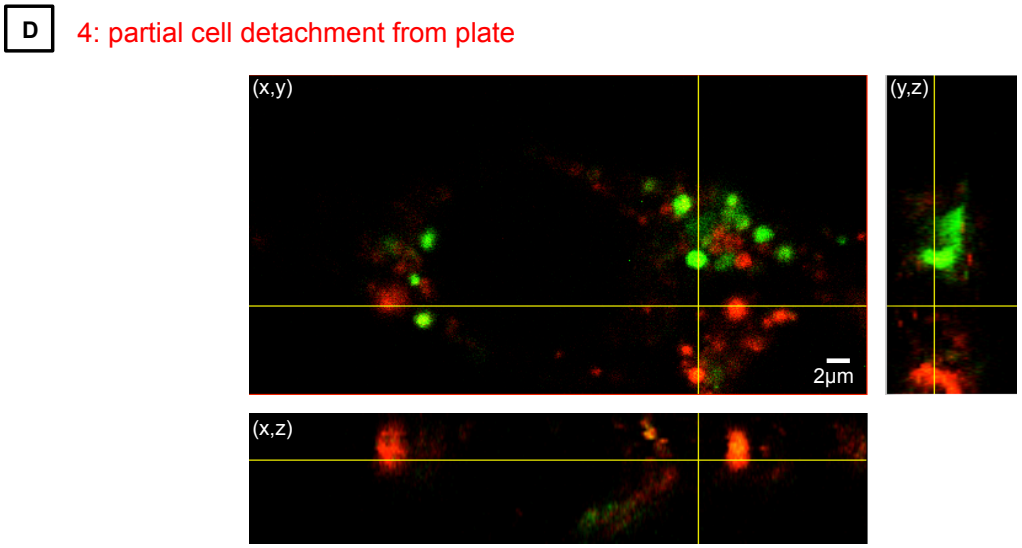

Figure 6.18: Confocal fluorescence images, with orthogonal (x,z) and (y,z) views, showing fluroescently labelled SiHA (green) and lysosomes (red) with high resolution insets of colocalisation to varying degrees in relation to the cases of partial cell detachment from the culture plates.

6.5 Discussion

6.5.1 Structure and composition analysis

X-ray diffraction patterns of as-precipitated HA and SiHA along with HA and SiHA sintered at $650\,^{\circ}\mathrm{C}$ (HA-650 and SiHA-650, respectively) were obtained and are shown in figure 6.6. The broad diffraction peaks of the as-precipitated HA and SiHA samples suggested that they were of low crystallinity and composed of sub-micron sized crystals, which was expected from a room temperature precipitation method without thermal treatment[18, 167, 168]. In contrast, sintering did not increase the crystallinity of SiHA since no change in the sharpness of the diffraction peaks and little or no change in the peak intensity was observed when compared to as-precipitated SiHA. These observations are consistent with other works that have explored the effect of sintering temperature on Si doped HA where the lack of change (or decrease in cases of Si doping above 2-3%wt) in crystallinity has been attributed to Si incorporation into the HA crystal lattice[61, 60, 14]. Silicon substitution did not appear to change the angular position or relative intensity of the peaks when compared to HA and HA-650.

The difficulty in detecting all peaks relating to silicon substitution in the FTIR data of both the SiHA and SiHA-MPTS samples could have been due to overlapping of the silicon and phosphate vibrational modes, which have been noted to happen in the following cases:i) 470cm^{-1} (Si-O-Si band) and 472cm^{-1} (the O-P-O bending modes of the phosphate groups) and ii) 945cm^{-1} (Si-O symmetric stretching mode) and the weak 962cm^{-1} (P-O symmetric stretching mode). The translational mode of water associated to HA generally exists between 300cm^{-1} and 600cm^{-1}, which would also obscure the peaks within this range related to the presence of SiO_4^{4-}. However, Atomic Absorption Spectroscopy of dissolved SiHA (16 mg/mL) confirmed that silicon ions were indeed a component of the material to a measured ion concentrations of 0.47 mg/mL. This equated to a measured silicon ion content of approximately 2.93%wt which agreed with the theoretical silicon ion content of 2.85%wt within experimental error.

With respect to confirming the MPTS modification, the identification of a second Si-O vibration mode for SiHA-MPTS, which as not present in the unmodified SiHA, suggests there

might have been an additional silicon source in the sample. It was postulated that the source was elemental silicon from the MPTS modification - namely the Si-O-Si bonds from the binding of MPTS via the oxygen atom to the SiHA surface. This may explain why the peak was most prominent in SiHA-MPTS compared to HA-MPTS as the presence of SiO_4^{4-} on the surface increased the number of potential binding sites for MPTS. Other works have reported difficultly in detecting -SH groups in silane using IR techniques due to the low absorption coefficient of these groups [136]. Indeed, the Ellman's assay for free thiols showed a higher thiol presence with SiHA-MPTS compared to unmodified SiHA and HA, which appeared to support the earlier hypothesis of the additional Si-O peak from the FTIR results coming from successful binding of MPTS. Most notably, the zeta potential of SiHA-MPTS was measured to be -11.66mV and the change in the zeta potential suggested that this sample exhibited a different surface chemistry to both SiHA and HA. The result compared well with the work of Shyue *et al.* which also reported a decrease in the zeta potential due to the presence of thiols [169]. HA-MPTS did not show the same change in zeta-potential as SiHA-MPTS, which may further suggests that either none or significantly less thiol groups were attached to the HA surface in comparison to SiHA-MPTS.

6.5.2 Demonstration of application: Live cell imaging of SiHA internalisation by MC3T3 cells using a thiol reactive fluorescent probe

Successful thiol modification was shown by the attachment of the thiol-reactive fluorescent dye, fluorescein-5-maleimide (F5M), and subsequent imaging using confocal fluorescence microscopy (figure 6.9). The weak fluorescence shown by the unmodified SiHA sample demonstrated the effectiveness of the washing procedure in removing non-specifically bound dye molecules. This contrasts with the brighter fluorescence from the SiHA modified with MPTS (SiHA-MPTS), which colocalised with the vast majority of the material shown in the bright field image. The increased fluorescence intensity was attributed to the proportion of dye molecules bound to the thiols of the SiHA-MPTS, since unbound molecules were expected to be removed during the washing procedure.

Fluorescence could not be clearly seen in the low magnification image (figure 6.11a), which

would most likely have been due to the low particle concentration and low numerical aperture of the objective lens used to acquire the image. However, some fluorescence was detected in multiple cells at a higher magnification (Figure 6.11b). The live-dead assay data suggested that SiHA-MPTS-F5M was not cytotoxic at a concentration of 0.6μg/mL over 24 hours (figure 6.10). However, it should be noted this assay only labels already dead cells (or possibly cells close to death if the membrane was subject to significant physical damage). The assay is not designed to show cells undergoing early to advanced stages of cell death and furthermore does not discriminate between apoptosis (”programmed” cell death initiated by the cell in response to particular changes in the cell environment) or death by physical damage of the cell itself leading to compromised cell function. Therefore, while it can be concluded that the labelled particles at the imaging concentration did not kill a significant number of cells compared to the control and that the cells were still capable of cellular internalisation after 24 hours, the precise functional state of the cell cannot be commented upon. The live cell images do, however, show that the 24 hour window is more than adequate for potential tracking of the material across the cell membrane in order to understand their cellular fate. In fact, further trial experiments showed clear internalisation after around 3 hours.

In situ fluorescence spectroscopy (figure 6.12) confirmed that the detected light fitted the expected emission profile of a fluorescein based dye and therefore conclude that the detected signal was dominated by the labelled particles. The internalised structures measured approximately 400-500nm in diameter and appeared to localise at various points within the cytoplasm of the MC3T3 cell, but could not determine whether this was the result of either i) individual particles being internalised and then concentrated within the cell, or ii) the aggregates being internalised as a whole. However, the localisation and strong intensity of the fluorescence did indicate that the fluorescent labels were still attached to the particle surface and photoactive after 24 hours in culture media and post internalisation.

6.5.3 Cellular processing and fate of internalised material: An initial semi-quantitative investigation

The demonstration of the ability to label and track SiHA and its potential use in understanding the internationalisation, cellular processing and fate of such materials was extended through a limited study on cells with fluorescently labelled lysosomes. Computational processing of the particle/aggregate fluorescence image channel enabled the size distribution of the material to be generated, which showed structures up to 1μm were most prevalent by number within the cells, but sizes of the order of several microns up to 3-4 μm were observed. However, the lysosomes were generally only found to contain structures of up 2-3μm, leaving the larger sizes within the overall cell. Lysosomes are generally considered to have a maximum size of 2-3μm which may explain the upper size limit on colocalisation. No clear relationship was found between the volume of material transferred to lysosomes and the total material internalised by the cell as a whole and therefore no 'saturation point' could be established. The only remark is that, generally, no more than 20μm^3 of material was found within entire lysosome populations of any of the cells irrespective of the volume of material anywhere else in the cell. This may indicate a limit to the internalisation capacity of MC3T3 cells vis the lysosome route, although one must consider that limited sample size of this initial study does not allow for this 'limit' to be fully quantified.

Correlation of observations of changes in cell behaviour during the live cell imaging experiments and volume/size quantification of the internalised material within these cells indicated that cell fate is not dictated by the volume of material internalised alone. While generally the vast majority of nanoscale structures were found within the lysosomes after 24 hours, it is the location of particulates larger than 1μm (regardless of the total volume of material) that appears to be an additional factor. Cases where cell morphology changed from elongated to rounded correlated with the majority of the entire internalised particulate population (ranging from 0.2-3μm) colocalising with the lysosomes. With comparatively little solid material left exposed within the cell, the physical effect on the cell may be a response to the byproduct of lysosomal degradation of the SiHA. Exposure of HA-based materials to highly acidic conditions, results

in dissolution of the crystal structure into its constituent ions (or protonated versions thereof) - a key example being Ca^{2+} ions. Ca^{2+} ions are abundant in animal cells and implicated in the apoptosis signalling pathway [170, 171, 172]. Rounding of the general cell morphology in the absence of any obvious physical damage could be an indicator of the cell undergoing apoptosis. Of course, complete dissolution of the apatite, and potentially the labelling chemistry, ends the ability to track the event further and the experiment design did not permit visualisation of Ca^{2+} ion release.

Dramatic increase in the number of lysosomes appeared to correlate with particulates larger than 2μm begin left in the cytoplasm. This could have been merely a time lapse effect - i.e the large degree of lysosome recruitment and convergence around the largest particulates may have resulted in their eventual colocalisation over time and simulate the situation observed in the case of the cell rounding (case 1). Finally, at partial detachment and retraction of cells, no particulates larger than 1μm were observed colocalised with the lysosomes. These cases of cell detachment perhaps best showed that the total amount of material internalised by the cell is still a relevant second variable. Both cases involved cells containing between 105-215 μm^3 of material, with approximately 12% - 3% (v/v) located within lysosomes respectively. However, there were cases of cells containing approximately 150 μm^3 but with 45% of this located within the lysosomes, yet these cells retained normal elongated morphology and attachment to the culture plate.

Overall, this initial study has demonstrated the ability to track and quantify size and volume of SiHA particulates with a view to further understanding their mechanism of uptake and fate. The preliminary data presented within section 6.4 suggested that cellular response to internalisation of such materials is dependent on both the total volume of material within the cell and the size distribution of that material.

6.5.4 Concluding statement

A method for the modification of SiHA to present thiol groups from the particle surface has been described. Through engraftment of a fluorescent dye, this modification has been used as a

tool for the visualisation and tracking of SiHA particles in live cells. Quantification of the total volume and the size distribution of the internalised material has revealed a size window where material above $>1\mu$m in size not processed by the cell through lysosomal degradation may lead to the onset of cell death. This result may have wider implications to the understanding of the effect of wear-debris from ceramic implants on the surrounding tissues and lead to optimisation of their corrosive and mechanical wear characteristics.

CHAPTER 7

RESULTS CHAPTER 2: FORMATION OF CALCIUM PHOSPHATE-BASED MATRICES THROUGH SILANE CROSSLINKING

The chapter presents a strategy to the formation of functionalised CaP-based materials on a bulk scale (millimetres), as opposed to single CaP crystals, by crosslinking MPTS to form a network that entraps HA powder particles to form a single pliable monolith of the order of 10mm in size. This work involved the development of the silane chemistry described in Chapter 6 by the formation of MPTS polymer chains in solution, which are then condensed around the HA powder particles through a change in reaction pH. The overall structure is effectively HA powder dispersed in a gel of MPTS, which collectively herein is referred to as a HA-MPTS 'matrix'. Crosslinking was primarily achieved through Si-O-Si bonding between hydrolysed MPTS molecules while in principle the -SH groups were left available for the potential attachment of other biomolecules such as fluorescent tags, peptides and therapeutic drugs. Extensive Raman Spectroscopy analysis investigated the nature of the bonding in the MPTS gel phase along with the chemical interaction between the cross linked MPTS and the surface of the HA powder particles. At this stage, the two strategies of CaP functionalisation described in Chapters 6 and 7 enables the formation of a biomaterial on at the macro scale combined with the ability to incorporate therapeutic molecules through selective attachment. Finally, this technology of CaP functionalisation and drug attachment was demonstrated by the attachment of a novel antimicrobial peptide (developed within the University of Birmingham and the Royal Centre for Defence Medicine, Queen Elizabeth Hospital Birmingham) to a functionalised HA pellet, which acted as a model ceramic implant surface. The efficacy of this system in minimising bacteria proliferation and biofilm formation was assessed using surface thiol functionalised

and non-functionalised pellets and free in solution. Thus, this experiment served to assess the real potential of the surface modification and cross linking methods as a biomedical technology.

7.1 Materials and Methods

7.1.1 Formation of HA-polymerised MPTS networks

A solution consisting of 3% (v/v) MPTS (95%, 175617, Sigma-Aldrich Ltd., Dorset, UK), 3% (v/v) Millipore® water and 94% (v/v/) methanol (No: R40121, Fisher Scientific UK Ltd., Loughborough, UK) was prepared to a total volume of 30mL in a chemical resistant plastic screw cap bottle (note: water added to the methanol before the MPTS). Three bottles were prepared in total and each one adjusted to a different pH value - pH 4, 7 and 10 by addition of 1M hydrochloric acid or ammonium hydroxide. The solutions were left to hydrolyse overnight before adding 0.2g of ground HA powder to each reaction bottle and leaving to react overnight on a shaker plate at 300rpm. The solid product was filtered using a Büchner funnel and washed three times with absolute methanol and 5 times with Millipore® water. The confirmation of silane surface binding, functional group modification and polymerisation in relation to the solid product was investigated using Raman spectroscopy as described in 5.1.4.

7.1.2 Thiol coating of hydroxyapatite surfaces - towards novel antimicrobial coatings

Preparation of hydroxyapatite pellets

Hydroxyapatite (HA) was synthesised according to the method outlined in section 5.2.2. Dried hydroxyapatite powder was mixed with deionised water (830μL for each gram of HA) to form a thick paste. Cylindrical pellets were formed by manipulating the paste into the holes (6mm in diameter and 12mm in height) of a homebuilt PTFE mould (figure 7.1) using a spatula. 1 gram of HA provided enough solid material to make 2 pellets and a total 90 pellets were made.

During the filling process, the entire mould rig was on a vibrating plate to ensure that the paste filled the bottom of each hole before applying more paste. The filled mould was then placed in an oven at $60\,^{\circ}\mathrm{C}$ overnight before removing the formed pellets and transferring them to a furnace for sintering at $1100\,^{\circ}\mathrm{C}$ for 6 hours with a temperature ramp rate of $5\,^{\circ}\mathrm{C}$/min. The pellets designated for surface modification were then cut into thirds across their length so they could inside the wells of a 96 well-plate. The remainder were kept intact for characterisation and/or as spare pellets.

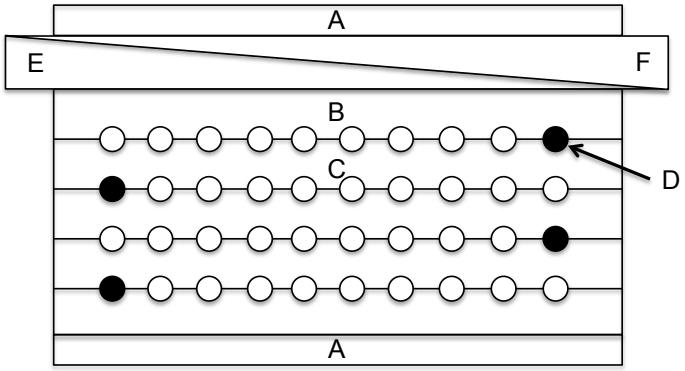

Figure 7.1: Schematic diagram, with components labelled A-F, of the mould used to form cylindrical HA pellets measuring 6mm in diameter and 12mm in height. The main body (A) housed repeating sets of blocks (B,C) which formed an array of equally sized holes when aligned with the pegs (D). The moulds were held in place by two wedges (E,F).

Determination of pellet porosity by Helium Pycnometry

Bulk density of each pellet was estimated from measurements its dimensions and mass prior to analysis. The true density of all samples was evaluated using an AccuPyc II 1340 (Micromeritics, U.S.A) helium pycnometer: each sample was subject to ten purges with helium prior to ten volume measurements. The porosity, p, of each pellet was then estimated using the following equation:

$$p = 1 - \frac{\rho_{solid}}{\rho_{bulk}} \tag{7.1}$$

where ρ_{solid} is the density of the solid material component of the pellet and ρ_{bulk} is the

average density of the pellet, which includes the solid CaP and air/liquid within the pores. By convention, the final value is then expressed as a percentage by multiplying the calculated porosity by 100.

Thiol coating process

A solution consisting of 2% (v/v) MPTS (95%, 175617, Sigma-Aldrich Ltd., Dorset, UK), 3% Millpore® water and 95% (v/v) methanol was prepared to a total volume of 90mL in a chemical resistant plastic screw cap bottle (note: water added to the methanol before the MPTS). The pH of the reaction solution was then adjusted slowly to 4.00 by addition of 1M hydrochloric acid and left to hydrolyse for 4 hours. The hydrolysed MPTS solution was then adjusted to pH 7.00 by addition of ammonium hydroxide before adding the cut HA pellets (prepared as described in section 7.1.2) and leaving to react overnight while on a flat shaker plate running at 300rpm (ThermoScientific Inc., Waltham, MA, USA). No more than 30 pellets were placed in each reaction bottle in order to ensure adequate separation and coating of the pellets. The pellets were carefully washed five times in 20% methanol before drying in an oven for 2 hours at 60 °C.

7.1.3 Application: Attachment of novel antimicrobial agents

A detailed protocol describing the moieties of the antimicrobial peptide cannot be disclosed within this thesis due to the commercial sensitivity of the developed peptide. The general approach used for the attachment of the peptide involved adding a small amount of the peptide dispersed in a buffer solution to the substrate surface and incubating for a short period of time. The peptide attached to the thiol-modified surface via an engineered binding moiety on the peptide and hence was immobilised on the surface. In the case of non-modified surfaces, the peptide was expected to attach purely by adsorption.

7.2 Phase composition of the solid CaP component

The broad X-ray diffraction peaks of the as-precipitated material used to form the pellets prior to sintering (Figure 7.2) enveloped the most intense peaks of the hydroxyapatite reference diffraction pattern, suggesting that this material consisted mostly of hydroxyapatite (HA) of very low crystallinity. The major peak for both α and β- Tricalcium phosphate (TCP), which exist 31° were not detected. From the diffraction pattern of the pellet after sintering at $1100\,^\circ\mathrm{C}$ for 6 hours, sharp and intense peaks were identified at 25.85°, 28.11°, 28.94°, 31.77°, 32.19°, 32.92°, 39.85° and several peaks between $46 - 53^\circ$. These peaks corresponded to those of the hydroxyapatite pattern to within +/- 0.05°. The detection of a peak at 30.72° corresponded to the main peak of α-TCP, but was approximately 15 times weaker in intensity compared to the main hydroxyapatite peak at 31.77°. No other peaks in the experimental data could be uniquely assigned to α-TCP. Peaks at approximately 17°, $22.80 - 23^\circ$ and 34° could belong to either HA or α-TCP based on their angular position alone due to their broadness in comparison to the spacing of the peaks in this angular region in the reference patterns. However, the 34° peak was determined to belong to HA after considering the lack of an additional α-TCP peak at 34.60 in the XRD pattern after sintering. The relative intensity of the 34.60 peak to the 34.18° peak in the α-TCP reference dataset was calculated to be 0.6. Considering that the experimental peak at 34° was detected with an intensity of 89 counts, then the proposed additional α-TCP peak at 34.60 would theoretically have had an intensity of 0.6*89 = 53 counts. One would expect that such peak would be clearly distinguishable from the background, but this additional α-TCP peak was not evident in the diffraction pattern. None of the main β-TCP peaks were identified in the diffraction patterns. Overall, the diffraction data presented in figure 7.2 suggested that the powder was initially composed of HA and that the composition remained mostly HA with a small amount decomposing to α-TCP upon sintering.

Helium pycnometry analysis showed that the unsintered HA pellets had a porosity of 72.55% (+/- 1.21%) while the sintered HA pellets had a porosity of 58.63% (+/- 0.64%).

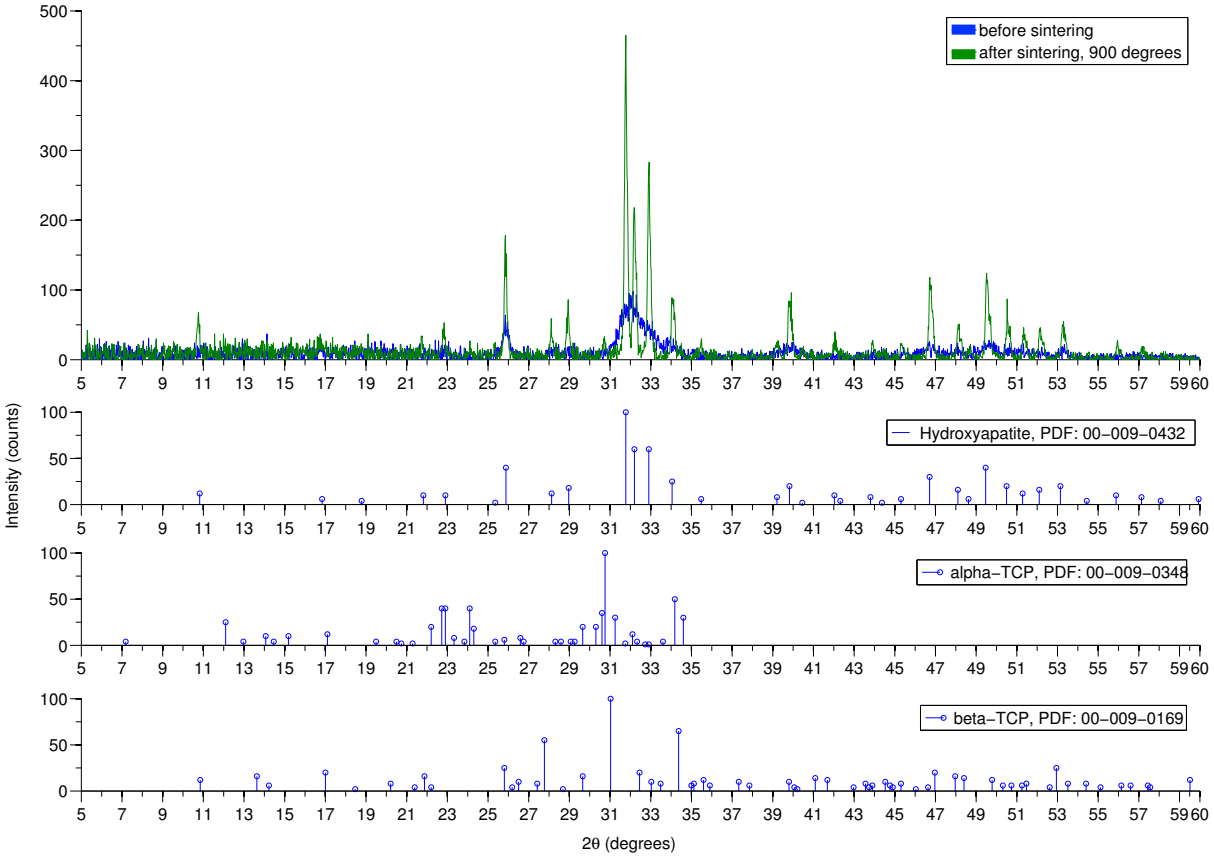

Figure 7.2: X-ray diffraction patterns of crushed pellets before and after sintering along with reference patterns for hydroxyapatite, α-tricalcium phosphate (α-TCP) and β-TCP. The diffraction peaks of the material both before and after sintering, corresponded very well to those of the hydroxyapatite reference pattern with a small amount of α-TCP detected through the peak just below $32\,^{\circ}\mathrm{C}$.

7.3 The effect of silane condensation pH on the formation of HA-MPTS matrices

Upon hydrolysis of the silane under acid conditions (pH 4.00), the reaction pH was increased to induce condensation of the silane molecules into polymer chains. Raman spectra of the solid material obtained from the reaction performed at condensation pH values 4.00, 6.00 and 10.00 were collected and are presented in figure 7.3 with a list of detected Raman peaks located in table 7.1.

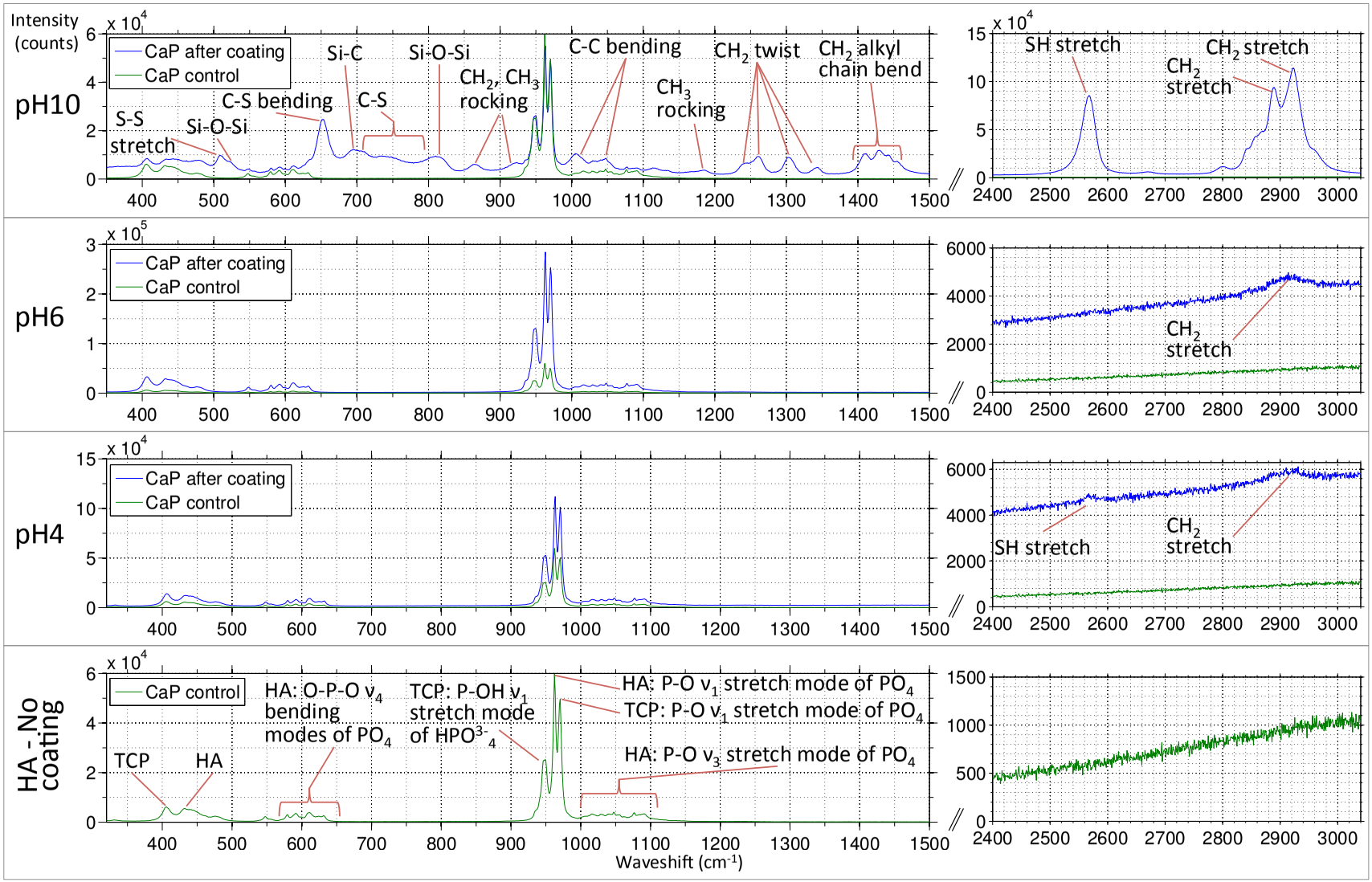

Figure 7.3: Raman spectra of the CaP after the silane condensation reaction at pH 10, 6 and 4 along with a Raman spectrum of the unmodified sintered CaP material as a control. Raman peaks belonging to the CaP material are labelled in the "HA-No coating" spectrum, but not in the other spectra for clarity while identifying the MPTS peaks. Spectra are split in the x-axis (300-1500 and 2400-3400).

Table 7.1: List of Raman scattering peaks of HA, TCP and MPTS detected from the products of the condensation reaction at pH 4, 6 and 10 along with a control HA sample not subjected to the reaction. Raman peaks for MPTS are further attributed specifically to the pure, gelled, hydrolysed and condensed (to form oligomers) form of the molecule where appropriate. *[*ref*] refers to the same bond identified in studies of a different organosilane.

Peak (cm^{-1})	Assignment	References
Raman peaks for HA		
330	OH^- translational mode	[173, 174]
432, 447	double degenerate O-P-O bending mode (ν_2) of PO_4 group	[161, 174]
592, 610, 620	triple degenerate O-P-O bending mode (ν_4) of the PO_4 group	[161, 174]
962	symmetric P-O stretching mode (ν_1) of the PO_4 group	[161, 174]
1030, 1047, 1055, 1076	triple degenerate asymmetric P-O stretching mode (ν_3) of PO_4 group	[161, 173]
Raman peaks for TCP		
408	O-P-O bending mode (ν_2) of HPO_4^{2-} group	[161]
599, 624	P-O and O-P-O stretching and bending modes (ν_4) of the PO_4 group	[161]
949	P-O stretching mode (ν_1) of HPO_4^{2-} group	[161, 174]
962, 970	symmetric P-O stretching mode (ν_1) of the PO_4 group	[161, 174]
1015, 1040	P-O stretching mode (ν_1) of HPO_4^{2-} group	[161, 175]
1090	P-O stretching mode (ν_3) of HPO_4^{2-} group	[161]
Raman peaks for MPTS (pure and gelled forms)		
508	S-S stretching mode (gel)	[176]
520-523	Si-O-Si (gel)	[176]
651	S-C gauche stretching mode (MPTS pure and gel)	[177]
694	Si-C trans mode (gel)	
725-776	S-C trans stretching mode (pure and gel)	[176]
783-840	Si-O-Si (800-811: gel[a]), 795: Si-O-Si dimers[b], 830: Si-O-Si 'network'[b]	[176][a],[178][b]
864	CH_2 rocking mode (gel)	[176]
922	CH_2/CH_3 rocking mode (gel[a])	[176][a], [177]
1003	C-C trans mode (gel)	[176]
1044	C-C gauche mode (pure)	[176]
1116	CH_2 rocking mode (gel)	[176]
1185	CH_3 rocking mode (gel)	[176]
1244, 1261, 1303, 1344	CH_2 twisting modes (gel)	[176]
1411, 1430, 1444, 1455	CH_2 alkyl chain bending modes	[134]
2568	SH stretching mode	[179, 177]
2843	CH_3 (pure)	[176]
2890, 2923	CH_2 vibrations of propyl chain (hydrolysed and condensed)	[180]*

The powder was confirmed to be HA by the detection of the characteristic PO mode at around 962cm^{-1} along with the weak asymmetric P-O modes at 1030cm^{-1}, 1047cm^{-1}, 1055cm^{-1} and 1076cm^{-1} with relative intensities confirmed in other works [161, 173]. TCP was also identified in the sample by the major P-O stretching mode at 949cm^{-1} and symmetric P-O stretching mode at 970cm^{-1}. A second strong P-O peak was identified at 962cm^{-1}, but this peak exists for both HA and TCP. O-P-O bending modes of HA at 432cm^{-1} and 447cm^{-1} were detected, but the 447cm^{-1} peak was found to be broader and weaker compared with other reports showing a moderate intensity [161, 173]. The mostly likely explanation is the merging of this peak to the 439cm^{-1} O-P-O bending mode of TCP, given that other major peaks of TCP had already been identified. Additional peaks corresponding to TCP including the P-O stretching modes at 599cm^{-1}, 624cm^{-1}, 1015cm^{-1}, 1049cm^{-1} and 1090cm^{-1} were also identified. The OH^- translational mode common to apatites was detected at 330cm^{-1}, but the second mode usually located around 3573cm^{-1} [173] was beyond the range of detection of the experimental setup used for this work. Carbonates were expected to be present in the starting unsintered material given the use of a low temperature precipitation synthesis method. Post sintering, the strongest CO_3^{2-} peak at 1070cm^{-1}, but presence of the second major peak at 1076cm^{-1} could not be ruled out due to the overlap with the PO_4 peak of HA. No A-type CO_3^{2-} peak at 1106cm^{-1} was identified in any of the samples. From a qualitative point of view, the weak presence (or complete lack) of carbonate peaks suggested that most of the carbonate content that may have been present in the starting material had been removed by the sintering process.

Polymerisation of MPTS to form a gel was most pronounced from the reaction held at pH 10 where Si-O-Si modes were detected at 520cm^{-1} and between 800-811cm^{-1} (broad shoulder peak). The lack Si-OC peaks at 1108cm^{-1} or 1088cm^{-1} indicated hydrolysis of the methoxy groups of the silane in agreement with other studies on silane hydrolysis [177]. This complimented the existence of Si-O-Si MPTS oligomers, as such a bond would only have formed after the hydrolysis of at least one of the methoxy groups bound to the silicon atom of two MPTS molecules. The very weak shoulder peak located at 2843cm^{-1} corresponded to the presence of CH_3 groups and therefore showed that there was a small amount of pure non-hydrolysed MPTS

remaining in the product of the reaction. Further evidence that of the MPTS existing in gel form was found by the shifting of the CH_2 rocking (864cm^{-1} and 1116cm^{-1}) and twisting (1244cm^{-1}, 1261cm^{-1}, 1303cm^{-1} and 1344cm^{-1}) modes to higher wave shifts as reported by Thompson *et al.*[176]. Most interesting was evidence of an additional form of MPTS cross linking via disulphide bonding through the identification of the S-S peak at 508cm^{-1}. The S-C gauche peak at 651cm^{-1} was found to have a higher Raman scattering intensity compared to the wide S-C trans mode located 725cm^{-1}-776cm^{-1}, which Thompson *et al.* reported as being consistent with considerable disorder in the propyl chain of the MPTS molecule when in liquid or gel form [176]. Vasiliev *et al.* reported a doublet peak at 990cm^{-1})-1003cm^{-1}) corresponding to Si-O-P bonding, which was attributed to chemical bonding between the phosphate bound OH^- and the silane [148]. This bond was not evident in any of Raman spectra presented in figure 7.3. However, a subtle decrease in the intensity of the OH^- group peak was observed without a shift in peak position.

At pH 6, no Raman peaks corresponding to Si-O-Si or S-S cross linking or varying degrees of hydrolysis were identified. The C-C trans mode of MPTS was detected at 1003cm^{-1}-1004cm^{-1} and has been reported to specifically correspond to C-C bonds in the gelled form of MPTS[176]. A broad weak band spanning 2860cm^{-1} to 2980cm^{-1} appeared to envelope the CH_2 vibration peak in the same waveshift region as in the case of condensation at pH10. It was not possible to determine whether the detected MPTS was in pure or hydrolysed (but not condensed) form from this envelope peak as the peak width was much larger than the typical 1-4cm^{-1} shifts which distinguish these forms of MPTS. However, the identification of a Si-OC peak in the 1088cm^{-1}-1095cm^{-1} region suggest that any MPTS molecules present were not completely hydrolysed. In contrast to the reaction at pH 10, the OH^- peak of these sample has shifted from 330cm^{-1} to 333cm^{-1}.

At pH4, the weak and broad envelop of the CH_2 peaks was detected between 2860cm^{-1} and 2980cm^{-1}. No evidence of Si-O-Si or S-S peaks to suggest cross linking or oligomerisation of the MPTS to any extent, but a weak SH group peak was detected at 2568cm^{-1}. As in the case at pH 6, evidence of incomplete hydrolysis of the MPTS present in the final product was found

by the Si-OC peak in the 1088cm^{-1}-1095cm^{-1} region. Shifting of the OH^- peak from 300cm^{-1} to 333cm^{-1} was also observed with no change in intensity relative to the same peak in the HA control sample.

The solid material extracted from the reactions where the condensation pH was set to 4.00 and 6.00 closed resembled the looseness and consistency of the initial HA powder. In stark contrast, the product obtained at pH 10.00 was a monolith with the consistency of chewing gum under gentle agitation with a spatular as shown in the photographs in figure 7.4. The material deformed plastically, i.e did not return to original dimensions and morphology, in response to a compressive force (figure 7.4c and could be dissected under moderate force with a spatula. No expulsion of liquid from the monolith was observed while applied compressive force and the retained the described mechanical properties even after drying for 24 hours at $37\,^{\circ}\mathrm{C}$. Measurements of the monolith mass while submerged in Millipore water showed that swelling of up to 10% of initial mass over the first 24-48 hours before returning to within 2% of initial mass thereafter and maintaining this mass for a period of 2 weeks in solution. No fragmentation of the monolith in solution was observed during this period in the absence of any applied force or excessive agitation of the monolith. Moulding of the monolith with a spatula after the same period resulted in the creation of a few fragments estimated to be 1mm in diameter.

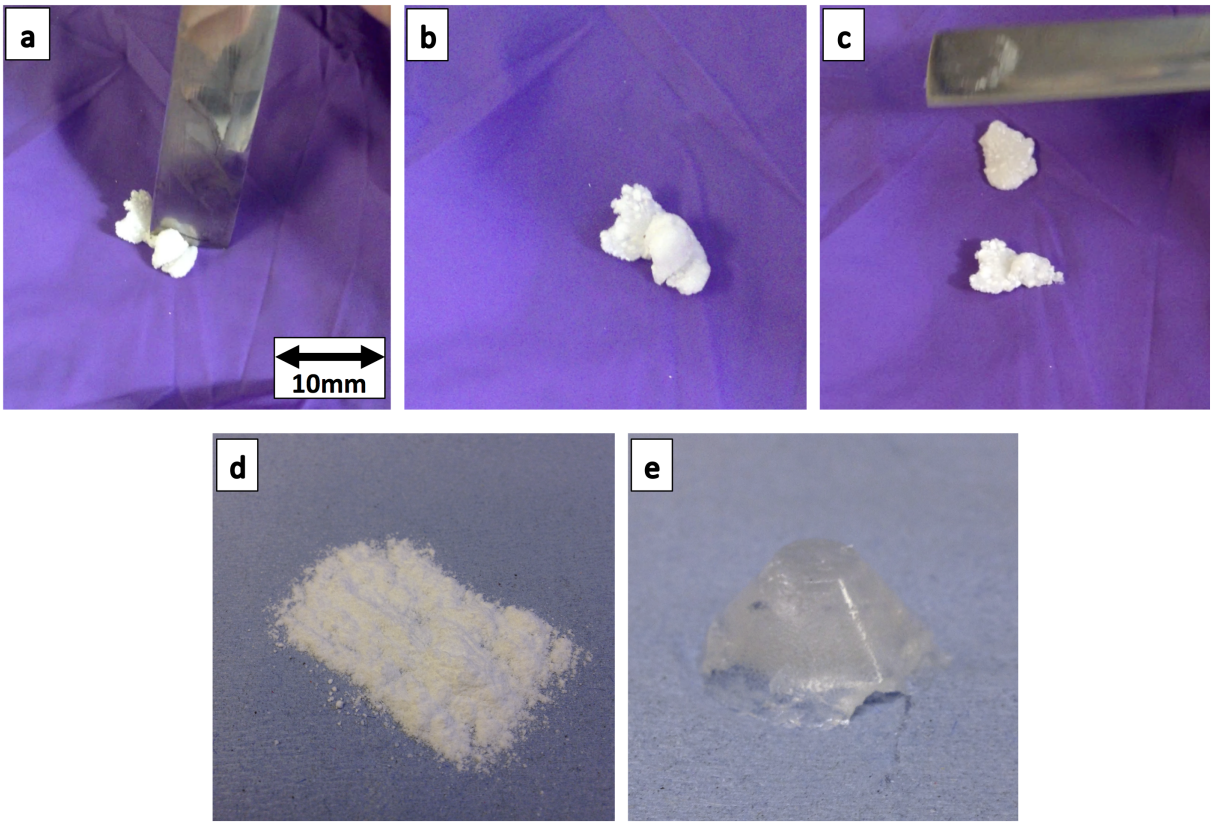

Figure 7.4: Top row: A series of images showing a pliable material formed from hydroxyapatite powder encapsulated within a polymerised MPTS network. The images were extracted from a video which shows the material being subjected to a 'cutting' action (a,b), and compression (c) using a spatula. The full video has been included on a CD which accompanies this thesis. Filename: *HA-MPTS matrix.m4v*. Bottom row: Images showing the two components of the matrix - CaP powder (d) and a MPTS gel, without powder, as a control. The conical shape of the MPTS gel mirrored the shape of the bottom of the 50mL centrifuge tube.

7.4 Novel antimicrobial coating of calcium phosphate surfaces through thiol modification

Most antibiotic agents are adsorbed on to ceramic surfaces through dip coating processes, which can lead to inconsistent coverage and coating stability over time while under physiological conditions between batches. There is a drive in the biomaterials field to develop implant materials that can also act as platforms for controlled release, selective attachment or patterning of therapeutic drugs to tissue replacement implants and ensure clinically relevant doses are administered during the healing process. However, the clinical need for drugs such as antibiotics may last from several days to a couple of weeks and coatings maybe subject to significant biological or mechanical degradation within that time. A novel antimicrobial peptide has been developed by Prof. Ann Logan, Felicity de Cogan (Clinical and Experimental Medicine, University of Birmingham), Wg Cdr Robert Scott (Royal Centre for Defence Medicine, Queen Elizabeth Hospital Birmingham), Dr. Anna Peacock (School of Chemistry, University of Birmingham) with a higher potency than current antibiotics on the market. A collaboration was set up to combine the antimicrobial agent and the process for thiol modification of apatites and demonstrate covalent attachment of antibiotics to a potential implant material. Fluorescent tagging of the antimicrobial agent enabled visualisation of the evenness of the coating while viability assays with a G1 Pseudomomas Aeruginosa bacterial strain verified the potency of the agent. Due to the commercial sensitivity of the work, details of the chemical structure and mode of action of the antimicrobial agent will not be disclosed within this thesis.

In this application, HA pellets were coated using the condensation process used in section 7.3 with the silane presenting thiol groups from the surface of the pellet, which enabled the attachment of the antimicrobial agent. Figure 7.5 shows epi-fluorescence images of the surface of a HA pellet after reaction with the antimicrobial agent both with (figure 7.5a) and without (figure 7.5b) the thiol coupling provided by the MPTS. The antimicrobial agent used in this experiment was modified to include a Green Fluorescent Protein (GFP) to enable visual confirmation of it's presence on the HA surface. Bright green coloured fluorescence from the

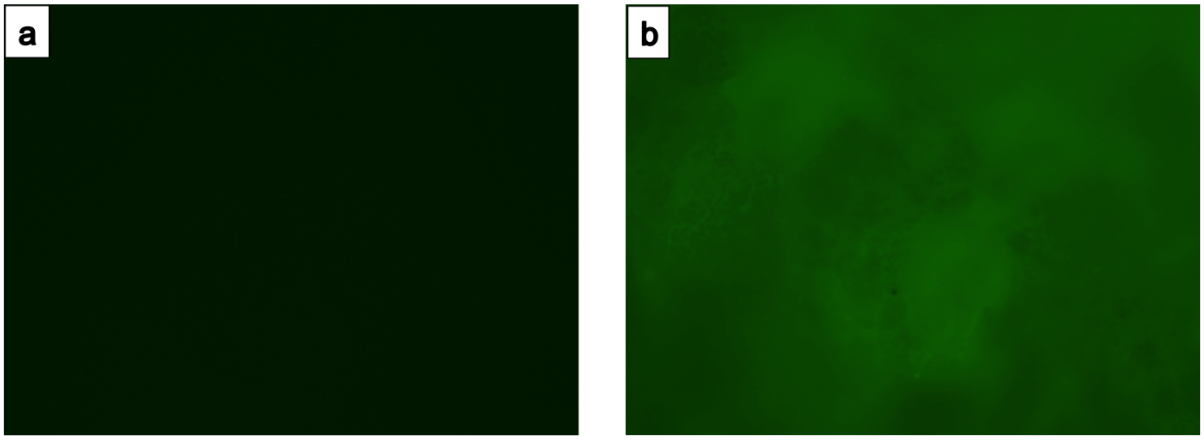

Figure 7.5: Epi-fluorescence microscopy images of calcium phosphate pellets without thiol modification (a) and with thiol modification (b) and both treated with the antimicrobial agent, which was fluorescently labelled for this experiment. The lack of fluorescence in (a) demonstrated that the agent was easily removed by washing when relying on adsorption to the material surface. The bright and relatively even fluorescence shown in (b) demonstrated a more robust attachment of the agent to the thiol modified material. Both images were obtained with the same excitation light intensity and camera signal gain. Data collected by Dr. Felicity De Cogan, School of Clinical and Experimental Medicine, University of Birmingham.

antimicrobial agent was detected over the entire field of view on the functionalised surface compared to the non-functionalised surface indicating that the agent was washed away in the latter case. Some variation in the intensity of the fluorescence was observed on the functionalised surface, which can be seen in figure 7.5b, suggesting some degree of spatial variation in the attachment density on some regions of the pellet.

Bacteria cell viability tests were performed on antimicrobial peptide deposited on thiol functionalised and non-functionalised HA pellets to assess the potency of the systems in preventing biofilm formation on the pellet surface (figure 7.6). Studies on biofilm formation on the surface of the HA pellets revealed that the free antimicrobial peptide in solution prevented biofilm compared to the penicillin-streptomycin in solution control and that this level of potency was maintained when the peptide was immobilised on the HA surface through thiol functionalisation. On the other hand, removing the thiol linkage between the HA surface and the peptide resulted in up to a factor four times increase in biofilm formation in terms of cell number.

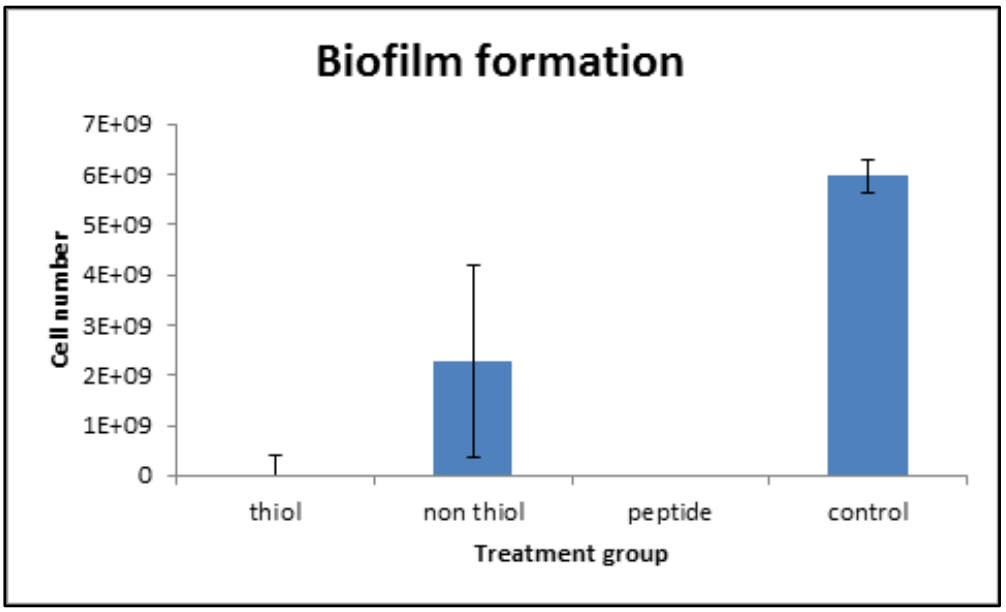

Figure 7.6: Bacteria cell (G1 Pseudomomas Aeruginosa) viability test of the novel antimicrobial agent on thiol functionalised and non-functionalsied HA pellets along with the free peptide. Cell number represents the number of bacteria remaining after exposure to the antimicrobial peptide with an untreated control population of bacteria cells as a reference. Treatment groups: ”thiol” = HA pellet + MPTS functionalisation + peptide, ”nonthiol” = HA pellet + peptide, ”peptide’ = free peptide in solution, and ”control” = bacteria alone. The antimicrobial peptide attached to a HA surface via thiol functionalisation almost entirely prevented biofilm formation compared to the non-functionalised case. Data collected by Dr. Felicity De Cogan, School of Clinical and Experimental Medicine, University of Birmingham.

7.5 Discussion

7.5.1 Phase and composition of the solid CaP component

X-ray diffraction and Raman spectroscopy results confirmed that the powder used as the solid phase in the matrix and in the pellets for engraftment of the antimicrobial was mostly composed of HA after sintering at $1100\,^{\circ}\mathrm{C}$, with some TCP as byproduct. Raman spectra of the sintered HA powder showed traces of carbonate in the material as is common when using a low temperature precipitation method of synthesis under ambient conditions. Most of this impurity was expected to have been removed during the sintering process. Carbonates are well known to modulate the solubility of HA and TCP such that their solubility increases at a given pH value with carbonate content %wt. Raman spectra of the products from the MPTS condensation reactions used to form the HA-MPTS matrices showed no obvious change in the chemical

structure of the HA powder at pH 4, 6 or 10 compared to the sintered HA powder control. Retrospectively, although there may not have been any transformation in the chemical structure of the solid material, Raman spectroscopy cannot indicate any mass loss of the material due to dissolution in the absence of careful calibration. Therefore, although the data did not reflect any unwanted change in the phase composition of the HA powder or pellets, direct loss of the HA material under the acid conditions cannot be ruled out.

7.5.2 The effect of silane condensation pH on the formation of HA-MPTS matrices

The pH change induced in the reaction in the transition from hydrolysis to condensation processes was found to have an effect on the physical form of the product. Adjustment of the reaction to pH 10 led to the formation of a monolith which appeared to 'encapsulate' all of the loose HA powder initially added to the reaction which was pliable under moderate compressive and shearing force using a spatula by hand. Raman spectroscopy of the monolith confirmed that the MPTS molecules had crosslinked via Si-O-Si bonds as shown by the presence of the two peaks spanning 520cm^{-1}-523cm^{-1} and 800cm^{-1}-811cm^{-1}. It was clear from the Raman spectra at pH 10 that not all of the MPTS was completely hydrolysed i.e all three alkoxy groups removed from the parent MPTS molecule. A small amount of non-hydrolysed MPTS was indicated by the weak shoulder peak located at 2843cm^{-1}. However, these MPTS molecules would not necessarily have been in their pure form with all three CH_3 groups intact and that they could existed with just or two CH_3 groups remaining. A schematic diagram proposing how different stages of hydrolysis would ultimately contribute to the condensation process is shown in figure 7.7.

Incomplete hydrolysis of MPTS could potentially have a knock on effect on the formation and final chemical structure of a gel network. Two distinct scenarios can be hypothesised - i) that hydrolysis was incomplete on all three CH_3 groups of the molecule and therefore was not bonded at all within the cross linked network or, ii) these cases of incomplete hydrolysis were sparse across the entire population of MPTS molecules such that only one or two out of the three CH_3 groups were hydrolysed and hence there was still potential for bonding into the cross

linked network. Of course, the non-hydrolysed groups would then become 'defects' (stemming from the colloquial use of the phrase 'monolayer defects' for breaks in single the chemical bonds within an organic monolayer formed on a substrate). The underlying importance of these two scenarios resides in the fact that these unreacted groups could undergo hydrolysis at a letter stage with the byproduct, methanol CH_3OH, potentially being toxic to cells. The approach to minimising or completely removing these groups from the bulk material depends on which of the two scenarios is most prevalent. MPTS molecules where no hydrolysis has taken place could be removed all together by more extensive washing. Meanwhile, partial hydrolysis of a population of molecules could only be resolved by increasing the hydrolysis time prior to the condensation step to form the matrix. Interestingly, the Raman data showed more evidence of incomplete hydrolysis at pH 4 and 6 compared to pH 10 through the detection of Si-OC peaks only in the first two cases. Generally, hydrolysis of silanes is the most dominant process under acidic conditions [179]. On this basis one would have expected that the ideal hydrolysis conditions would have existed in the sample where the pH remained at 4 for both the hydrolysis and condensation processes. However, other studies into the reaction dynamics of silanes have revealed that hydrolysis still occurs under basic conditions [176, 179]. One report by Scott *et al.* showed the highest hydrolysis rate actually occurred at pH 10, but the reaction is tempered by the more favoured condensation processes at this pH [179]. This alone may explain why there was a greater degree of hydrolysis occurring the HA-MPTS sample at pH 10. The authors go on to conclude that hydrolysis and condensation occur at roughly the same rates at neutral pH values, but that the rates are so low that it would take several days to observe any attachment to their alloy substrates. This mirrors the findings from the Raman data presented in this work where at pH 6, there was the least evidence of any attachment of MPTS.

There was evidence of some of additional cross linking via S-S bonds from the thiol groups of the MPTS molecules by the existence of a peak at 508cm^{-1}. Crosslinking via S-S bonds was not anticipated as preliminary experiments related to this work found that the use of a strong oxidising agent such as iodine was required. Furthermore, there was a realistic possibility that any oxygen in the water present in the reaction would have oxidised individual SH groups and

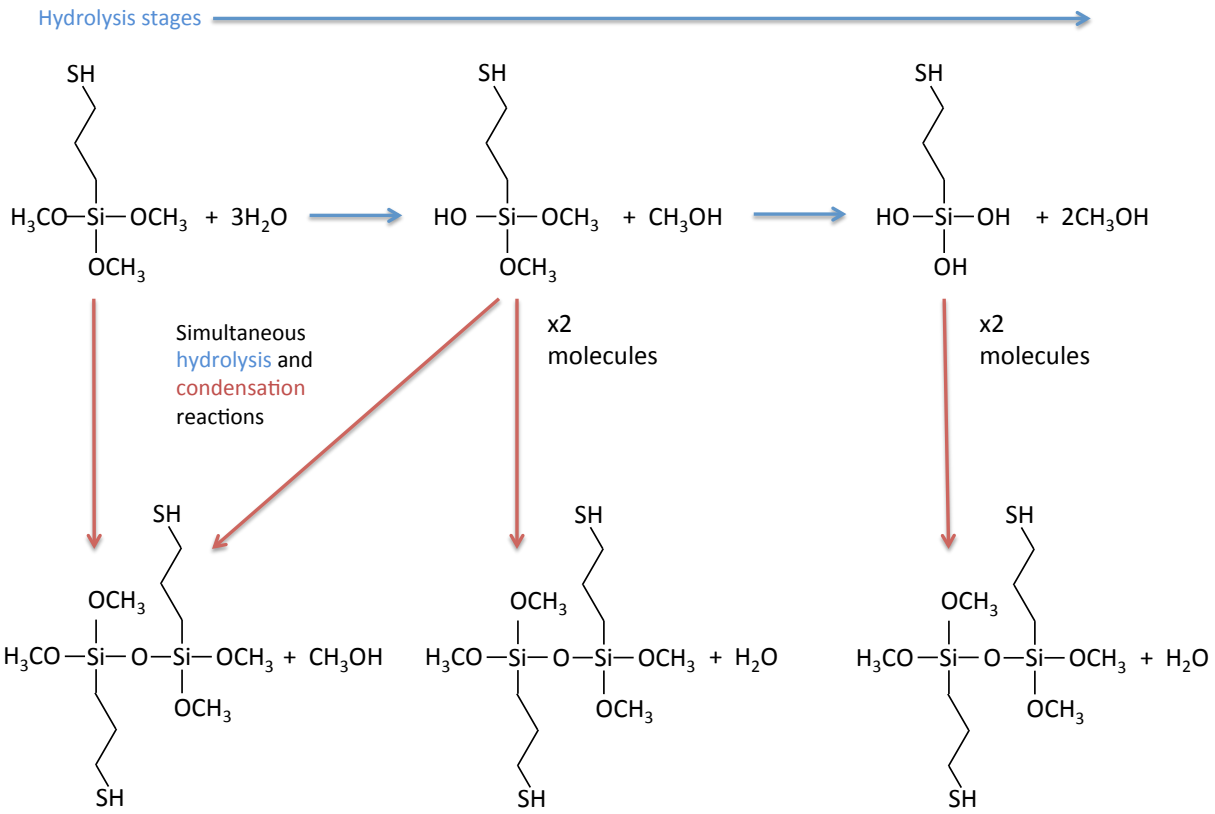

Figure 7.7: Schematic diagram showing the chemical reactions involved in the hydrolysis (blue product arrows) and subsequent onset of condensation of (red product arrows) of (3-mercaptopropyl)trimethoxysilane (MPTS). Hydrolysis entails the addition of water to reduce the methoxy groups. Condensation then joins two or more MPTS molecules via the exposed oxygens from the reduction processes to form silicon-oxygen-silicon bonds. In reality, the hydrolysis and condensation processes can occur at the same time in a reaction which explains the presence of the Raman peaks representing hydrolysed, surface bound and polymerised functional groups in the Raman spectroscopy data figure 7.3. For clarity, potential S-S cross linking via the -SH groups from multiple MPTS molecules have been ignored in this diagram.

hence prevented S-S formation between pairs of MPTS molecules. Experimentally, this potential source of interference with S-S cross linking did not appear to be a prevalent issue given the identification of the SH stretching mode at 2568cm^{-1}, which represented sulfhydryl groups in a reduced state available for cross linking. Figure 7.8 shows a diagram proposing the nature of the cross linking that may exist within the HA-MPTS matrix given the findings from Raman spectroscopy. Crosslinking through Si-O-Si and S-S occur at different intermolecular geometries and it could be hypothesised that this facilitates linking between discrete MPTS oligomers/polymer chains to form the 3D gel structure or strengthens any pre-existing 3D structure provided by the Si-O-Si bonding alone. This is consistent with the considerable propyl chain disorder inferred from the relative S-C Raman peak intensities.

At pH 4 and 6, the product from the reactions resembles the loose powder originally placed in the reaction and showed no sign of linking or gelling of the powder on the bulk scale. This was reflected in the Raman spectroscopy data by the lack of any peaks corresponding to Si-O-Si or S-S bonds between multiple MPTS molecules. Traces of MPTS which has formed oligomers at pH 6 were indicated by the C-C trans mode, but the lack of any of the CH_2 and CH_3 rocking modes specific to the gelled form indicated that none of these oligomers had condensed sufficiently to form a gel. No peaks corresponding to pure MPTS were observed, which led to the proposal that the majority of the MPTS (pure or in oligomer form) had been washed away. Similar observations were made for the product from the condensation reaction at pH 4, except for an additional weak SH peak. In principle, condensation of hydrolysed MPTS to form oligomers and/or MPTS gel at pH 4 would be less favoured over pH 6 and hence one would expect almost no sign of MPTS in the Raman spectrum at pH 4. However, the hydrolysis process was carried out at pH 4 for all three samples and so this sample underwent a significantly longer hydrolysis process compared to the samples at pH 6 and 10 albeit ultimately without any condensation to follow. In this case it would be reasonable to suggest that the more extensive hydrolysis period may have increased the likelyhood of complete hydrolysis of the vast majority of MPTS molecules.

There was no direct evidence in this study of MPTS associating with OH^- on the surface of

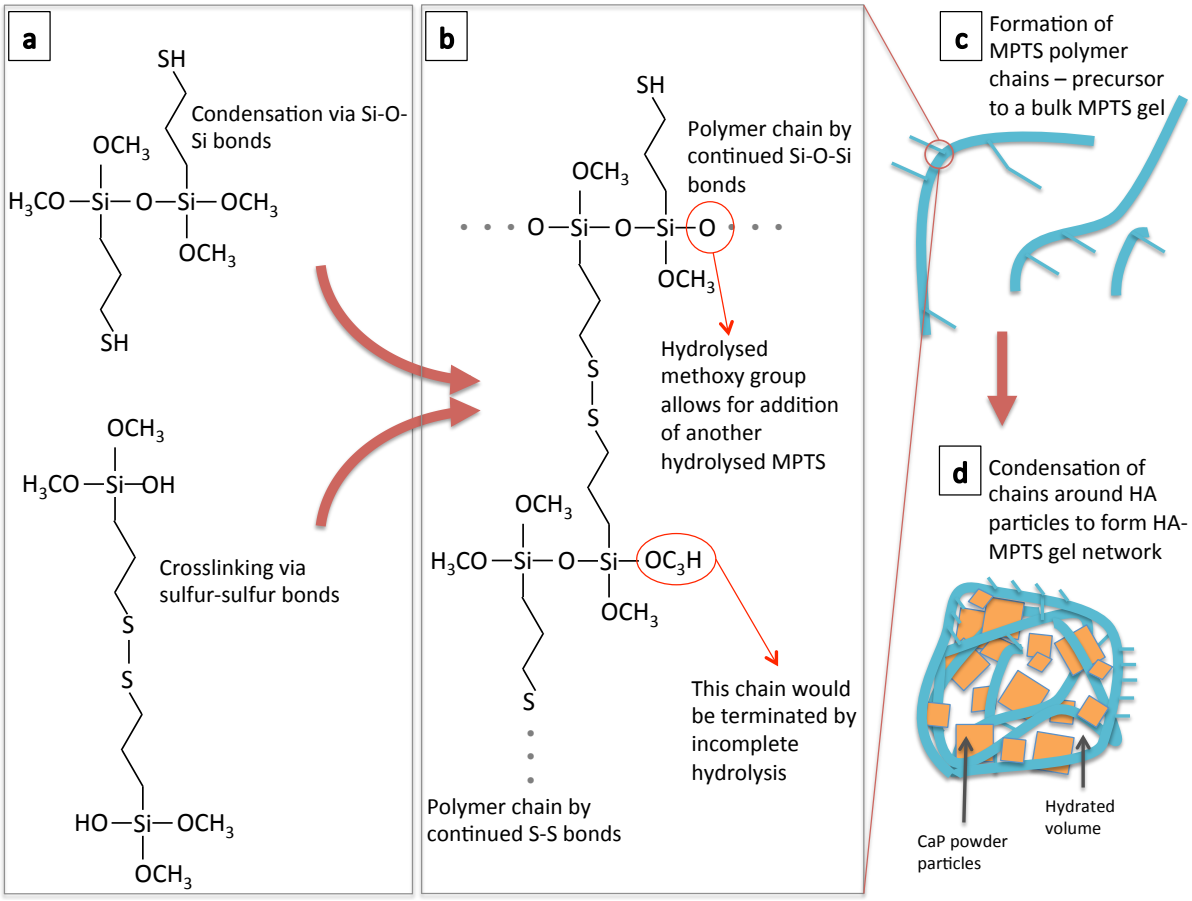

Figure 7.8: Schematic diagram of the proposed mechanisms of polymerisation and cross linking involved in the formation of the pliable HA-MPTS matrix. Two cross linking modes for the MPTS are available: i) partial condensation of the hydrolysed Si-O groups to form Si-O-Si oligomers (a) or, ii) oxidisation of SH groups to form S-S bridges across two molecules. Potentially, cross linking can occur via both modes (b). Hydrolysis is incomplete if one or two of the three CH_3 groups remain on the MPTS molecule(s) and would prevent additional monomers from bonding to the chain at that terminal. Increasing to pH to 10, causes condensation reactions to dominate to form polymer chains. Hence, under varying degrees of hydrolysis, polymer chains of varying length are produced (c). Condensation of the polymer chains encapsulates the solid phase (HA particles) to form a hybrid HA-MPTS matrix (d).

HA as the Si-O-P Raman peak was not detected. A subtle decrease in the intensity of theOH^- Raman band of HA at condensation pH 10 compared to HA control was observed, but without any measurable shift in the peak position to conclusively indicate a change in the binding chemistry of the OH^- group. However, a shift from $330cm^{-1}$ to $333cm^{-1}$ in this peak was identified in samples undergoing condensation at pH 6 and 4. In the absence of any other conclusive reports relating MPTS-HA chemisorption to changes in the OH^- Raman translational peak, the nature behind any potential bonding between the MPTS polymerised network and the surface of the HA powder particles cannot be confirmed. It can be speculated that there is a chemical interaction between the MPTS Si-O groups and the OH^- surface groups via weak hydrogen bonding to an extent defined by the availability of both the OH^- groups on the HA surface and the Si-O groups of MPTS not already involved in the cross linking of the MPTS gel. This is supported by the observations of OH^- peak shifting at pH 4 and 6 where cross linking of MPTS was not favoured and therefore increasing the probability of MPTS interacting with the HA surface. Additionally, the work of Liu *et al.* on hexamethylene diisocyanate functionalisation of HA reported that OH^- do have reactivity towards towards the silane [142]. MPTS-HA interactions may well have occurred during the initial stages of condensation at pH 10, but stopped upon saturation of the available OH^- groups and/or favouring of MPTS self interaction through Si-O-Si bonding. From this point in the reaction onwards, the powder particles would have progressively surrounded by cross linked MPTS and possibly mask the detection of any chemical bonding with the particle surfaces.

7.5.3 Novel antimicrobial coating of calcium phosphate surfaces through thiol modification

The potential of this surface modification method in biomedical application was demonstrated by exploiting the exposed thiol groups as a binding site for the engraftment of a novel antimicrobial peptide. Successful attachment of the antimicrobial peptide was confirmed through fluorescence imaging of the GFP-tagged petted, which revealed bright green fluorescence over the entire field of view on the thiol modified HA surface compared to deposition on unmodified

HA. The slight variation in fluorescence intensity between regions of the image shown in figure 7.5 may have been due to some thiols presenting in an oxidised state, which would prevent further attachment of the peptide unless an intermediate 'reduction' step was introduced, or that some thiols were involved in disulphide crosslinking.

Although the peptide alone was found to be more potent in solution than the gold standard penicillin-streptomycin, it's potency while immobilised on a HA surface was improved in the thiol functionalised treatment group. This correlated with the earlier observations from the epi-fluorescence images implying increased presence of the peptide on thiol modified HA and supports the suggestion that this improved potency was due to greater peptide coverage. Conversely, the peptide on unmodified HA surfaces exhibited a drop in potency shown by the increase in biofilm formation and the lack of fluorescence in the corresponding image in figure 7.6 suggested that this reduced potency was due to decreased peptide coverage. In this case it is likely that the peptide could only bind through weak adsorption and easily washed off of the surface.

7.5.4 Concluding statement

The surface modification method described in Chapter 6 has been developed to enable the modification of HA. The ability of these modified materials to bind an antimicrobial agent has been demonstrated and shown to provide a robust and more effective platform for drug attachment than non-specific adsorption. As a result, this technology provides an alternative strategy to localised drug delivery on and around implant sites with a view to minimising infection and promoting local tissue regeneration.

CHAPTER 8

CONCLUSIONS

8.1 Thiol modification of silicon-substituted hydroxyapatite nanocrystals

8.1.1 Chemical modification enabling tracking in live cells

- Nano crystalline SiHA was prepared using a wet chemical precipitation technique at room temperature without additional thermal treatment. Presentation of thiol functional groups on the surface of SiHA via silane functionalisation was achieved without perceptible change in the bulk composition of the HA or SiHA itself as determined by XRF. Zeta potential measurements showed a change in the surface chemistry of the SiHA particle surface, but not to that of HA subjected to the functionalisation process.

- The presence of MPTS could not be confirmed by FTIR alone as the Si-O-C stretching mode could not be reliably resolved from the phosphate peaks. However, thiols were detected using Ellman's reagent and showed that using the functionalisation method on SiHA produced approximately 10^{-5} moles of thiols per milligram of solid material above the base line measurements for HA and HA-MPTS alone.

- Thiol group modification was visually demonstrated by the detection of fluorescence from fluorescein-5-maleimide specifically bound to the thiol groups of the modified SiHA surface despite extensive washing of the samples, suggesting that the thiol groups were covalently bonded to the SiHA surface via a Si-O-Si surface network.

- This was further demonstrated in the confocal fluorescence and bright field images of

SiHA-MPTS-F5M internalised by MC3T3, where the bright fluorescence allowed the particles to be discriminated from other cellular material with similar morphology. Furthermore, the fluorescent labels remained attached to the particle and photoactive for 24 hours after internalisation and intact and photoactive after 3 months storage at $4\,^{\circ}\mathrm{C}$. This method of functionalisation could allow time course tracking of internalisation of calcium phosphates by various bone cells in order to understand their localisation and fate during bone formation and resorption.

8.1.2 Cellular processing and fate of internalised material: An initial semi-quantitative investigation

- Computational processing of the particle/aggregate fluorescence images showed that structures up to 1μm were most prevalent by number within the cells, but sizes of the order of several microns up to 3-4 μm were observed. Of those, only particles of up to 2-3μm were found inside the lysosomes where the material would normally undergo dissolution with the rest remaining in the cytoplasm of the cell. This correlated with the general 2-3μm maximum size of lysosomes.

- An initial study into quantifying material internalised by cells suggested that the fate of the cell upon exposure to SiHA was not solely dependent on the volume/mass of material internalised by the cell and that the size distribution of the internalised material also plays a role. The only observation of pure volume/mass dependence was that none of the lysosomes in any of the cells analysed contained more than 20μm^3 of material, which may represent a 'maximum capacity' for this cell line.

- Particulates measuring more than 1μm (regardless of total internalised volume of material) appeared to be implicated most in determining cell fate. Particulates ranging from a few hundred nm to 3μm, with the majority of all particulates engulfed by lysosomes, appeared to result in 'rounding' of the cells. Any particles larger than 2μm left exposed in the cytoplasm results in a dramatic increase in lysosome recruitment in terms of both

number and convergence around these structures and nucleus. Particles larger than 1μm left exposed inside the cell were found to result in the onset of cellular detachment from the culture dish.

8.2 Formation of calcium phosphate-based matrices through silane crosslinking

8.2.1 HA-MPTS matrix formation, cross linking chemistry and basic handling properties

- A pliable CaP-based material can be formed by adding HA powder particles to a 3% (v/v) solution of hydrolysed MPTS at pH 4-5 and condensing the MPTS to form polymer chains around the particles by increasing the reaction pH to 10. The resulting monolith then referred to as a HA-MPTS or HA-silane Matrix.

- Adjustment of the pH post-hydrolysis is critical to the formation of the material. Leaving the pH at 4 results in powdered product with some attachment of the MPTS to the surface rather than a single body of material.

- The cross linking of the MPTS primarily occurred through covalent Si-O-Si bonding, while in principle the -SH functional groups are made available for the potential further attachment of biomolecules e.g. thiol-reactive fluorescent dye or homo/hetero-bifunctional cross linking agent. A proportion of at the -SH groups were found to have formed S-S bridges between polymer chains to serve as a secondary mode of cross linking. This is supported by the Raman analysis which suggested high disorder in the orientation and bending of the propyl chains of the MPTS molecules.

- The ability to form S-S cross linking within this matrix provides an interesting alternative direction for the development of the HA-MPTS matrix. S-S bonds are proteolytically cleaved *in vivo* which opens the possibility of producing a material which degrades under

very specific physiological conditions i.e in the presence of particular enzymes or chemical compounds in addition to a particular pH or pH range. Such a mechanism could also be exploited for drug release.

- Defects in the cross linked MPTS network arose from incomplete hydrolysis of MPTS molecules. This could have occurred either in the form of residual pure MPTS (with all three methoxy groups intact) or partially hydrolysed MPTS (where only one or two out of the three methoxy groups were hydrolysed). These defects prevented further attachment of MPTS monomers to the MPTS polymer chain, hence chain length is modulated by the hydrolysis process. The need to develop the hydrolysis step in order to remove or process pure and/or partially hydrolysed MPTS remaining in the matrix was highlighted.

- The exact nature of the chemical binding or interaction between the cross linked MPTS and the HA particles could not be fully determined. Shifting of the OH^- Raman peak together with other studies of silane-hydroxyl interactions suggest the interaction at least involved hydrogen bonding. P-O-Si (P-OH of the HA reacting with the OH-Si from the silane) is an alternative bonding mechanism, but may have been masked by the 3D optically opaque nature of the sample preventing confocal Raman spectroscopy below the surface.

- The HA-MPTS matrix deformed plastically and could be cut under compression by hand with a spatula. No mass loss or fragments from the HA-MPTS matrix were observed from a degradation study in water over two weeks. However, a full degradation study under different solvent conditions along with mechanical testing would be required to provide a more comprehensive characterisation of the material before assessing its potential as a bone defect filler.

- The ability to form this organic-inorganic matrix with exposed thiol groups opens the possibility of drug attachment and release through volume rather than restriction to a surface. Using either of the cross linking modes described, this finding is important as a potential degradation mechanism of drug-loaded capsules within the body.

8.2.2 Attachment of novel antimicrobial peptides to CaP surfaces modified by MPTS cross linking

- The potential of this surface modification method in biomedical application was demonstrated by exploiting the exposed thiol groups as a binding site for the engraftment of a novel antimicrobial peptide. The application proposed to remove the reliance on adsorption of such drugs on to implant surfaces using methods such as dip coating or electrospraying.

- Qualitative analysis of the surface coverage of the antimicrobial peptide through GFP-tagging showed that thiol modification enabled a higher amount of the peptide to bind to the surface over the entire field of view. The attachment was robust through persistent washing steps. In contrast, little of the GFP-tagged antimicrobial peptide was seen on the non-functionalised surface which relied upon adsorption.

- The variation in the intensity in parts of the epi-fluorescence image of HA-Thiol-Peptide may have reflected variations in the availability of free thiol groups on the surface. Possible explanations include: i) S-S bonding had occurred between pairs of thiol groups, which prevented them from forming a complex with the peptide, ii) The thiol group(s) were in an oxidised state due to prolonged exposure in air, which would also render them unable to bind with the peptide or, iii) there some variation in the coverage of the MPTS network on the pellet surface. Premature and unwanted reactions of the thiol groups could be prevented by the addition of a washing step with a reducing agent, e.g. Dithiolthreitol (DTT), immediately prior to attachment of the peptide.

- The potency of the antimicrobial agent against G1 Pseudomomas Aeruginosa bacterial strain was improved while attached to the thiol modified pellets compared to non-functionalised pellets. Most notably the ability of the peptide to completely prevent biofilm formation was maintained upon attachment on thiol-functionalised pellets compared to non-functionalised pellets.

CHAPTER 9

FUTURE WORK

9.1 Thiol modification of silicon-substituted hydroxyapatite nanocrystals

9.1.1 Developing our understanding of cellular interactions with CaP nano- and micro- particles

- Live/dead assay cannot be used to determine the method of cell death or stage of apoptosis. The assay does not allow for the discrimination between cells at various stages of apoptosis, which would ultimately lead to obvious cell death. Furthermore, the ingression of the red dye may well result from physical injury of the cell membrane. Alternative methods include Annexin V conjugates that bind to phopsphatidyserines which have undergone translocation from the inner to the outer membrane during the intermediate stages of apoptosis. Measurement of Caspase activity may also report early stages of cellular apoptosis.

- The mechanism of cellular uptake of any functionalised CaP could be determined by process of elimination between the various internalisation pathways. For example, the commercially available inhibitor 'Dynasore' inhibits the endocytic pathway. Also, early and late endosome markers would allow tracking from a much earlier stage of internalisation.

- Attempts should be made to detect (or imply the presence of) Ca^{2+} and PO_4^{3-} ions released from the degrading CaP material either completely engulfed or partially covered by lysosomes. The Ca^{2+} ion concentration can be spatially resolved around cells through the

use of Fura2, which preferentially binds to free Ca^{2+} ions with the fluorescence intensity proportional to the ion concentration. Ca^{2+} is ubiquitous in animal cells and implicated in cell signalling pathways including those responsible for apoptosis. Colocalisation of Ca^{2+} intensity spikes with the remnants of the internalised material within the lysosomes would enable quantification and tracking of the degradation products that were not detectable within the confocal imaging work carried out within this thesis. This would have been particularly useful during the cases within this work where lysosomes appeared to burst out in to the cytoplasm. If future work were to prove that release of Ca^{2+} ions into the cytoplasm occurred, then one could speculate that the degradation products from the internalised material interferes with (or triggers) the apoptosis signalling pathway given that cellular detachment has been observed.

9.1.2 Exploring the potential of HA-Silane matrices as an implant material/coating

- The mechanical properties of any CaP-silane combination matrix needs to be quantified so that proper comparisons can be drawn to similar properties of human tissues and their current biomaterial replacements. Although the CaP and silane concentrations used for the matrix in this thesis do not appear to make the material a good load bearing material, other concentrations and types of CaP be could tested. It would also be of interest to test the shear properties of this material as there is great interest in the development of cartilage replacement biomaterials.

- The degradation rate of any bone replacement or defect filler is of great importance in order to allow the body to replace the material with natural tissue. To that end, tuning of the degradation profile in response to its chemical environment or enzymatic/cellular interactions could be controlled through the inclusion of carbonates in apatites. The apatite component would potentially offer the best load bearing capability upon implantation, while the carbonate would increase its solubility (given that HA is generally considered

to take too long to degrade *in vivo*).

- In order to pursue potential bone replacement (both load and non-load bearing) applications, the formulation of the CaP-silane matrix could perhaps include additional polymers already established in bone replacement products such as polyglycolic acid and semi-crystalline thermoplastics.

- The crosslinking of the silane needs to occur in a controlled an repeatable manner to in scaling this process to produce grams, or even kilogram, quantities of the material. A robust method of estimating the number of functional groups available on the silane polymer network is required. As discussed in the results, some of the thiol groups intended for use as a coupling agent for biomolecules (such as antimicrobial peptides) were involved in S-S crosslinking. Ellman's reagent involves measuring the absorbance of its reaction products and therefore would not be suitable in a 3D optically opaque sample such as a HA-silane matrix. Such a method will be important in verifying that correct modes of cross linking are present throughout the material and that the functional groups are in a reduced state ready for further biomolecule attachment. Raman spectroscopy may still be suitable provided the material was compressed to a thin layer.

- Production of CaP-silane matrices could be expanded to included variations of the functional besides thiols - e.g. amines, carboxylic acids etc or even a combination of several different dilates with different functional groups. These alternative functional groups equally suitable for the selective attachment of peptides and fluorescent dyes, but may not provide a secondary unwanted source of crosslinking while forming the matrix. However, the choice of functionalisation should consider the practical aspects behind handling and processing the particular silane. Some silanes are very sensitive to ambient air environments and require processing under vacuum for the duration of the modification process. Such specialist requirements for the synthesis of the matrix may not be viable for scale up.

9.1.3 Understanding the precise role of silicon/silicates in Si-substituted apatite-biomolecule/cell interactions

- The role of silicon in osteogenesis, bone matrix formation and osteoblast differentiation has been widely reported and has led to extensive work on incorporating silicon into or on CaP-based implants to promote fast tissue regeneration. However, it was clear whilst undertaking the work described within this thesis on SiHA, that there is no general understanding of the precise role of silicon in the biochemical processes involved in tissue regeneration. Does silicon directly enhance cellular attachment to Si-substituted CaPs through chemical interaction with cells? Or does Si influence the surface topography/chemistry of CaP material which in turn modulates cellular attachment? (and therefore plays an indirect role). While investigating this issue is perhaps beyond the immediate scope of future work from this thesis, attention should be paid to other future works presenting new insights on the importance and role of ion substitutes in CaPs with respect to tissue regeneration. These findings may then highlight what CaPs or ion substituted CaPs would be most beneficial as the solid phase in the CaP-silane matrix. Furthermore, efforts to optimise ion concentration for bulk material strength along with 'ideal' degradation and tissue regenerative properties can be focused accordingly.

9.2 Formation of calcium phosphate-based matrices through silane crosslinking

- The effect of the CaP powder particle size and morphology on the bulk mechanical properties of the CaP-silane matrices should be investigated. Similar to cements, the particle size and morphology will dictate the volume of the intercies between the particles and the ease in which the silane polymer chains can infiltrate these areas and form the gel phase. Knowledge of the accessibility of these inter-particle volumes would be useful in developing the protocol for washing out unreacted and hydrolysing partially cross linking silanes. One approach could include measurements of specific surface area of the matrix.

Binding of the silane gel across a number of particles in close proximity would prevent access to the space between particles and hence a decrease in the specific surface area would be observed.

- Studies of silane coating of metal surfaces revealed that surface roughness had no effect on the chemical attachment of the silanes [176]. However, silanes have been shown to exhibit preferential binding to edge defect sites of clay minerals [149] and do not coat the particle surface itself. This suggests that surface chemistry may influence silane attachment and crosslinking more than macroscopic surface properties such as roughness. Future studies into the precise nature of silane-CaP bonding could be obtained through NMR experiments, which have already been used to understand silane hydrolysis.

- Fundamentally there is a need to improve the understanding of, and control over, the hydrolysis process. Although numerous studies have been carried out on the hydrolysis and condensation dynamics of silane monolayers, there is no literature exploring this dynamic at relatively high silane concentrations (>2% v/v) while in a 3D conformation such as a gel or gel-particle system. In such a system, future studies will need to monitor the hydrolysis and condensation state of the silane in correlation with particle size and morphology which would dictate the accessibility of the material to liquid. An optimum hydrolysis pH should then be determined that maximises conversion of silane from pure to hydrolysed form within a period of a few hours, in order to reduce the reliance on a washing step to remove unwanted unreacted silane.

- The issues surrounding characterising and processing unreacted silanes located deep within the volume of the bulk material could be circumvented by forming CaP-silane 'sheets' as a building block for forming 3D structures. 'Ladder' and 'Cube' silanes with long range order in the x,y plane are reported to have good thermal stability and physiological inertness [181, 182]. A material in sheet form should in principle yield much higher accessibility to the crosslinked silane molecules and thus reduce the need for extensive washing of unreacted material. In addition, the thin form of the material avoids the previously de-

scribed difficulty in acquiring depth resolved composition and bonding information with optical opaque materials. Multiple CaP-silane sheets could then be stacked to form 3D structures.

- There is potential for the S-S cross-linking detected in the matrices formed in this work to be used as the main mode of cross-linking of CaP-silane matrices. S-S bonds can be degraded within the reducing intracellular environment or through enzyme assisted cleavage and therefore act as a drug release mechanism. The principle has been demonstrated on thin films and microcapsules by Zelikin *et al.* which employed transferrin as a model drug [183, 184].

APPENDIX A

PUBLICATION OF THIOL MODIFICATION, CELLULAR INTERNALISATION AND LIVE CELL IMAGING OF SIHA WORK FROM RESULTS CHAPTER 1

Journal of Materials Chemistry B

Materials for biology and medicine

www.rsc.org/MaterialsB

Volume 1 | Number 35 | 21 September 2013 | Pages 4351–4522

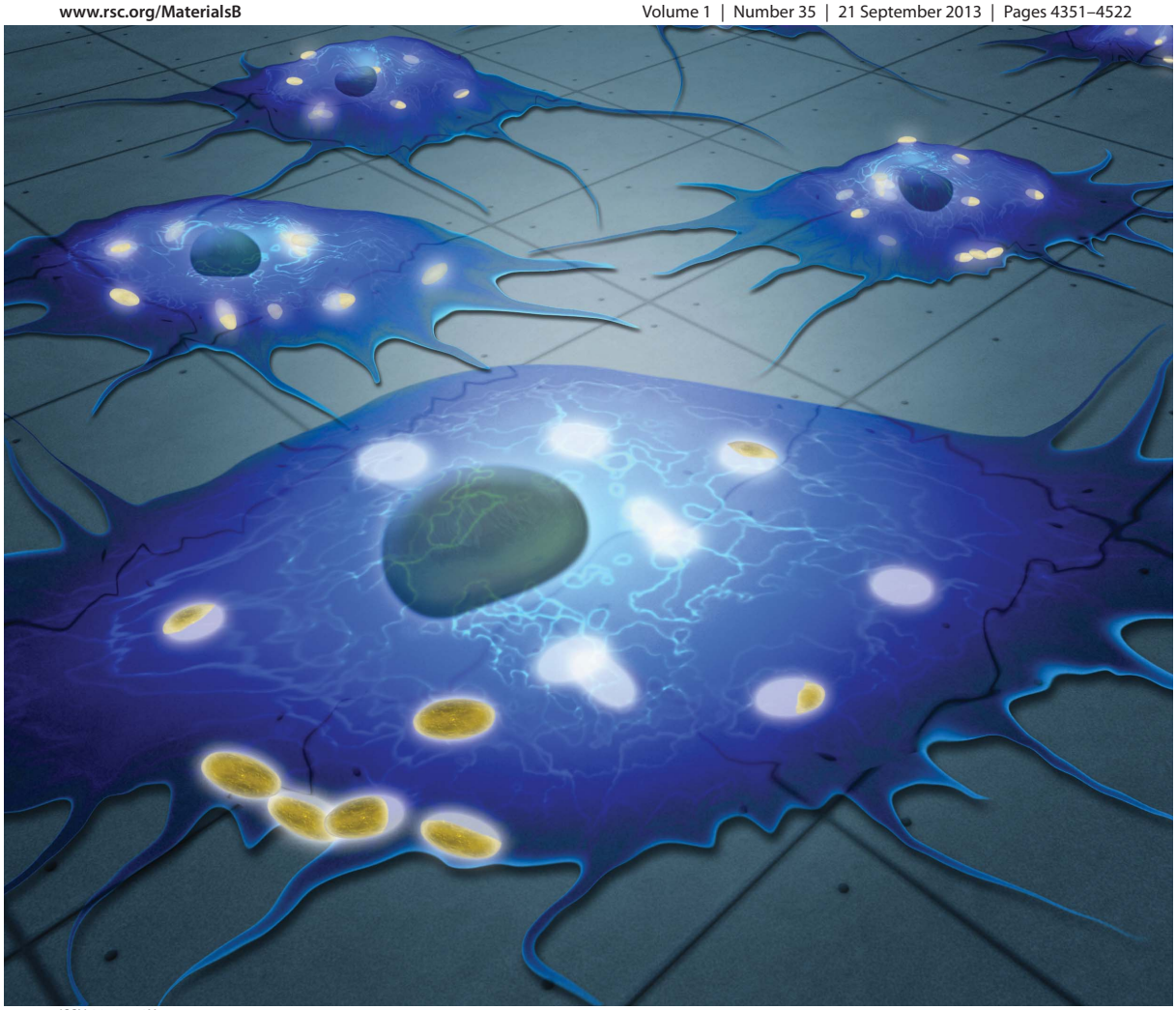

ISSN 2050-750X

RSC Publishing

PAPER

Liam M. Grover *et al.*

Thiol modification of silicon-substituted hydroxyapatite nanocrystals facilitates fluorescent labelling and visualisation of cellular internalisation

2050-750X(2013)1:35;1-R

Journal of
Materials Chemistry B

RSC Publishing

PAPER

View Article Online
View Journal | View Issue

Open Access Article. Published on 22 July 2013. Downloaded on 14/08/2013 16:02:30.
This article is licensed under a Creative Commons Attribution 3.0 Unported Licence.

Cite this: *J. Mater. Chem. B*, 2013, **1**, 4370

Thiol modification of silicon-substituted hydroxyapatite nanocrystals facilitates fluorescent labelling and visualisation of cellular internalisation†

Richard L. Williams,[ab] Martin J. Hadley,[b] Peih Jeng Jiang,[b] Neil A. Rowson,[b] Paula M. Mendes,[b] Joshua Z. Rappoport[c] and Liam M. Grover*[b]

Received 1st June 2013
Accepted 19th July 2013

DOI: 10.1039/c3tb20775g

www.rsc.org/MaterialsB

Calcium phosphates are used widely as orthopaedic implants and in nanocrystalline form to enable the transfer of genetic material into cells. Despite widespread use, little is known about their fate after they have crossed the cell membrane. Here we present a method of surface modification of silicon-substituted hydroxyapatite (SiHA) through a silane group, which enables the engraftment of a fluorescent dye to facilitate real-time biological tracking. Surface modification of the nanocrystal surface was undertaken using (3-mercaptopropyl)trimethoxysilane (MPTS), which presented a thiol for the further attachment of a fluorophore. Successful modification of the surface was demonstrated using zeta potential measurements and fluorescence microscopy and the number of thiol groups at the surface was quantified using Ellman's reagent. *In vitro* experiments using the fluorescently modified particles enabled the discrimination of the calcium phosphate particulate from other biological debris following internalisation by a population of MC3T3 (pre-osteoblast) cells and the particles were shown to maintain fluorescence for 24 hours without quenching. The successful modification of the surface of SiHA with thiol groups offers the tantalising possibility of the intracellular growth factor delivery.

1 Introduction

Calcium phosphate ceramics such as hydroxyapatite (HA) have been used widely for the restoration of function in diseased and damaged hard tissue. In addition, they have found application in a diverse selection of sectors as food additives, adsorbents in chromatography columns and even as substrates to enable absorption of pollutants from wastewater.[1,2] Within the biomedical sector, calcium phosphate salts have been used principally because of their similarity to the mineral component of bone and also since their dissolution products are non-toxic. Relatively recent work has seen calcium phosphate salts used for the delivery of biological materials into cells in the form of peptides, polymers and DNA sequences.[3–8] Calcium phosphate salts have a critical safety advantage over other vectors such as viruses in that they pose no risk of pathogenicity due to mutation. Although it is known that calcium phosphate–DNA complexes cause no apparent cytotoxicity, the fate of the particles upon internalisation is not yet known. The difficulty in tracking the particles can be related to the visual similarity to granulation within the cells.

The large crystal lattice of the apatites means that their structure may incorporate numerous substitutions, which can be used to tailor material chemistry to induce a particular biological reaction.[9–12] One main focus of research into the development of new calcium phosphate based materials has been the substitution of silicon into the hydroxyapatite lattice (SiHA) to enable additional biomolecule attachment and controlled release *in vivo*. Silicon substitution is of particular interest since silicon is well established to be an important factor in the production of new bone matrix and functions to assist in the production of collagen by osteoblasts.[12–15] Calcium phosphate composites have been used widely as implant materials due to the low toxicity of their ionic components and the intimate bond that they are able to form with a wide range of hard and soft tissues. There have been proposed to be two sites in crystalline HA that may be exploited for functionalisation; a hydroxyl group and the phosphate group.[16–18] Previous studies have shown that the surface hydroxyl (OH) groups of HA may react with organic isocyanate groups and this has been exploited for the attachment of polymers such as poly(ethylene glycol) (PEG), poly(methyl methacrylate) (PMMA), poly(*n*-butyl methacrylate) (PBMA), poly(2-hydroxyethyl methacrylate) (poly(HEMA)) to the crystal surfaces.[19,20] In addition, it has been found that substitution by alkylphosphonates causes calcium

[a]*The Physical Sciences of Imaging in the Biomedical Sciences (PSIBS) Doctoral Training Centre, University of Birmingham, Birmingham, UK*

[b]*The School of Chemical Engineering, University of Birmingham, Birmingham, UK. E-mail: l.m.grover@bham.ac.uk*

[c]*The School of Biosciences, University of Birmingham, Birmingham, UK*

† Electronic supplementary information (ESI) available: Movie of confocal *z*-stack used in Fig. 6, S1: epi-fluorescence images from the live/dead assay of SiHA-MPTS-F5M, and Fig. S2: fluorescence spectrum of SiHA-MPTS-F5M inside MC3T3 cells. See DOI: 10.1039/c3tb20775g

This journal is © The Royal Society of Chemistry 2013

Open Access Article. Published on 22 July 2013. Downloaded on 14/08/2013 16:02:30.
This article is licensed under a Creative Commons Attribution 3.0 Unported Licence.

phosphate monolith structures to become mesoporous with high specific surface area,[21] which is of course crucial for biological applications where cell attachment, proliferation, bioresorbability, and tissue/interface regeneration rely on materials with specific surface areas approaching that of native biomineral. Of these reagents containing hydroxyl groups, phosphoric acid based reactants are favoured because the P–OH groups facilitate the adsorption of proteins, as demonstrated for the model protein, bovine serum albumin.[22] However, the limited availability and reactivity of OH groups can result in low numbers of biomolecules being grafted on to the HA surface.[7,23] The Ca^{2+} ions in calcium phosphates, including HA, have been exploited for the ionic bonding of various functional groups. For example, Lee *et al.*[7] have reported the thiol modification of HA using 3-mercaptopropionic acid and Ganesan *et al.*[8] attached porphyrins to the HA surface as a potential drug carrier. Silicon substitution has drawn much attention as a route to surface modification[24] with organosilanes, particularly those containing amino or thiol terminal groups. For example, previous work has demonstrated that osteoblast adhesion to HA is increased when functionalised with 3-aminopropyltriethoxysilane.[25] Although much attention has been given to the use of (3-mercaptopropyl)trimethoxysilane (MPTS) for the surface modification of silicon oxide,[26–28] there is scarcely any research on the surface modification of calcium phosphates with MPTS.

Here we report a new method for the surface modification of SiHA nanoparticles that enables the engraftment of fluorescent markers onto the surface of the nano particulate. The method involves the functionalisation of SiHA nano particles with the silane MPTS *via* covalent bonding, which in turn presents a thiol functional group from the particle surface. The influence of the modification method on the physicochemical properties of the material were determined using X-ray diffraction (XRD), X-ray fluorescence (XRF), Zeta potential (ZP) measurement, and Fourier Transform Infra-red Spectroscopy (FTIR). The surface modification of the SiHA particles was evaluated by the attachment of the commercially available thiol reactive probe fluorescein-5-maleimide (Fig. 1) and demonstrated by live cell confocal fluorescence imaging of the particles after internalisation by MC3T3 cells.

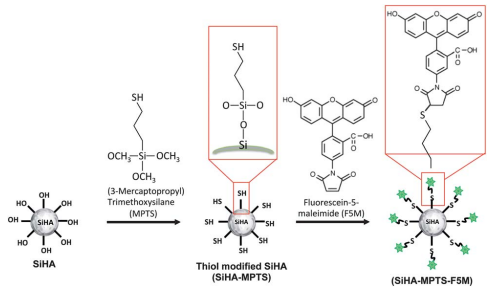

Fig. 1 Schematic diagram of the thiol functionalisation process of SiHA using MTPS and the subsequent labelling with fluorescein-5-maleimide (F5M).

2 Experimental

2.1 HA/SiHA synthesis, functionalisation and dye labelling

HA and SiHA synthesis: HA was synthesised by a wet chemical precipitation method. A 250 mL solution of $(NH_4)_2HPO_4$ (239 mM) and a 350 mL solution of $(CaNO_3)_2 \cdot 4H_2O$ (264 mM) were prepared with Millipore water, which was pre-boiled under reflux for 2 hours to remove CO_2 and cooled to room temperature. The $(CaNO_3)_2 \cdot 4H_2O$ was transferred to a closed glass reaction vessel during magnetic stirring at 200 rpm and nitrogen bubbling. The pH of the solution was adjusted to 10 by the addition of NH_4OH. The $(NH_4)_2HPO_4$ solution was added to the reaction vessel drop wise by burette, while maintaining the pH of the reaction at 10 by addition of NH_4OH, then left to age overnight. The resulting HA precipitate was washed 5 times with Millipore water by centrifugation at 4000 rpm for 10 minutes and resuspended in water for later use at a concentration of approximately 10 mg mL^{-1}. SiHA was synthesised using the method outlined above, but with a 250 mL aqueous solution of $Si(OCOCH_3)_4$ (41 mM) and $(NH_4)_2HPO_4$ (203 mM) added drop wise to a 350 mL aqueous solution of $(CaNO_3)_2 \cdot 4H_2O$ (290 mM). *Attachment of thiol functional groups via MPTS*: 230 mg of HA/SiHA in double distilled water was centrifuged at 4000 rpm for 10 min and the supernatant removed. The particles were then resuspended in 16.4 mL of absolute ethanol filtered with a 0.22 μm pore size syringe filter before adding 100 μL of 3-mercaptopropyltrimethoxysilane (MPTS). The samples were mixed using a ThermoMixer (ThermoMixer Comfort, Eppendorf UK Ltd., UK) at 37 °C for 3 hours at a mixing speed of 1000 rpm and then washed 5 times with double distilled water by centrifuging at 4000 rpm for 10 minutes. *Dye labelling with Fluorescein-5-Maleimide (F5M)*: A stock solution of 5.2 mg Fluorescein-5-Maleimide (Life Technologies Ltd, UK) in 1 mL PBS (without Mg^{2+} and Ca^{2+}). 1 mL of MPTS functionalised SiHA/HA (SIHA/HA-MPTS) (approximately 6 mg solid material in water) was centrifuged at 4000 rpm for 10 min. The supernatant was removed and the pellet resuspended in 500 μL of PBS before adding 470 μL of the fluorescein-5-maleimide stock solution and mixed on a ThermoMixer for 2 h at 37 °C. Finally, the SiHA-MPTS-F5M particles were washed twice with absolute ethanol and five times with double distilled water (both filtered beforehand using a 0.2 μm pore size filter). As a control, SiHA particles, without thiol modification, were mixed with fluorescein-5-maleimide using the above method.

2.2 XRD

X-ray diffraction was used to determine the crystalline composition of the samples. HA/SiHA in solution was centrifuged at 4000 rpm for 10 min. The pellet was removed, dried in an oven at 65 °C overnight and ground into a fine powder. XRD patterns of the powder samples were obtained with a X-ray diffractometer (D5000, Bruker Corp. USA.) using the Cu K_α line. Data were collected from $2\theta = 5$ to 60° with a 0.02° step-size and a step time of 0.5 s/°. These as-precipitated samples are referred to as HA and SiHA herein. To allow a better comparison between HA/SiHA and the ICDD reference patterns, a proportion of the

Open Access Article. Published on 22 July 2013. Downloaded on 14/08/2013 16:02:30.
This article is licensed under a Creative Commons Attribution 3.0 Unported Licence.

precipitated materials were sintered at 650 °C prior to XRD analysis. Sintered samples are referred to as HA-650 and SiHA-650 herein.

2.3 TEM

HA and SiHA samples were diluted from 10 mg mL^{-1} to 400 μg mL^{-1} and a 5 μL drop placed on mesh-400 copper TEM grid (Agar Scientific). Samples for TEM were imaged using a JEOL JEM 1200EX microscope with a beam energy of 80 kV.

2.4 XRF

HA and SiHA solution was dried in an incubator set to 85 °C. The elemental composition of each sample was also determined using an X-ray fluorescence spectrometer (S8 TIGER, Bruker Corp., U.S.A). Powder forms of the samples were prepared as described above. 500 mg of the sample powder was mixed with 2.5 grams of wax and pressed into a pellet.

2.5 FTIR

HA, SiHA, HA-MPTS and SiHA-MPTS powders were prepared as previously described and heated overnight at 85 °C to remove moisture prior to analysis. 2 mg of sample powder was mixed with 198 mg of KBr (1%w/w), milled and then pressed into a pellet. FTIR spectra were acquired using a ThermoScientific Nicolette 380 FTIR instrument (ThermoScientific, UK) and represent an average of 64 runs corrected with a background measurement of a 200 mg pure KBr pellet.

2.6 Zeta-potential measurements

HA, SiHA, HA-MPTS and SiHA-MPTS particle dispersions were mixed with 10 mM KCl solution at a concentration of 0.05 mg mL^{-1}. The pH of the sample solutions was adjusted by the addition of 100 mM HCl and 100 mM KOH at 25 °C and left overnight to equilibrate. Zeta potential profiles as a function of cell z-position were collected using a Beckman Coulter Delsa Nano C. At each of the 9 z-positions 10 accumulations were performed repeated over three runs before repeating the whole process with a fresh sample three times. The pH of each sample was checked and recorded immediately before analysis, corrected (if necessary) and recorded again after analysis.

2.7 Quantitating thiol groups of the silane functionalised HA/SiHA

Thiol presentation on the particle surface was quantified based on an assay using 5,5′-dithio-bis-(2-nitrobenzoic acid) (DTNB), also known as Ellman's Reagent, that binds to free –SH groups to form the yellow-coloured product 2-nitro-5-thiobenzoic acid (TNB). The absorbance of the assay solution is proportional to the concentration of free –SH groups in the sample. First, a 'Reaction Buffer' was made consisting of 100 mM $Na(PO)_4$ and 1 mM EDTA in deionised water set to pH 8.0 by drop wise addition of Na(OH). 50 μL of Ellman's reagent solution (4 mg Ellman's reagent in 1 mL Reaction Buffer) was added to 2.50 mL of Reaction Buffer in a centrifuge tube with a separate tube for each sample plus an additional tube for a control sample. 250 μL of the functionalised HA/SiHA particle dispersion was then added to the tube, mixed using vortex mixer and incubated at room temperature for 15 minutes to form an 'assay solution'. For the control, an addition 250 μL of reaction buffer was added to the tube instead of HA/SiHA particle solution. After incubation, 1 mL of the assay solution was transferred to a clean cuvette and the absorbance measured at 412 nm using a spectrophotometer (Cecil CE7500, Buck Scientific, US) zeroed on the control sample. The relationship between molar absorptivity, E (M^{-1} cm^{-1}), and concentration of TNB, c (moles per litre), can be defined as follows:

$$E = \frac{A}{bc} \quad (1)$$

where A = measured absorbance and b = path length of the cuvette in centimetres. The concentration of TNB (and hence concentration of free –SH groups) in the solution in the cuvette was then calculated by solving eqn (1) for c and substituting $b = 1$ cm and $E = 14\,150$ M^{-1} cm^{-1}. The number of moles of –SH groups in the assay solution, m_{assay}, was then calculated using eqn (2):

$$m_{assay}(\text{moles}) = 2.80\ \text{mL} \times \left[c(\text{moles per L}) \times \frac{1\ \text{L}}{1000\ \text{mL}}\right] \quad (2)$$

where the factor '2.80 mL' represents the total volume of the assay solution when 250 μL of sample and 50 μL of Ellman's reagent is added to the 2.5 mL of reaction buffer. Given that the –SH groups were contributed solely by the 250 μL fraction of the assay solution from the addition of the particle solution, the final molar concentration of free –SH groups in the original particle solutions, C_{sample} was determined to be:

$$C_{sample}(\text{moles per litre}) = \frac{m_{assay}(\text{moles})}{0.25\ \text{mL}} \times \frac{1000\ \text{mL}}{1\ \text{L}} \quad (3)$$

2.8 DNA binding to HA, SiHA and SiHA-MPTS

100 μg of particles in solution was mixed with 10, 20, 50, 80 and 100 μg of DNA (31149, Sigma-Aldrich, Dorset, UK) and incubated for 15 minutes at 37 °C. The particle-DNA solutions were then centrifuged and the absorption of the supernatant at 260 nm was measured using a Varian Cary 5000 Spectrophotometer (Agilent Technologies UK Limited, Stockport, UK). The absorbance of the sample was proportional to the amount of DNA not bound to the particle as determined through a calibration curve.

2.9 Live/dead assay

MC3T3 cells seeded on to glass coverslips with 2 mL of supplemented media containing 0.6 μg mL^{-1} of SiHA-MPTS-F5M particles. After 24 hours, 7 μL of Calcein AM and 25 μL of Propidium Iodide solutions in supplemented media to a total volume of 2 mL was added to the cells and incubated at 37 °C for 15 minutes prior to imaging with an epi-fluorescence microscope.

2.10 Uptake of HA/SiHA by MC3T3 osteoblast precursor cells

MC3T3 (passage 10) osteoblast precursor cells were cultured in DMEM (D6545, Sigma-Aldrich, Dorset, UK) supplemented with

This journal is © The Royal Society of Chemistry 2013

Open Access Article. Published on 22 July 2013. Downloaded on 14/08/2013 16:02:30.
This article is licensed under a Creative Commons Attribution 3.0 Unported Licence.

(v/v) 10% Fetal Bovine Serum (A15-105 Mycoplex, PAA, Yeovil, UK), 2.4% Hepes Buffer (H0887, Sigma-Aldrich, Dorset, UK), 2.4% L-Glutamine (G7513, Sigma-Aldrich, Dorset, UK) and 1% Penicillin/Streptomycin (P4333, Sigma-Aldrich, Dorset, UK). The cells were seeded at a density of 3×10^4 cells per quadrant in a 4-segmented live cell imaging dish (code: 627870, Greiner-Bio One Ltd., Gloucester, UK) and incubated overnight at 37 °C in the supplemented media. HA and SiHA in supplemented media was prepared at concentrations of 0 μg mL^{-1} and 300 μg mL^{-1}, mixed using a vortex mixer and sonicated for 5 min before being kept in a water bath at 37 °C until required. After 24 h, the media was removed from each well and replaced with 1 mL of supplemented media before adding 1 mL HA or SiHA-media solutions to each quadrant while gently agitating the dish to ensure even distribution of the particles across the surface. The media was removed 24 hours after exposure to the particles, the cells in each quadrant washed three times with 1 mL PBS and replaced with 1 mL per quadrant of cell imaging media.

Fluorescein stained samples were imaged with a Zeiss LSM 710 ConfoCor 3 confocal system (Carl Zeiss Ltd, U.K.) attached to a Zeiss Axio Observer.Z1 inverted microscope and equipped with a Zeiss EC Plan-Neofluar ×63 NA = 1.40 oil objective lens, 488 nm laser diode, a 458 nm/488 nm beam splitter and a 34-channel spectral detector, which was used to divert fluorescence between 500 nm and 650 nm to a photomultiplier tube detector. Bright field images were obtained simultaneously with the fluorescence images by detecting the transmitted excitation laser light with a second photomultiplier tube detector.

3 Results and discussion

3.1 Structure and composition analysis

X-ray diffraction patterns of as-precipitated HA and SiHA along with HA and SiHA sintered at 650 °C (HA-650 and SiHA-650 respectively) were obtained and are shown in Fig. 2. The broad diffraction peaks of the as-precipitated HA and SiHA samples suggested that they were of low crystallinity and composed of sub-micron sized crystals, which was expected from a room temperature precipitation method without thermal treatment.[17,29,30] Peaks were identified at around 26°, 32°, 40° and between 47 and 53° and appeared to align well with the most intense peaks from reference data for HA (ICDD PDF card no. 00-009-0432). However, it was evident that the broad HA peak at 32° in Fig. 2 was an envelope of the three most intense peaks in the reference pattern data and thus imposing a limit on quality of the match between the measured data and the HA reference. Two shoulder peaks were identified within the main peak of SiHA, but were still poorly resolved. Furthermore, it is known that the XRD patterns of various apatites could resemble those of as-precipitated HA and therefore an assessment of the chemical/structural changes in sintered samples is required in order to confirm the phase composition and structure of the original as-precipitated samples. Fig. 2 shows the XRD pattern of HA sintered at 650 °C for 2 hours. Dominant peaks were identified at 25.83°, 31.81°, 32.20°, 32.88° and were attributed to the (002), (211), (112) and (300) planes of HA respectively.

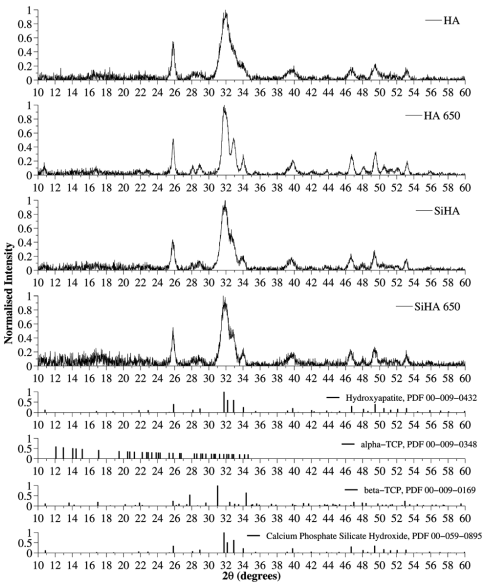

Fig. 2 XRD patterns of as precipitated HA/SiHA and HA/SiHA sintered at 650 degrees (HA 650/SiHA 650) and JCPDS card number 00-009-0432 (Hydroxyapatite). Intensity values of all samples were normalised to the most intense diffraction peak of the HA sample. The broad diffraction peaks suggested the samples were made of nanosized crystals and no other phases of calcium phosphate were detected.

Sharper and more intense peaks were observed in sintered HA (HA 650) compared to as-prepared HA, indicating an increase in the crystallinity of the sample. In contrast, sintering did not increase the crystallinity of SiHA since no change in the sharpness of the diffraction peaks and little or no change in the peak intensity was observed when compared to as-precipitated SiHA. These observations are consistent with other works that have explored the effect of sintering temperature on Si doped HA where the lack of change (or decrease in cases of Si doping above 2–3%wt) in crystallinity has been attributed to Si incorporation into the HA crystal lattice.[13,31,32] Silicon substitution did not appear to change the angular position or relative intensity of the peaks when compared to HA and HA-650. Secondary phases consisting of α-TCP and β-TCP were not observed in the diffraction patterns of the HA or SiHA samples when compared to ICDD reference patterns 00-009-0348 and 00-009-0169 respectively. TCP phases were not detected in HA even after sintering at 900 °C, but SiHA decomposed into a mixture of HA and α-TCP (data not shown). The TEM images of HA and SiHA shown in Fig. 3 displayed the needle like morphology commonly reported with wet chemical precipitation methods.[7,33,34] Additional phases such as α-TCP, β-TCP and $CaCO_3$, which normally have a plate-like morphology, were not observed in either the HA or SiHA samples. The SiHA crystals appeared smaller and their edges were not as clearly defined

Open Access Article. Published on 22 July 2013. Downloaded on 14/08/2013 16:02:30.
This article is licensed under a Creative Commons Attribution 3.0 Unported Licence.

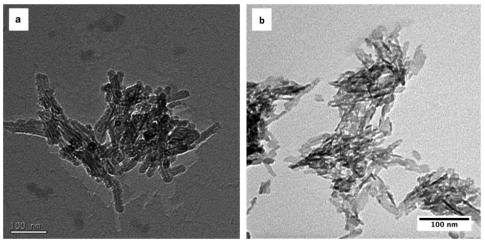

Fig. 3 TEM images of as-precipitated (a) HA and (b) SiHA. Both samples showed the well reported needle-like morphology, but the crystal edges are not as well defined compared to those of HA, indicating reduced crystallinity.

compared with HA which may indicate that the SiHA sample was of lower crystallinity compared to HA. This observation corresponds well with the broad peaks observed for SiHA in the XRD patterns.

XRF was used to determine the %wt of Ca and P oxides and corresponding mole ratios of the elements are presented in Table 1. The Ca : P ratio of the HA sample was 1.64 and compares well with the theoretical Ca : P ratio of HA of 1.67 to within experimental error using this technique. Ca : P ratio of HA-MPTS (1.95) was higher than expected and may have been due to CO_3^{2-} ions substituting the PO_4^{3-} ions in the crystal structure, thus reducing the phosphorous content of the sample and hence increasing the Ca : P ratio.

Fig. 4 shows the FTIR spectra of HA, SiHA along with thiol-terminated silane functionalised HA and SiHA (HA-MPTS and SiHA-MPTS respectively). A summary of the peaks identified from the spectra, along with the chemical bond and mode the peak was assigned to, is presented in Table 2. The characteristic peaks of hydroxyapatite were identified in all of the samples including the OH modes (3569 cm^{-1} and 632 cm^{-1}), the P–O stretching modes (1091, 1044–1032 and 962 cm^{-1}), the O–P–O bending modes (602, 575–561 cm^{-1}) and the O–P–O stretching modes (473, 463–460 cm^{-1}) from the PO_4^{3-} groups. The OH stretching mode at 3569 cm^{-1} was partially obscured by the water band between 2500 and 3800 cm^{-1} as the samples were not sintered prior to FTIR analysis. Evidence of some B-type carbonate substitution was found in both HA and SiHA by the presence of peaks located at 1454 cm^{-1}, 1423 cm^{-1} and 873 cm^{-1}. A peak assigned to the Si–O vibrational mode of the SiO_4^{4-} ions was detected in the SiHA-MPTS sample at around

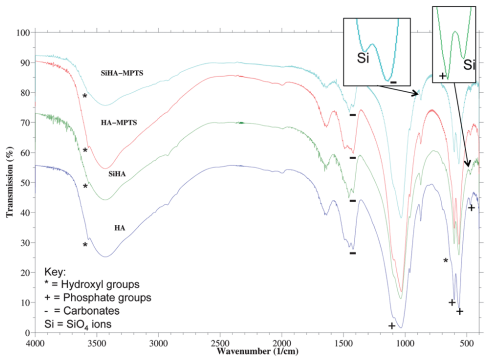

Fig. 4 FTIR spectra of as-precipitated HA and SiHA along with thiol functionalised HA and SiHA (HA-MPTS and SiHA-MPTS respectively).

Table 2 FTIR absorption peaks identified in HA, HA-MPTS, SiHA and SiHA-MPTS along with references to other works which support the peak assignments

Peak (cm^{-1})	Assignment	
Absorption peaks for hydroxyapatite:		
3569	Stretching mode of OH group	17, 31, 36 and 37
1454	ν_4 or ν_3 bending mode of CO_3^{2-} groups in A- and B-type carbonated HA	17, 36 and 38
1423	B-type CO_3^{2-} stretching mode	36
1091, 1044–1032	Triply degenerated asymmetric stretching mode of P–O bond of the PO_4 groups	17, 31, 36, 39 and 40
962	Symmetric stretching mode of the P–O bonds	17, 31, 36, 39 and 40
873	ν_4 or ν_3 bending mode of CO_3^{2-} groups in carbonated HA	36
632	Vibrational mode of OH group	31 and 36
602, 575–561	Triply degenerated O–P–O bending modes	36
473, 463–460	Double degenerated O–P–O bending modes of the PO_4 groups	31 and 36
Absorption peaks for silicates in SiHA:		
880	Si–O vibrational mode of SiO_4^{4-}	39
875	Si–O vibrational mode of SiO_4^{4-}	31 and 38
470	Si–O–Si vibrational mode of SiO_4^{4-}	38
Absorption peaks for MPTS:		
1100	Si–O–C stretching from MPTS	41

Table 1 Ca : P ratios determined from XRF data and zeta potential data for HA, HA-MPTS, SiHA and SiHA-MPTS

Sample	Ca : P ratio	Zeta potential (mV) at pH 7.4
HA	1.64	−1.97
HA-MPTS	1.95	−1.99
SiHA	1.97	−1.66
SiHA-MPTS	1.94	−11.66

875 cm^{-1}. Although the corresponding peak in the SiHA sample was not as well resolved, another SiO_4^{4-} vibrational mode at 470 cm^{-1} SiO_4^{4-} was identified. An additional source of Si–O–Si bonds could have come from the binding of MPTS *via* its O atom to the SiHA surface. This may explain why the peak was most prominent in SiHA-MPTS compared to HA-MPTS as the presence of SiO_4^{4-} on the surface increased the number of

This journal is © The Royal Society of Chemistry 2013

Open Access Article. Published on 22 July 2013. Downloaded on 14/08/2013 16:02:30.
This article is licensed under a Creative Commons Attribution 3.0 Unported Licence.

potential binding sites for MPTS. The difficulty in detected all peaks relating to silicon substitution in both the SiHA and SiHA-MPTS sample could have been due these vibrational modes overlapping with the phosphate modes, which been noted to happen in the following cases: (i) 470 cm^{-1} (Si–O–Si band) and 472 cm^{-1} (the O–P–O bending modes of the phosphate groups) and (ii) 945 cm^{-1} (Si–O symmetric stretching mode) and the weak 962 cm^{-1} (P–O symmetric stretching mode). The translational mode of water associated to HA generally exists between 300 cm^{-1} and 600 cm^{-1}, which would also obscure the peaks within this range related to the presence of SiO_4^{4-}.

Evidence of surface modification was obtained from zeta potential measurements of HA, SiHA, HA-MPTS and SiHA-MPTS at pH 7.4, shown in Table 1. The zeta potential of HA and SiHA was measured to be −1.97 mV and −1.66 mV respectively. Most notably, the zeta potential of SiHA SiHA-MPTS was measured to be −11.66 mV and the change in the zeta potential suggested that this sample exhibited a different surface chemistry to both SiHA and HA. The result compares well with the work of Shyue *et al.* which also reported a decrease in the seat potential due to the presence of thiols.[35] HA-MPTS did not show the same change in zeta-potential as SiHA-MPTS, which may further suggests that either none or significantly less thiol groups were attached to the HA surface in comparison to SiHA-MPTS. The presence of thiol groups was confirmed and quantified using an Ellman's reagent assay. For SiHA-MPTS, the thiol content was estimated to be 1.60×10^{-5} moles per mg of solid material. DNA binding efficiency experiments showed that 100 μg of SiHA-MPTS particles could completely bind up to 10 μg DNA whereas only 85% and 65% of this DNA mass was bound to 100 μg of unfunctionalised SiHA and HA respectively. At higher DNA masses of 50–100 μg, 20% of the DNA was bound to SiHA-MPTS while only 1–10% of the DNA was bound to SiHA and HA.

3.2 Demonstration of application: live cell imaging of SiHA internalisation by MC3T3 cells using a thiol reactive fluorescent probe

Using confocal fluorescence microscopy, unmodified SiHA treated with fluorescein-5-maleimide showed very weak fluorescence (Fig. 5b) in the regions of the image where particles could be seen in bright field (Fig. 5a and c), which demonstrated the effectiveness of the washing procedure in removing non-specifically bound dye molecules. The fluorescence from SiHA modified with MPTS (SiHA-MPTS) shown in Fig. 5e was brighter than the fluorescence from unmodified SiHA. Furthermore, the intensity of the fluorescence was even across the vast majority of the structures shown in Fig. 5d and f. The increased fluorescence intensity was attributed to the proportion of dye molecules bound to the thiols of the SiHA-MPTS since unbound molecules were expected to be removed during the washing procedure.

The images in Fig. 6 are combined confocal fluorescence and brightfield images of MC3T3 cells after a 24 hour exposure to thiol-terminated silane functionalised SiHA particles conjugated to fluorescein-5-maleimide dye (SiHA-MPTS-F5M). Fluorescence could not be clearly seen in the low magnification image (Fig. 6a), which would most likely have been due to the low particle concentration and low numerical aperture of the objective lens used to acquire the image. However, some fluorescence was detected in multiple cells at a higher magnification (Fig. 6b). SiHA-MPTS-F5M was not found to be cytotoxic at a concentration of 0.6 μg mL^{-1} over 24 hours after performing a live-dead assay (Fig. S1†). In Fig. 6(c–e), the SiHA-MPTS-F5M particles appeared to form small aggregates, approximately 500–1000 nm in diameter, which aligned along the cell membrane. These structures could not be removed from the cell membrane despite repeated washing in PBS, indicating a strong affinity for the cell membrane. When focusing on an image plane through the middle of the cell (Fig. 6f–j), bright fluorescence was detected in new locations within the boundary of the cell as shown in the composite image. Furthermore, fluorescence from the few particles on the coverslip could no longer be detected at this new focal plane, demonstrating that any detected fluorescence was not an integration of fluorescence from particles at the bottom of or underneath the cell. Fluorescence spectroscopy of the sample during imaging revealed an emission profile matching that of the dye with an emission peak between 519 and 529 nm (Fig. S2†). The internalised structures measured approximately 400–500 nm in diameter and appeared to localise at various points within the cytoplasm of the MC3T3 cell, but could not determine whether this was the result of either (i) individual particles being internalised and then concentrated within the cell, or (ii) the aggregates being internalised as a whole. However, the localisation and strong intensity of the fluorescence did indicate that the fluorescent labels were still attached to the particle surface and photoactive after 24 hours in culture media and post internalisation. Internalised particles were observed again while focusing up towards the top of the cell.

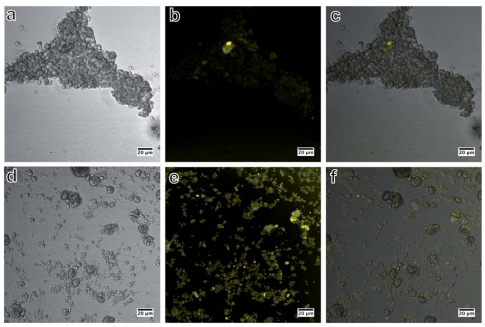

Fig. 5 Bright field, confocal fluorescence and composite images of SiHA exposed to fluorescein-5-maleimide (SiHA-F5M) (a–c) and MPTS functionalised SiHA particles conjugated to fluorescein-5-maleimide dye (SiHA-MPTS-F5M) (d–f); specific binding of fluorescein-5-maleimide to the thiol group of SiHA-MPTS was demonstrated by the even fluorescence across the particulates (d–f) and very weak non-specific fluorescence in the samples not treated with MPTS (a–c).

Open Access Article. Published on 22 July 2013. Downloaded on 14/08/2013 16:02:30.
This article is licensed under a Creative Commons Attribution 3.0 Unported Licence.

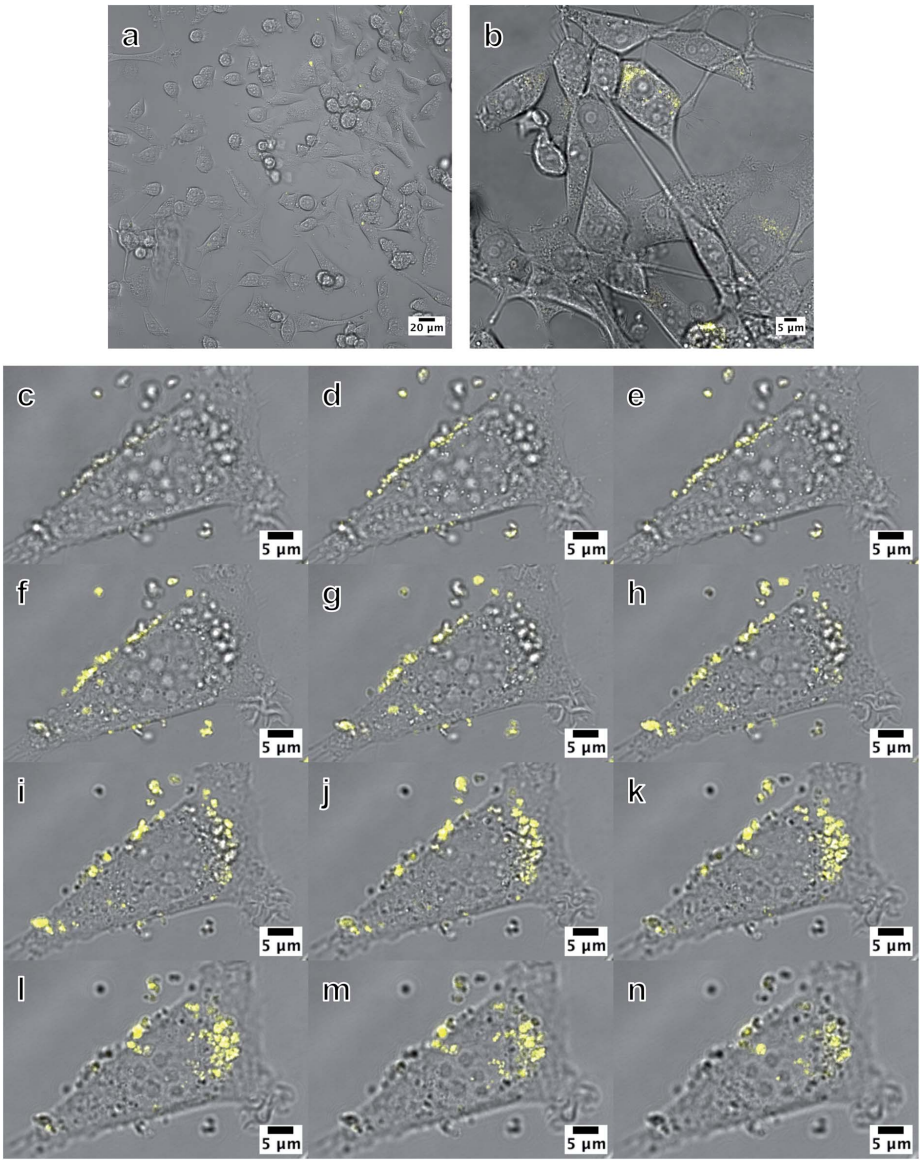

Fig. 6 Combined bright field and fluorescence images of MC3T3 cells exposed to 0.6 μg mL^{-1} SiHA-MPTS-F5M particles. (a) is a low magnification image showing a population of cells and (b) is a higher magnification image where fluorescence was just visible. Images (c)–(n) are slices from a confocal z-stack taken at: the coverslip/bottom of the cell plane (c–e), through the middle of the cell (f–j) and at the top of the cell (k–n). Bright localised fluorescence was observed within the cell and enabled internalised SiHA to be visually discriminated from the other cellular material of similar morphology and optical contrast as shown in the bright field images. The entire z-stack is presented as a movie in Multimedia ESI with the filename: ESI SiHA uptake Fig. 6. Movie.†

This journal is © The Royal Society of Chemistry 2013

Open Access Article. Published on 22 July 2013. Downloaded on 14/08/2013 16:02:30.
This article is licensed under a Creative Commons Attribution 3.0 Unported Licence.

4 Conclusions

In this study, we have prepared nano crystalline SiHA using a wet chemical precipitation technique at room temperature without additional thermal treatment. Presentation of thiol functional groups on the surface of SiHA *via* silane functionalisation was achieved without perceptible change in the chemical composition of the HA or SiHA itself as determined by XRF. Zeta potential measurements showed a significant change in the surface chemistry of the SiHA particle surface, but not that of HA subjected to the functionalisation process. The presence of SiO_4^{4-} in SiHA and SiHA-MPTS was identified by two different Si–O vibrational modes together with the characteristic reduction in the intensity of the OH peak in the FTIR spectra. The presence of MPTS could not be confirmed by FTIR alone as the Si–O–C stretching mode could not be reliably resolved from the phosphate peaks. However, thiols were detected using Ellman's reagent and showed that the using the functionalisation method on SiHA produced approximately 10^{-5} moles of thiols per milligram of solid material above the base line measurements for HA and HA-MPTS alone. Thiol group modification was visually demonstrated by the detection of fluorescence from fluorescein-5-maleimide specifically bound to the thiol groups of the modified SiHA surface despite extensive washing of the samples, suggesting that the thiol groups were covalently bonded to the SiHA surface *via* a Si–O–Si surface network. This was further demonstrated in the confocal fluorescence and bright field images of SiHA-MPTS-F5M internalised by MC3T3, where the bright fluorescence allowed the particles to be discriminated from other cellular material with similar morphology. Furthermore, the fluorescent labels remained attached to the particle and photoactive at for least 24 hours after internalisation. This method of functionalisation could allow time course tracking of internalisation of calcium phosphates by various bone cells in order to understand their localisation and fate during bone formation and resorption.

Acknowledgements

We would like to thank the EPSRC for funding this project (EPSRC ref: EP/F50053X/1), Advantage West Midlands for the provision of the zeta-sizer, Birmingham Advanced Light Microscopy (BALM) facility for access to the confocal microscope, Birmingham Science City for the provision of the XRD and XRF instruments and Dr Alan Smith (School of Applied Sciences, University of Huddersfield, Queensgate, Huddersfield) for the access to an alternative zeta-sizer. We would also like to acknowledge Parastoo Jamshidi (School of Chemical Engineering, University of Birmingham, Birmingham), for her assistance with XRD and XRF measurements; Dr Javier Salado (Inorganic Chemistry, Zientzia eta Teknologia Fakultatea, UPV/EHU, 644 Postakutxa, 48080, Bilbo); Laura Rowley (PSIBS, University of Birmingham, Birmingham.) for the loan of the heating mantle and their involvement in technical discussions; and Dr. James Bowen (School of Chemical Engineering, University of Birmingham, Birmingham), for his technical support.

References

1 E. Landi, L. Orlandi, G. Spagna, A. Tampieri and N. Zaffaroni, *Key Eng. Mater.*, 2000, **192**, 901–904.
2 A. Nzihou and P. Sharrock, *Waste Biomass Valoriz.*, 2010, **1**, 163–174.
3 V. Sokolova, A. Kovtun, O. Prymak, W. Meyer-Zaika, E. A. Kubareva, E. A. Romanova, T. S. Oretskaya, R. Heumann and M. Epple, *J. Mater. Chem.*, 2006, **17**, 721–727.
4 C. Ribeiro, C. Barrias and M. Barbosa, *Biomaterials*, 2004, **25**, 4363–4373.
5 S. J. Kalita, A. Bhardwaj and H. A. Bhatt, *Mater. Sci. Eng., C*, 2007, **27**, 441–449.
6 J. Klesing, S. Chernousova and M. Epple, *J. Mater. Chem.*, 2012, **22**, 199–204.
7 S. C. Lee, H. W. Choi, H. J. Lee, K. J. Kim, J. H. Chang, S. Y. Kim, J. Choi, K.-S. Oh and Y.-K. Jeong, *J. Mater. Chem.*, 2007, **17**, 174–180.
8 K. Ganesan, A. Kovtun, S. Neumann, R. Heumann and M. Epple, *J. Mater. Chem.*, 2008, **18**, 3655–3661.
9 T. White, C. Ferraris, J. Kim and S. Madhavi, *Rev. Mineral. Geochem.*, 2005, **57**, 307–401.
10 N. Rameshbabu, T. Sampath Kumar, T. Prabhakar, V. Sastry, K. Murty and K. Prasad Rao, *J. Biomed. Mater. Res., Part A*, 2007, **80A**, 581–591.
11 A. Bigi, E. Boanini, C. Capuccini and M. Gazzano, *Inorg. Chim. Acta*, 2007, **360**, 1009–1016.
12 E. S. Thian, J. Huang, S. M. Best, Z. H. Barber, R. A. Brooks, N. Rushton and W. Bonfield, *Biomaterials*, 2006, **27**, 2692–2698.
13 A. M. Pietak, J. W. Reid, M. J. Stott and M. Sayer, *Biomaterials*, 2007, **28**, 4023–4032.
14 M. Shie, H. Chang and S. Ding, *Int. Endod. J.*, 2012, **45**, 337–345.
15 M. Vallet-Regí and D. Arcos, *J. Mater. Chem.*, 2005, **15**, 1509–1516.
16 H. J. Lee, S. E. Kim, H. W. Choi, C. W. Kim, K. J. Kim and S. C. Lee, *Eur. Polym. J.*, 2007, **43**, 1602–1608.
17 I. Gibson, S. Best and W. Bonfield, *J. Biomed. Mater. Res.*, 1999, **44**, 422–428.
18 D. Arcos, J. Rodrıguez-Carvajal and M. Vallet-Regí, *Solid State Sci.*, 2004, **6**, 987–994.
19 J. Engstrand, A. López, H. Engqvist and C. Persson, *Biomed. Mater.*, 2012, **7**, 035013.
20 B. M. Barth, R. Sharma, E. İ. Altınoğlu, T. T. Morgan, S. S. Shanmugavelandy, J. M. Kaiser, C. McGovern, G. L. Matters, J. P. Smith, M. Kester, *et al.*, *ACS Nano*, 2010, **4**, 1279–1287.
21 A. Bahdod, S. El Asri, A. Saoiabi, T. Coradin and A. Laghzizil, *Water Res.*, 2009, **43**, 313–318.
22 K. Kandori, S. Oda, M. Fukusumi and Y. Morisada, *Colloids Surf., B*, 2009, **73**, 140–145.
23 X. Qiu, Z. Hong, J. Hu, L. Chen, X. Chen and X. Jing, *Biomacromolecules*, 2005, **6**, 1193–1199.
24 K. Duan and R. Wang, *J. Mater. Chem.*, 2006, **16**, 2309–2321.

Open Access Article. Published on 22 July 2013. Downloaded on 14/08/2013 16:02:30.
This article is licensed under a Creative Commons Attribution 3.0 Unported Licence.

25 M. Nelson, G. Balasundaram and T. J. Webster, *Int. J. Nanomed.*, 2006, **1**, 339.
26 N. D. Meeks, S. Rankin and D. Bhattacharyya, *Ind. Eng. Chem. Res.*, 2010, **49**, 4687–4693.
27 A. Wani, E. Muthuswamy, G. H. L. Savithra, G. Mao, S. Brock and D. Oupickỳ, *Pharm. Res.*, 2012, 1–12.
28 S. B. Hartono, S. Z. Qiao, J. Liu, K. Jack, B. P. Ladewig, Z. Hao and G. Q. M. Lu, *J. Phys. Chem. C*, 2010, **114**, 8353–8362.
29 I. Mobasherpour, M. S. Heshajin, A. Kazemzadeh and M. Zakeri, *J. Alloys Compd.*, 2007, **430**, 330–333.
30 M. H. Santos, M. d. Oliveira, L. P. d. F. Souza, H. S. Mansur and W. L. Vasconcelos, *Mater. Res.*, 2004, **7**, 625–630.
31 Z. Qiu, G. Li, Y. Zhang, J. Liu, W. Hu, J. Ma and S. Zhang, *Biomed. Mater.*, 2012, **7**, 045009.
32 E. Thian, J. Huang, M. Vickers, S. Best, Z. Barber and W. Bonfield, *J. Mater. Sci.*, 2006, **41**, 709–717.
33 E. Bouyer, F. Gitzhofer and M. Boulos, *J. Mater. Sci.: Mater. Med.*, 2000, **11**, 523–531.
34 V. Uskoković and D. P. Uskoković, *J. Biomed. Mater. Res., Part B*, 2011, **96**, 152–191.
35 J.-J. Shyue, M. R. De Guire, T. Nakanishi, Y. Masuda, K. Koumoto and C. N. Sukenik, *Langmuir*, 2004, **20**, 8693–8698.
36 S. Koutsopoulos, *J. Biomed. Mater. Res.*, 2002, **62**, 600–612.
37 S. Sprio, A. Tampieri, E. Landi, M. Sandri, S. Martorana, G. Celotti and G. Logroscino, *Mater. Sci. Eng., C*, 2008, **28**, 179–187.
38 A. Bianco, I. Cacciotti, M. Lombardi and L. Montanaro, *Mater. Res. Bull.*, 2009, **44**, 345–354.
39 T. Tian, D. Jiang, J. Zhang and Q. Lin, *Mater. Sci. Eng., C*, 2008, **28**, 57–63.
40 J. Vandiver, D. Dean, N. Patel, C. Botelho, S. Best, J. D. Santos, M. A. Lopes, W. Bonfield and C. Ortiz, *J. Biomed. Mater. Res., Part A*, 2006, **78A**, 352–363.
41 C. Wu, T. Xu and W. Yang, *J. Membr. Sci.*, 2003, **224**, 117–125.

This journal is © The Royal Society of Chemistry 2013

LIST OF REFERENCES

[1] E Landi, L Orlandi, G Spagna, A Tampieri, and N Zaffaroni. Calcium phosphate ceramics as drug-delivery system for anticancer therapy. *Key Engineering Materials*, 192:901–904, 2000.

[2] A Nzihou and P Sharrock. Role of phosphate in the remediation and reuse of heavy metal polluted wastes and sites. *Waste and Biomass Valorization*, 1(1):163–174, 2010.

[3] V Sokolova, A Kovtun, O Prymak, W Meyer-Zaika, E A Kubareva, E A Romanova, T S Oretskaya, R Heumann, and M Epple. Functionalisation of calcium phosphate nanoparticles by oligonucleotides and their application for gene silencing. *J. Mater. Chem.*, 17(8):721–727, 2006.

[4] C C Ribeiro, C C Barrias, and M A Barbosa. Calcium phosphate-alginate microspheres as enzyme delivery matrices. *Biomaterials*, 25(18):4363–4373, 2004.

[5] S J Kalita, A Bhardwaj, and H A Bhatt. Nanocrystalline calcium phosphate ceramics in biomedical engineering. *Materials Science and Engineering: C*, 27(3):441–449, 2007.

[6] J Klesing, S Chernousova, and M Epple. Freeze-dried cationic calcium phosphate nanorods as versatile carriers of nucleic acids (dna, sirna). *Journal of Materials Chemistry*, 22(1):199–204, 2012.

[7] S C Lee, H W Choi, H J Lee, K Ja Kim, J Ho Chang, S Y Kim, J Choi, K-S Oh, and Y-K Jeong. In-situ synthesis of reactive hydroxyapatite nano-crystals for a novel approach of surface grafting polymerization. *Journal of Materials Chemistry*, 17(2):174–180, 2007.

[8] K Ganesan, A Kovtun, S Neumann, R Heumann, and M Epple. Calcium phosphate nanoparticles: Colloidally stabilized and made fluorescent by a phosphate-functionalized porphyrin. *J. Mater. Chem.*, 18(31):3655–3661, 2008.

[9] R L Williams, M J Hadley, P J Jiang, N A Rowson, P M Mendes, J Z Rappoport, and L M Grover. Thiol modification of silicon-substituted hydroxyapatite nanocrystals facilitates

fluorescent labelling and visualisation of cellular internalisation. *J. Mater. Chem. B*, 1(35):4370–4378, 2013.

[10] T White, C Ferraris, J Kim, and S Madhavi. Apatite–an adaptive framework structure. *Reviews in mineralogy and geochemistry*, 57(1):307–401, 2005.

[11] N Rameshbabu, TS Sampath Kumar, TG Prabhakar, VS Sastry, KVGK Murty, and K Prasad Rao. Antibacterial nanosized silver substituted hydroxyapatite: synthesis and characterization. *Journal of Biomedical Materials Research Part A*, 80(3):581–591, 2007.

[12] A Bigi, E Boanini, C Capuccini, and M Gazzano. Strontium-substituted hydroxyapatite nanocrystals. *Inorganica Chimica Acta*, 360(3):1009–1016, 2007.

[13] E S Thian, J Huang, S M Best, Z H Barber, R A Brooks, N Rushton, and W Bonfield. The response of osteoblasts to nanocrystalline silicon-substituted hydroxyapatite thin films. *Biomaterials*, 27(13):2692–2698, 2006.

[14] A M Pietak, J W Reid, M J Stott, and M Sayer. Silicon substitution in the calcium phosphate bioceramics. *Biomaterials*, 28(28):4023–4032, 2007.

[15] MY Shie, HC Chang, and SJ Ding. Effects of altering the si/ca molar ratio of a calcium silicate cement on in vitro cell attachment. *International Endodontic Journal*, 45(4):337–345, 2012.

[16] M Vallet-Regí and D Arcos. Silicon substituted hydroxyapatites. a method to upgrade calcium phosphate based implants. *J. Mater. Chem.*, 15(15):1509–1516, 2005.

[17] H J Lee, S E Kim, H W Choi, C W Kim, K J Kim, and S C Lee. The effect of surface-modified nano-hydroxyapatite on biocompatibility of poly (ε-caprolactone)/hydroxyapatite nanocomposites. *European polymer journal*, 43(5):1602–1608, 2007.

[18] I R Gibson, SM Best, and W Bonfield. Chemical characterization of silicon-substituted hydroxyapatite. *Journal of biomedical materials research*, 44(4):422–428, 1999.

[19] D Arcos, J Rodrıguez-Carvajal, and M Vallet-Regı. The effect of the silicon incorporation on the hydroxylapatite structure. a neutron diffraction study. *Solid state sciences*, 6(9):987–994, 2004.

[20] J Engstrand, A López, H Engqvist, and C Persson. Polyhedral oligomeric silsesquioxane (poss)–poly (ethylene glycol)(peg) hybrids as injectable biomaterials. *Biomedical Materials*, 7(3):035013, 2012.

[21] B M Barth, R Sharma, E İ Altınoğlu, T T Morgan, S S Shanmugavelandy, J M Kaiser, C McGovern, G L Matters, J P Smith, M Kester, et al. Bioconjugation of calcium phosphosilicate composite nanoparticles for selective targeting of human breast and pancreatic cancers in vivo. *ACS nano*, 4(3):1279–1287, 2010.

[22] A Bahdod, S El Asri, A Saoiabi, T Coradin, and A Laghzizil. Adsorption of phenol from an aqueous solution by selected apatite adsorbents: Kinetic process and impact of the surface properties. *Water research*, 43(2):313–318, 2009.

[23] K Kandori, S Oda, M Fukusumi, and Y Morisada. Synthesis of positively charged calcium hydroxyapatite nano-crystals and their adsorption behavior of proteins. *Colloids and Surfaces B: Biointerfaces*, 73(1):140–145, 2009.

[24] X Qiu, Z Hong, J Hu, L Chen, Xi Chen, and X Jing. Hydroxyapatite surface modified by l-lactic acid and its subsequent grafting polymerization of l-lactide. *Biomacromolecules*, 6(3):1193–1199, 2005.

[25] K Duan and R Wang. Surface modifications of bone implants through wet chemistry. *J. Mater. Chem.*, 16(24):2309–2321, 2006.

[26] M Nelson, G Balasundaram, and T J Webster. Increased osteoblast adhesion on nanoparticulate crystalline hydroxyapatite functionalized with krsr. *International journal of nanomedicine*, 1(3):339, 2006.

[27] N D Meeks, S Rankin, and D Bhattacharyya. Sulfur-functionalization of porous silica particles and application to mercury vapor sorption. *Industrial & Engineering Chemistry Research*, 49(10):4687–4693, 2010.

[28] A Wani, E Muthuswamy, G H Layan Savithra, G Mao, S Brock, and D Oupickỳ. Surface functionalization of mesoporous silica nanoparticles controls loading and release behavior of mitoxantrone. *Pharmaceutical research*, pages 1–12, 2012.

[29] S B Hartono, S Z Qiao, J Liu, K Jack, B P Ladewig, Z Hao, and G Q Max Lu. Functionalized mesoporous silica with very large pores for cellulase immobilization. *The Journal of Physical Chemistry C*, 114(18):8353–8362, 2010.

[30] K Onuma and A Ito. Cluster growth model for hydroxyapatite. *Chemistry of materials*, 10(11):3346–3351, 1998.

[31] V Uskoković and D P Uskoković. Nanosized hydroxyapatite and other calcium phosphates: chemistry of formation and application as drug and gene delivery agents. *Journal of Biomedical Materials Research Part B: Applied Biomaterials*, 96(1):152–191, 2011.

[32] P N Kumta, C Sfeir, D-H Lee, D Olton, and D Choi. Nanostructured calcium phosphates for biomedical applications: novel synthesis and characterization. *Acta Biomaterialia*, 1(1):65–83, 2005.

[33] S V Dorozhkin and M Epple. Biological and medical significance of calcium phosphates. *Angewandte Chemie International Edition*, 41(17):3130–3146, 2002.

[34] F CM Driessens and R MH Verbeeck. *Biominerals*. CRC Press, 1990.

[35] S V Dorozhkin. Amorphous calcium (ortho) phosphates. *Acta biomaterialia*, 6(12):4457–4475, 2010.

[36] E Boanini, M Gazzano, and A Bigi. Ionic substitutions in calcium phosphates synthesized at low temperature. *Acta biomaterialia*, 6(6):1882–1894, 2010.

[37] J.C. Elliot. *Structure and Chemistry of the Apatites and Other Calcium Orthophosphates (Studies in Inorganic Chemistry)*. Studies in Inorganic Chemistry (Book 18). Elsevier Science, 1st edition edition, 1994.

[38] A S Posner, F Betts, and N C Blumenthal. Formation and structure of synthetic and bone hydroxyapatites. *Progress in Crystal Growth and Characterization*, 3(1):49–64, 1980.

[39] Lj Brečević, V Hlady, and H Füredi-Milhofer. Influence of gelatin on the precipitation of amorphous calcium phosphate. *Colloids and surfaces*, 28:301–313, 1987.

[40] A Dey, P H H Bomans, F A Müller, J Will, P M Frederik, N A J M Sommerdijk, et al. The role of prenucleation clusters in surface-induced calcium phosphate crystallization. *Nature materials*, 9(12):1010–1014, 2010.

[41] S Kim, H-S Ryu, H Shin, H S Jung, and K S Hong. In situ observation of hydroxyapatite nanocrystal formation from amorphous calcium phosphate in calcium-rich solutions. *Materials chemistry and physics*, 91(2):500–506, 2005.

[42] C-G Wang, J-W Liao, B-D Gou, J Huang, R-K Tang, J-H Tao, T-L Zhang, and K Wang. Crystallization at multiple sites inside particles of amorphous calcium phosphate. *Crystal Growth and Design*, 9(6):2620–2626, 2009.

[43] X YangáLiu, H YaoáXu, et al. Mystery of the transformation from amorphous calcium phosphate to hydroxyapatite. *Chemical Communications*, 46(39):7415–7417, 2010.

[44] H Cölfen and S Mann. Higher-order organization by mesoscale self-assembly and transformation of hybrid nanostructures. *Angewandte Chemie International Edition*, 42(21):2350–2365, 2003.

[45] J D Termine and E D Eanes. Comparative chemistry of amorphous and apatitic calcium phosphate preparations. *Calcified tissue research*, 10(1):171–197, 1972.

[46] M Dutour Sikirić and H Füredi-Milhofer. The influence of surface active molecules on the crystallization of biominerals in solution. *Advances in colloid and interface science*, 128:135–158, 2006.

[47] D Mavrilas, A Apostolaki, J Kapolos, PG Koutsoukos, M Melachrinou, V Zolota, and D Dougenis. Development of bioprosthetic heart valve calcification in vitro and in animal models: morphology and composition. *Journal of crystal growth*, 205(4):554–562, 1999.

[48] N Stone, R Baker, K Rogers, A William Parker, and P Matousek. Subsurface probing of calcifications with spatially offset raman spectroscopy (sors): future possibilities for the diagnosis of breast cancer. *Analyst*, 132(9):899–905, 2007.

[49] I Cacciotti, A Bianco, M Lombardi, and L Montanaro. Mg-substituted hydroxyapatite nanopowders: synthesis, thermal stability and sintering behaviour. *Journal of the European Ceramic Society*, 29(14):2969–2978, 2009.

[50] P Habibovic and JE Barralet. Bioinorganics and biomaterials: bone repair. *Acta biomaterialia*, 7(8):3013–3026, 2011.

[51] M M Dvorak, A Siddiqua, D T Ward, D Howard Carter, S L Dallas, E F Nemeth, and D Riccardi. Physiological changes in extracellular calcium concentration directly control osteoblast function in the absence of calciotropic hormones. *Proceedings of the National Academy of Sciences of the United States of America*, 101(14):5140–5145, 2004.

[52] M Vallet-Regi and J María González-Calbet. Calcium phosphates as substitution of bone tissues. *Progress in Solid State Chemistry*, 32(1):1–31, 2004.

[53] E M Carlisle. Silicon: a possible factor in bone calcification. *Science*, 167(3916):279–280, 1970.

[54] E M Carlisle. Biochemical and morphological changes associated with long bone abnormalities in silicon deficiency. *The Journal of nutrition*, 110(5):1046–1056, 1980.

[55] K Schwarz and D B Milne. Growth-promoting effects of silicon in rats. *Nature*, 239:333 – 334, 1972.

[56] D M Reffitt, N Ogston, R Jugdaohsingh, H F J Cheung, B A J Evans, R P H Thompson, J J Powell, and G N Hampson. Orthosilicic acid stimulates collagen type 1 synthesis and osteoblastic differentiation in human osteoblast-like cells in vitro. *Bone*, 32(2):127–135, 2003.

[57] K Schwarz. A bound form of silicon in glycosaminoglycans and polyuronides. *Proceedings of the National Academy of Sciences*, 70(5):1608–1612, 1973.

[58] F Balas, J Pérez-Pariente, and M Vallet-Regí. In vitro bioactivity of silicon-substituted hydroxyapatites. *Journal of Biomedical Materials Research Part A*, 66(2):364–375, 2003.

[59] X L Tang, X F Xiao, and R F Liu. Structural characterization of silicon-substituted hydroxyapatite synthesized by a hydrothermal method. *Materials Letters*, 59(29):3841–3846, 2005.

[60] E S Thian, J Huang, M E Vickers, S M Best, Z H Barber, and W Bonfield. Silicon-substituted hydroxyapatite (siha): A novel calcium phosphate coating for biomedical applications. *Journal of materials science*, 41(3):709–717, 2006.

[61] Z Y Qiu, G Li, Y Q Zhang, J Liu, W Hu, J Ma, and S M Zhang. Fine structure analysis and sintering properties of si-doped hydroxyapatite. *Biomedical Materials*, 7(4):045009, 2012.

[62] A E Porter, N Patel, J N Skepper, S M Best, and W Bonfield. Comparison of in vivo dissolution processes in hydroxyapatite and silicon-substituted hydroxyapatite bioceramics. *Biomaterials*, 24(25):4609–4620, 2003.

[63] K A Hing, P A Revell, N Smith, and T Buckland. Effect of silicon level on rate, quality and progression of bone healing within silicate-substituted porous hydroxyapatite scaffolds. *Biomaterials*, 27(29):5014–5026, 2006.

[64] A E Porter, N Patel, J N Skepper, S M Best, and W Bonfield. Effect of sintered silicate-substituted hydroxyapatite on remodelling processes at the bone–implant interface. *Biomaterials*, 25(16):3303–3314, 2004.

[65] N Patel, S M Best, W Bonfield, I R Gibson, K A Hing, E Damien, and P A Revell. A comparative study on the in vivo behavior of hydroxyapatite and silicon substituted hydroxyapatite granules. *Journal of Materials Science: Materials in Medicine*, 13(12):1199–1206, 2002.

[66] W Lai, J Garino, and P Ducheyne. Silicon excretion from bioactive glass implanted in rabbit bone. *Biomaterials*, 23(1):213–217, 2002.

[67] A E Porter, C M Botelho, M A Lopes, J D Santos, S M Best, and W Bonfield. Ultrastructural comparison of dissolution and apatite precipitation on hydroxyapatite and silicon-substituted hydroxyapatite in vitro and in vivo. *Journal of Biomedical Materials Research Part A*, 69(4):670–679, 2004.

[68] A Gisep, R Wieling, M Bohner, S Matter, E Schneider, and B Rahn. Resorption patterns of calcium-phosphate cements in bone. *Journal of Biomedical Materials Research Part A*, 66(3):532–540, 2003.

[69] C Ritchlin. Fibroblast biology: Effector signals released by the synovial fibroblast in arthritis. *Arthritis Res*, 2(5):1–5, 2000.

[70] K Gomi, B Lowenberg, G Shapiro, and JE Davies. Resorption of sintered synthetic hydroxyapatite by osteoclasts¡ i¿ in vitro¡/i¿. *Biomaterials*, 14(2):91–96, 1993.

[71] M B Pabbruwe, O C Standard, C C Sorrell, and C Rolfe Howlett. Effect of silicon doping on bone formation within alumina porous domains. *Journal of Biomedical Materials Research Part A*, 71(2):250–257, 2004.

[72] M Bohner. Silicon-substituted calcium phosphates–a critical view. *Biomaterials*, 30(32):6403–6406, 2009.

[73] C M Botelho, M A Lopes, I R Gibson, S M Best, and J D Santos. Structural analysis of si-substituted hydroxyapatite: zeta potential and x-ray photoelectron spectroscopy. *Journal of Materials Science: Materials in Medicine*, 13(12):1123–1127, 2002.

[74] G Gasqueres, C Bonhomme, J Maquet, F Babonneau, S Hayakawa, T Kanaya, and A Osaka. Revisiting silicate substituted hydroxyapatite by solid-state nmr. *Magnetic Resonance in Chemistry*, 46(4):342–346, 2008.

[75] E Gentleman, Y C Fredholm, G Jell, N Lotfibakhshaiesh, M D O'Donnell, R G Hill, and M M Stevens. The effects of strontium-substituted bioactive glasses on osteoblasts and osteoclasts *in vitro*. *Biomaterials*, 31(14):3949–3956, 2010.

[76] C Capuccini, P Torricelli, E Boanini, M Gazzano, R Giardino, and A Bigi. Interaction of sr-doped hydroxyapatite nanocrystals with osteoclast and osteoblast-like cells. *Journal of Biomedical Materials Research Part A*, 89(3):594–600, 2009.

[77] E Landi, A Tampieri, G Celotti, S Sprio, M Sandri, and G Logroscino. Sr-substituted hydroxyapatites for osteoporotic bone replacement. *Acta Biomaterialia*, 3(6):961–969, 2007.

[78] D Laurencin, N Almora-Barrios, N H De Leeuw, C Gervais, C Bonhomme, F Mauri, W Chrzanowski, J C Knowles, R J Newport, A Wong, et al. Magnesium incorporation into hydroxyapatite. *Biomaterials*, 32(7):1826–1837, 2011.

[79] T A Fuierer, M LoRe, S A Puckett, and G H Nancollas. A mineralization adsorption and mobility study of hydroxyapatite surfaces in the presence of zinc and magnesium ions. *Langmuir*, 10(12):4721–4725, 1994.

[80] S Kannan, IAF Lemos, JHG Rocha, and JMF Ferreira. Synthesis and characterization of magnesium substituted biphasic mixtures of controlled hydroxyapatite/¡ i¿ β¡/i¿-tricalcium phosphate ratios. *Journal of Solid State Chemistry*, 178(10):3190–3196, 2005.

[81] S J Kalita and H A Bhatt. Nanocrystalline hydroxyapatite doped with magnesium and zinc: Synthesis and characterization. *Materials Science and Engineering: C*, 27(4):837–848, 2007.

[82] E Landi, G Logroscino, L Proietti, A Tampieri, M Sandri, and S Sprio. Biomimetic mg-substituted hydroxyapatite: from synthesis to in vivo behaviour. *Journal of Materials Science: Materials in Medicine*, 19(1):239–247, 2008.

[83] F Ren, R Xin, X Ge, and Y Leng. Characterization and structural analysis of zinc-substituted hydroxyapatites. *Acta Biomaterialia*, 5(8):3141–3149, 2009.

[84] A Bigi, E Foresti, M Gandolfi, M Gazzano, and N Roveri. Inhibiting effect of zinc on hydroxylapatite crystallization. *Journal of inorganic biochemistry*, 58(1):49–58, 1995.

[85] S Hayakawa, K Ando, K Tsuru, A Osaka, E Fujii, K Kawabata, C Bonhomme, and F Babonneau. Structural characterization and protein adsorption property of hydroxyapatite particles modified with zinc ions. *Journal of the American Ceramic Society*, 90(2):565–569, 2007.

[86] C Ergun, T J Webster, R Bizios, and R H Doremus. Hydroxylapatite with substituted magnesium, zinc, cadmium, and yttrium. i. structure and microstructure. *Journal of biomedical materials research*, 59(2):305–311, 2002.

[87] F Miyaji, Y Kono, and Y Suyama. Formation and structure of zinc-substituted calcium hydroxyapatite. *Materials Research Bulletin*, 40(2):209–220, 2005.

[88] X Li, Y Sogo, A Ito, H Mutsuzaki, N Ochiai, T Kobayashi, S Nakamura, K Yamashita, and R Z LeGeros. The optimum zinc content in set calcium phosphate cement for promoting bone formation *in vivo*. *Materials Science and Engineering: C*, 29(3):969–975, 2009.

[89] Y Tang, H F Chappell, M T Dove, R J Reeder, and Y J Lee. Zinc incorporation into hydroxylapatite. *Biomaterials*, 30(15):2864–2872, 2009.

[90] T J Webster, E A Massa-Schlueter, J L Smith, and E B Slamovich. Osteoblast response to hydroxyapatite doped with divalent and trivalent cations. *Biomaterials*, 25(11):2111–2121, 2004.

[91] I Mayer, O Jacobsohn, T Niazov, J Werckmann, M Iliescu, M Richard-Plouet, O Burghaus, and D Reinen. Manganese in precipitated hydroxyapatites. *European Journal of Inorganic Chemistry*, 2003(7):1445–1451, 2003.

[92] I Mayer, FJG Cuisinier, S Gdalya, and I Popov. Tem study of the morphology of Mn^{2+}-doped calcium hydroxyapatite and β-tricalcium phosphate. *Journal of inorganic biochemistry*, 102(2):311–317, 2008.

[93] A Bigi, B Bracci, F Cuisinier, R Elkaim, M Fini, I Mayer, IN Mihailescu, G Socol, L Sturba, and P Torricelli. Human osteoblast response to pulsed laser deposited calcium phosphate coatings. *Biomaterials*, 26(15):2381–2389, 2005.

[94] JC Merry, IR Gibson, SM Best, and W Bonfield. Synthesis and characterization of carbonate hydroxyapatite. *Journal of Materials Science: Materials in Medicine*, 9(12):779–783, 1998.

[95] A Porter, N Patel, R Brooks, S Best, N Rushton, and W Bonfield. Effect of carbonate substitution on the ultrastructural characteristics of hydroxyapatite implants. *Journal of Materials Science: Materials in Medicine*, 16(10):899–907, 2005.

[96] G Spence, N Patel, R Brooks, and N Rushton. Carbonate substituted hydroxyapatite: resorption by osteoclasts modifies the osteoblastic response. *Journal of Biomedical Materials Research Part A*, 90(1):217–224, 2009.

[97] E Landi, G Celotti, G Logroscino, and A Tampieri. Carbonated hydroxyapatite as bone substitute. *Journal of the European Ceramic Society*, 23(15):2931–2937, 2003.

[98] F Velard, J Braux, J Amedee, and P Laquerriere. Inflammatory cell response to calcium phosphate biomaterial particles: an overview. *Acta biomaterialia*, 9(2):4956–4963, 2013.

[99] J R Porter, T T Ruckh, and K C Popat. Bone tissue engineering: a review in bone biomimetics and drug delivery strategies. *Biotechnology Progress*, 25(6):1539–1560, 2009.

[100] M Manzano and M Vallet-Regí. Revisiting bioceramics: Bone regenerative and local drug delivery systems. *Progress in Solid State Chemistry*, 40(3):17–30, 2012.

[101] S Bose and S Tarafder. Calcium phosphate ceramic systems in growth factor and drug delivery for bone tissue engineering-a review. *Acta Biomaterialia*, 2011.

[102] R Shu, R McMullen, MJ Baumann, and LR McCabe. Hydroxyapatite accelerates differentiation and suppresses growth of mc3t3-e1 osteoblasts. *Journal of Biomedical Materials Research Part A*, 67(4):1196–1204, 2003.

[103] M Kamitakahara, C Ohtsuki, and T Miyazaki. Review paper: behavior of ceramic biomaterials derived from tricalcium phosphate in physiological condition. *Journal of biomaterials applications*, 23(3):197–212, 2008.

[104] P Roach, D Eglin, K Rohde, and C C Perry. Modern biomaterials: a review—bulk properties and implications of surface modifications. *Journal of Materials Science: Materials in Medicine*, 18(7):1263–1277, 2007.

[105] C Combes and C Rey. Adsorption of proteins and calcium phosphate materials bioactivity. *Biomaterials*, 23(13):2817–2823, 2002.

[106] A A Campbell, L Song, X S Li, B J Nelson, C Bottoni, D E Brooks, and E Schuyler DeJong. Development, characterization, and anti-microbial efficacy of hydroxyapatite-chlorhexidine coatings produced by surface-induced mineralization. *Journal of biomedical materials research*, 53(4):400–407, 2000.

[107] S Li, H Garreau, and M Vert. Structure-property relationships in the case of the degradation of massive poly (α-hydroxy acids) in aqueous media. *Journal of Materials Science: Materials in Medicine*, 1(4):198–206, 1990.

[108] H Li and J Chang. ph-compensation effect of bioactive inorganic fillers on the degradation of plga. *Composites science and technology*, 65(14):2226–2232, 2005.

[109] J E Barralet, S Aldred, A J Wright, and A G A Coombes. In vitro behavior of albumin-loaded carbonate hydroxyapatite gel. *Journal of biomedical materials research*, 60(3):360–367, 2002.

[110] H Tin Ong, J SC Loo, F Y C Boey, S J Russell, J Ma, and K-W Peng. Exploiting the high-affinity phosphonate–hydroxyapatite nanoparticle interaction for delivery of radiation and drugs. *Journal of Nanoparticle Research*, 10(1):141–150, 2008.

[111] P Frayssinet, N Rouquet, and D Mathon. Bone cell transfection in tissue culture using hydroxyapatite microparticles. *Journal of Biomedical Materials Research Part A*, 79(2):225–228, 2006.

[112] D Olton, J Li, M E Wilson, T Rogers, J Close, L Huang, P N Kumta, and C Sfeir. Nanostructured calcium phosphates (nanocaps) for non-viral gene delivery: influence of the synthesis parameters on transfection efficiency. *Biomaterials*, 28(6):1267–1279, 2007.

[113] B Mostaghaci, B Loretz, R Haberkorn, G Kickelbick, and C Michael Lehr. One-step synthesis of nanosized and stable amino-functionalized calcium phosphate particles for dna transfection. *Chemistry of Materials*, 25(18):3667–3674, 2013.

[114] T Welzel, I Radtke, W Meyer-Zaika, R Heumann, and M Epple. Transfection of cells with custom-made calcium phosphate nanoparticles coated with dna. *Journal of Materials Chemistry*, 14(14):2213–2217, 2004.

[115] V V Sokolova, I Radtke, R Heumann, and M Epple. Effective transfection of cells with multi-shell calcium phosphate-dna nanoparticles. *Biomaterials*, 27(16):3147–3153, 2006.

[116] V Sokolova, S Neumann, A Kovtun, S Chernousova, R Heumann, and M Epple. An outer shell of positively charged poly (ethyleneimine) strongly increases the transfection efficiency of calcium phosphate/dna nanoparticles. *Journal of materials science*, 45(18):4952–4957, 2010.

[117] C E Pedraza, D C Bassett, M D McKee, V Nelea, U Gbureck, and J E Barralet. The importance of particle size and dna condensation salt for calcium phosphate nanoparticle transfection. *Biomaterials*, 29(23):3384–3392, 2008.

[118] R W Walters and M J Welsh. Mechanism by which calcium phosphate coprecipitation enhances adenovirus-mediated gene transfer. *Gene therapy*, 6(11), 1999.

[119] F Labat-Moleur, A-Marie Steffan, C Brisson, H Perron, O Feugeas, P Furstenberger, F Oberling, E Brambilla, and JP Behr. An electron microscopy study into the mechanism of gene transfer with lipopolyamines. *Gene therapy*, 3(11):1010–1017, 1996.

[120] M Jordan and F Wurm. Transfection of adherent and suspended cells by calcium phosphate. *Methods*, 33(2):136–143, 2004.

[121] C Andres, V Sinani, D Lee, Y Gun'ko, and N Kotov. Anisotropic calcium phosphate nanoparticles coated with 2-carboxyethylphosphonic acid. *Journal of Materials Chemistry*, 16(40):3964–3968, 2006.

[122] O Rotan, V Sokolova, P Gilles, W Hu, S Dutt, T Schrader, and M Epple. Transport of supramolecular drugs across the cell membrane by calcium phosphate nanoparticles. *Materialwissenschaft und Werkstofftechnik*, 44(2-3):176–182, 2013.

[123] R Gonzalez-McQuire, J-Y Chane-Ching, E Vignaud, A Lebugle, and S Mann. Synthesis and characterization of amino acid-functionalized hydroxyapatite nanorods. *Journal of Materials Chemistry*, 14(14):2277–2281, 2004.

[124] M B Murphy, J D Hartgerink, A Goepferich, and A G Mikos. Synthesis and in vitro hydroxyapatite binding of peptides conjugated to calcium-binding moieties. *Biomacromolecules*, 8(7):2237–2243, 2007.

[125] S Haque, I Rehman, and J A Darr. Synthesis and characterization of grafted nanohydroxyapatites using functionalized surface agents. *Langmuir*, 23(12):6671–6676, 2007.

[126] S C D'Andre and A Y Fadeev. Covalent surface modification of calcium hydroxyapatite using n-alkyl-and n-fluoroalkylphosphonic acids. *Langmuir*, 19(19):7904–7910, 2003.

[127] H J Lee, H W Choi, K J Kim, and S C Lee. Modification of hydroxyapatite nanosurfaces for enhanced colloidal stability and improved interfacial adhesion in nanocomposites. *Chemistry of materials*, 18(21):5111–5118, 2006.

[128] L Borum-Nicholas and OC Wilson Jr. Surface modification of hydroxyapatite. part i. dodecyl alcohol. *Biomaterials*, 24(21):3671–3679, 2003.

[129] H Tanaka, A Yasukawa, K Kandori, and T Ishikawa. Modification of calcium hydroxyapatite using alkyl phosphates. *Langmuir*, 13(4):821–826, 1997.

[130] H Tanaka, A Yasukawa, K Kandori, and T Ishikawa. Surface modification of calcium hydroxyapatite with hexyl and decyl phosphates. *Colloids and Surfaces A: Physicochemical and Engineering Aspects*, 125(1):53–62, 1997.

[131] L Chen, J M Mccrate, J CM Lee, and H Li. The role of surface charge on the uptake and biocompatibility of hydroxyapatite nanoparticles with osteoblast cells. *Nanotechnology*, 22(10):105708, 2011.

[132] L Borum and OC Wilson. Surface modification of hydroxyapatite. part ii. silica. *Biomaterials*, 24(21):3681–3688, 2003.

[133] G L Witucki. A silane primer: chemistry and applications of alkoxy silanes. *Journal of coatings technology*, 65:57–57, 1993.

[134] U Johansson, A Holmgren, W Forsling, and R L Frost. Adsorption of silane coupling agents onto kaolinite surfaces. *Clay Minerals*, 34(2):239–246, 1999.

[135] D L Allara, A N Parikh, and F Rondelez. Evidence for a unique chain organization in long chain silane monolayers deposited on two widely different solid substrates. *Langmuir*, 11(7):2357–2360, 1995.

[136] D G Kurth and T Bein. Surface reactions on thin layers of silane coupling agents. *Langmuir*, 9(11):2965–2973, 1993.

[137] P E Laibinis and G M Whitesides. . omega.-terminated alkanethiolate monolayers on surfaces of copper, silver, and gold have similar wettabilities. *Journal of the American Chemical Society*, 114(6):1990–1995, 1992.

[138] H Ishida, C-h Chiang, and J L Koenig. The structure of aminofunctional silane coupling agents: 1. γ-aminopropyltriethoxysilane and its analogues. *Polymer*, 23(2):251–257, 1982.

[139] Dow Corning Corporation. A guide to silane solutions: Silane coupling agents. Electronic PDF, 2014.

[140] S Wang, S Wen, M Shen, R Guo, X Cao, J Wang, and X Shi. Aminopropyltriethoxysilane-mediated surface functionalization of hydroxyapatite nanoparticles: synthesis, characterization, and in vitro toxicity assay. *International journal of nanomedicine*, 6:3449–3459, 2010.

[141] GK Toworfe, RJ Composto, IM Shapiro, and P Ducheyne. Nucleation and growth of calcium phosphate on amine-, carboxyl-and hydroxyl-silane self-assembled monolayers. *Biomaterials*, 27(4):631–642, 2006.

[142] Q Liu, J R de Wijn, K de Groot, and C A van Blitterswijk. Surface modification of nano-apatite by grafting organic polymer. *Biomaterials*, 19(11):1067–1072, 1998.

[143] Z Demjen, B Pukánszky, E Földes, and J Nagy. Interaction of silane coupling agents with caco¡ sub¿ 3¡/sub¿. *Journal of colloid and interface science*, 190(2):427–436, 1997.

[144] Z Demjén, B Pukanszky, and J Nagy. Evaluation of interfacial interaction in polypropylene/surface treated caco¡ sub¿ 3¡/sub¿ composites. *Composites Part A: Applied Science and Manufacturing*, 29(3):323–329, 1998.

[145] Z Demjén, Bela Pukanszky, and J Nagy Jr. Possible coupling reactions of functional silanes and polypropylene. *Polymer*, 40(7):1763–1773, 1999.

[146] M-Christine Durrieu, S Pallu, F Guillemot, R Bareille, J Amédée, CH Baquey, C Labrugère, and M Dard. Grafting rgd containing peptides onto hydroxyapatite to promote osteoblastic cells adhesion. *Journal of Materials Science: Materials in Medicine*, 15(7):779–786, 2004.

[147] G Balasundaram, M Sato, and T J Webster. Using hydroxyapatite nanoparticles and decreased crystallinity to promote osteoblast adhesion similar to functionalizing with rgd. *Biomaterials*, 27(14):2798–2805, 2006.

[148] A N Vasiliev, E Zlotnikov, J G Khinast, and R E Riman. Chemisorption of silane compounds on hydroxyapatites of various morphologies. *Scripta Materialia*, 58(12):1039–1042, 2008.

[149] N N Herrera, J-M Letoffe, J-L Putaux, L David, and E Bourgeat-Lami. Aqueous dispersions of silane-functionalized laponite clay platelets. a first step toward the elaboration of water-based polymer/clay nanocomposites. *Langmuir*, 20(5):1564–1571, 2004.

[150] Abraham Clearfield. *Principles and Applications of Powder Diffraction*. John Wiley and Sons, Ltd, 2009.

[151] Bruker ASX Gmbh. S8 tiger spectrometry solutions. Brochure, 2011.

[152] T Dieing, O Hollricher, and J Toporski. *Confocal raman microscopy*, volume 158. Springer, 2011.

[153] The exomars rover instrument suite. http://exploration.esa.int/mars/45103-rover-instruments/?fbodylongid=2130, accessed 1st January 2014.

[154] Beckman Coulter. *Calcium (Arsenazo) Instructions*. Beckman Coulter, Inc., 250 S. Kraemer Blvd. Brea, CA 92821, USA, May 2010.

[155] Pointe Scientific Inc. *Calcium (Arsenazo) Reagent Set Instruction Manual*. Pointe Scientific, Inc. 5449 Research Drive, Canton, MI 48188, December 2009.

[156] P McFadyen and D. Fairhurst. Zeta potentials of nanoceramic materials - measurement and interpretation. Technical report, Brookhaven Instruments, Brookhaven Instruments Limited, Chapel House, Stock Wood, Worcestershire, B96 6ST, UK Brookhaven Instruments Limited, Chapel House, Stock Wood, Worcestershire, B96 6ST, UK., 1999.

[157] B. J Kirby and E. F. Hasselbrink Jr. Zeta potential of microfluidic substrates: 1. theory, experimental techniques, and effects on separations. *Electrophoresis*, 25:187–202, 2004.

[158] Malvern Instruments Ltd. Zeta potential an introduction in 30 minutes. Technical report, Malvern Instruments Ltd., Malvern Instruments Ltd., Enigma Business Park, Grovewood Road, Malvern, Worcestershire, WR14 1XZ., 2005.

[159] Pierce Biotechnology. *Instructions: Ellman's Reagent*. Thermo Fisher Scientific Inc, PO Box 117, 3747 N. Meridian Road, Rockford, lL 61105 USA., 2011.

[160] E Bouyer, F Gitzhofer, and M I Boulos. Morphological study of hydroxyapatite nanocrystal suspension. *Journal of Materials Science: Materials in Medicine*, 11(8):523–531, 2000.

[161] S Koutsopoulos. Synthesis and characterization of hydroxyapatite crystals: A review study on the analytical methods. *Journal of biomedical materials research*, 62(4):600–612, 2002.

[162] S Sprio, A Tampieri, E Landi, M Sandri, S Martorana, G Celotti, and G Logroscino. Physico-chemical properties and solubility behaviour of multi-substituted hydroxyapatite powders containing silicon. *Materials Science and Engineering: C*, 28(1):179–187, 2008.

[163] A Bianco, I Cacciotti, M Lombardi, and L Montanaro. Si-substituted hydroxyapatite nanopowders: synthesis, thermal stability and sinterability. *Materials Research Bulletin*, 44(2):345–354, 2009.

[164] T Tian, D Jiang, J Zhang, and Q Lin. Synthesis of si-substituted hydroxyapatite by a wet mechanochemical method. *Materials Science and Engineering: C*, 28(1):57–63, 2008.

[165] J Vandiver, D Dean, N Patel, C Botelho, S Best, J D Santos, M A Lopes, W Bonfield, and C Ortiz. Silicon addition to hydroxyapatite increases nanoscale electrostatic, van der waals, and adhesive interactions. *Journal of Biomedical Materials Research Part A*, 78(2):352–363, 2006.

[166] C Wu, T Xu, and W Yang. A new inorganic–organic negatively charged membrane: membrane preparation and characterizations. *Journal of membrane science*, 224(1):117–125, 2003.

[167] I Mobasherpour, M Soulati Heshajin, A Kazemzadeh, and M Zakeri. Synthesis of nanocrystalline hydroxyapatite by using precipitation method. *Journal of Alloys and Compounds*, 430(1):330–333, 2007.

[168] M Helena Santos, M de Oliveira, L P de Freitas Souza, H S Mansur, and W L Vasconcelos. Synthesis control and characterization of hydroxyapatite prepared by wet precipitation process. *Materials Research*, 7(4):625–630, 2004.

[169] J-J Shyue, M R De Guire, T Nakanishi, Y Masuda, K Koumoto, and C N Sukenik. Acid-base properties and zeta potentials of self-assembled monolayers obtained via in situ transformations. *Langmuir*, 20(20):8693–8698, 2004.

[170] S Orrenius, B Zhivotovsky, and P Nicotera. Regulation of cell death: the calcium–apoptosis link. *Nature Reviews Molecular Cell Biology*, 4(7):552–565, 2003.

[171] M P Mattson and S L Chan. Calcium orchestrates apoptosis. *Nature cell biology*, 5(12):1041–1043, 2003.

[172] G Hajnóczky, G Csordás, S Das, C Garcia-Perez, M Saotome, S S Roy, and M Yi. Mitochondrial calcium signalling and cell death: Approaches for assessing the role of mitochondrial Ca^{2+} uptake in apoptosis. *Cell calcium*, 40(5):553–560, 2006.

[173] M Markovic, B O Fowler, and M S Tung. Preparation and comprehensive characterization of a calcium hydroxyapatite reference material. *Journal of Research of the National Institute of Standards and Technology*, 109(6):553–568, 2004.

[174] P N De Aza, F Guitian, C Santos, S De Aza, R Cusco, and L Artus. Vibrational properties of calcium phosphate compounds. 2. comparison between hydroxyapatite and β-tricalcium phosphate. *Chemistry of materials*, 9(4):916–922, 1997.

[175] R G Carrodeguas and S De Aza. α-tricalcium phosphate: Synthesis, properties and biomedical applications. *Acta biomaterialia*, 7(10):3536–3546, 2011.

[176] W R Thompson, M Cai, M Ho, and J E Pemberton. Hydrolysis and condensation of self-assembled monolayers of (3-mercaptopropyl) trimethoxysilane on ag and au surfaces. *Langmuir*, 13(8):2291–2302, 1997.

[177] PTK Shih and JL Koenig. Raman studies of the hydrolysis of silane coupling agents. *Materials Science and Engineering*, 20:137–143, 1975.

[178] I Artaki, M Bradley, TW Zerda, and J Jonas. Nmr and raman study of the hydrolysis reaction in sol-gel processes. *The Journal of Physical Chemistry*, 89(20):4399–4404, 1985.

[179] AF Scott, JE Gray-Munro, and JL Shepherd. Influence of coating bath chemistry on the deposition of 3-mercaptopropyl trimethoxysilane films deposited on magnesium alloy. *Journal of colloid and interface science*, 343(2):474–483, 2010.

[180] J Gnado, P Dhamelincourt, C Pelegris, M Traisnel, and A Le Maguer Mayot. Raman spectra of oligomeric species obtained by tetraethoxysilane hydrolysis-polycondensation process. *Journal of non-crystalline solids*, 208(3):247–258, 1996.

[181] Y Abe and T Gunji. Oligo-and polysiloxanes. *Progress in polymer science*, 29(3):149–182, 2004.

[182] H Seki, T Kajiwara, Y Abe, and T Gunji. Synthesis and structure of ladder polymethylsilsesquioxanes from sila-functionalized cyclotetrasiloxanes. *Journal of Organometallic Chemistry*, 695(9):1363–1369, 2010.

[183] A N Zelikin, J F Quinn, and F Caruso. Disulfide cross-linked polymer capsules: en route to biodeconstructible systems. *Biomacromolecules*, 7(1):27–30, 2006.

[184] A N Zelikin, Q Li, and F Caruso. Disulfide-stabilized poly (methacrylic acid) capsules: formation, cross-linking, and degradation behavior. *Chemistry of materials*, 20(8):2655–2661, 2008.